Understanding on-surface structure formation and chemical transformations from theoretical spectroscopy

Hazem Aldahhak

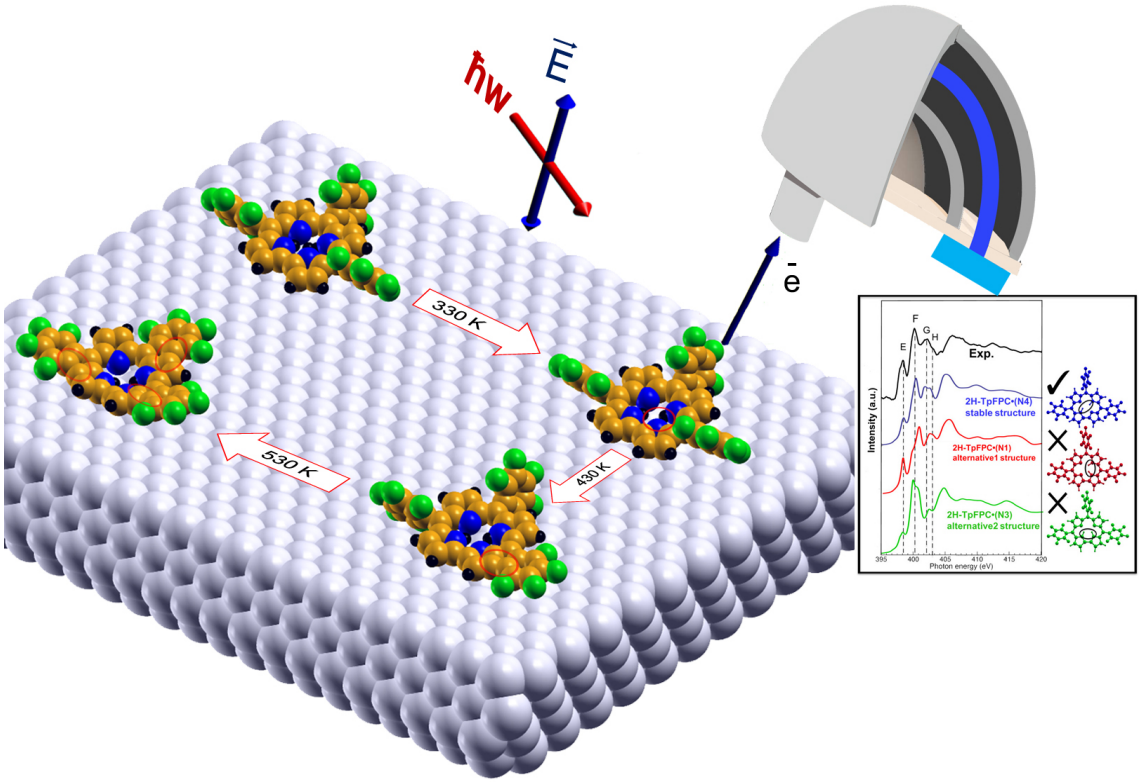

The cover image shows a free base corrole adsorbed on Ag(111) and its thermally-induced derivatives formed upon annealing up to 530 K. These chemical conversions (red ovals) have been determined at the microscopic scale. Furthermore, detailed information on the adsorption geometries of different corrole species have been provided. It is also demonstrated that the insight gained by theory-assisted NEXAFS enables us to address in a site-sensitive fashion the on-surface chemical reactions.

When you have eliminated the impossible, whatever remains, however improbable, must be the truth.

(Arthur Conan Doyle)

Universität Paderborn - Lehrstuhl für Theoretische Physik Dissertation zur Erlangung des akademischen Grades Doktor der Naturwissenschaften (Dr. rer. nat.)

Vorgelegt dem Department Physik der Fakultät für Naturwissenschaften Universität Paderborn

Hazem Aldahhak, MSc

Paderborn, den 20.09.2018

Name:	Hazem Aldahhak
Matrikelnummer:	6557045
Fakultät:	Naturwissenschaften
Department:	Physik
Eingereicht am:	20.09.2018

Promotionskommission:

Vorsitzender:	Prof. Dr. rer. nat. habil. Cedrik Meier (Universität Paderborn)
Erstgutachter:	Prof. Dr. rer. nat. habil. Wolf Gero Schmidt (Universität Paderborn)
Zweitgutachter:	Prof. Dr. rer. nat. Eva Rauls (Universität Stavanger)
Beisitzer:	Dr. rer. nat. Matthias Reichelt (Universität Paderborn)

Hazem Aldahhak, Understanding on-surface structure formation and chemical transformations from theoretical spectroscopy. PhD Thesis (in English), Department of Physics, Faculty of Science, University of Paderborn, Germany (2018).

Abstract

Organic molecules experience appealing applications in the industry of electronic devices. The key to developing the functionality of these applications lies in the thorough understanding of the electronic structure of the employed molecules and their interactions with the unavoidable surfaces.

In the first part of this thesis, state-of-the-art density functional theory (DFT) calculations in close collaboration with experiment have been presented to exemplary address the on-surface structure formation in the prototypical *(i)* perylene-based diindenoperylene molecule (DIP) on a reactive surface and in *(ii)* a functional molecule with a nonuniform internal charge distribution, namely the perylene-3,4,9,10-tetracarboxylic diahydride (PTCDA), on ionic surfaces. For both systems, the adsorption mechanisms have been rationalised and compared.

The second part of this thesis presents a DFT-guided multi-technique investigation on the interfacial chemistry of a macrocyclic low-symmetry molecule, namely the free-base 5,10,15-tris(pentafluorophenyl)corroles (H_3TpFPC), adsorbed on Ag(111). Combining structural modelling with high-level calculations of relevant X-ray core-levels and absorption edges, a detailed insight into the complex on-surface chemistry of corroles has been achieved. Beside corroborating the on-surface reactions and providing valuable information on the geometries of corrolic species, it is demonstrated that theory-assisted near edge X-ray absorption fine-structure (NEXAFS) spectroscopy enables the site-sensitive monitoring of on-surface chemical reactions, thus, providing information not accessible by other techniques.

Kurzfassung

Organische Moleküle erfahren derzeit wegen ihrer besonderen Anwendungen auf dem Gebiet der elektronischen Bauelementen große wissenschaftliche sowie industrielle Aufmerksamkeit. Der Schlüssel zur Entwicklung der Funktionalität dieser Anwendungen liegt im grundlegenden Verständnis der elektronischen Struktur der verwendeten Moleküle und ihrer Wechselwirkungen mit den erforderlichen Oberflächen.

Im ersten Teil dieser Arbeit werden DFT-Rechnungen in enger Zusammenarbeit mit dem Experiment eingesetzt, um die Ausbildung Oberflächenüberstrukturen zu untersuchen. Das geschieht anhand zweier organischer Moleküle, nämlich *(i)* zum einen Perylen-basierte Diindenoperylenmolekül (DIP) adsorbiert auf einer reaktiven Oberfläche, zum anderen *(ii)* ein funktionelles Moleküls mit einer ungleichmäßigeren Ladungsverteilung, nämlich das Perylen-3,4,9,10-tetracarbonsäuredihydrid (PTCDA), adsorbiert auf ionischen Oberflächen.

Im zweiten Teil der Arbeit wird eine DFT-unterstützte Multi-Technik-Untersuchung zur Grenzflächenchemie eines makrocyclischen niedersymmetrischen Moleküls, nämlich "free-Base" 5,10,15-tris(pentafluorophenyl)corroles (H_3TpFPC) auf Ag(111) präsentiert. Durch die Kombination von Strukturmodellierung mit der Berechnungen von relevanten Core-Level-Spektren und Röntgenabsorptionskanten wird dabei ein Zugang zu den Eigenschaften der auf der Oberfläche stattfindenden chemischen Reaktionen ermöglicht. Neben der Aufklärung der chemischen Reaktionen und der Bereitstellung von wertvollen Informationen über die allgemeine Geometrien von Free-base-Corroles, konnte somit gezeigt werden, dass die theorieunterstützte Röntgen-Nahkanten-Absorptions-Spektroskopie (NEXAFS) eine ortssensitive Überwachung von chemischen Reaktionen auf Oberflächen ermöglicht.

Contents

1 Introduction

> I have no special talent. I am only passionately curious.
>
> *(Albert Einstein)*

Scientific curiosity is an important key component for driving and inspiring the innovations in our ever evolving world. For many findings, which have positively affected our lives, we are all in dept for those with inquisitive minds and an insatiable thirst for discovery. In the past, many innovations have entirely changed our world and guided massive developments in our societies, e.g., the invention of the wheel, electricity, steam engines, printing press and penicillin. In the 20th century, the innovation of microelectronics in combination with the raised communication techniques, i.e., the Internet, broke new ground. They have changed our lifestyles in communicating, working and even shopping. Moreover, they opened up new possibilities for health care, energy production, education- and environment-related technologies.

The conventional technology of microelectronics is mostly based on inorganic materials, i.e. silicon. Owing to its fascinating properties, e.g., high stability, naturally abundance and high ability to be purified, silicon has led the development and the industry of microelectronic devices. After the great improvements in fabrication techniques, silicon-based devices have been manufactured with remarkable performance (e.g., transistors, diodes, and solar cells). However, the production process of silicon-based devices is rather expensive since it requires high temperatures and extensive cleaning procedures for material purity. Moreover, because of its optical properties and crystallinity, silicon is not a suitable material for applications where flexible setup or optical transparency of the devices is required.

In contrast, organic molecules are attracting increased attention as extremely promising candidates for future technology. They have the potential to be produced in transparent, light-weighted, easily processed, flexible and cheap components. Such unique properties have promoted intensive research on organic-based microelectronics and gave rise to novel industrial concepts beyond non-flexible and expensive silicon technology. Recently, various regular supramolecular architectures of organic molecules adsorbed on crystals have been designed [2] and many related products have arrived at the market (e.g., flexible displays, organic field-effect transistors (OFETs), organic light-emitting diodes (OLEDs) or photovoltaic solar cells). However, the realisation of organic electronics into industrially competing devices still facing challenges related to the limitations of charge transport and low stability against thermal decomposition. Apparently, the resulting properties are

strongly related to the employed molecules and to the structure in which they are arranged. Thus, careful understanding of the molecular structure on the atomic scale as well as improving of the synthesis techniques are crucial for alleviating the drawbacks of produced organic electronic devices and for optimising their properties to fulfil the technologically desired requirements [3, 4, 5, 6, 7].

The present work introduces theoretical calculations in collaboration with experimental measurements on the adsorption of three prototypes organic molecules on different metallic and insulator surfaces. The calculations analyse the structure formation in the studied systems and answer questions related to the role of the molecule-surface interactions, intermolecular interactions and the surface defects to steer the self-organisation patterns. Furthermore, the calculations address multiple-techniques for identification and full-characterisation of unknown molecular species and their covalent conversions on surfaces.

The key ingredients for designing organic-based devices with better performance lie in the interdisciplinary collaboration between experiment and theory. The experiment tells us what happens for a system upon certain circumstances, while the theory tries to conceptualise the system and to explain what happened on the atomic scale. Like this, the theory could provide a framework suitable for studying similar systems or could suggest better circumstances which assist cost- and time-efficient experimental setups. However, state-of-the-art theoretical methods are still facing challenges related to the accuracy of calculations and to the high computational costs. Thus, a suitable computing method, which provides sufficiently accurate results and requires less computational resources, should be well chosen. As a theory tool, the density functional theory (DFT) has been employed in the whole work. This theory, which receives more explanation in the second chapter, is one of the most known and versatile methods in the computational physics and chemistry fields. This is because it can provide accurate results for low computational costs. DFT is an exact scheme in principle, but it relies on approximations in practice (e.g., the so-called exchange-correlation functional) that the calculated property can differ from the measurement depending on the employed exchange-correlation functional [8].

In the first part of this work, the structure formation in Diindenoperylene (DIP, $C_{32}H_{16}$) molecules on metallic Cu(111) surfaces is analysed. DIP molecules have attracted a considerable interest due to their potential applications in optoelectronic devices (see Refs. [9, 10, 11]). DIP molecules are reported to exhibit on Cu(111) surfaces different adsorption patterns depending on the substrate width [1]. They arrange in short range orders on wide terraces, but in one-dimensional structures parallel or perpendicular to step edges on narrow terraces. According to Ref. [1], this behaviour might arise from the packing effects between the step edges. To illustrate this behaviour and to further address on the electronic and geometric properties of different adsorption patterns, section 3.1 presents first principles DFT calculations to investigate the balance between intermolecular and molecule-substrate interactions of DIP molecules on planar surfaces and near step-edges.

The second part of this work introduces the adsorption of a functional molecule on ionic surfaces. In the past, metal surfaces have frequently been used as substrate. Experimentally, metal substrates induce screening and quenching effects and thus hamper the detailed spectroscopy of the adsorbed overlayer [12]. In contrast, molecular adsorption on ionic crystals like sodium or potassium chloride induces minimal structural modifications of the molecular electronic structure. Consequently, the molecular intrinsic properties (e.g. the molecular orbitals and the optical response) are better preserved allowing for studying molecular properties with help of sophisticated surface analysis techniques, e.g. scanning tunnelling microscopy [13, 14, 15]. Furthermore, ionic surfaces like KCl and NaCl have wide band gaps of 8.4 eV and 8.5 eV, respectively [16] and can be used to insulate electronic device regions. However, constructing well-defined electric contacts on insulating substrates is still a difficult task, but with great hopes for future applications. The organic-insulator interfaces tailor the band gap of the insulator, which opens the door for many applications in the field of optical devices [17, 18]. In the context of investigating the adsorption of organic materials on ionic surfaces, section 3.2 presents and compare the adsorption of PTCDA on KCl and NaCl(100) surfaces. Similar to the steps done for DIP on Cu(111), the electronic and geometric aspects of single molecules on planar terraces, the diffusion barriers, the monolayers patterns, and the influence of monoatomic steps to initiate the structure formation have been investigated in detail.

The third part (see chapter 4) presents theory-guided multi techniques to illustrate the on-surface chemistry of a complex molecular system. In particular, it addresses the identification of unknown molecular species and their covalent conversions on surfaces in a site-selective fashion. This is highly relevant for various fields ranging from traditional ones such as heterogeneous catalysis to more timely ones such as the pulsating topic of on-surface synthesis. It is well known that unambiguous insights are notoriously complicated to achieve in these research areas. As an example, X-ray photoemission spectroscopy is often employed to unravel the on-surface chemistry of smaller molecules. However, for challenging tasks, e.g., the distinction of highly similar species such as tautomeric or isomeric structures of larger compounds, the obtained information remains ambiguous. Here, a methodological advancement extending the existing tools for analysing on-surface chemical conversions have been introduced. We demonstrate that by analysing angle-dependent near-edge X-ray absorption fingerprints on the bases of a high-quality theoretical description it is possible to go beyond the power of XPS and to trace on-surface reactions in a complex system reaching site-selectivity. On the example of free-base corrole adsorbed on a silver surface, we show that the employed approach features the resolving power to distinguish between the possible tautomers of the intact species, discriminate between three potential dehydrogenation places, and identify at which out of six sites a defluorinative ring-closure reaction actually occurs.

The remainder of this thesis is organised as follows: the second chapter shortly introduces the theoretical concepts which are required for the derivation of structural and spectral properties. In chapter 3, the structure formation in Diindenoperylene on Cu(111) and in PTCDA on KCl(100) and NaCl(100) surfaces are presented and compared. Based on

the achieved results, suggestions for getting long-ranged orders of DIP on Cu(111) are proposed. Chapter 4 is devoted to investigate the free base corroles on Ag(111) from the multilayer reference to the on-surface chemical transformations. Thereby, the identification of unknown molecular species and their covalent conversions on surfaces are addressed. Finally, chapter 5 summaries the main results of the present work and suggest ideas for future work.

2 Theoretical concepts and Methods

Wer die Sicherheit der
Mathematik verachtet, stürzt sich
in das Chaos der Gedanken

(Leonardo da Vinci)

After the tremendous development of computers in recent 30 years, the computer-aided methods and techniques have enabled a deep understanding of the matter on the atomic scale and, thus, assisted the great development of materials science research and industry. This chapter presents the basic concepts a prominent method in the field of computational materials science, namely the density functional theory (DFT) as workhorse of this thesis. After introducing the general framework of the theory, the approximations and concepts which make it practical are shortly presented (see Refs. [19, 20, 21, 22] for further reading). Then, an approach to account for the van-der-Waals (vdW) interactions and the basic theoretical concepts to calculate the X-ray Photoelectron Spectroscopy (XPS) as well as the Near-Edge X-ray-Absorption Fine Structure (NEXAFS) fingerprints are shortly presented.

2.1 The Many Body Problem

The fundamental description of the chemical or physical properties of a material implies an understanding of its structure at the microscopic scale. At this scale, the matter can be considered as a collection of mutually interacting nuclei and electrons (many-particle system) defined by an associated Hamiltonian $\mathbb{H}$ and a quantum mechanical wave function $|\Psi\rangle$. In the static non-relativistic case, such system can be described by the solution of the time-independent Schrödinger equation:

$$\mathbb{H}\Psi(r,R) = E\Psi(r,R) \tag{2.1}$$

with the Hamiltonian operator of the general form:

$$\mathbb{H} = T_{\mathrm{K}} + T_{\mathrm{e}} + V_{\mathrm{KK}} + V_{\mathrm{eK}} + V_{\mathrm{ee}}, \tag{2.2}$$

where $\{r\}$ and $\{R\}$ represent the coordinates of the electrons and the nuclei, respectively. The other operators describe the kinetic energy of moving nuclei (T_{K}), the kinetic energy of moving electrons (T_{e}), the nucleus-nucleus interaction (V_{KK}), the potential energy of

the electrons in the field of the nuclei (V_{eK}) and the electron-electron interaction (V_{ee}), respectively.

Except for very small systems, e.g., a hydrogen atom or small molecules, it is impossible to solve equation 2.1 neither analytically nor numerically, at least by the state-of-art computers. Therefore, approximations must be introduced to treat the investigated systems more efficiently.

The first approximation used here is the so-called Born-Oppenheimer approximation [23]. This approximation is justified by the fact that the mass of a nucleus is larger than that of an electron by at least three orders of magnitude. The electrons are, thus, moving much more faster compared to the relatively "slow" motion of the nuclei. Accordingly, it is allowed to separate the degrees of freedom $\{r\}$ of the electrons from those of the nuclei $\{R\}$, where it can be assumed that the electrons instantaneously adapt to the movements of the ions. Thus, the *electronic* many-body problem could be, first, solved for a fixed positions of ions $\{R\}$, i.e., by solving

$$\mathbb{H}_{\mathrm{el}}\psi_{\mathrm{el}} = E_{\mathrm{el}}\psi_{\mathrm{el}}, \tag{2.3}$$

where $\mathbb{H}_{\mathrm{el}} = T_{\mathrm{e}} + V_{\mathrm{ee}} + V_{\mathrm{eK}}$ and ψ_{el} are the electronic Hamiltonian and wave function, respectively. Then, the positions of the ions can be optimised by minimising the system's total energy, where the electronic many-body problem is solved for each altered positions of the ions.

Even after the application of the Born-Oppenheimer approximation, the direct solution of equation 2.3 is still very complicated for a system composed of N electrons. In particular, it turns out to be numerically very demanding in cases of large or spatially extended systems, like e.g., molecules. The next section presents the DFT as a particular methodology to deal with this problem, whereby the many-body problem of N electrons, possessing 3N spatial coordinates, is reduced to a problem with only three spatial coordinates.

2.1.1 Density Functional Theory (DFT)

The basic idea of Density functional theory (DFT) is to employ the density of particles $n(\vec{r})$ to characteristically calculate all properties of a system without even knowing the many-dimensional wave function, whose calculation is not only painstaking but also impractical in many cases. This particular property of DFT enables it to be applicable to very large systems since the calculations do not depend on the coordinates of individual electrons anymore, but only on their density which is always three dimensional quantity irrespective of their numbers within the system [19, 22].

Before discussing the core parts of the DFT, namely the Hohenberg-Kohn (HK) theorems and the Kohn-Sham equation, we come back to equation 2.3, which describes an N-electron system, and classify the Hamiltonian into an internal part $\mathrm{V}_{\mathrm{int}}$ (the kinetic energy of the

electrons and the mutual Coulomb interaction with each other) and an external part V_{ext} which describes the Coulomb interaction with the nuclei as it follows:

$$\mathbb{H}_e = \underbrace{T_e + V_{ee}}_{:=V_{int}} + \underbrace{V_{eK}}_{:=V_{ext}}, \tag{2.4}$$

Since V_{int} is always the same for a given system, the eigenfunctions and thus the associated eigenvalues depend only on the external potential V_{ext}.

2.1.1.1 Hohenberg-Kohn theorems

The Hohenberg-Kohn (HK) theorems [24] legitimise the employment of the electron density as the basic variable in the DFT. According to the first HK theorem, the external potential $V_{ext}(\vec{r})$ and thus also the ground state energy E_0 are uniquely determined by the ground state electron density $n_0(\vec{r})$. The total energy of the system can be, thus, expressed as a functional of the charge density:

$$E[n] = T[n(r)] + V[n(r)] + V_{ext}[n(r)] = F_{HK}[n(r)] + \int \nu_{ext}(r) \cdot n(r) \cdot dr \tag{2.5}$$

The by Hohenberg and Kohn introduced functional amount $F_{HK}[n(r)]$ expresses the internal energy (it does not depend on V_{ext}) in dependence on the electron density.
The second Hohenberg-Kohn (HK) theorem gives rise to a variational principle, where it proves that the ground state density n_0 minimises the total energy of the system E[n] to the ground state energy E_0 which renders the DFT as a primarily ground state theory (see Ref. [24] for further information).

2.1.1.2 The Kohn-Sham equations

The HK theorems explicitly validate the calculation of the ground-state energy by minimising the energy functional with respect to the electron density. However, these theorems do not tell us how to obtain the ground-state density in practice. Furthermore, the quantity $F_{HK}[n(r)]$ is completely unknown, rendering the direct minimisation of $E[n]$ as impractical.

A possible scheme to make DFT feasible is the so-called Kohn-Sham (KS) formulation [25]. Within this approach, the many-body Schrödinger equation is re-introduced as a set of independent particle problem, while all other many-body effects are combined into one entity denoted as exchange-correlation functional $E_{xc}[n]$.
Considering the functional $F_{HK}[n(r)]$, it can be decomposed into the following terms:

$$F_{HK}[n(r)] = T_s[n] + V_H[n] + E_{xc}[n] \tag{2.6}$$

By this, the kinetic energy of the interacting particles is replaced by that of the non-interacting particles $T_s[n]$ of density n (known only for jellium systems). The second

term $V_{\mathrm{H}}[n] = \frac{1}{2}\int \frac{n(r)\cdot n(r')}{|r-r'|} d^3r d^3r'$ is the classical term of the electron-electron interaction (replaced by the Hartee energy), while the term E_{xc} is the so-called exchange-correlation energy. As already mentioned, this term represents the differences between an interacting and a non-interacting system, i.e. T - $\mathrm{T_s}$ and V - $\mathrm{V_H}$. The electronic ground state can be determined by variating $E[n]$ with respect to the electron density δn:

$$\frac{\delta E[n]}{\delta n} \stackrel{!}{=} 0. \tag{2.7}$$

As a constraint for this variation, the number of particles must be preserved ($N_{\mathrm{e}} = \int n(r) \cdot d^3r$), where the formulation of the additional condition can be realised by a Lagrange multiplier [26] μ as follows:

$$\frac{\delta}{\delta n}\left\{E[n] - \mu\left(\int n(r)\cdot d^3r - N_{\mathrm{e}}\right)\right\} = 0 \tag{2.8}$$

Inserting these equations together yields:

$$\mu = \frac{\delta E[n]}{\delta n} = \frac{\delta T_{\mathrm{s}}[n]}{\delta n(r)} + \underbrace{\frac{\delta}{\delta n}\left\{\int n(r)\nu_{ext}(r)d^3r + \frac{1}{2}\int \frac{n(r)\cdot n(r')}{|r-r'|} d^3r d^3r' + E_{\mathrm{xc}}[n]\right\}}_{:=V_{\mathrm{eff}}} \tag{2.9}$$

Note that, despite equation (2.9) describes an interacting system, it looks like an equation of non-interacting particles moving in an effective potential $\mathrm{V_{eff}} = \mathrm{V_H} + \mathrm{V_{xc}} + \mathrm{V_{ext}}$ [27]. This implies a transformation of the interacting system into a single-particle picture with *exactly* the same ground-state density. Up to this point, no approximations have been introduced and everything is accurate. The following approximation enables us to introduce one-particle wave functions for the "independent" particles:

$$n(r) = \sum_{i=1}^{\infty} f_i \left|\phi_i(r)\right|^2 \tag{2.10}$$

where f_i denotes the occupation number of the orbital $\phi_i(r)$. Notably, the terms $T_{\mathrm{s}}[n]$ and $E_{\mathrm{xc}}[n]$ are still unknown. The kinetic energy of the independent particles system can be expressed by the one-particle wave functions as:

$$T_{\mathrm{s}}[n] = \sum_{i=1}^{\infty} f_i \left\langle \phi_i \left| -\frac{\nabla^2}{2} \right| \phi_i \right\rangle \tag{2.11}$$

By substituting 2.11 into 2.9 and performing a functional derivation with respect to $\phi_i^*(r)$, one obtains a corresponding Schrödinger equation [25]:

$$\left[-\frac{\hbar^2\nabla^2}{2m} + V_{\mathrm{eff}}(r)\right]\left|\phi_i(r)\right\rangle = \epsilon_i \left|\phi_i(r)\right\rangle \tag{2.12}$$

This one-electron Schrödinger-like equation is known as Kohn-Sham equation. It yields the Kohn-Sham eigenvalues ϵ_i and the Kohn-Sham orbitals $\phi_i(r)$, through which the ground-state density $n_0(r)$ can be calculated.

Since V_{eff} depends on $n(r)$ which in turn depends on $\phi_i(r)$ (which in turn depends on V_{eff}), the Kohn-Sham equations must be solved in an iterative self-consistent procedure. By this, one starts with an initial guess of the electron density to construct the effective potential via Eq. (2.9). Then Eq. (2.12) is solved to get a set of Kohn-Sham orbitals $\phi_i(r)$, which enable the calculation of the new density according to Eq. (2.10). After getting the new density, these steps are repeated until the self-consistency is achieved (in practice: until the difference between two consecutive steps is below a definite threshold).

As long as all terms in the Kohn-Sham equation are known, the exact ground-state density and the exact ground-state energy can be achieved. Unfortunately, the exchange-correlation functional $E_{\text{xc}}[n]$, which includes the non-classical aspects of the electron-electron interactions, is not exactly known and has to be approximated for the practical application of the theory.

2.1.1.3 Exchange-correlation (XC) functionals

After the widespread employment of DFT within the literature, a huge variety of approximations, differing in their forms and complexity, have been suggested to calculate the exchange-correlation functional. For example, the so-called local density approximation (LDA) is one of the most simple, but often successful, approaches. By which the energy functional is expressed as:

$$E_{\text{xc}}^{LDA}[n] = \int n(r) \cdot \epsilon_{\text{xc}}(n(r)) \cdot dr \tag{2.13}$$

where ϵ_{xc} is the exchange-correlation energy per electron of a uniform electron gas of density $n(r)$ [25]. It is possible to further separate the term ϵ_{xc} into exchange and the correlation entities [28]:

$$\epsilon_{\text{xc}}(n(r)) = \epsilon_{\text{x}}(n(r)) + \epsilon_{\text{c}}(n(r)) \tag{2.14}$$

The term ϵ_{x} is explicitly known (see Ref. [28], page 71-72), while the correlation energy is calculated from highly precise Quantum Monte Carlo calculations performed on the homogeneous electron gas. Such work was mostly done by Ceperley and Alder [29, 30], while the other commonly used LDA functionals, e.g., Perdew-Zunger [31] and Perdew-Wang [32], have just shown other methods to parameterise ϵ_{c} based on sophisticated interpolation schemes. Since LDA is derived from the homogeneous electron gas model, it provides good description for slowly varying density systems (simple metals). However, it turns out to be less satisfactory for molecules due to the large density variations over short distances within their structures [28]. In particular, LDA is reported to often overestimates molecular binding energies and, consequently, underestimates the corresponding bond lengths (see Ref. [22] for further reading).

In an apparent converse to the picture of the homogeneous electron gas model, real systems are spatially inhomogeneous and exhibit varying densities. This information was included within the next generation of the exchange-correlation functionals, namely the so-called

generalised gradient approximation (GGA), where the density gradients $\nabla n(r)$ were taken into account beside the density itself, i.e.,

$$E_{\mathrm{XC}}^{\mathrm{GGA}} := \int d^3r \cdot n(r) \cdot \epsilon_{\mathrm{XC}}(n, \nabla n, \nabla^2 n, ..) \tag{2.15}$$

The inclusion of the density gradients within GGAs have yielded better results for some properties, e.g., hydrogen bonded systems are better described by GGA [33]. However, GGA does not give better results for systems like metals and their surfaces [22]. In particular, there is a huge variety of GGA functionals which are different in their explicit dependence on $n(r)$ and $\nabla n(r)$. A familiar approach within surface science fields is the so-called PW91 (Perdew-Wang) [34], which is used in this thesis. Another known approximations is the so-called PBE (Perdew, Burke, Enzerhof) [35], which has many editions [36, 37].

2.1.2 Periodic boundary conditions

2.1.2.1 Basis sets

As already mentioned, the Kohn-Sham (KS) equations enable us to calculate the ground-state properties of many-body system. To solve these equations in practice, the wave function $|\phi(r)\rangle$ is required to be spanned in Hilbert space with a complete basis set, e.g., atomic orbitals or plane-waves. In principle, the selection of such basis functions strongly depends on the investigated system. For a system like a small molecule, the hydrogen-like basis-sets, being localised on the atomic nuclei, exhibit an optimal choice so that the total solution is presented as a linear combination of atomic orbitals. However, this thesis concentrates on extended systems featuring a high degree of periodicity. Therefore, the delocalised plane-waves basis sets, which e.g., better reflect the periodicity of our problem, are apparently suitable approach for the present study. For better overview on different types of basis functions and their properties, Refs. [22, 38] are recommended.

To shortly illustrate the concept behind employing the plane-waves basis sets, one has to come back to the Bloch's theorem [39]. According to this theory, the wave function $\phi_j(r)$ of an electron being in a periodic potential $v_{\mathrm{ext}}(\vec{r}) = v_{\mathrm{ext}}(\vec{r} + \vec{a})$, can be expressed in *any* periodic function $u_i(r)$ which has the periodicity of the lattice:

$$\phi_j^{\vec{k}}(\vec{r}) = u_j^{\vec{k}}(\vec{r}) \cdot e^{i\vec{k}\cdot\vec{r}} \qquad \text{with} \qquad \phi_j^{\vec{k}}(\vec{r} + \vec{a}) = u_j^{\vec{k}}(\vec{r}).e^{i\vec{k}\cdot\vec{r}} \tag{2.16}$$

where $e^{i\vec{k}\cdot\vec{r}}$ is a phase factor and $\vec{k}$ is the corresponding wave vector in the Brillouin zone (BZ). The quantity $u_i(r)$ can be expressed by plane waves in reciprocal lattice vectors $\vec{G}$, so that the electronic wave functions can be obtained as a discrete Fourier transform:

$$\phi_j^{\vec{k}}(\vec{r}) = \frac{1}{\sqrt{\Omega}} \cdot \sum_{G=0}^{\infty} A_j^{\vec{k}}(\vec{G}) \cdot e^{i(\vec{k}+\vec{G})\cdot\vec{r}} \tag{2.17}$$

where $A_j(\vec{G})$ are the so-called Fourier coefficients and Ω is the volume of the unit cell. Analogously, the effective potential can be obtained in a similar transform

$$V_{\text{eff}}(r) = \sum_G V_{\text{eff}}(\vec{G}) \cdot e^{i\vec{G}\cdot\vec{r}} \tag{2.18}$$

By this, the terms within the Kohn-Sham equation (2.12) are simply formulated in reciprocal space, e.g., the kinetic energy:

$$E_{kin} = \Omega \cdot \sum_{j,\vec{k}} f_j^{\vec{k}} \sum_{G=0}^{\infty} \frac{1}{2} \left|\vec{k} + \vec{G}\right|^2 \cdot \left|A_j^k(\vec{G})\right|^2, \tag{2.19}$$

while the boundary conditions are automatically included over the G-space.

In principle, the exact numerical solution implies an extention of the summation over infinite Fourier series. This is technically prohibitive and a cut-off energy E_{cut} must be presented after a finite number of terms to reduce the required number of employed basis functions:

$$\frac{\hbar^2}{2m} |k + G|^2_{\text{max}} \leq E_{\text{cut}} \tag{2.20}$$

The power of this approach is that only one parameter, namely E_{cut}, completely controls the size of the plane-wave basis set, while the plane-wave basis functions are still orthogonal with no superposition errors. The increment of E_{cut} systematically improves the quality of the resulting electronic wave functions and energies but on an expense of further computational costs. Within the calculations, the selected E_{cut} should be the smallest one, which provides the accurate description of the system. Therefore, it must be carefully tested to ensure the convergence of the total energy with respect to it.

2.1.2.2 k-space integration

In oder to calculate many properties of the system (e.g., density of states, charge density, etc.), the KS equations should be formally integrated over the whole Brillouin zone (BZ), i.e., by calculating

$$\bar{A} = \frac{1}{\Omega_{\text{BZ}}} \int_{\Omega_{\text{BZ}}} d^3k \cdot A(k) \tag{2.21}$$

where $A(k)$ is a lattice-periodic function. In practise, the integral is reduced to a sum over a finite number of k-points within the BZ (N_{k}) which yields enough accuracy and accounts for the periodicity of $A(k)$. For example, according to Chadi and Kohn [40], the mean value $\bar{A}$ can be calculated as a weighted sum over $A(k)$:

$$\bar{A} \approx \sum_k^{N_k} w_k A(k) \qquad \text{with} \qquad \sum_k w_k = 1 \tag{2.22}$$

A common approach which does not depend on the type of the crystal cell is the so-called Monkhorst-Pack (MP) approach [41], which is used in this thesis. Within this scheme, the

sampling points are homogeneously distributed within the BZ. This is very advantageous since it is easy to construct N_k equidistant points along the reciprocal basis vectors of the unit cell, while the accuracy can be increased by choosing sufficiently large number of sampling points.

The MP scheme yields very good results for semiconductors and the insulators. In case of metals, which exhibit discontinuous at the Fermi energy for T = 0 K (change of the occupation from 1 to 0 at this temperature), smearing functions make the integrand smoother should be introduced. Within this thesis, the so-called Gaussian smearing has been employed. It is a known function, whereby a small artificial electronic temperature is created by employing the Gaussian-type delta function to broaden the energy levels around the Fermi level (note that beside the Gaussian smearing, other functions are known like, e.g., Fermi-Dirac for T $\neq$ 0 K, and so-called „cold“ smearings of Methfessel and Paxton [42] or Marzari and Vanderbilt [43]).

2.1.2.3 Supercell method

The supercell method is a model to artificially apply the three dimensions translational periodicity of the plane wave approach and its formulations to lower dimensional systems such as surfaces (2D system), nano wires (1D system) or atoms („0D“ system). By this, it is allowed to periodically repeat a structure in the three spatial dimensions despite it has no actual symmetry in all directions. As an example, we consider the case of a surface. Within this method, a surface is modelled as a three dimensional superstructure consists of alternating slabs of bulk material and vacuum regions (see Figure 2.1). The vacuum regions separate the slabs in z-direction and should be thick enough to guarantee negligible interactions with other slabs.

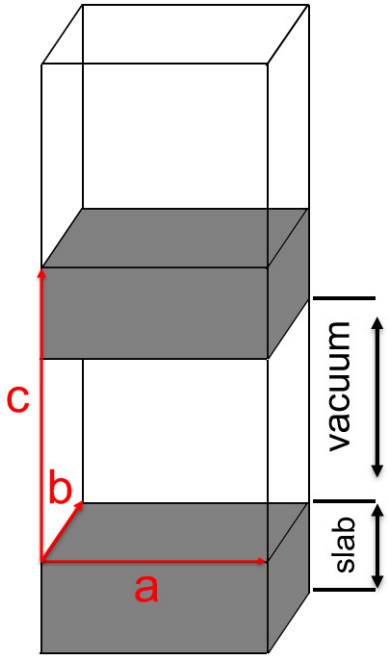

Figure 2.1: Representation of a surface by forming repeated slabs separated from each other by a vacuum, where a, b, c are basis vectors that show the periodicity of the supercell.

In cases of polar surfaces, the molecular adsorption on one side of the slab yields a non-vanishing dipole moment, which results into an artificial jump of the electrostatic potential in the direction of the surface normal. The created potential is unphysical and it should be corrected upon calculation. One way for correction is to symmetrically adsorb the molecule on both sides of the slab (see e.g., Ref. [44]). However, this method is sometimes impractical where it requires larger cells and larger number of atoms. Another way is to introduce a uniform dipole field along the surface normal which cancels the

artificial field (see Ref. [45]). The advantage the latter approach comes from the ability to include cells, which have a dipole moment without forcing the electrostatic potential to be periodic anymore [44].

2.1.3 The pseudopotential approach

The expansion of the electron wave function into plane waves of energies up to E_{cut} should provide an adequately accurate physical description of the system within manageable computational efforts. However, the KS wave functions feature strong oscillations in the vicinity of a nucleus due to the strongly fluctuating Coulomb potential in this region. Therefore, the expansion of the KS wave functions in the vicinity of the nucleus requires large number of plane waves ($\sim E_{cut}^{3/2}$) to converge, which is computationally demanding. Fortunately, the interesting physics and chemistry happen in the region of valence orbitals, while core electrons contribute less significantly to chemical properties of a matter. By this and since the description of the highly localised core wave function is computationally very expensive, it is possible to alleviate the problem of high computational costs by employing the so-called pseudopotential method.

The pseudopotential method eliminates the dependence on the corresponding degrees of freedom of core electrons and deals only with the chemically active valence electrons [46, 19]. Thereby, it deals with the core electrons as being „frozen“ and replaces both them and the nuclei by a rigid non-polarisable effective nucleus of charge of $Z_v = Z - Z_{core}$, where Z and Z_{core} are the charge of the atomic nucleus and that associated to core electrons, respectively. By this, the full atomic potential (all-electron), which results from the nucleus and core electrons, is replaced by an effective potential (pseudopotential). Besides, the wave functions of the valence electron, which strongly oscillate in the core region, is replaced by a smoothly varying pseudo-wave functions in the core region (see Figure 2.2).

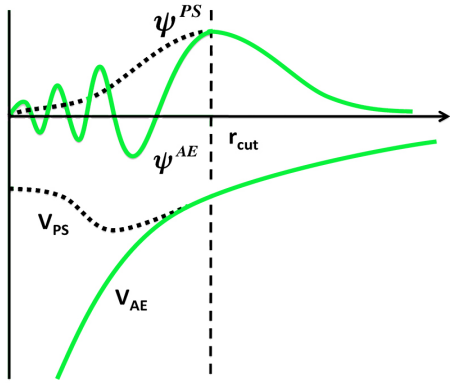

Figure 2.2: In the lower part, a schematic illustration of all-electron potential (V_{AE}, green) compared to pseudopotential (V_{PS}, black). The corresponding wave functions ψ^{AE} and ψ^{PS} are shown in the upper part, respectively. V_{PS} matches V_{AE} for $r > r_{cut}$.

The pseudopotential requires that both pseudo- and all-electron potentials exhibit the same energies and amplitude (the same density) in the region outside a definite core cut-off radius r_{cut}. The most common two classes of pseudopotentials, which are used in the plane-wave electronic structure codes, are the so-called norm-conserving (NCPP) [47] and ultrasoft [48] pseudopotentials. The norm-conserving pseudopotentials are constructed in a way that they must fulfil the following conditions: *(i)* Within the region up to the cut-off

radius (r_c) the *norm* of the pseudo-wave function is identical to the corresponding all-electron wave function.
(ii) Both pseudo- and all-electron wave functions are identical outside r_c.
In some cases, it turn out that high cutoff energies are required for reliable description of the system by means of NCPP, e.g. for the case of first-row elements (N, O, F) where the 2p all-electron wave functions are strongly localised near the core regions. For such cases, it is possible to reduce the cutoff energies and the accompanied computational costs by eliminating the charge associated with the orbitals from the core region allowing the wave functions to be as soft as possible but on the expense of violating the norm-conservation condition. Within the cutoff region, the all-electron wave function can also be mathematically reconstructed for the so-called projector augmented wave (PAW) pseudopotentials [49, 50].

It is important to note that despite the pseudopotential methods neglect the degrees of freedom of core electrons, they yield sufficiently accurate close to the fully self-consistent all-electron results [51].

2.1.4 Calculation of the forces: Hellmann-Feynman theorem

Up to now, the presented DFT framework concentrated on the *electronic* ground state energies and the Kohn-Sham wave functions for a given atomic configuration. However, finding the actual ground-state of a system implies the identification of the equilibrium atomic geometries, for which the forces at all atoms are at their minimum.

The description of the dynamic of atomic positions can be done in the framework of the Hellmann-Feynman theorem, which states that for an *exact* eigenstate ϕ the derivative of the ground-state energy of a Hamiltonian $\mathcal{H}_\lambda$ with respect to any degree of freedom λ (it is here the atomic coordinates) is equal the ground-state expectation value of the derivative of $\mathcal{H}_\lambda$ [52], i. e.,

$$\frac{\partial E}{\partial \lambda} = \frac{\partial}{\partial \lambda} \langle \phi | \mathcal{H}_\lambda | \phi \rangle = \left\langle \frac{\partial \phi}{\partial \lambda} \middle| \mathcal{H}_\lambda \middle| \phi \right\rangle + \left\langle \phi \middle| \frac{\partial \mathcal{H}_\lambda}{\partial \lambda} \middle| \phi \right\rangle + \left\langle \phi \middle| \mathcal{H}_\lambda \middle| \frac{\partial \phi}{\partial \lambda} \right\rangle = \left\langle \phi \middle| \frac{\partial \mathcal{H}_\lambda}{\partial \lambda} \middle| \phi \right\rangle . \tag{2.23}$$

Since the force in quantum mechanics can be expressed as $F = -\nabla_r \langle E \rangle$ where $\langle E \rangle = \min \langle \phi | E | \phi \rangle$ and $\langle \phi \mid \phi \rangle = 1$, the Eq. 2.23 is a useful recipe for calculating the ionic forces, where the energy is optimised with respect to the atomic coordinates.

However, the calculated wave function is definitely not exact if finite local basis sets are used. Thereby, the two terms $\left\langle \frac{\partial \phi}{\partial \lambda} \middle| \mathcal{H}_\lambda \middle| \phi \right\rangle$ and $\left\langle \phi \middle| \mathcal{H}_\lambda \middle| \frac{\partial \phi}{\partial \lambda} \right\rangle$ do not vanish anymore and the left and right terms within equation 2.23 are, then, not exactly equal. Indeed, this problem can be solved if ϕ is selected in way where it does not depend on λ anymore. This condition, which is known as Hurley condition [53, 54], is already satisfied in case of plane-wave basis set (The Hilbert space spanned by these basis function does not depend

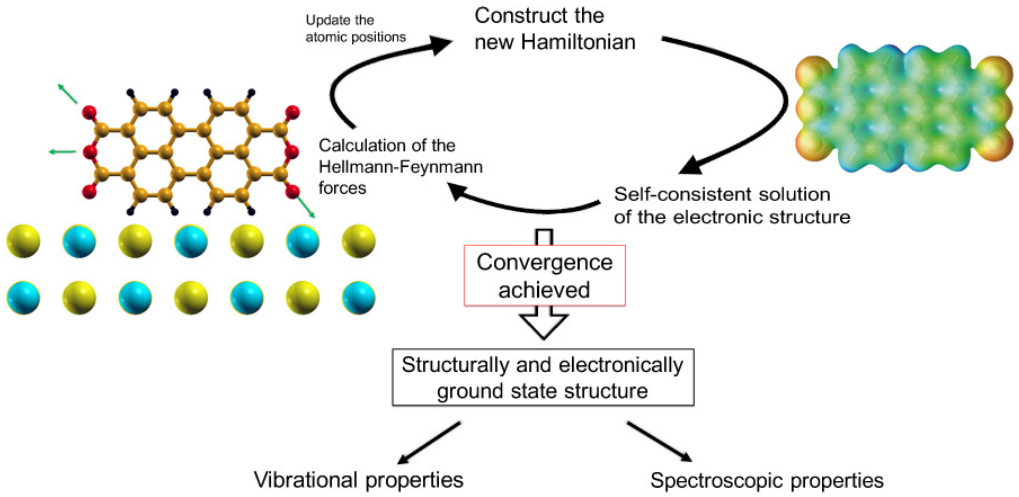

Figure 2.3: The general DFT procedure to calculate the ground state of a given system.

on the ionic positions). By this the forces can be directly derived from the ground-state wave function according to Hellmann-Feynman theorem:

$$F(r) = -\left\langle \phi \left| \frac{\partial \mathcal{H}}{\partial r} \right| \phi \right\rangle \tag{2.24}$$

Figure 2.3 shows the general DFT procedures to get the ground state of a given system. The calculations start with a good initial user-supplied atomic structure. For the corresponding geometries of the initial structure, the external potential V_{ext} is constructed with help of pseudopotentials and the electronic Kohn-Sham equations are self-consistently solved. After that, the forces are calculated according to the Hellmann-Feynman theorem and the atomic positions are updated to new geometries, which enter repeated loops until the Hellmann-Feynman forces are minimised.

2.1.5 The van-der-Waals interactions

Despite the local LDA and the semi-local GGA approaches (see section 2.1.1.3) provide successful descriptions for many systems (see e.g., Ref. [55]), they are far from accurate in describing other structures where the van der Waals interactions are dominant, like e.g., proteins and biomolecular surfaces. Benzene dimers are also a known example in this context, where employing the GGA alone does not yield any binding at all [56]. As already mentioned, these shortcomings can be traced back to the missing dispersion contributions within LDA and GGA. In principle, it is possible to accurately account for the dispersion interactions by performing high-level quantum mechanical wave function or quantum Monte Carlo methods or by the combination of exact exchange and correlation energy within the adiabatic-connection fluctuation-dissipation theorem. However, such

schemes are either very expensive, or complex or, sometimes, not transferable [57, 58, 59, 60].

Within this thesis, the dispersion interactions play an important role in the adsorption process. In order to approximately account for the influence of these interactions, an efficient semiempirical, so-called DFT-D scheme (see Ref. [61, 62]) based on the London dispersion formula has been considered. This approach was developed by Schmidt and co-workers and has been proven to be not only computationally extremely inexpensive but also sufficiently accurate in many cases [63, 64, 65].

The idea of this approach is that, despite the quantum-mechanical nature of the electron correlation, it is possible to understand the vdW interactions as an interaction between instantaneously fluctuating dipoles. This implies a behaviour proportional to R^{-6} (R is the distance between two neutral fragments), which enables a replacement of the vdW-energy by an empirical approach to describe the dispersion interactions [61]. Indeed, this approach is based on the description of London for the dispersive interactions [66, 67]. In order to account for the long-range electron correlation within this scheme, the interaction for each atom pair i and j separated with a distance $R = |R_i - R_j|$ is corrected with the attractive energy

$$\epsilon_{ij}^{vdW} = -f_{ij}(R)\frac{C_6^{ij}}{R^6} \tag{2.25}$$

whereby $f_{ij}(R)$ represents a damping function, which takes the value one for large values of R and zero for small values. The entity C_6^{ij} is called the virtual coefficient, which can be given as $C_6^{ij} = \frac{3}{2}\alpha_i\alpha_j\frac{I_iI_j}{I_i+I_j}$. The variables α_i and I_i are the polarisability and the ionisation potential of the atom at R_i, respectively. In principle, the latter quantities can be determined by ab initio calculations (see Ref. [61] for details). Since the vdW-interactions do not play a considerable role at small distance, an exponential damping function to cancel the R^{-6} singularity is suggested

$$f_{ij} = 1 - exp\left[-\lambda\left(\frac{R}{r_i^{cov} + r_j^{cov}}\right)^n\right] \tag{2.26}$$

where the intermolecular distance R is normalised to the covalent radius r_i^{cov}. The remaining parameters of the exponent and the damping constant are chosen so that they reproduce the lattice constant of graphite: $\lambda = 7.5 \times 10^{-4}$ and $n = 8$. The resulting vdW-energy $E^{vdw} = 0.5\sum_{i,j}\epsilon_{ij}^{vdW}$ is, then, added to the total DFT-energy.

2.2 X-ray Photoelectron Spectroscopy (XPS)

X-ray photoelectron spectroscopy (XPS) is a popular analysis technique that provides information on the structure of a material and its chemical states. In principle, it is a photoelectric effect and refers to irradiating a sample with X-ray photons to stimulate

core electrons beyond its vacuum level[1], while simultaneously analysing the kinetic energy of escaped electrons [69]. In some textbooks, XPS is also referred as ESCA (electron spectroscopy for chemical analysis). This nomenclature was denoted by Siegbahn et *al.* [70] to highlight the ability of XPS to provide chemical characterisation of the materials.

The basic physics of XPS is shown in Figure 2.4. The irradiation of a material with X-ray photons of energy $\hbar w$ (1) enables some electrons, which absorb the photons, to leave the probed sample (2) with a kinetic energy E_{kin}:

$$E_{\text{kin}} = \hbar\omega - E_{\text{b}} - \varphi. \tag{2.27}$$

In this equation, E_{b} represents the binding energy of an electron before being emitted (initial state), while $\varphi = E_{\text{vac}} - E_{\text{F}}$ is the required energy to excite the electron from the Fermi energy E_{F} to the vacuum energy E_{vac}, i.e., the binding energies are referenced to the Fermi level. By measuring the kinetic energies of emitted electrons it is possible to determine the chemical composition of the analysed material (see below).

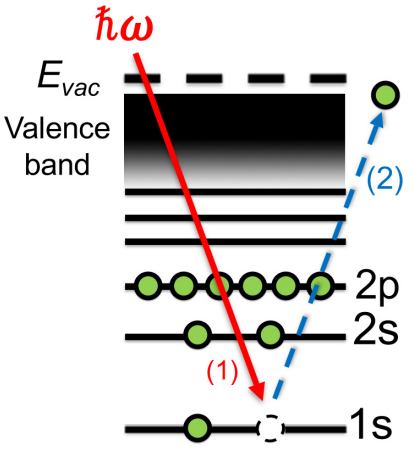

Figure 2.4: Schematic process of the X-ray photoelectron spectroscopy (XPS): The absorption of a photon of energy $\hbar w$ (1) results into an emission of a core electron (2).

Considering an electron in a specific energy level of a free atom (e.g., 1s), the binding energy (BE) refers to its interaction with the nucleus on one hand and to the electrostatic screening of this interaction on the other hand [68]. Thus, BE represents a characteristic fingerprint of each atomic element (see Table 2.1). However, for cases where the atom is involved in a chemical structure, the binding energy is shifted within few eVs according to the local chemical environment. Such change is denoted as the chemical shift or the core level shift (CLS), where its quantitive amount exclusively depends on the type of the environment (type of neighbour atom, surface potential, etc). As an example, an electron-withdrawing neighbour usually causes chemical shift to higher binding energies, whereas the electron-donating substituents cause chemical shifts to lower binding energies (see Table 2.2). By this, BE presents not only a sensitive tool to discriminate different atomic species, but also a fingerprint quantity to identify chemical environments.

For typical XPS measurements, the photon intensities are plotted in dependence with binding energies. This yields a number of peaks, each situated at a characteristic binding energy[2], assigned to a specific species, with a certain intensity related to the ratio of the

[1] The energy of the incident photon is typically in the range of 0.1-10 keV [68]. In cases of lower energies, e.g. up to 50 eV, the incident photons probe the valence energy levels of the material. The latter case is the called ultraviolet photoelectron spectroscopy (UPS) technique.

[2] If the emitted electron comes from s orbital, one peak is obtained. However, more than one peak result from p, d or f orbitals, according to the orbital degeneracy.

Element	Be	B	C	N	O	F
1s binding energy [eV]	113	191	287	402	531	686

Table 2.1: Average values of 1s binding energies some elements of the second row of the periodic table (values taken from Ref. [73]).

Functional group		C 1s [eV]	$\triangle 1s$ [eV]
alkanes	C-H, C-C	285.0	0.0
amine	C-N	286.0	1.0
Alcohols, ethers	C-OH,C-O-C	286.5	1.5
Chloride	C-Cl	286.5	1.5
Fluoride	C-F	287.8	2.8
Carbonyl	C=O	288	3.0
Trifluoride	$-CF_3$	293.0-294.0	8.0-9.0

Table 2.2: Typical C 1s binding energies of carbon atoms attached to a variety of different functional groups. The shifts $\triangle 1s$ with respect to the pure alkane are depicted. The more electron-withdrawing the chemical environment of carbon is, the more the XPS signal shifts to higher energies [74].

species within the sample (see chapter 4 for examples) [71, 72]. Based on this measurement, one could directly address the stoichiometric ratios of the investigated system and possibly the chemical structure of the investigated system. However, the direct assignment of binding energies to clear chemical environments and atomistic types is in many cases an elusive task. The reason for that might be the low experimental resolution or the large line-width compared to the separation of different species contributions. This circumvents their characteristic determination and allows the neighboured peaks to convolute into a single peak. For such cases, one has to rely on predictive calculations to interpret the experimental data.

The calculation of the CLS in the context of DFT has been presented in a variety of works, where different approaches to describe the dynamics of photoemission process have been employed [75, 76, 77, 78]. The most common and predictive models are the so-called initial state and the $\triangle$SCF approximations [79, 80, 81, 82]. The two approaches are similar in many aspects, e.g., both of them do not take into account the broadening of the line shape, which results from the dynamical process, but they deal the system as being static and could exist in a single, well-defined final state. However, within the initial state method, only what happens before the photoemission process is concerned. In other words, the relaxation of the core and valence electrons in the presence of core hole upon the ionisation of the core electron are neglected. The CLS can be, thus, calculated as the changes in the potential, which the core electrons feel as a result of different chemical environments. Conversely, the $\triangle$SCF method avoids the charge impurities which result from the electron removal and permits the valence electrons to fully relax and screen the extra charge. The latter method has been employed within this thesis. Therefore, it will be shortly described

in more details.

Suppose that a core electron has been ionised from an i-th atom, the corresponding chemical shift can be calculated according to the $\triangle$SCF method as the differences in the total energies between the initial state with N electrons (E^0) and the final state with $N-1$ electrons (E_i^+), where the valence electrons are fully relaxed to their ground state energies before and after the removal of the core electron[3]. The problem of this equation is that E_i^+ is an all-electron calculation, while only pseudopotentials are employed here. To deal with such difficulty one can follow the suggestion of Ref. [82], where a total energy calculation is performed by employing a special type of generated pseudopotential, which includes a hole in the corresponding core level (1s in this thesis), for the atom where the photoemission process has taken place.

It is important to note that the screening of the core hole strongly depends on the system. For a system containing plenty of free charges available to screen the core hole, e.g., a metal surface, an extra electron can be considered at the Fermi level leaving the system to have zero charge. In contrast, for an insulating systems or molecules in the gas phase (like those considered in this thesis), there is no free charges to screen the core hole and, thus, the calculated system carries an integer charge of $+1|e|$.

2.3 Near Edge X-ray Absorption Fine Structure Spectroscopy (NEXAFS)

It has been already mentioned that XPS provides valuable information on the chemical composition of the studied systems. However, this thesis concerns, beside identifying the chemical conversions, the subsequent geometrical changes of free base corroles on Ag(111) upon thermal annealing. Therefore, a complementary method suitable for this purpose has been employed, namely the Near Edge X-ray Absorption Fine Structure (NEXAFS).

2.3.1 Principles

NEXAFS is a powerful spectroscopic method for exploring the electronic and structural properties of the molecular structures. The history of this technique began in the 1920s by the works of Kossel [83] and Kronig [84]. Nevertheless, the first successful measurements were realised in early 1980s after the evolution of synchrotron radiation [85]. Since then, NEXAFS spectroscopy has been enormously progressed and successfully employed in different solid state and chemistry fields (e.g., ionic liquids [86, 87, 88], self-assembled monolayers and adsorption of gas molecules on surfaces [89, 90, 91, 92]. Indeed, this technique has shown a high ability to address the electronic structure of many investigated

[3] It is assumed that no geometrical modifications take place upon the photoemission process.

systems with high sensitivity to even small structural modifications [93], interfacial charge transfer [94, 95] and chemical modifications [96].

Despite NEXAFS is a X-ray-based technique, it differs from XPS in some fundamentals. XPS provides information on the occupied (core) levels of the system and involves a stimulation of a photoelectron to the vacuum level (ionisation potential), while the emitted electron itself is measured. In contrast, NEXAFS allows for studying the unoccupied bound or continuum states up to about 50 eV above the absorption edge (near edge). Within this technique, the photoelectron is excited to higher states without leaving the sample. Consequently, the core hole is filled by an Auger electron or by an electron from another shell followed by an emission of a fluorescent photon. Like this, the absorption is not directly measured by the excited electron, but by monitoring one of these secondary products [97].

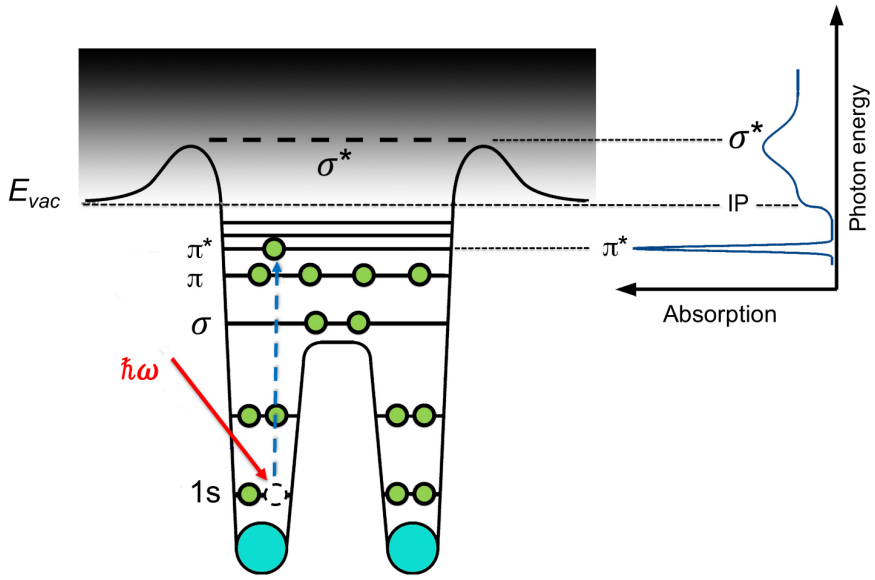

Figure 2.5: Schematic representation of NEXAFS principle for a diatomic molecule (blue): A core electron, which absorbs a photons of energy $\hbar w$, is excited into an unoccupied energy below the vacuum level (E_{vac}). The sharp peak corresponds to resonances in the π^* region. The broadened σ^* region lies above the ionisation potential (IP = E_{vac}), which appears as a step in the spectrum.

The overall shape of a NEXAFS spectrum is a series of characteristic peaks (resonances) situated at specific photon energies with given intensities. In order to understand the origin of these features, a schematic K-edge spectrum of a diatomic molecule is presented (see Figure 2.5). The transition of a core electron from the initial state 1s of energy E_i to a higher unoccupied molecular state (final state) of energy E_f is only possible if the energy of the absorbed photon ($\hbar w$) exactly matches the energy difference between these

two states:[4]

$$\hbar w = E_f - E_i \tag{2.28}$$

Now, if the photon energy is slowly varied and the photoabsorption cross section is recorded, only photons fulfilling Eq. 2.28 can be absorbed (see Figure 2.5). The excitation of a photoelectron to an unoccupied electronic state is reflected as a characteristic peak within the spectrum and can be related to a specific bond in a given geometry or chemical environment, i.e., it is possible to report on its electronic structure of the system.

Within the literature, the unoccupied states are categorised according to their symmetry as π^* or σ^* regions. Typically, the π^* resonances exist below the ionisation potential (IP) featuring sharp peaks. In contrast, the σ^* resonances appear at higher photon energies superimposed on the continuum with broader resonances. A characteristic feature of the measured spectra is their broadening. The experimental setup results into a Gaussian lineshape, while the vibrational motion of the molecules are responsible for the unsymmetrical broadenings [98]. Important to note that the broadenings of individual peaks are strongly influenced by their different lifetimes (results into Lorentzian lineshapes). Within the π^* region, the final state lifetime is determined by the de-excitation of excited electron resulting into well separated peaks within this region. In contrast, the larger broadening within the σ^* region can be traced back to the large overlap with the continuum, where the core hole probably decay to its states featuring, thus, rather short lifetimes. As a rule of thumb, the higher the photon energy, the larger is its linewidth [99, 100, 101].

2.3.2 Angular dependence: Information on the molecular structure

Beside the ability of giving deep insight into the electronic structure of unoccupied orbitals, NEXAFS is a particular technique to provide information on the geometries of adsorbed molecules and their fragments with respect to the substrate. The concept of this technique is that the intensities of the resonance peaks depend on the orientation of the molecule with respect to the polarisation of the radiation (hence the incident angle). Thus, by taking the NEXAFS measurements at different incidence of X-rays and comparing the intensity of peaks, it is possible to conclude on the spatial orientations on the interatomic bonds.

To further illustrate this idea, a simple example following Ref. [102] has been calculated. The planar conjugated benzene molecule (C_6H_6) adsorbs on Au(111) completely parallel to the surface featuring sp^2-hybridisation (see Figure 2.6). The σ-bonds lie in the molecular plane while the p_z-orbitals are perpendicular to the ring plane. Like that the final states π^* are parallel $\vec{O}$, which lies parallel to the surface normal. If δ is defined as the angle

[4] It should be also kept in mind that the transition follows the restrict selection rule that the quantum number of the final state (l_f) must differ from that of the initial state (l_i) by one: $l_f = l_i \pm 1$. Thus, transitions between s-type orbitals are not allowed and excitations from s into p-orbitals appear predominantly.

between $\vec{O}$ and the electric field $\vec{E}$, the intensity of a resonance (I) in case of linearly polarised light follows [103]:

$$I \propto \left|\vec{E} \cdot \vec{O}\right|^2 \propto cos^2(\delta) \tag{2.29}$$

Figure 2.6 illustrate how the intensities of the π^*-resonances are suitable parameters for quantitative evaluation of the angular dependence and thus the molecular geometries. For a normal incidence of X-ray beam (Figure 2.6 a), the intensity of the π^* resonances is virtually zero while it is maximal for the σ^* resonances. This is because the vector $\vec{E}$ is perpendicular to $\vec{O}$ and the overlap between them is at its minimum (according to Eq. 2.29, $\cos\,\delta = 0 \Rightarrow \delta = 90^o$). In contrast, for grazing incidence (here 20^o, Figure 2.6 b), $\vec{E}$ is almost parallel to $\vec{O}$. Consequently, the π^* resonances have almost a maximum intensity, while the σ^* resonances are almost quenched. Such difference in spectra depending on the incidence angle is denoted as linear dichroism; it is an indicator for existing a predominant conformation of adsorbed molecules on the surface[5].

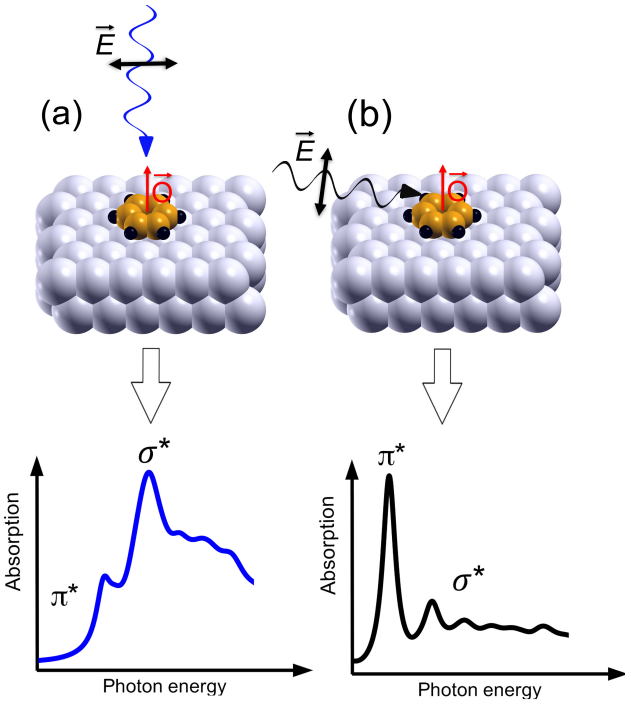

Figure 2.6: Schematic representation of the angular dependence of C K-edge NEXAFS of a benzene molecule on Ag(111). The π^* orbitals in this conjugated system are parallel to $\vec{O}$, while the σ^* orbitals are in the surface plane. (a) The case of a normal incidence: the overlap between $\vec{E}$ and the direction of the final state orbitals $\vec{O}$ is minimum. Thus the π^* resonances vanish, while the σ^* resonances are at their maximum. (b) The case of grazing incidence: π^* resonances have almost maximal intensity, while σ^* resonances are almost quenched.

In general, the spatial orientation of the molecules is different from such simple planar adsorption. Nevertheless, the already presented rules are still completely valid. If an interatomic bond is oriented with unknown angle (β) with respect to the underlaying surface, it is possible to report on such direction by comparing the relative intensities of the resonance for different incidence angle (θ). For a surface featuring threefold or higher symmetry (as the one in this thesis) the

[5] Note that XPS exhibits here a single peak for the C 1s spectrum of benzene. Thus, it can not tell anything about the geometries of the molecule.

peak intensities follow:

$$\begin{aligned} I &\propto \left\{ P.\left[cos^2\theta cos^2\beta + \frac{1}{2} sin^2\theta sin^2\beta \right] + (1-P)\left[\frac{1}{2} sin^2\beta \right] \right\} \\ &\propto \left\{ P.\frac{1}{3}\left[1 + \frac{1}{2}\left(3cos^2\theta - 1 \right)\left(3cos^2\beta - 1 \right) \right] + (1-P)\left[\frac{1}{2} sin^2\beta \right] \right\} \end{aligned} \tag{2.30}$$

where P is the polarisation of the light (see Ref. [102] for further details).

The interpretation of the NEXAFS spectra can be often obtained by employing the so-called "building block principle". This principle is based on the fact that a lot is known about the NEXAFS spectra of some chemical structures (e.g., benzene), molecular sub-units or molecular functional groups. Thus, it is possible to derive the structure of the unknown spectrum by combining the spectra of simpler known parts [104], e.g., benzoic acid can be decomposed into benzene and formic acid building blocks. Indeed, this approach has shown a considerable success to interpret the polymer systems [105] and to report on chemical conversions like cyclodehydrogenation [106, 107] and coupling processes [108, 109, 110]. However, the correct assignment of individual peaks to simpler building blocks can become a challenging task for complex systems (interacting functional groups) or for those providing many resonances at overlapping energies [111, 112]. In such cases, predictive-quality calculations should be helpful and crucial for the interpretation of the experimental data and will be the subject of the next section.

2.3.3 Calculations of NEXAFS cross-sections

The calculation of the NEXAFS cross sections have been intensively presented in the literature. Some schemes, e.g., based on band-structure calculations [113], constrained DFT calculations [114], and cluster models [115, 95, 116], have been employed to study surface-related structures and yielded reasonable agreements with the experiment. In this thesis, we use a plane wave-based DFT approach implemented in the Xspectra code [117, 118] of the Quantum ESPRESSO package [119]. The strength of this approach lies in its ability to effectively report on the absorption cross section without calculating a single unoccupied band. A detailed description can be found in the work of Taillefumier et *al.* [117]. However, a short overview is presented in the following.

In general, a NEXAFS measurement involves a transition of a core electron from the initial core state ψ_i of energy E_i (localised on an absorbing atom R_0) to a final unoccupied state ψ_f of energy E_f upon an absorption of a photon of energy $\hbar w$. The probability of such transition can be determined with help of the Fermi's Golden Rule, which relates ψ_f and ψ_i to the absorption cross section $\sigma(\hbar w)$:

$$\sigma(\hbar w) = 4\pi^2 \alpha_0 \hbar w \sum_f \left| \langle \psi_f \left| \mathcal{O} \right| \psi_i \rangle \right|^2 \delta(E_f - E_i - \hbar w) \tag{2.31}$$

In this equation, α_0 is the fine structure constant while $\mathcal{O}$ are the transition amplitudes between the initial and the final states being governed by the electric dipole (1) and quadrupole transitions (2) [120].

$$\mathcal{O} = \underbrace{\epsilon \cdot r}_{(1)} + \underbrace{\frac{i}{2}(k \cdot r)(\epsilon \cdot r)}_{(2)} \tag{2.32}$$

Within this thesis, we use pseudopotentials to self-consistently calculate the charge density within large supercells. By this, we obtain pseudo wave functions different from the real (all-electron) wave functions. However, the initial and the final states presented in equation (2.31) are all-electron wave functions and such aspect should be reconstructed within our calculations. Actually, this can be done by employing the projected augmented wave method (PAW) of Blöchl [49]. According to the PAW formalism, the all-electron wave functions $|\psi_f\rangle$ are related to the corresponding final pseudo wave functions $\left|\tilde{\psi}_f\right\rangle$ by a linear operator τ:

$$|\psi_f\rangle = \tau \left|\tilde{\psi}_f\right\rangle \tag{2.33}$$

Since the pseudo wave function is different from the all-electron wave function only in the core region, the operator τ differs from the identity only in the core region. This difference can be introduced as a sum of local atom-centered contributions acting only within spherical augmentation regions:

$$\tau = 1 + \sum_{R,n} \left(|\phi_{R,n}\rangle - \left|\tilde{\phi}_{R,n}\right\rangle \right) \langle \tilde{p}_{R,n}| \tag{2.34}$$

where $|\phi_{R,n}\rangle$ and $\left|\tilde{\phi}_{R,n}\right\rangle$ are atomic all-electron and pseudo partial waves, respectively. The vectors $\langle \tilde{p}_{R,n}|$, which are called projector functions, are equal to zero outside the augmentation region and satisfy the condition $\left\langle \tilde{p}_{R,n} \mid \tilde{\phi}_{R',n'} \right\rangle = \delta_{RR'}\delta_{nn'}$. The index n refers to the angular momentum quantum numbers (ℓ,m) and to an additional number, used if there is more than one projector per angular momentum channel.
At the end, a simple expression for the absorption cross section is obtained:

$$\sigma(\hbar w) = 4\pi^2 \alpha_0 \hbar w \sum_f \left| \left\langle \tilde{\psi}_f \mid \tilde{\phi}_{R_0} \right\rangle \right|^2 \delta(E_f - E_i - \hbar w) \tag{2.35}$$

where

$$\left|\tilde{\phi}_{R_0}\right\rangle = \sum_n |\tilde{p}_{R_0,n}\rangle \langle \phi_{R_0,n} |\mathcal{O}| \psi_i\rangle \tag{2.36}$$

In principle, the calculation of the absorption cross requires: *(i)* the core wave function of the absorbing atom (e.g., 1s state for K-edge) without a core hole (within the frozen core approximation, it can be taken from an all-electron ground state atomic calculations), *(ii)* the all-electron partial waves centred on the absorbing atom R_0 and *(iii)* PAW projectors. However, coming back to Eq. (2.35), it is clear that the summation should be done over

all unoccupied states, which dramatically increases the computational costs. Instead, it is possible to introduce a Green's operator whose imaginary part is associated with the pseudo-Hamiltonian $\tilde{\mathcal{H}} = \tau^\dagger \mathcal{H} \tau$ (with $E = E_i + \hbar w$):

$$-\frac{1}{\pi} \cdot \Im m \left[\tilde{G}(E)\right] = \sum_f \left|\tilde{\psi}_f\right\rangle \delta(E_f - E) \left\langle\tilde{\psi}_f\right| \tag{2.37}$$

Thus, the cross section of Eq. (2.35) can be rewritten as:

$$\sigma(w) = 4\pi^2 \alpha_0 \hbar w \Im m \left\langle \tilde{\phi}_{R_0} \left| (E_i + \hbar w - H + i\gamma)^{-1} \right| \tilde{\phi}_{R_0} \right\rangle \tag{2.38}$$

Like this, the scheme does not require the empty states explicitly. Thus, the sum over empty states can be calculated via the occupied bands exclusively. Even in this form (after the sum over empty states is removed) the numerical task remains very large as the calculation of $\left\langle \tilde{\phi}_{R_0} \left| (E_i + \hbar w - H + i\gamma)^{-1} \right| \tilde{\phi}_{R_0} \right\rangle$ requires a matrix inversion for each energy. Instead, it is possible to follow the works of Lanczos [121, 122] which introduce a new basis $\{|u_i\rangle\}$ allowing for a tridiagonal representation of the pseudo-Hamiltonian in a continued fraction form. Like that, the absorption cross section is computed as:

$$\sigma(w) = -4\pi\hbar w \Im m \cfrac{\left\langle \tilde{\phi}_{R_0} \mid \tilde{\phi}_{R_0} \right\rangle}{a_0 - E - i\gamma - \cfrac{b_1^2}{a_1 - E - i\gamma - \cfrac{b_2^2}{\ddots \cfrac{}{a_{N-1} - E - i\gamma - \cfrac{b_N^2}{a_N - E - i\gamma}}}}} \tag{2.39}$$

where γ is the broadening parameter, $\{a_i\}$ and $\{b_i\}$ are two sets of real parameters obtained by $a_i = \left\langle u_i \left| \tilde{H} \right| u_i \right\rangle$ and $b_i = \left\langle u_i \left| \tilde{H} \right| u_{i-1} \right\rangle = \left\langle u_{i-1} \left| \tilde{H} \right| u_i \right\rangle$ and N the number of iterations required to converge the calculations.

2.4 Program Packages (VASP, QE)

The DFT calculations presented in this thesis have been performed with two codes: The Vienna ab-initio simulation package (VASP) and the Quantum Espresso (QE).

VASP is a commercial software providing solutions to the Kohn-Sham equation in the framework of DFT. With help of this program, it is possible to calculate the total energy of the system, the self-consistent electronic structure, the geometric relaxation, the molecular dynamics, etc. The KS wave functions are expanded in plane wave basis functions being implemented in reciprocal space. The nuclei-electron interactions can be described by either the norm-conserving or ultrasoft pseudopotentials or projector-augmented-wave method. To obtain the solutions of the KS equations, iterative matrix diagonalisation techniques (block Davidson scheme or residual minimisation techniques) have been employed. The charge density, i.e., the potential, is calculated through the Broyden-Pauly

procedure and updated after each self-consistency step, while the criterion for the ionic relaxation is the minimisation of the Hellmann-Feynman forces through conjugate gradient or quasi-Newton procedures [123, 124].

Quantum Espresso (QE) is a free and open source software distribution runs DFT based simulations. Its name is an abbreviation of Quantum opEn Source Package for Research in Electronic Structure Simulation and Optimisation. It resembles VASP in many aspects. However, the self-consistency is performed by employing the modified Broyden method [125], while the structure optimisation is achieved by using the Broyden-Fletcher-Goldfarb-Shanno (BFGS) quasi-Newton algorithm [119]. In this thesis, QE has been employed to calculate the spectroscopic properties (XPS and NEXAFS).

2.5 Technical Parameters

In order not to repeat the employed technical parameters within each section, their determinations have been summarised here. However, any deviations from general case will be pointed out within the text.

The total energy calculations and the simulated STM images have been carried out using the VASP DFT-code [123]. The Perdew-Wang 1991 functional (PW91) [34] is used to model the electron exchange and correlation interactions within the GGA. The electron-ion interactions are described by the projector-augmented wave (PAW) method [126], which allows for a relatively moderate energy cutoff of 400 eV for the plane-wave basis (340 eV for Diindenoperylene (DIP) on Cu(111)). The adsystems were modelled by periodically repeated supercells, containing six atomic layers of KCl(100), NaCl(100) and Cu(111) surfaces. However, four layers appear to be sufficient in case of Ag(111). The calculations ensure that using these thicknesses of slab yields numerical error bars of about 1 meV for relative adsorption energies. During structure optimisation, the two lowest layers were kept fixed while all other layers and adsorbates were allowed to relax freely. The sampling of the Brillouin zone was done by using either a $(2 \times 2 \times 1)$ or $(1 \times 1 \times 1)$ k-point grid (see text). The total energies have been complemented by the aforementioned London-type correction [61, 62] in order to numerically account for dispersive forces. To optimise the configuration of the molecule-substrate system, a full atomic relaxation was performed until the forces on the atoms were less than 0.03 eV/Å. A vacuum separation of 40 Å and 30 Å are found to be sufficient for obtaining converged results for the ionic and the metallic surfaces, respectively. The same setup was used to model the step edges in a saw tooth like model system (see Figure A.1). The adsorption energies (E_{ads}) have been calculated as $E_{ads} = E_{sys} - E_{sur} - E_{mol}$, where E_{sys} is the energy of the adsystem, while E_{sur} and E_{mol} are the energies of the substrate and of the molecule in gas phase, respectively. The simulated scanning tunneling microscopy (STM) images are obtained using the Tersoff-Hamann approach [127]. The latter is generated with the aid of the integrated charge density between the Fermi energy E_f of the system and an energy $E_f + U$, where U is the desired voltage.

It is important to note here that the employed DFT-D approach (see 2.1.5) accounts only *approximately* for the vdW forces. The semiempirical approach used here [61], i.e., by the addition of a pairwise interaction energy C_6R^{-6} with suitable cutoff functions, is not only a computationally inexpensive approach but also a rather an accurate one. According to Reuter et *al.* [63], whose work compare the adsorption energies of different molecules obtained by employing the DFT-D [61, 62] approach with the experimental data, this approach is able to yield results within error bars, while the deviations from the experiment depend more or less on the investigated molecule and surface. Since the present calculations compare the differences of the adsorption energies for identical molecules, the employed DFT-D approach is expected to be accurate to a good extent allowing us to draw proper conclusions.

For the calculation of the X-ray absorption spectra (XAS), the PAW scheme was applied in a gauge-including (GI) way: Using the Xspectra code [117, 118] of the Quantum ESPRESSO package, [119] NEXAFS spectra of the C and N species were computed in a 40 eV wide energy range above the respective K-edge. The technical details like DFT-functional, dispersion correction and plane wave basis set were chosen identical to those used in the VASP total energy calculations. The 1s core hole is incorporated by generating scalar-relativistic multiprojector GIPAW pseudopotentials with a corresponding occupation of the inner shells. This allows for a reliable, but computationally very efficient description of excitonic effects [129]. The Lanzcos recursion scheme is employed to expand the Green's function of the empty states (continued-fraction expansion) [121, 122, 130]. This muli-projector approach reliably describes the near- as well as far-edge features of the absorption spectrum [131, 132, 133, 134]. The quadrupole contributions require s → d excitations and are, thus, often restricted to 3d/4d transition metal atoms. Indeed, their contributions in the pre-edge regions are found to be very small and negligible compared to those of the dipole term. Hence, we restrict the calculations to the latter. The absorption spectra are calculated for each related atom within the molecular structure. Subsequently, the total X-ray spectrum of the molecular system is obtained from the superposition of the individual

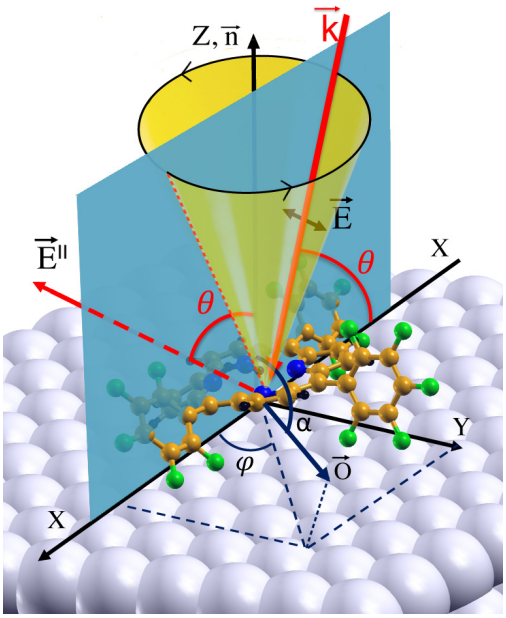

Figure 2.7: Sketch of the angle-dependent NEXAFS setup. The direction of a transition dipole $\vec{O}$, is defined by the angles α and φ [128]. The incident X-ray (exemplarily shown in the xz-plane) is tilted by θ with respect to the surface plane (tilt angle of the $\vec{E}$-field component $E^{\parallel}$ with respect to the surface normal $\vec{n}$). The cross-sections σ_{XAS} are calculated without considering a "preferred molecular orientations", that is, by averaging with respect to φ (wave vector ($\vec{k}$) at the shown cone-surface).

spectra offset by the corresponding core level shift (CLS). The latter are calculated using a delta-scf approach, which yields highly accurate CLS for light elements such as nitrogen [135, 136, 79]. The resulting total XAS signals have been rigidly shifted to match the experimental K-edges energies. The line width is chosen energy dependent [137], rising arctan-like from 0.2 at 395 eV (280 eV) to 2.0 at 435 eV (320 eV) for the N (C) K-edge spectra. The broadening used in the XAS calculations thus follows qualitatively the trend in the experimental spectra, but is chosen somewhat smaller, in order to prevent it from masking the spectral fine structure. The XP spectra on the other hand are obtained from a superposition of individual CLS broadened by a constant Gaussian line width of 0.7 eV as observed in experiment.

The angle-dependent X-ray absorption spectra are calculated for a given wave vector $\vec{k}$ and polarisation vector ϵ of the incident X-rays. In order to compare with the experimental situation where the molecules are differently oriented within islands featuring the three-fold symmetry of the surface, the XAS cross-sections σ_{XAS} have been calculated from angular average of an electric field tilted by an angle θ with respect to the surface normal (oriented along the z-axis), that is, by evaluating

$$\sigma(\theta) = \frac{1}{2}[\sigma_{\mathrm{XAS}}(\theta, \varphi_0) + \sigma_{\mathrm{XAS}}(\theta, \varphi_0 + 90^o)]$$

for an arbitrary angle ϕ_0 (see Figure 2.7).

3 Structure Formation of Organic Molecules On Metallic and Ionic Surfaces

> What we know is a drop. What we don't know is an ocean.
>
> *(Isaac Newton)*

One goal of this work is to generate a solid knowledge and detailed understanding of the structure formation in two prototypes molecules on metallic and ionic surfaces. For such purpose, total energy DFT calculations supported with scanning tunnelling microscopy (STM) measurements have been presented *(i)* to analyse the self-organisation patterns of the Diindenoperylene (DIP) molecules on Cu(111) and *(ii)* to rationalise the adsorption of perylene-3,4,9,10-tetracarboxylic diahydride (PTCDA) molecule on KCl and NaCl(100) surfaces. Based on the achieved results and on the comparison between the studied systems, we discuss the experimental circumstances which might assist a formation of the long-range orders of DIP-based structures on Cu(111).

3.1 Diindenoperylene (DIP) Thin Films On Cu(111) Surfaces

The first section discusses a previous STM study [1] reporting that well-defined arrangements of DIP molecules on Cu(111) appear *only* on narrow terraces and near step edges. The upcoming calculations will show that well-ordered arrangements are energetically more favourable and expect them to appear irrespective of the terrace width. The STM measurements, which support our point of view, were done by S. Matencio, E. Barrena, and C. Ocal from the Instituto de Ciencia de Materials de Barcelona (ICMAB-CSIC). The results of this section have been already published in Refs. [138, 139].

3.1.1 Introduction

Diindenoperylene (DIP, $C_{32}H_{16}$) is a planar perylene-based molecule, (see Figure 3.1 a). This molecule has recently attracted great attention due to its ambipolar properties [140], its exceptional ability to form highly ordered structure (a requirement for high charge carrier mobility) [141, 142, 143], and its high stability against oxidation and elevated temperatures (up to 730 K) [144]. All these aspects suggest this molecule as a promising candidate for organic optoelectronic devices [9, 10, 11].

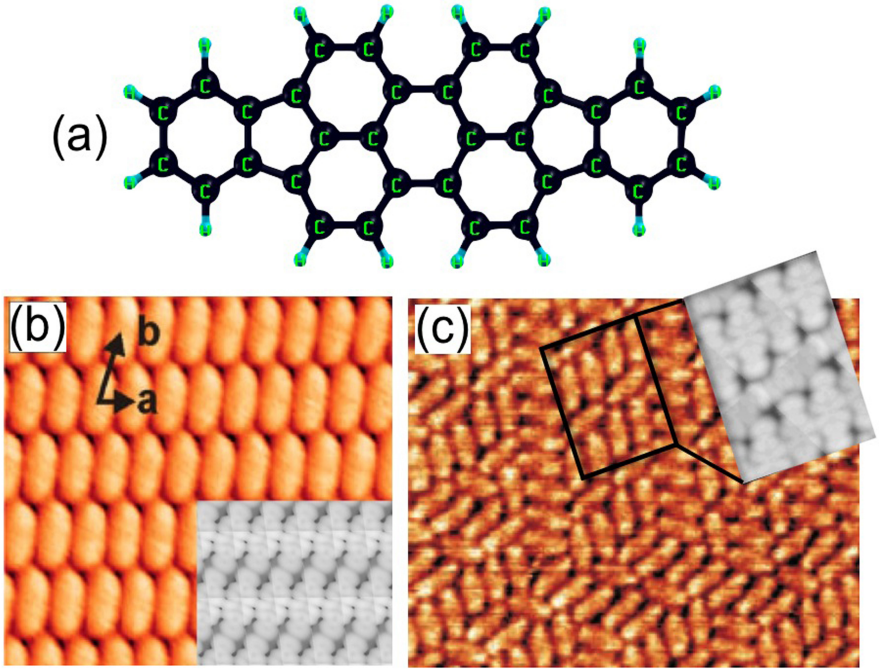

Figure 3.1: (a) Ball-and-stick model of the DIP molecule. (b) The long-range (LR) and (c) the short-range (SR) arrangements of DIP molecules observed experimentally on Cu(111) [1]. Gray micrographs show STM simulations according to the Tersoff-Hamann model [127].

In the following, the previously reported results related to this work as summarised: Oteyza et *al.* found in their STM investigations that the self-assembled pattern of DIP on Cu(111) is in dependence on the terrace width [1]: On narrow terraces ($\leq$ 15 nm), molecules are found to be arranged in a well-defined long range (LR) adsorption order (Figure 3.1 b) with adjacent molecules oriented co-directionally in oblique cells described by a = 8.7 $\pm$ 0.4 Å, b = 18.5 $\pm$ 0.7 Å, $\gamma = 71 \pm 1^{o}$. In contrast, on wider terraces ($\geq$ 15 nm), DIP molecules are reported to adsorb in short range (SR) orders, where only few molecules adsorbed co-directionally in small domains. It is also reported that these domains are oriented along the three equivalent crystal directions determined by the substrate symmetry (Figure 3.1 c). Another study, which is done by employing the normal incidence X-ray standing wave techniques on single molecule system (see Ref. [145]), yielded an adsorbate-substrate distance of 2.51 $\pm$ 0.03 Å. Based on their investigations, they concluded that the vertical DIP position weakly depends on the surface coverage. Schuler et *al.* [146] reported using non-contact atomic force microscopy that the geometries of the singly adsorbed DIP molecules slightly deviate from the planar form (see Ref. [145] and the supplemental material of Ref. [146]). In all these studies, the systematic descriptions of the electronic and geometric properties of the molecular aggregates are missing.

3.1.2 Diindenoperylene (DIP) molecules on planar Cu(111) surfaces

3.1.2.1 Single molecule adsorption

As a starting point, the most favourable adsorption geometries of *single* DIP molecules on Cu(111) have been determined. A single molecule adsorption is a model where it is supposed that the electronic and the geometric properties of the molecule upon adsorption are related only to the influence of the underlying surface. Therefore, one should perform the calculations within laterally enough large cells in order to suppress the unwanted interactions with the neighbouring molecules.

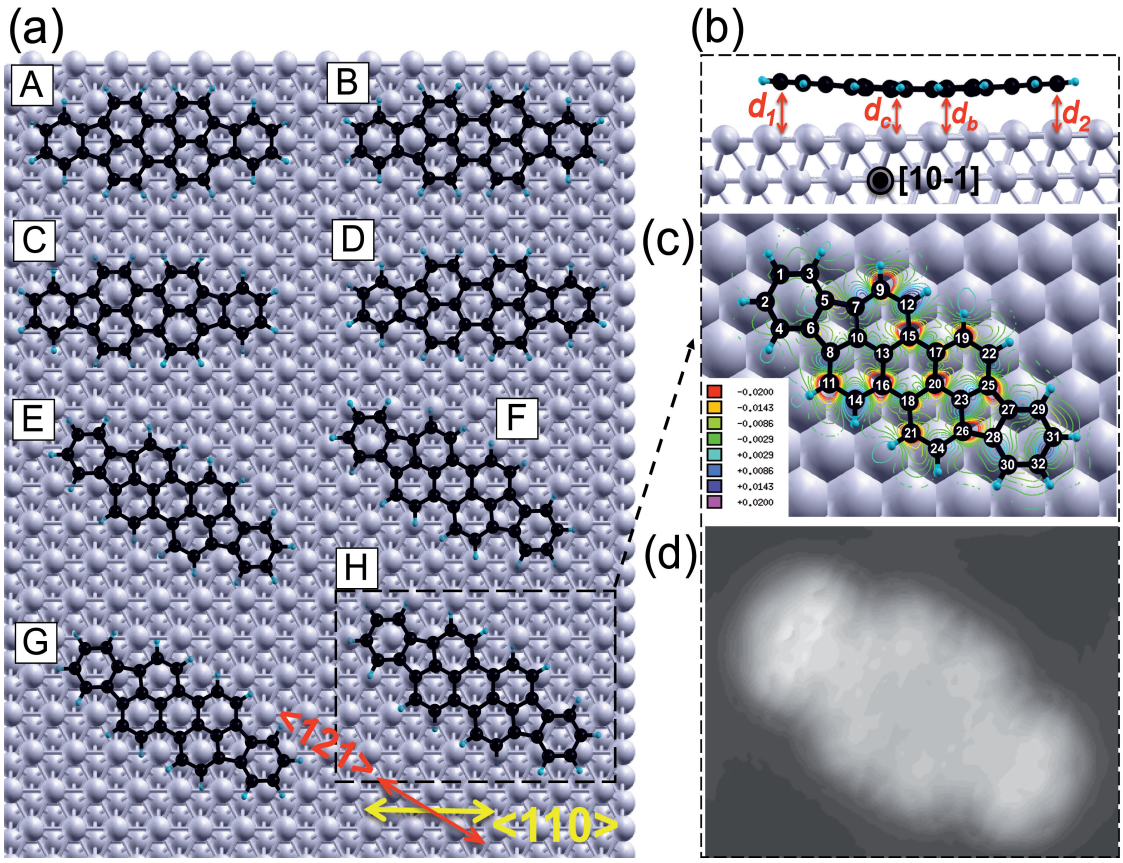

Figure 3.2: (a) Top views of different adsorption geometries of single DIP molecules on planar Cu(111). The long molecular axis is aligned parallel to one of the surface directions <110>, while the molecular centre ring resides on (A) top, (B), (C) bridge, or (D) hollow positions. In the other structures, the molecules are directed along one of the <121> directions with the centre ring in (E), (F) bridge, (G) top or (H) hollow positions. (b) Side view of the most favourable structure (H). (c) Coloured iso-lines indicate the calculated charge density redistribution upon adsorption. Positive (negative) values (in e) indicate electron accumulation (depletion). (d) simulated STM micrograph of structure (H) according to the Tersoff-Hamann method [127] for V = -1.5 eV and I = 0.05 mA.

In this work, supercells of dimensions (9×8) surface unit cells are most feasible (480 atoms per a supercell). In such supercells, various adsorption sites (top, bridge, hcp– and fcc–hollow) and orientations with respect to the underlying surface have been probed. The centre of the molecule is taken as a reference for the molecular registries, while the molecular long axis (an imaginary line via atoms 10, 13, 20 and 23) is taken as a reference for the molecular orientation (see Figure 3.2).

The most stable structure is the one denoted as (H) on Figure 3.2 a. In such structure, single DIP molecule adsorbs almost parallel to the surface. It is namely in a slight concave and asymmetric form (see Figure 3.2 b). Compared to the molecular centre, the outer carbon atoms are vertically shifted upwards by 0.12 Å and 0.4 Å. The different vertical shifts result from the different registries of the outer rings (atoms 1 to 6 and 27 to 32 in Figure 3.2 c) with respect to the underlying surface. The slight asymmetry of the adstructure found here explains the small molecular torsion observed in Refs. [145] and [146]. The molecular long axis (LA) is parallel to one of the three equivalent <121> orientations of Cu(111), while the molecule centre resides on hollow site where three out of the six inner carbon atoms (13, 17 and 18 see Figure 3.2 c) are on top of Cu atoms, while the other three inner carbon atoms (15, 16 and 20) are located on hollow sites of the surface. For the adsorbate-substrate distances defined in Figure 3.2 b, the calculations yield $d_{1/2} = 2.93/2.63$ Å (distance between carbon atoms 1/31 (or 2/32) and the Cu atoms beneath) and $d_{b/c} = 2.48/2.54$ Å (distance between carbon atoms 13/17 to the Cu atoms beneath). If one defines the height of the molecular centre as average of d_c and d_b, the calculated distance between the centre of the molecule and the surface fits perfectly to the experimental value of 2.51 Å [145]. It is also in good agreement with the calculated value by Bürker et *al.* (2.59Å) [145]. The small deviation with respect to Ref. [145] might be due to the thinner slab (3 layers compared to 6 layers in this work) they used to model the Cu(111) surface. The adsorption energy of structure (H) is -4.84 eV which agrees well with the results obtained by Bürker et *al.* [145] (-4.74 eV). This comparatively large adsorption energy is on the one hand simply related to the size of the molecule, but implies on the other hand a noticeable molecule-substrate interaction.

In order to further illustrate the molecule-surface interaction, the charge redistribution upon adsorption has been calculated. In Figure 3.2 c the charge accumulations and depletions have been shown in a selected plane resides 0.2 Å beneath the molecular centre (the plane where the total charge transfer is at the largest value of 0.34 e). Obviously, the charges accumulate mainly underneath the carbon atoms which are directly above Cu atoms, e.g., atoms 12 and 14, while charge depletion can be observed at C atoms atop hollow sites, e.g., atoms 15, 16, and 20. In general, the charge density shows stronger redistribution in the molecular centre compared to that at the outer rings. This apparently induces the molecular asymmetric bonding configuration. The small asymmetrical configuration upon adsorption is also reflected in the simulated STM images (see Figure 3.2 d). As a result of the asymmetric parabolic adsorption geometries, both sides of the molecule look brighter than the centre, but one of them is brighter than the another.

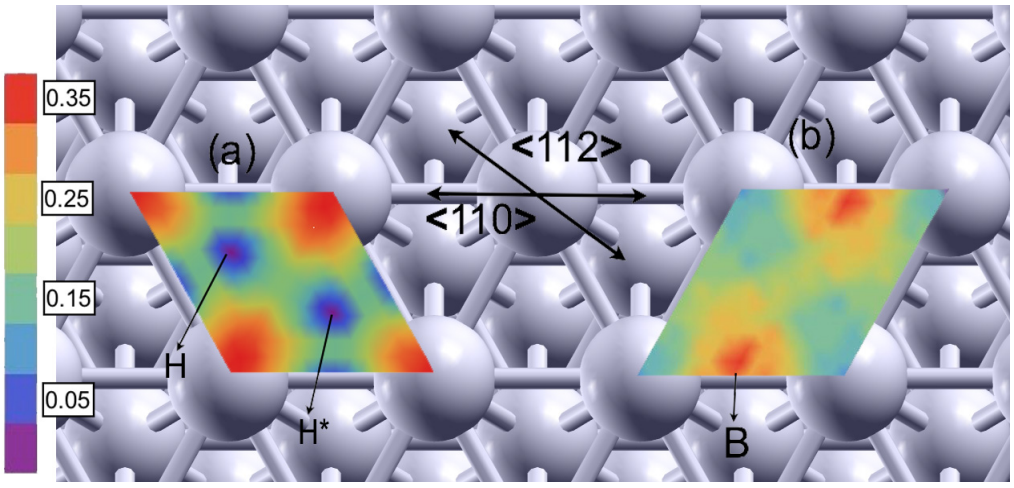

Figure 3.3: The calculated PESs for single DIP molecules on Cu(111). The molecule was moved laterally and the LA was kept parallel to the (a) $[1\bar{1}2]$ and (b) $[1\bar{1}0]$ direction of the surface. The energetically most favoured structure H (see Figure 3.2) is considered as the zero point on the scale (in eV). The most favourable hollow site H, the equivalent H^* site and the most unfavourable structure B are shown.

In order to assess the mobility of the molecule on the surface and to determine the diffusion barriers, the potential energy surfaces, which are *maps* of adsorption energies calculated at lateral positions throughout the surface unit cell, have been plotted (see Figure 3.3). The adsorption energies are calculated on dense mesh of points separated by 0.1 Å between the grid points throughout the surface unit cell. Two cases are considered: in the first one, the molecular LA is kept parallel to the $[1\bar{1}2]$ (see Figure 3.3 a). In the second one, it was kept parallel to the $[1\bar{1}0]$ direction of the surface (Figure 3.3 b). In both cases, the centre of the molecule is taken as a reference. The lateral position of carbon atoms 13 and 20 (Figure 3.2 c) were fixed, whereas all other degrees of freedom were structurally relaxed. Obviously, the calculated PESs show a small corrugation of 0.35 eV in spite of the strong molecule–surface interactions. Accordingly, the DIP molecules are highly mobile already at low temperatures, thus enabling efficient molecular assembling. For the most unfavourable structure, the centre of the molecule resides on a bridge site, while its LA is parallel to the $[1\bar{1}0]$ direction (denoted as B on Figure 3.3 b). The adsorption energy of this structure is -4.49 eV. While the top position is unfavourable when the LA is parallel to the $[1\bar{1}2]$ direction of the surface (-4.51 eV), it is more favourable (-4.72 eV) when the LA is parallel to the $[1\bar{1}0]$ direction. Accordingly, some favourable diffusion paths (e.g. from hollow to top positions) involve molecular rotations.

It should be noted that doing the calculations for substrates modelled with four atomic layers does not lead to converged results. On Figure 3.4, the adsorption energies of structures (A-H) are calculated for different slab thicknesses and k-point samplings (see Figure 3.4). In case of using four-layer slabs, for example, the structure (H) is most favourable for a $(1 \times 1 \times 1)$ k-point grid, while structure (A) is most favourable when using a $(2 \times 2 \times 1)$

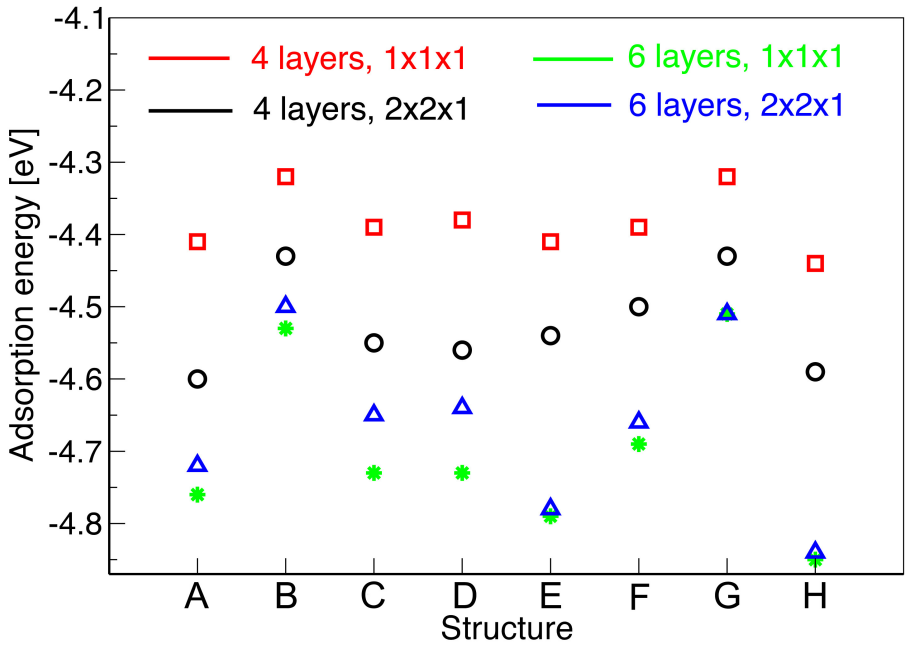

Figure 3.4: Calculated adsorption energies for the structures defined in Figure 3.2 a in dependence on the k-point grid and the numbers of slab layers.

k-point sampling. Using six-layer slabs leads to adsorption energies that have an error bar for relative adsorption energies that is below 0.1 eV. In this case also the energetic ordering of the adsorption structures does not depend on the k-point sampling anymore.

3.1.2.2 Molecular monolayers

In the previous section, it was mentioned that calculating the single molecule adsorption requires adequately large supercells. However, smaller supercells should be used here in order to explicitly account for the influence of the intermolecular interactions. In such cells, the geometries of the single molecule were considered, first, as a start configuration. Then all degrees of freedom are allowed to relax freely until they are fully relaxed.

The calculations yielded for (9×6), (9×4), (7×8), (7×6) and (7×4) supercells, adsorption energies of -4.82, -5.55, -5.05, -4.91 and -5.49 eV, respectively. This indicates attractive molecule-molecule interactions which stabilise the molecular aggregates. By allowing denser molecular arrangements close to those experimentally observed [1] one obtains the highest adsorption energies (see Figure 3.5). In contrast, DIP molecules exhibit in further small supercells strong distorted geometries and, consequently, less stable structures (e.g. for a supercell of dimension (5×4) the adsorption energy is -4.49 eV).

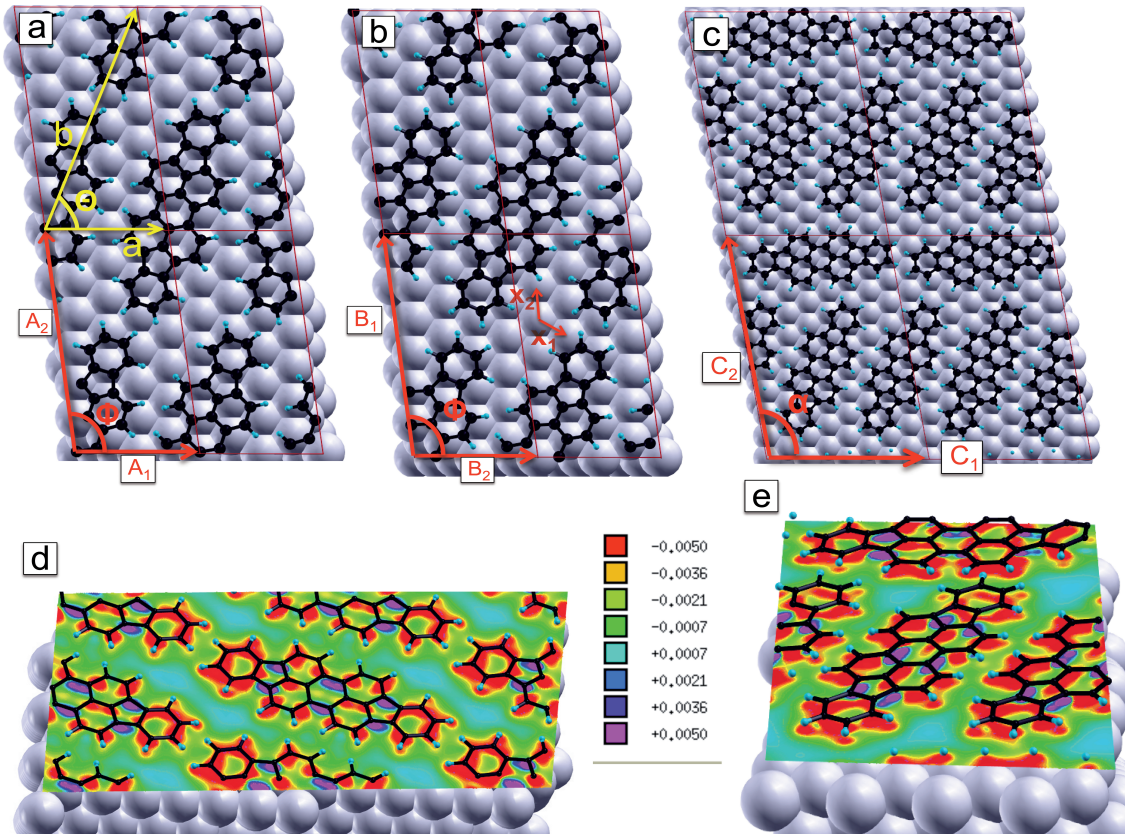

Figure 3.5: Models of the most stable LR arrangements: (a) phase A and (b) phase B as well as the (c) SR order. The induced charge density for phase A (d) and for the SR order (e) are shown. The charge redistribution aspects are plotted on a plane located 0.4 Å below the molecular plane (see text).

The most stable structures, which are found in the calculations, are the so-called A and B phases (see Figure 3.5 a and b) which have adsorption energies of -5.63 eV and -5.76 eV, respectively. These structures are characterised by a $\begin{pmatrix} A_1(B_1) \\ A_2(B_2) \end{pmatrix} = \begin{pmatrix} 4 & 2 \\ -1 & 6 \end{pmatrix} \begin{pmatrix} x_1 \\ x_2 \end{pmatrix}$ translational symmetry, where x_1 and x_2 are the primitive unit cell vectors of the Cu(111) surface. Like this, the A and B structures have dimensions of $A_1 = B_1 = 8.77$ Å, $A_2 = B_2 = 16.82$ Å, and $\Phi = 97.77^{o}$, which correspond to a = 8.77 Å, b = 17.89 Å, and $\theta = 69.68^{o}$ according to the notation used in Ref. [1], see red and yellow arrows in Figure 3.5 a. Apparently, both phases have the same dimensions, but they differ in the orientation of the molecules within the unit cell. The registries of the molecules here are similar to those of the singly adsorbed molecules. However, the LA is rotated by 10^{o} with respect to the $[1\bar{1}2]$ direction of the surface in order to avoid the repulsion between the hydrogen atoms of neighbouring molecules. Obviously, the different properties of both A and B phases, e.g., the dimensions, the molecular arrangement within the adstructures as well as

the molecular density (σ_{LR} = 0.68 molecules/nm^2), are pretty close to the so-called LR structure reported in Ref. [1] which was observed experimentally *only* on narrow terraces. Before introducing the calculations of the SR order, it should be noted that LR orders of DIP monolayers were observed on other surfaces even on large terraces like e.g. Cu(100) and Au(111) surfaces, with lattice parameters of a = 10.5 Å, b = 18.6 Å, θ = 92^o and dimensions of a = 13.4 Å, b = 14.8 Å, θ = 97^o on Cu(100) [147] and Au(111) [148], respectively.

The short-range order is calculated for a variety of structures, each includes three molecules differing in their registries as well as their orientations within the unit cell. The most favourable structure calculated which resembles the experimentally observed SR order is the shown in Figure 3.5 c. This structure has dimensions of C_1 = 17.61 Å, C_2 = 25.83 Å, α = 99.96^o, so that the molecular density of 0.66 molecules/nm^2 perfectly fits with the experimentally reported [145]. It is characterised by three molecules within the unit cell, two of them are azimuthally oriented in the same direction, whereas the third is rotated by 60^o with respect to them. The registries of the individual molecules are similar to the LR arrangement. The adsorption energy per molecule for this structure amounts to -5.47 eV.

A comparison between the single molecule adsorption on one side with the LR and SR orders on the other side shows that the molecule-molecule interactions gain importance in the latter at the expense of weakening the molecule-surface interactions. The molecule-surface interaction energies of the SR and LR order phases amount to about 4.5 eV, while that of the single molecule adsorption to about 4.8 eV. This is reflected in: *(i)* a slight charge redistribution where the charge density is accumulated into the intermolecular regions and depleted from the region between the molecules and the surface underneath (see Figures 3.5 d and 3.5 e), and in *(ii)* a slightly increased molecule-surface distance to about 2.9 Å. In particular, the finding that the vertical distance depends slightly on the molecular coverage is in agreement with experiment [145].

structure	phase A (LR)	phase B (LR)	short-range order (SR)
E_{ads} in eV	-5.63	-5.76	-5.47
MS in eV	-4.47	-4.50	-4.48
MM in eV	-1.16	-1.26	-0.99

Table 3.1: A comparison between the molecule-surface (MS) and the molecule-molecule (MM) contributions to the calculated total adsorption energy (E_{ads}) in the LR and SR order adstructures.

Before comparing the calculated LR and SR orders energies, a word of caution is probable. While one obtains reliable adsorption energies in case of single molecule adsorption by systematically scanning of all plausible adsorption geometries, the situation is more complicated in case of thin monolayers cases, e.g. SR and LR orders. This is because of large number of structural degrees of freedom and the huge numerical expense of well-converged calculations which hinder a complete sampling of all possible structures. Therefore, it is not completely excluded that other, and even more favourable, SR or LR configurations

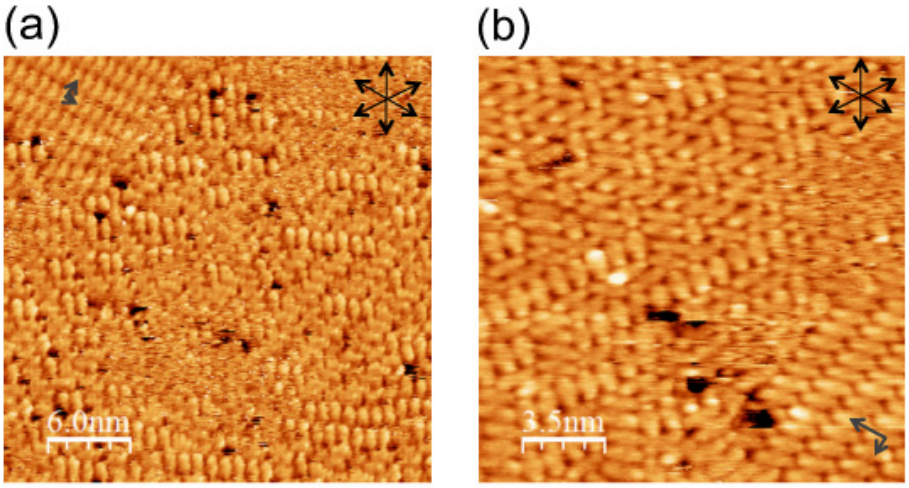

Figure 3.6: STM images of DIP on Cu(111) for a submonolayer coverage, showing coexistence of LR ordered domains, SR order and a two-dimensional gas of mobile disordered molecules. (a) I = 370 pA, bias = -0.37 V and (b) I = 130 pA, bias = -1.25 V. The <110> substrate directions are indicated by black arrows, while grey arrows indicate the lattice vectors of the LR ordered domains.

not considered here to be observed experimentally. Moreover, the present calculations do not consider the temperature effects, where vibrational and configurational entropy contributions to the adstructure free energy may modify the energetics at finite temperatures [149]. However, if it is assumed that the adsorption energies calculated here correctly describe the energy trend, there seems to be a contradiction with the experimental findings: The calculations predict that a monolayer of DIP on Cu(111) should show long-range domains even on large terraces, or at least long-range order islands should be formed in co-existence with the short-range orders.

This fact is confirmed by our collaborators S. Matencio, C. Ocal and E. Barrena at the instituto de Ciencia de Materiales de Barcelona (ICMAB-CSIC). Their STM experiments, done for a submonolayer coverage of molecules, showed that *several structures with LR order have been observed in co-existence with SR order and a two-dimensional gas of mobile molecules. The LR domains observed in Figure 3.6 a (top left) and Figure 3.7 (domain I) agree reasonably well with the predicted structures A and B shown in the Figure 3.5 (A_1 = 9.1 Å, A_2 = 16.3 Å, $\Phi = 100^o$). In addition, other domains with slightly different packing and orientation (Figure 3.6 b, Figure 3.7 a and b) are also observed. Notice in Figure 3.6 a the different alignment of the DIP molecules in single rows with their long axis oriented along the compact directions of the surface, i.e. <110> directions.*

The STM data shown in Figure 3.7 demonstrate the formation of a LR ordered domain far from the step edge (domain I) which in this case appears surrounded by a region with SR order and mobile molecules. At the step edge of the lower terrace another ordered area is observed (domain II), which is 30^o *rotated with respect to domain I and has therefore*

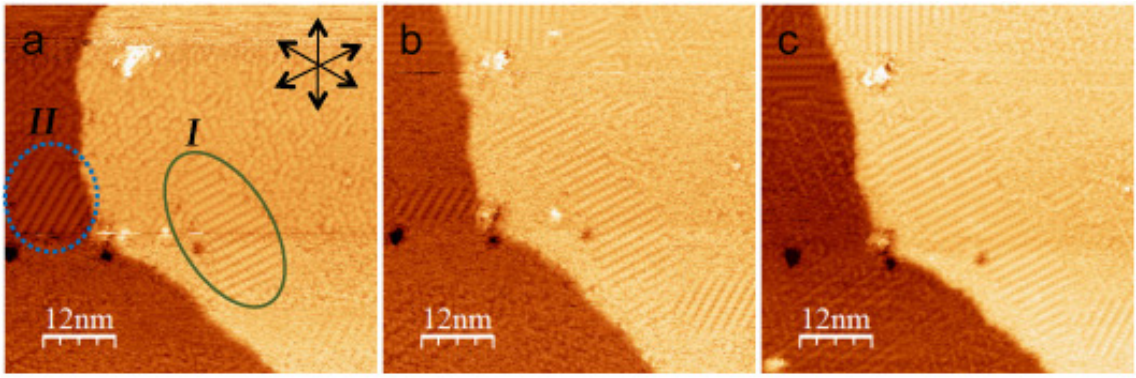

Figure 3.7: (a)-(c) STM images acquired by continuous scanning in the same area (I = 90 pA, bias = -0.45 V). (a) The LR ordered domain I is circled with a green continuous line, while domain II is circled with dotted blue line (see text for details). (b), (c) Consecutive tip scanning causes an increase of long-ranged ordering of I-type domains and the disappearance of the domain II.

the long axis of DIP aligned along one of the <110> directions. Consecutive scanning in the same area shows tip-induced reordering with two main effects: i) Increased area of domain I and growth of other domains equally oriented at expenses of regions with mobile molecules. ii) Reduction and disappearance of the domain II giving rise to SR order.

Although for these growth conditions, domains with DIP aligned along the <110> directions are formed, we conclude from the measurements that such an orientation is just metastable in agreement with the calculations.

3.1.3 DIP molecules at step edges

In the previous section, the calculations have shown that the SR arrangement is less favourable than the LR order, while the two phases co-exist on wide terraces as shown by STM. In this section, the role of the reactive Cu(111) step edges to initiate the structure formation is reported. First, the previous experimental results are summarised. Then, the behaviours of single as well as rows of DIP molecules at step edges are presented.

Oteyza et *al.* [148] reported the role of step edges to initiate and steer the molecular assembly of DIP molecules on Au(111). In particular, DIP molecules are arranged in head-to-tail configurations parallel to the step edges and completely following their orientations. However, this is not the case on more reactive surfaces. On Ag(111), for example, single DIP molecules [150] decorate their step edges randomly, where they adsorb either parallel to the surface, with their molecular long axes parallel to the step edge orientation, or tilted or bridging between the upper and the lower terraces. On the stepped Cu(100) surface, as well, the molecular orientation is determined by the substrate, not by the step direction [147]. On this surface, large ordered 2D islands of side-by-side DIP rows have been found to grow from the step edges, while smaller 2D islands on the terrace sites are formed [147].

In general, all these surfaces step edges are reported as preferred nucleation sites for the molecular aggregations.

3.1.3.1 Single molecules at Cu(111) step edges

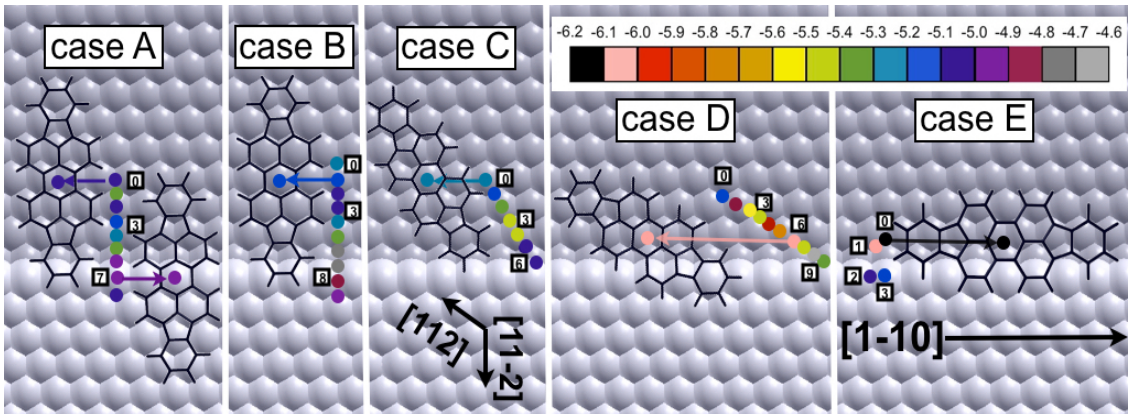

Figure 3.8: Calculated adsorption geometries of DIP molecules at step edges. In case A and B, the LA is perpendicular to the step edge and parallel to the $[1\bar{1}2]$ direction of the lower surface. The molecule binds to one atom (two atoms) of the step edge in case A (case B). In case C (case D), the LA is tilted with respect to the step edge and it is oriented along the high symmetry $[\bar{1}01]$ ($[112]$) direction of the surface. In case E, the LA is parallel to the step-edge direction. For each case, a variety of registries with respect to the lower terrace have been tested. The centre of the molecule is used as reference. The energies of the different structures are denoted as coloured circles according to the energy scale on the upper panel. The atomic vdW-radius has been used for the Cu atoms.The upper terraces atoms have slightly lighter colours and some examples of the structures such as (A0, A7, B1, C0, D6 and E0) have been depicted in detail.

In order to describe the behaviour of single DIP molecules in the vicinity of the Cu(111) steps, monoatomic step edges along the $[1\bar{1}0]$ direction of the surface are modelled using the saw-tooth model (see Appendix A.1). In enough large supercells, a variety of structures, including different possible orientations and registries of the single DIP molecules with respect to the lower and upper terraces, have been tested (see Figure 3.8). The molecules are here subject to the influence of the active step edge sites beside the strong molecule-surface interactions. At Cu(111), DIP molecules show a variety of local probable structures with different orientations and registries with respect to the planar surface and to the step edge. For structures like A1, B4, C3, D6 and E0, adsorption energies of -5.36 eV, -5.27 eV, -5.47 eV, -5.99 eV and -6.17 eV, respectively, have been calculated (Figure 3.8). In these structures, the molecules interact with the step edge with the molecular main body residing on the lower terrace, while the outer carbon atoms bind to the upper terrace (see e.g. structures D6 and E0 in Figure 3.9). Like this, step edges are preferential adsorption sites for the mobile molecules, where these can finally be immobilised. This result, which is in agreement with similar systems [147, 148, 150], indicates that step edges serve as

nucleation sites for structure formation. The influence of copper step edges on single DIP molecules is similar to Ag(111) surfaces but in contrast to Au(111) surfaces. This is plausible given the more reactive Ag and Cu surfaces compared to the Au(111) surface, which shows only weak molecule-surface interactions with the DIP aggregates [148]. In contrast to Ag(111), DIP molecules on Cu(111) avoid bridging between the upper and lower terraces in agreement with the experiment [1]. Structures like A7, B7, C5, D8 and E2, which are direct examples of these cases, have adsorption energies of -4.95 eV, -4.69 eV, -5.02 eV, -4.6 eV and -5 eV, respectively. Thereby, they are locally less probable compared the previously mentioned structures (A1, B4, C3, D6 and E0). For structures, where the molecules extend on both the lower and the upper terrace suffer from strongly distorted geometries. This distortion manifests itself in deformation energies[1] of +0.37 eV, +0.42 eV, +0.33 eV, +1.37 eV and +1.15 eV for A7, B7, C5, D8 and E2, respectively, which destabilise the corresponding structures. Two pronounced stable structures are D6 (Figure 3.9 a) and E0 (Figure 3.9 b) with adsorption energies of -5.99 eV and -6.17 eV, respectively. In both of them, the centre of the molecule resides on the hollow surface position on the lower terrace. The LA forms an angle of 20° with the step-edge orientation in D6, while it is completely parallel to it in E0. The major parts of molecules reside on the lower surface, while the outer atoms bind to the step edge.

3.1.3.2 Molecular rows next to a step edge

Upon further deposition, i.e. at higher coverage, diffused molecules occupy the preferred nucleation step edges completely. The molecules, then, form a row close to the step edge. In this case, beside the influence of the step edge and the substrate, the molecule-molecule interactions play a crucial role to steer and reorganise adjacent molecules. This forces the single molecules to arrange into an organised domain. In order to quantify this effect, we calculated the adsorption energies for a variety of commensurable and incommensurable structures, starting from the stable structures (A1, B4, C3, D6 and E0). The size of each aforementioned supercell has been reduced, in order to increase the molecule-molecule interactions, until we got the lowest adsorption energies. For the cases of incommensurable structures, two molecules in the unit cell were included. The most stable structure of one row of DIP molecules is depicted in Figure 3.9 c. In this structure, the adsorption geometries of the two molecules contained in the unit cell are slightly different and denoted as α and β, respectively. The orientation and the registries of both α and β molecules resemble that of D6. With respect to the step edge direction, the α (β) molecule is rotated by 22° (20°), the centre of each molecule is still on a hollow site of the surface. The adsorption energy per molecule in this structure is -6.26 eV. The distance between the centre of the α and β molecules is 16.47 Å, which is very close to that of the LR arrangement on the planar surface. It should be noted that the behaviour

[1] Upon adsorption, structures of the adsorbate and the surface are distorted under the presence of one-another. If the energy of the adsorbate/surface in the current position with the current distorted geometry is given as E^*_{mol}/E^*_{sur}, the deformation energy E_{def} is then $E_{def} = (E^*_{sur} - E_{sur}) + (E^*_{mol} - E_{mol})$.

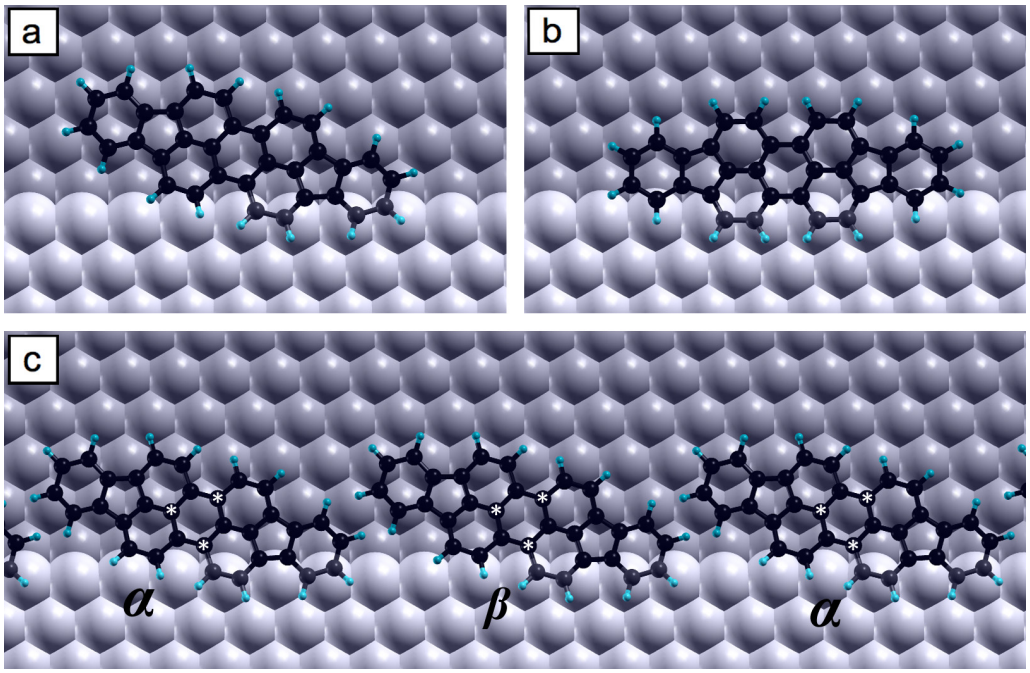

Figure 3.9: Ball-and-stick representation of single DIP molecules at the Cu(111) step edges in the so-called (a) D6 and (b) E0 structures. (c) One row of molecules is shown. The molecules are arranged in incommensurable structures, where each one contains α and β molecules. Note that inner carbon atoms which are marked by $*$ are residing on atop position in β-type but almost on a hollow site in α-type molecules.

of the first row of DIP molecules at Cu(111) step edges resembles that at the step edges of the Cu(100) surface, where DIP molecules are tilted with respect to step edges forming side-by-side rows [147], but is in contrast to Au(111) step edges, where DIP molecules adsorb at the step edges in rows in a head-to-tail configuration with their long molecular axis aligned parallel to the step direction [148].

3.1.3.3 Discussion

The total-energy calculations presented in this section showed that the SR arrangement of DIP molecules on Cu(111) is less favourable than the LR order in an apparent contrast to a previous experimental results [1]. The STM study, done by our collaborators, supports the theoretical findings by showing that the two phases co-exist. According to the calculations, the simultaneous appearance of different phases is likely to be related to the subtle balance between molecule-surface and the molecule-molecule interactions in both the LR and the SR order phase, see Table 3.1. As it is shown, the molecule-surface interactions are almost the same for all phases, and far stronger than the molecule-molecule interactions, which might then give rise to a possibly long-lived metastable state: One expects that

when the molecules are less densely packed on the surface they are mainly subject to the rather strong influence of the comparatively reactive Cu(111) surface, which determines the azimuthal molecular orientation and gives rise to three discrete equivalent orientations of the molecules on the surface. The energy barrier that needs to be overcome from this initial configuration towards formation a SR order structure is lower than towards formation of the LR order structure, because in the latter case a collective rearrangement of the molecules that is kinetically hindered at room temperature.

One should state that the considerations so far do not take temperature effects into account [149]. Vibrational and configurational entropy contributions to the adlayer free energy will additionally modify the energetics at finite temperatures. A simple estimate for the configurational entropy difference between the LR and SR ordered phase yields at 300K a free energy gain of about 0.1 eV/molecule for the latter. Also the slightly lower molecular density of the latter phase is expected to result in overall lower vibrational frequencies, which will for finite temperatures stabilise the SR order [149]. However, the existence of a coherent nucleation sites, e.g., straight step edges, in combination with more gentle thermodynamic circumstances (i.e. higher substrate temperature and lower deposition rate) might help the molecules to be arranged in the LR order. Consequently adsorbed molecules will, at sufficiently low deposition rate, condense at the already existing LR domain and lead to an overall LR order.

Later, we suggest experimental circumstances which might assist a formation of the long-range orders of DIP-based structures. However, such information are based on the results of the next section and, thus, they will be introduced at the end of this chapter.

3.2 PTCDA on Terraces and at Step Sites of KCl and NaCl

The previous section showed an example of a perylene-based molecule adsorbed on a reactive surface. Thereby, a mixture of less ordered phases beside the well-defined, energetically more favourable long-ranged phases have been observed. This section presents the adsorption of a functional molecule on ionic surfaces, where the interaction is predominantly facilitated by vdW and electrostatic forces. Such case is of special interest (see e.g., Refs. [151, 152, 153, 154, 155]). The Coulomb attractions between the molecular partial charges and the surface anions or cations anchor the molecule to specific sites of the surface enabling possible commensurate long-range ordered structures and influencing the lateral diffusion of the molecule on the ionic surfaces. As a prototype system, the perylene-3,4,9,10-tetracarboxyl acid dianhydride (PTCDA) molecule adsorbed on the KCl(100) and NaCl(100) have been considered. The two surfaces are similar in their structures but they have different lattice constants. In order to explore and rationalise the structure formation of these systems in detail, this section presents total energy DFT calculations supported with low-temperature scanning tunnelling microscopy (STM) to analyse the molecular adsorption on terraces and at step edges. The results of this section have been already published in Refs. [156, 157, 158, 159, 160]. The measurements for the

latter system were performed in the group of M. Sokolowski from the university of Bonn. Our contribution is dominant in Refs. [156, 157, 158], but minor in Refs. [159, 160], where it is restricted to employ the geometries of the relaxed structures and the corresponding adsorption energies to interpret the experimental results.

3.2.1 PTCDA molecules

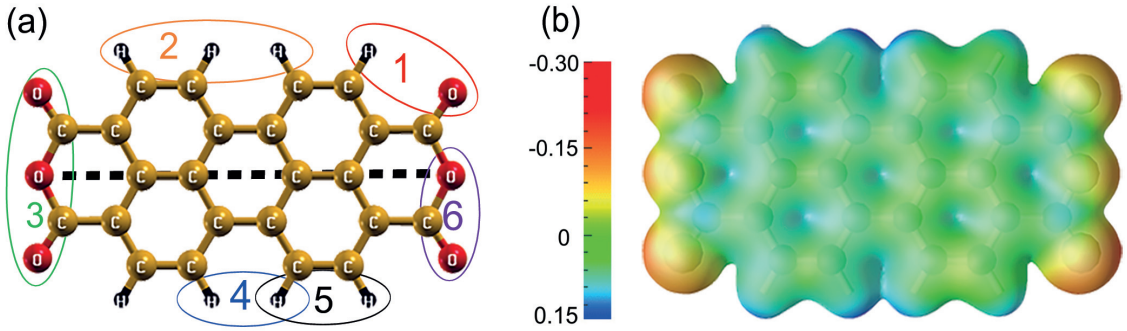

Figure 3.10: (a) Structural model of the PTCDA molecule. The different specific binding sites are marked by the numbered ovals. Sites 3 and 6 have acceptor character, sites 2, 4, and 5 have donor character, and site 1 combines both. The dashed line indicates the long axis of the molecule. (b) Calculated local electrostatic potential of the PTCDA molecule (in eV) shown along the charge density isosurface 0.1 e/Å^3. Red/blue regions indicate low/high values of the electrostatic potential.

PTCDA ($C_{24}H_8O_6$) is a prototypical functional molecule with nonuniform internal charge distribution (Figure 3.10). In comparison with DIP molecules (see section 3.1), negatively charged side groups are substituted at the benzene rings. This allows the negative charge to be localised on the two anhydride groups, in particular on the four carboxylic O atoms on the corners, while the hydrogen-terminated edges of the molecule to carry partial positive charges (Figure 3.10 b). This molecule has been attracted great interest because of its remarkable ability of good epitaxial growth and its particular properties to form well-defined long-range orders on various surfaces [161, 162]. These properties can be ascribed to the molecular inherent structure (Figure 3.10 a): PTCDA is a planar molecule and bears different non-equivalent binding sites of either pure donor (sites 2, 4, and 5 where the molecule can form either double or triple hydrogen bonds), pure acceptor (sites 3 and 6) character or both (site 1). Thus, the combination of these non-equivalent sites of the adjacent PTCDA molecules in different ways further helps the formation of the already mentioned long-range orders [161].

3.2.2 Previous studies

Many experimental and theoretical investigations have been devoted to study the growth properties and the molecular arrangements of PTCDA on KCl and NaCl surfaces [161,

163, 164, 165, 166, 167, 168, 169, 170]. PTCDA is found to adsorb on both surfaces in long-range commensurable square-cell monolayers structures [166, 168, 170, 167]. In particular, these studies concerned complete monolayers of molecules so that the intermolecular interactions dominantly constitute the molecular properties (e.g., geometries, optical spectra, etc). However, the major part of this study concerns the case where the intermolecular interactions are negligible (single molecules case). Experimentally, this interesting situation arises when very small quantities of PTCDA are deposited on the surface. Hence, the adsorption is only dominated by the surface, while the relatively large distances separating the molecules allow for neglecting the intermolecular interactions. This case was first studied by Karacuban et *al.* for PTCDA deposited on NaCl(100) [162], and, then by Paulheim et *al.* for PTCDA deposited on KCl(100) [171]. Karacuban et *al.* reported that single PTCDA molecules adsorb preferably at defective <100> oriented step edges. In particular, they identified a so-called vacancy site as most stable. Paulheim et *al.* showed in their polarisation dependent fluorescence spectroscopy investigations that single PTCDA molecules adsorb at very low temperatures (< 20 K) at initial states as follows: PTCDA molecules adsorb parallel to the surface with slightly out-of-plane geometries while their long axes are azimuthally oriented along the [110] or [1$\bar{1}$0] directions of the surface. They corresponded this state to the terrace site. After thermal annealing or intensive optical illumination, they showed that the molecules were irreversibly diffused to energetically favoured sites. At the new sites, they proved that the molecular orientations remain similar to that at the initial state (terraces sites). They corresponded the energetically favoured sites to step edge sites analogous to Karacuban et *al.* [162].

3.2.3 Experimental results

In the following, the accompanied experimental measurements are shortly introduced. As already mentioned, the measurements were performed in the group of M. Sokolowski concerning PTCDA on KCl(100) surface [158]. Apparently, the results can be extended to NaCl(100) surface. The STM measurements were recorded after about 1% of a full monolayer of PTCDA had been deposited onto a thin KCl(100) film of about 3 layers in thickness on Ag(100) at about 100 K. The sample was transferred into the STM chamber and cooled down below 40 K (see Appendix B for details).

In Figure 3.11 a, the KCl bilayers, i.e., terraces of KCl, which consist of two atomic layers, can be identified from straight edges in the non-polar <100> orientation. Figure 3.11 b shows an STM image of the same layer but with higher magnification. PTCDA molecules are found to be statistically distributed on the terraces with no signs for a preferential adsorption at step edges. Interestingly, all molecules are imaged with a coffee bean-like shape, where the large distances separating the molecules causes the submolecular resolution to be absent, and only the node plane along the long molecular axis of the PTCDA molecule (see Figure 3.10) is imaged yielding the coffee-bean-like shape. Important in the context of the present results is that all molecules are oriented with their long axis

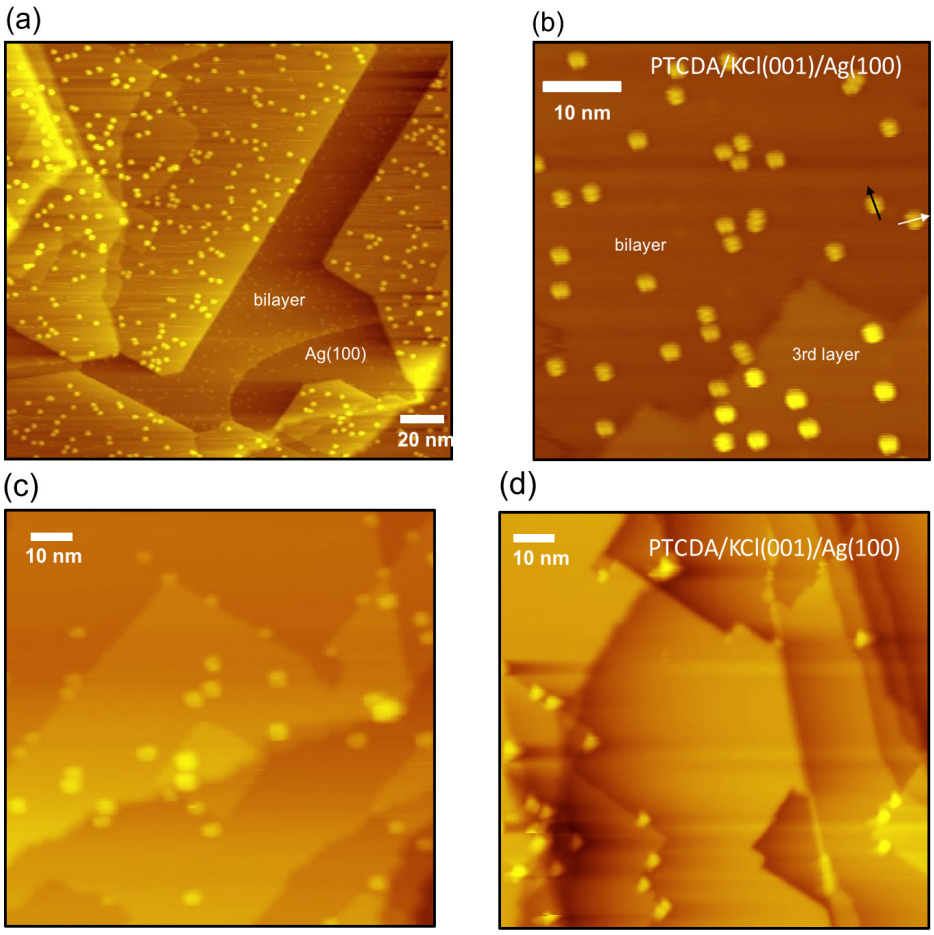

Figure 3.11: (a) Overview of isolated PTCDA molecules deposited at about 100 K on a KCl film of about 3 ML thickness on average (190.2 nm × 209.0 nm). The nominal molecular coverage is about 1% of a full monolayer. The image was recorded at cryostat temperature of 12 K (U_{bias} = -2.1 V; I = 113 pA). The PTCDA molecules are found to be statistically distributed on the terraces. (b) STM image of a smaller area (53.9 nm × 52.2 nm, U_{bias} = 2.5 V; I = 83 pA) with high resolution. Note that only PTCDA molecules with azimuthal orientations of the long axis along the two polar <011> orientations can be observed. (c, d) STM images (99.7 nm × 104.9 nm) after the first annealing cycle at 150 K (c), and a second additional annealing (10 min) at 200 K (d). Obviously, annealing causes the terraces to be emptied of molecules, which migrate towards step edge sites (U_{bias} = -1.5 V (c) and -1.4 V (d); and I = 58 pA (c) and 59 pA (d)).

exclusively along two directions with a relative angle of 90° to each other. This is illustrated by the two molecules marked with arrows on the right-hand side of the image. The corresponding directions are the [110] or [1$\bar{1}$0], which define the <011> orientation. This is the polar orientation that is rotated by 45° with respect to the non-polar <001> orientation. The latter could be experimentally identified from the preferential direction of the straight non-polar KCl step edges, which are oriented along the <100> orienta-

tion. An earlier theoretical simulations (see Ref. [172]) already predicted the <100> NaCl step edges to be significantly more stable than <111> steps at all accessible values of the chlorine chemical potentials. The same result apparently holds for KCl.

Figures 3.11 c, d display two STM images recorded after the sample has been subject to additional annealing cycles after the deposition of PTCDA molecules onto the cold sample (100 K). After the sample was annealed to 150 K for 10 min, the molecules start to decorate the step edges, while many molecules are still on the terraces (Figure 3.11 c). After the second annealing cycle at 200 K for 10 min (Figure 3.11 d) the PTCDA molecules are exclusively found at the step edges.

3.2.4 PTCDA on KCl and NaCl terraces sites

In this section, it is aimed at calculating and comparing the adsorption of single PTCDA on planar KCl(100) and NaCl(100) terraces, and at giving an explanation of the exclusive orientation of PTCDA molecules along a <110> orientation of KCl(100) terraces for the deposition conditions. The calculated properties of KCl and NaCl bulk parameters and those of the (100) surfaces are shown in Appendix A.2.

3.2.4.1 Single PTCDA molecule on KCl(100) and NaCl(100)

In order to calculate the electronic and geometric properties of single PTCDA molecules on KCl and NaCl(100) surfaces, supercells of dimensions (4 × 4) surface unit cells have been used. For such dimensions, it is confirmed that intermolecular interactions between the periodic images are negligible. For supercells of the aforementioned dimensions, various adsorption geometries have been tested. Thereby, the azimuthal orientation of the molecular long-axis is variated between the [100] and [110] directions of the surface while the molecular centre is considered to reside either on top of an anion, on top of a cation or bridging between these sites. The corresponding adsorption energies have been calculated and compared (the adsorption energy of some probed structures can be deduced from Figure 3.13).

	d_1 [Å]	d_2 [Å]	φ°	m_1 [Å]	m_2 [Å]
KCl(100)	2.76	3.40	176.20	0.40	0.17
NaCl(100)	2.60	3.40	172	0.70	0.37

Table 3.2: Comparison of the geometries of single PTCDA molecules on KCl(100) and NaCl(100) in most stable structures (SQ). The quantity d_1 expresses the distance between the carboxyl oxygen atoms of PTCDA and the surface ions beneath, d_2 is the distance between the center of the molecule and the surface ion beneath. φ expresses the anhydride-O-center-anhydride-O angle. The quantities m_1 and m_2 denote the downwards movement of the carboxyl oxygen atoms and the anhydride oxygen atoms of the molecule compared to its center.

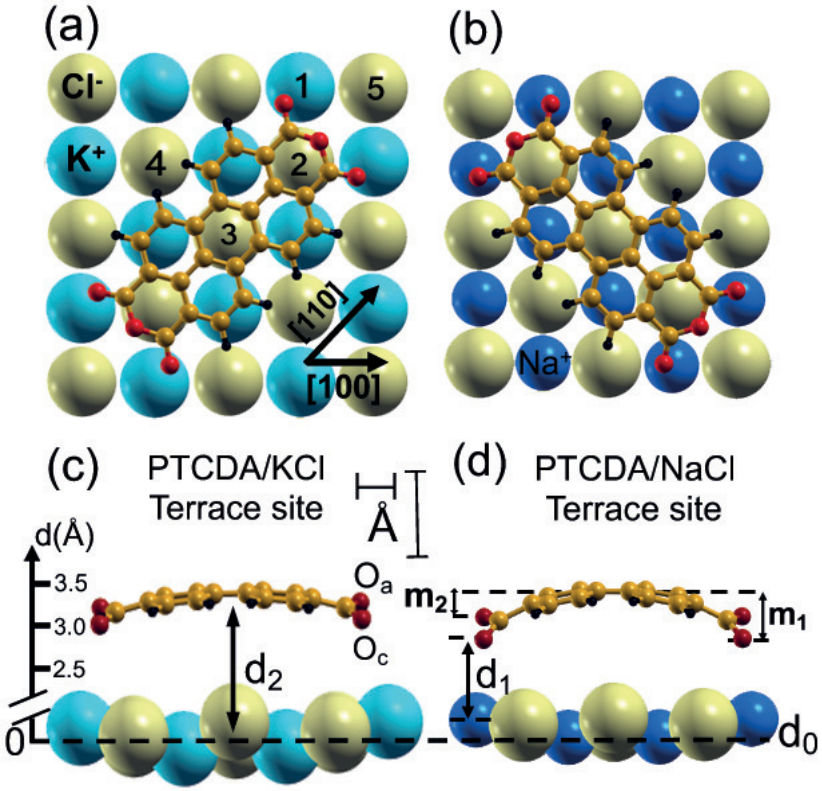

Figure 3.12: (a) Model structures (top view) of single PTCDA molecule on KCl(100) and (b) on NaCl(100) in the most stable structures (SQ). The inequivalent surface atoms beneath the molecule are labelled from 1 to 5. Their displacements upon the molecular adsorption are shown in Table 3.3. (c) and (d) show side-views of the SQ structures on KCl and NaCl, respectively. In the side-views, the vertical scale is enlarged by a factor of 3 for the molecular atoms and surface ions in order to better illustrate the buckling of the substrate and the vertical distortions of the molecule (in Å). The carboxyl (anhydride) oxygen atoms are denoted as O_c (O_a). The amount d_0 is the average vertical height of the top-most surface atoms without the adsorbed molecule and corresponds to zero vertical shift (in Å). All other quantities are defined and compiled in Table 3.2.

The calculations confirm the observed molecular orientation on KCl (see section 3.2.3) and can be extended to the case of NaCl [173]. In its most stable structure (which is denoted as SQ), a single PTCDA molecule adsorbs on both KCl(100) and NaCl(100) parallel to the surface with its long axis parallel to a <110> orientation (see Figure 3.12). Beyond the resolving power of the experiment, the calculations show that the molecular centre is residing above a surface anion, and the four carboxylic oxygen atoms (O_c) are above the surface cations, hence anchoring the molecule on its four corners by attractive Coulomb interactions. The adsorbed molecule is notably bent. Its distortion is in an arch-type and its symmetry is now C_{2v} (D_{2h} in gas phase). Compared to its adsorption on KCl(100), PTCDA has a higher adsorption energy on NaCl(100) and both the molecule and the surface are more strongly distorted (Tables 3.2 and 3.3). On KCl (NaCl), the carboxyl

atom number	1	2	3	4	5
on KCl(100)	+0.13	-0.10	-0.10	+0.02	-0.04
on NaCl(100)	+0.14	-0.10	-0.11	+0.04	-0.05

Table 3.3: Vertical shifts of the surface atoms upon the adsorption of PTCDA (surface buckling). Numbers 1 to 5 are associated to the atoms labelled in Figure 3.12. A positive/negative sign corresponds to the upwards/downwards movement. All values in [Å].

/anhydride oxygen atoms of the molecule are 0.4 (0.70)/0.17 (0.37) Å closer to the surface than the centre of the molecule. The distance between the carboxyl oxygen atoms of the molecule and the surface cations beneath is 2.76 (2.60) Å, while the distance between the centre of the molecule and the surface anion beneath is 3.40 Å (in a good agreement with the experiment (3.4 ± 0.2 Å [167]) for NaCl(100), while no experimental results are available for PTCDA on KCl(100)). The surface cations beneath the carboxyl oxygen atoms are pulled out of the surface by 0.13 (0.14) Å, and the surface anions underneath the molecular perylene rings are pushed into the substrate due to the repulsive interactions between the central perylene ring and the surface anion beneath it. In the SQ structure, the adsorption energy of PTCDA on KCl(100) is -2.49 eV, while it is -2.91 eV on NaCl(100). In both cases, about 72% of the adsorption energy originates from the vdW interactions. As reported by Möbus et *al.* [163] and Schlettwein et *al.* [164], the more distorted geometries and the higher adsorption energy of PTCDA on NaCl can be understood as a result of the smaller lattice constant of NaCl (5.6 Å) compared to KCl (6.25 Å), offering a better overlap between the carboxyl oxygen atoms of PTCDA molecules and the surface cations on the one hand and between the hydrogen atoms of PTCDA and the surface anions on the other hand (Figure 3.12).

3.2.4.2 Lateral and rotational barriers

In section 3.2.3, it was mentioned that upon deposition at low temperatures, the molecules are statistically distributed on the terraces and exclusively oriented with their long-axes along the polar directions [110] or [1$\bar{1}$0] of the surface. This observation indicates that lateral diffusion is very small at temperatures below 100 K and that the molecules hit and stick during the deposition process. In other words, there should be considerable barriers which prevent the molecules to migrate to the more favourable step edge sites.

In order to explain the random distribution of molecules subsequent to deposition and to determine their lateral diffusion barriers, the potential energy surfaces (PESs) have been calculated on both surfaces. Thereby, the molecular adsorption energies are laterally sampled on a dense mesh with a distance of 0.1 Å between the grid points, taking the molecular centre as reference. The long axis of the molecule is kept parallel to the <110> orientation of the surface by constraining the lateral degrees of freedom of the two inner carbon atoms indicated in green, while all other atoms are allowed to move and relax freely. On KCl (NaCl), the calculations show a maximum corrugation of 0.87 eV (0.71 eV) for the

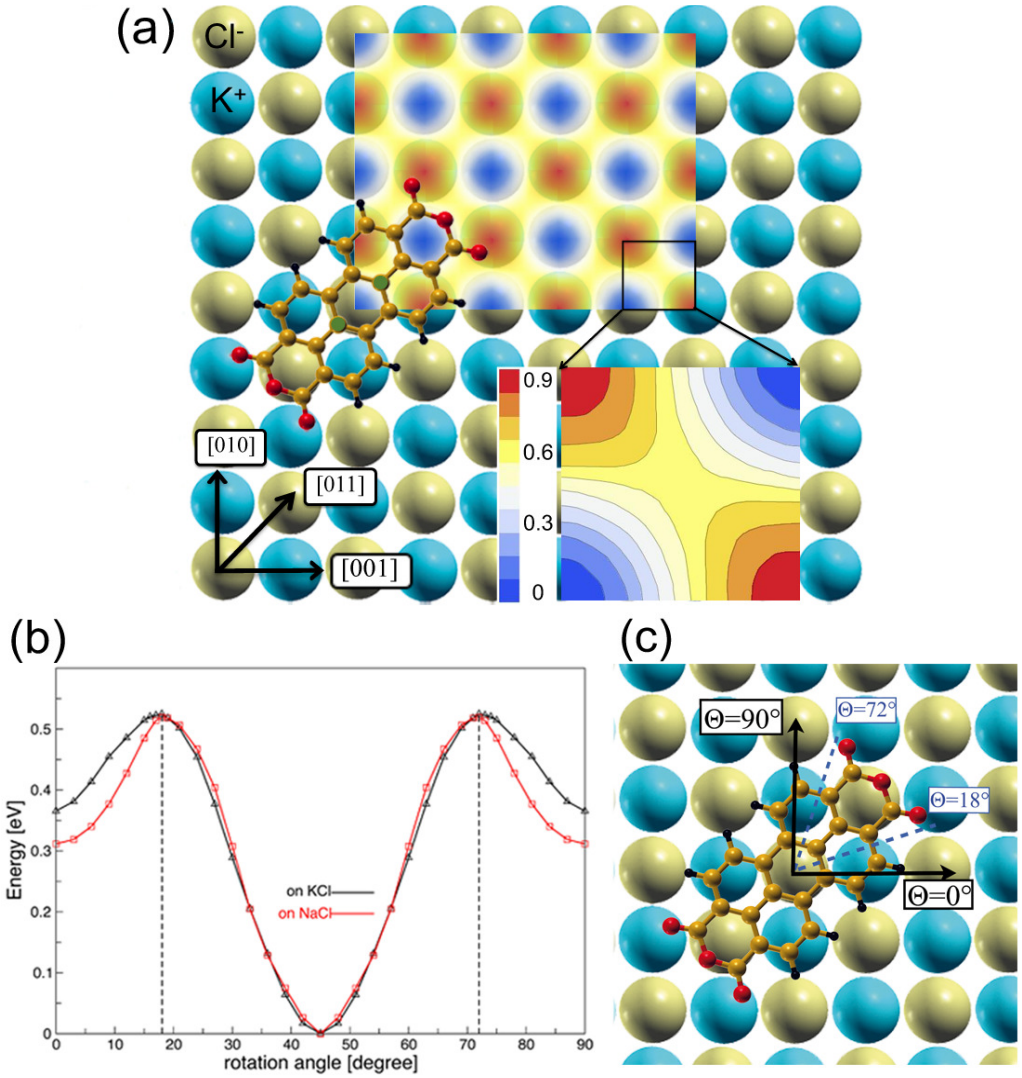

Figure 3.13: (a) Calculated potential energy surface (PES) for PTCDA on KCl(100). The energy of the most favoured structure (SQ) corresponds to zero energy (in eV). The less favourable adsorption configurations have, then, positive energies. The indicated green inner atoms were laterally fixed (see text for details). For NaCl, a similar map is calculated (not shown) with different corrugation of the surface 0.71 eV (0.87 eV for KCl) and diffusion barriers of 0.48 eV (0.58 eV for KCl). (b) The calculated rotational energy barriers of single PTCDA molecules on KCl(001) and NaCl(100). The molecular long axis forms an angle (θ) with respect to the substrate [100] direction (c). The energy of SQ is chosen as zero energy. It forms an angle of $\theta = 45°$.

PES and diffusion barriers of 0.58 eV (0.48 eV). These barriers explain the experimental observation (performed on KCl) about the azimuthal ordering present already at 100 K, where the lateral mobility of the molecules (to be activated by at least 0.58 eV) is still very limited at this temperature. Based on our calculations, this result can be extended to

NaCl. On both surfaces, the PESs are pretty similar. They show low energy anion-anion diffusion channel, while single PTCDA molecules avoid structures where their centres are above the surface cations (Figure 3.13 a). However, the lateral diffusion barriers on NaCl are smaller than on KCl, which might be due to the smaller lattice constant in case of NaCl. Note that for the <110> orientation on both surfaces, there is no other local minima beside SQ structures. Thus, we can conclude that the experimentally observed molecules with their long-axes parallel to the <110> exhibit also site-specific adsorption where they exclusively adsorb in the SQ structure.

In order to more rationalise the molecular orientation, the adsorption energies as a function of the molecular rotation angle have been calculated (Figure 3.13 b). The adsorption energies have been calculated for angles between $\theta = 0^o$ and $\theta = 90^o$ which correspond to the [100] and [010] directions of the surface (denoted as R structure). The energy of the SQ structure considered as zero on the energy scale ($\theta = 45^o$ in Figure 3.13 c). On both KCl and NaCl, PTCDA shows rotation barriers of 0.53 eV. The maximum is reached for angles of ($\theta = 18^o$ and $\theta = 72^o$) for both surfaces.

According to the lateral and rotational barriers, the SQ structure indeed corresponds to the global energy minimum on both surfaces, while the adsorption configuration with the molecular axis parallel to [100] (R structure) represents a local energy minimum. This most favourable 45^o orientation (SQ structure) can be reached by an activation energy of less than 0.15 eV (for KCl)/0.20 eV (for NaCl). Experimentally, no stable structures with long molecular axis parallel to [100] or [010] have been observed, even when the substrate temperature upon deposition is less than 20 K. Only stable or metastable states with $\theta = 45^o$ (corresponding to <110> orientation) are measured (see Appendix A.2 for more information about the meta stable states which appear upon adsorption at very low substrate temperatures).

It should be noted here that the translational and rotational barriers have been separately calculated. Thus, the full relaxation of both the lateral degrees of freedom and the orientation of the molecules can be expected to lower the diffusion barriers.

3.2.4.3 Role of the film thickness for diffusion

After the deposition of PTCDA molecules onto the "cold" sample (100 K) and the subsequent additional annealing cycles (first to 150 K for 10 min and then at 200 K for 10 min), PTCDA molecules are exclusively found at the step edge sites (see section 3.2.3 for further details). Obviously, lateral diffusion becomes possible above 150 K allowing the PTCDA molecules to move to the energetically more stable step edge sites. In fact, a similar result was deduced earlier from fluorescence spectroscopy on this system (see Ref. [171]). However, there diffusion was already possible at ∼70 K. This discrepancy in thermal barriers might be ascribed to different thicknesses of the KCl(100) film deposited on Ag(100) surfaces (∼10 layers in the optical experiments Ref. [171]), but only 2-3 layers in this STM experiment.

In order to explore the reason behind this apparent change of the diffusion barriers, additional calculations were performed. Decreasing or increasing the thickness slab to two or eight atomic layers, respectively, without including Ag(100) surfaces did not modify the diffusion barriers measurably. This indicates that the experimentally observed change of the diffusion barriers is not a direct result of the different film thicknesses. However, two additional factors conceivably affect the diffusion barriers: the change of the KCl lattice constant and the inclusion of Ag(100) layers beneath the bilayer KCl film. First, a distinct influence of the KCl lattice constant on the diffusion barrier is found: The compression/expansion of the KCl lattice constant by about 5% reduces/increases the calculated diffusion barriers by about 0.1/0.04 eV (see Appendix A.5). While this could have an measurable influence if the metal strains the KCl film (as reported, e.g., for NaCl on Cu(111) [174]), one also has to state that no changes of the KCl lattice constant upon epitaxial growth of KCl on Ag(100) have been observed experimentally [168]. Hence, this effect has to be ruled out. Next, the adsorption of PTCDA on two layers of KCl on top of an Ag(100) substrate was modelled (see Appendix A.4), starting from the structural configuration described in Ref. [168]. In comparison to the calculations for the six layer KCl slab without Ag substrate, it is found that the lateral diffusion barriers and surface corrugation are increased from 0.58 and 0.87 eV to 0.77 and 1.14 eV, respectively, while the orientation and the registry of the molecule with respect to the surface do not change, apart from very minor structural modifications that are below 0.03 Å. This agrees with earlier experimental findings [168]. Thus, the calculations conclude that an electronic rather than a structural effect of the Ag(100) substrate is responsible for the modification the molecular diffusion barriers. The metallic states, which extend through thin KCl film, are probably suppressed for thick KCl substrate in Ref. [171]. This is in line with the work of Repp et *al.* [14] who proven that the Cu substrate metallic states extend into the first few layers of a thin NaCl film.

Apparently, the investigations of the metal/insulator/organic interfaces are more complicated than such simple calculations. However, the detailed exploration of this effect is beyond the scope of the present study and must be systematically investigated to correctly address it (see Appendix A.6 for further information).

3.2.5 Monolayer of PTCDA on KCl(100) and NaCl(100)

Monolayers of PTCDA on KCl(100) have been experimentally studied by Dienel et *al.* [166] and Müller et *al.* [12]. Both studies showed that a monolayer of PTCDA tend to form highly ordered commensurate structures in domains of dimensions more than 100 Å. These domains consist of repeated square-cell structure of dimensions of a = b = 12.6 ± 0.1 Å. Within each unit cell, the molecules are arranged in a brick-wall form (abbreviated as BW-phase), where they adsorb in a flat-laying structure parallel to the surface and to each other while their long axis parallel to [110] or [1$\bar{1}$0]. Despite the registry of the molecules are experimentally unclear, it is plausible to suppose that their centres reside above anion sites of the surface and the carboxyl oxygens above cation sites.

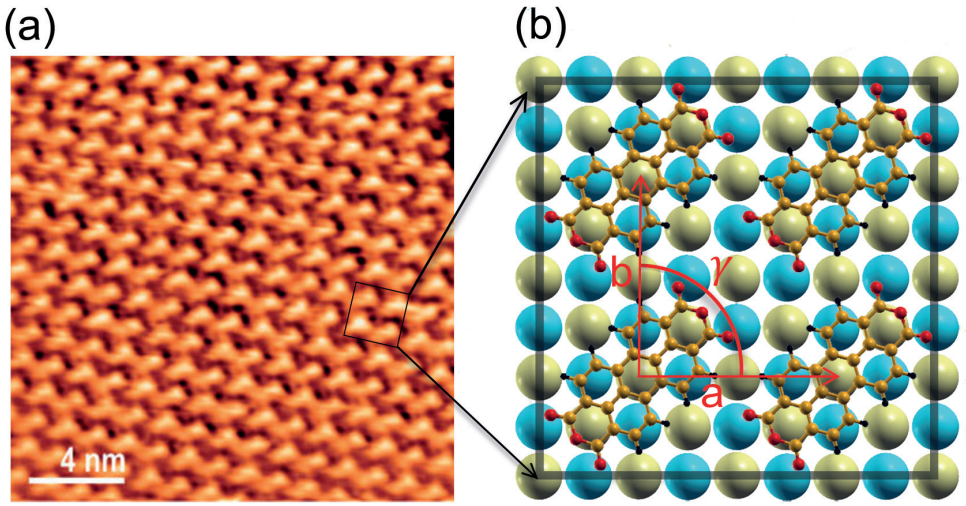

Figure 3.14: (a) AFM image of PTCDA on KCl(100) in the so-called brick-wall (BW)-structure. The supercell has the dimensions a = b = 12.6 ± 0.1 Å, $\gamma = 90^{o}$ (taken from Ref. [166]). (b) Calculated structural model of the BW-phase.

The calculations confirm the experimental findings for the BW-phase. In the energetically most favoured structures among the models investigated, the molecules adsorb in square-cells with dimensions a = b = 12.50 Å, $\gamma = 90^{o}$ (associated to 2 × 2 surface-cells). The molecule has the same orientation as observed experimentally. Its adsorption energy (-2.75 eV) is lower than that of the other suggested structures: Herringbone (HB) (-2.55 eV), Q-phase (-2.63 eV) (Figure 3.15). Furthermore, a slight energy gain compared to an isolated adsorbed molecule (-2.49 eV) is found, indicating the presence of stabilising intermolecular interactions. The registry of the molecule is similar in all these structures. In contrast to the BW-phase, which has one molecule in the unit cell, the HB- and the Q-phase unit cell contain two molecules per unit cell rotated by 90^{o} with respect to each other. A monolayer of molecules in the Herringbone-phase exhibits a commensurate $p2 \times 3$ film, while the Q-phase shows a larger strain with a $p3 \times 3$ film (Figure 3.15).

	d_1	d_2	φ^{o}	m_1	m_2	S_1	S_2
SQ-phase	2.76	3.40	176.20	-0.40	-0.17	+0.13	-0.10
BW-phase	2.80	3.42	176.90	-0.35	-0.14	+0.12	-0.10

Table 3.4: Comparison of the geometries of the SQ-phase (isolated molecule) and the BW-phase (monolayer of molecules). The quantities m_1 and m_2 are defined in Table 3.2. Quantities S_1 and S_2 denote the shifts of the surface cations beneath the carboxyl oxygen atoms and the movement of the surface anion beneath the center of the molecule, respectively. A positive/negative sign corresponds to the upwards/downwards movement. All values in [Å].

In the BW-phase, the vdW-interactions make up 73% of the adsorption energy. This adsorption energy can be divided into two terms: -0.38 eV (molecule–molecule interactions)

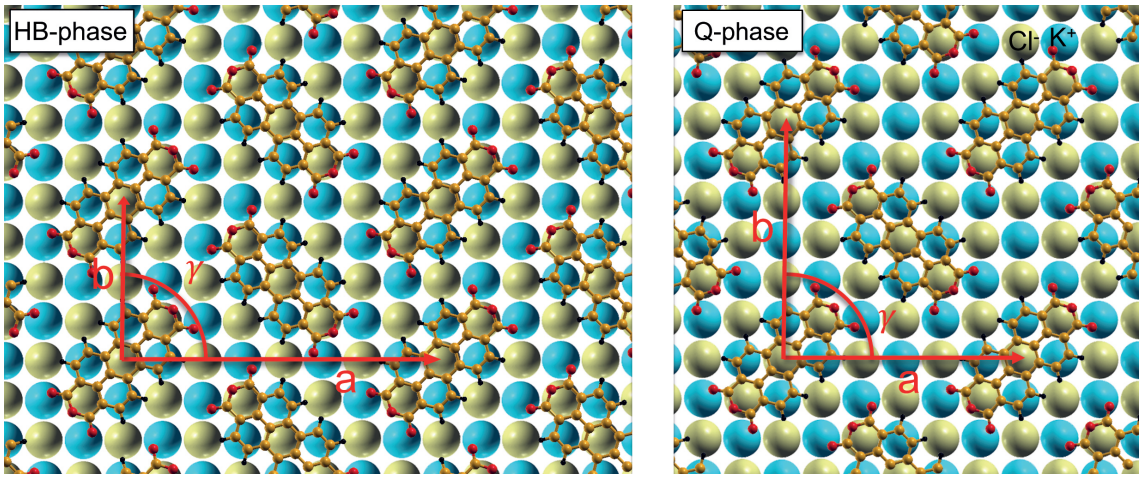

Figure 3.15: Structural model of the Herringbone phase (HB-phase) of PTCDA on KCl(100) (*left*). Cell dimensions are a = 18.75 Å, b = 12.5 Å and $\gamma = 90^{o}$. (*Right*) Square phase model for PTCDA on KCl(100) (Q-phase) with cell dimensions a = b = 18.75 Å and $\gamma = 90^{o}$.

and -2.37 eV (molecule–substrate interactions). Due to the smaller molecule–substrate interaction in the BW-phase, also the distortion of the molecule is smaller than for isolated molecules (see Table 3.4). The calculations yield different adsorption energies than previous force field calculations (-1.81 eV [166]), but the electrostatic part for both calculations (about -0.80 eV) is almost the same. To our knowledge, no experimental studies for measuring the distance between the PTCDA molecule and the KCl(100) surface either for the isolated molecules or for the monolayer have been reported.

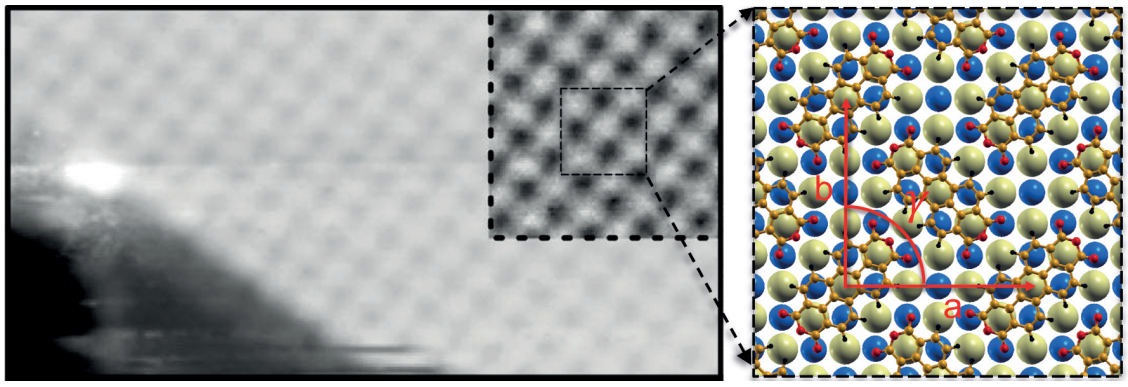

Figure 3.16: (Left) PTCDA on NaCl in the so-called Q-phase taken from the nc-AFM study (see Ref. [167]). (Right) DFT calculations for the adsorbed PTCDA molecule over NaCl(100) in the Q-phase arrangement. The cell dimensions are a = b = 16.80 Å, $\gamma = 90^{o}$.

The morphology of submonolayer and higher coverages of PTCDA on bulk NaCl has been experimentally investigated by Burke et *al.* by means of the nc-AFM [167]. Eric Le Moal et *al.* investigated the growth of PTCDA on 10 monolayer thick NaCl films by spot-

	d_1	d_2	φ°	m_1	m_2	S_1	S_2
SQ-phase	2.60	3.40	172	-0.70	-0.37	+0.14	-0.10
Q-phase	2.82	3.37	175	-0.48	-0.21	+0.08	-0.10

Table 3.5: Comparison between the geometries of the SQ-phase (isolated molecule) and the Q-phase (monolayer of molecules) for PTCDA on NaCl(100). A positive/negative sign corresponds to the upwards/downwards movement. All values in [Å].

profile-analysis low energy electron diffraction (SPA-LEED). Both studies reported similar results about the topography of PTCDA on NaCl(100): Similar to the case of KCl(100), PTCDA adsorbs on NaCl(100) in highly ordered commensurate structures in domains of dimensions more than 150 Å. However, in contrast to KCl, PTCDA molecules adsorb on NaCl(100) in square unit cells with lattice-constant of about 17 ± 0.1 Å (associated to 3×3 surface cells). Thereby, it is reported that in each unit cell of the adstructure a centred molecule has an opposite orientations to those on the corners of the unit cell (i.e., Q-phase).

As already mentioned for KCl, the registries and the orientation of each molecules in the Q-phase are identical with those of the single molecule (SQ). The calculated adsorption energy for the Q-phase is -3.32 eV (-2.91 eV for the single molecule). The adsorption energy can be divided into two parts: The molecule-surface interactions -2.84 eV and the molecule-molecule interactions -0.48 eV. Apparently, the intermolecular interactions play a role in stabilising the structure. As a result of higher molecule–surface interactions, the isolated molecule is distorted more strongly than the molecules in the Q-phase. The oxygen atoms come closer to the surface, and the surface cations beneath the carboxyl oxygen atoms are pulled up by larger amount (see Table 3.5). The calculated distance between the centre of the molecule and the surface anions beneath is 3.37 Å, while it is 2.82 Å between the carboxyl oxygen atoms of the molecule and the surface cations beneath. Our results are in a good agreement with the height of 3.4 ± 0.20 Å measured for the Q-phase by Kelvin probe force microscopy [167]. Their calculated distance is also in good agreement with previous DFT (3.50 Å) and molecular mechanics calculations (ranging from 2.71 Å to 3.73 Å [167]). The differences between our results and the DFT results from Ref. [167] can be attributed to the neglect of dispersive interactions in the latter.

3.2.6 PTCDA at step edges

The statical distribution of PTCDA molecules on KCl terraces upon deposition onto the cold sample (100 K) and their diffusion to step sites upon annealing to higher temperatures indicate that the adsorption on the terrace sites is only kinetically stabilised and step edges should be thermodynamically favoured adsorption sites. In this section, the calculations analyse the adsorption of single PTCDA at KCl and NaCl step edges in detail.

3.2.6.1 Different adsorption sites

Figure 3.17 shows an STM image with high resolution recorded after PTCDA molecules were deposited on the KCl film at room temperature. The higher deposition temperature was used to promote the tendency of PTCDA molecules to be trapped at step edges. Different adsorption configurations of PTCDA at the step edges can be identified in Figure 3.17 (denoted by A to G).

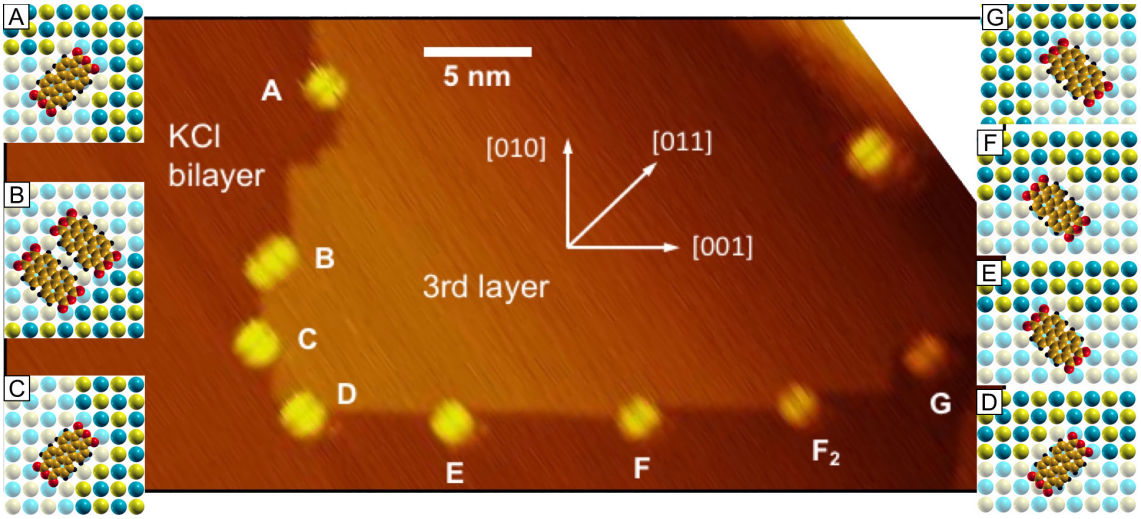

Figure 3.17: STM image of PTCDA molecules adsorbed at different adsorption sites at the step edges of an KCl island on the KCl bilayer on Ag(100) (22.7 nm × 46.6 nm; U_{bias} = -1.0 V and I = 95 pA). Deposition and imaging were both performed at room temperature. Note the image was rotated for clarity and that the scan direction is at about an angle of 45°. The insets show hard sphere models of the different adsorption sites.

The STM image shows that all molecules at step edges have their long axes parallel to the <011> orientation, as found before for the molecules on the terrace sites. This observation is in agreement with the result made by polarised fluorescence spectroscopy [171]. Since this technique averages over a large number of molecules, this agreement strongly suggests that the configurations seen in STM image can be considered as representative. None of the adsorption sites in Figure 3.17 corresponds to a simple non-polar step edge site, a Cl-terminated step edge, or a kink site (see lower part of Figure 3.18). Instead, it appears that all the PTCDA molecules have partially been embedded into the KCl island, i.e., the molecules exclusively adsorb at vacancies of the step edge. The vacancy site E in Figure 3.17 is the simplest of those. As already mentioned, this type of site was already found for step edge decoration of PTCDA on NaCl layers by Karacuban et *al.* [162]. Although one can not identify the polarity of the ions from the STM image, it appears plausible that the cations of the steps face the negatively charged anhydride groups of the PTCDA and thus lead to attractive interactions of the PTCDA with the step edge ions.

In order to explain and further illustrate the experimental findings, a variety of possible mono-atomic defected, straight non-polar and straight polar step edge sits have been modelled within supercells of dimensions 4 × 4 surface unit cells (large enough to suppress the unwanted intermolecular interactions). These sites are: the non-polar (T), the non-polar (S), the Cl-terminated and the K/Na-terminated step edges, various inequivalent kink sites (K/Na-terminated or Cl-terminated), and the vacancy sites (lower part of Figure 3.18). The non-polar step sites contain alternatively positive and negative ions, where they are defect-free and parallel to [100]. In contrast, the Cl-terminated and the K/Na-terminated step edges are parallel to [110] and they are polar, i.e. contain unequal numbers of sodium and chloride ions. The vacancy sites are apparently defective <100> oriented step edges. Irrespective of the defect type, the registry of the molecule is *almost* like that on the planar surface. Its long axis is parallel to a <110> orientation except for the non-polar (S) site. In this case, the molecular long axis is parallel to [010] and the registry of the molecule is similar to structure R (see section 3.2.4.2). The adsorption energies of PTCDA on these sites are given in Table 3.6.

site	KCl	NaCl
terraces sites	-2.49	-2.91
non-polar step edge (S)	-2.51	-3.05
non-polar step edge (T)	-2.57	-3.31
Cl-terminated kink site	-2.70	-3.60
K-terminated kink site	-2.86	-3.64
Cl-terminated step edges	-2.90	-3.47
K-terminated step edges	-3.05	-3.80
vacancy site	**-3.28**	**-4.13**

Table 3.6: Calculated adsorption energies (in eV) of PTCDA at flat terraces and at the adsorption sites illustrated in the lower panel of Figure 3.18.

In agreement with the experimental results and previous investigations [161, 162, 171], step edges are thermodynamically favored over terraces sites irrespective of the kind of the step edge site. At these sites, the molecular configurations take advantage of the further interactions between the ions of the step edge and the molecular partial charges. The trend of the adsorption energies on NaCl is similar to that on KCl for different types of step sites (Cl-terminated step edge sites are an exception). In particular, the vacancy site is the most probable adsorption site among the different suggested defective sites for both surfaces (Table 3.6). The molecular orientation fits with the experimental expectation for KCl and NaCl. Compared to the terraces sites, the energy gain at the vacancy site is 1.22 eV on NaCl and slightly smaller 0.79 eV on KCl (of the same order of magnitude as the activation energies). The difference between the two surfaces can be traced again to the smaller lattice constant of NaCl compared to KCl, which leads to smaller vacancies. This, in turn, increases the interaction between molecular oxygen and vacancy Na atoms as well as between the molecular hydrogen and vacancy Cl atoms: The respective O-Cl distances (d_{exp}, see Figure 3.18) are calculated to be 4.8 and 4.0 Åfor KCl and NaCl, respectively.

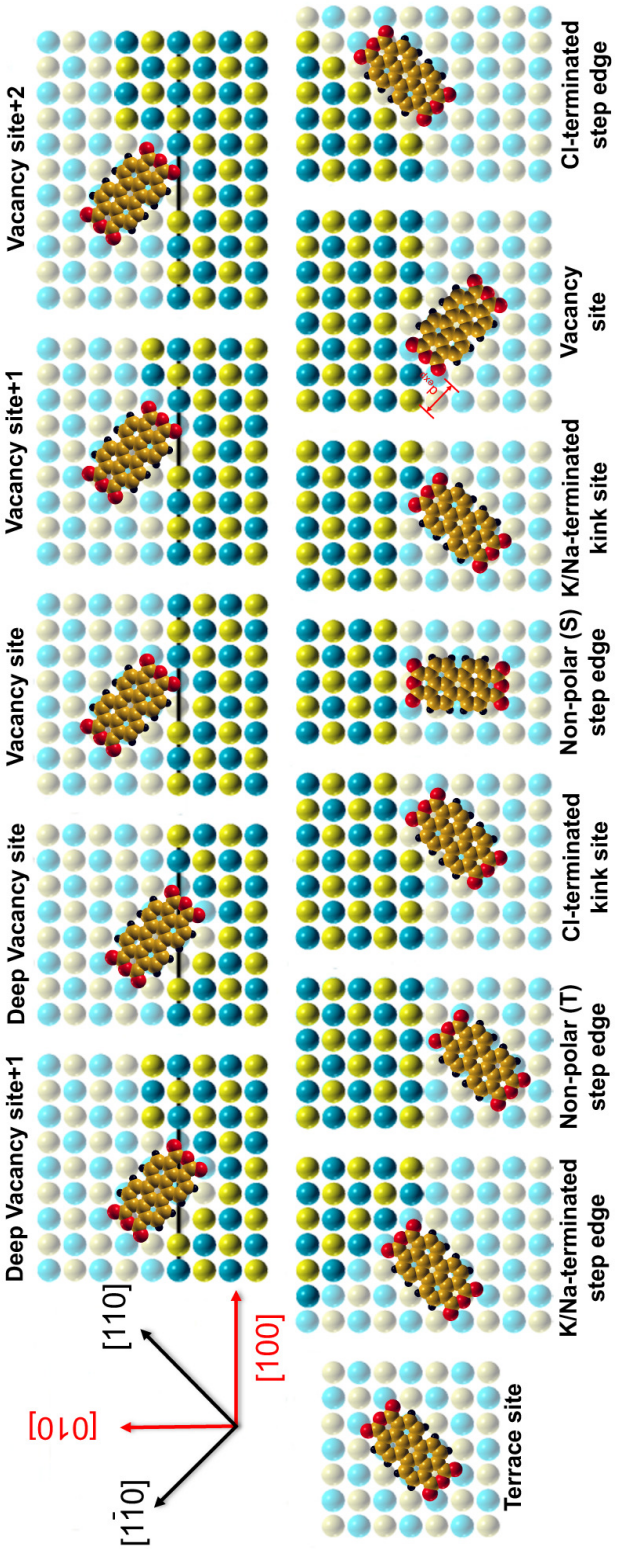

Figure 3.18: Different suggested models of defect-free and defected KCl step edge adsorption sites are shown in the lower part. The orientations of PTCDA molecules with respect to the surface and to the step-edge orientations are shown and compared with the terrace site (left part). The measured distance between the oxygen atoms of the PTCDA and the chloride atoms of the step edge as seen by STM is denoted as d_{exp} [162]. In the upper part, the different suggested models of vacancies are shown. A depicted black line shows the further molecular embedding into the step edges in the deep-vacancy (deep-vacancy +1) site compared to a simple vacancy site.

The latter value is in perfect agreement with the experiment [162], while no measurements have been reported for NaCl.

Starting from the adsorption at a vacancy site, even more favourable adsorption sites may be obtained by deepening the molecule within the step edge. Thereby, a larger facets of positively charged K/Na atoms could interact with all oxygen atoms of the molecule and the larger Cl-terminated facets attract the hydrogen atoms of the molecule. This case is denoted as deep vacancy site (see the upper part of Figure 3.18). The deep vacancy sites resemble the simple vacancy site. However, three K-Cl pairs must dissociate from the step edge in order to realise it. Thereby, the molecule is deeper embedded into the step edge. The adsorption energy of the molecule at this site amounts to -3.75 eV, which is far more favourable than for flat terraces. In Figure 3.17, the sites C and D can tentatively be assigned to such deep vacancy site, while E may correspond to a vacancy site. This assignment is supported by the finding that the molecule in D confirmation is deeper embedded into the step-edge compared to site E, while the steps outside of these sites are still straight. The other configurations highlighted in Figure 3.17, i.e., sites A, B, F, and G, do not have straight steps on the both sides of the molecule. On site F (F_2), it looks like one additional row (two additional rows) of K^+ and Cl^- ions forms along the retracted part of the vacancy site. Accordingly, these sites are denoted as vacancy site+1 (vacancy site+2). The molecule at site A is deeply embedded into the step-edge with extra K^+ and Cl^- ions. On the upper part of Figure 3.18 an overview of hard sphere models for the different plausible sites is given. On these sites, the calculations reveal the molecule to have adsorption energies of -3.44, -3.47, and -3.76 eV at a vacancy site+1, vacancy site+2, and a deep-vacancy+1 site, cf. Table 3.7.

adsorption site[a]	adsorption energy (eV)	defect formation energy (eV)[b]	net adsorption energy gain (eV)[c]
vacancy site	-3.28	0.57	-0.22
vacancy site+1	-3.44	1.28	0.33
vacancy site+2	-3.47	1.53	0.55
deep vacancy site	-3.75	1.51	0.25
deep vacancy site+1	-3.76	1.91	0.64

Table 3.7: Calculated energies related to the adsorption of PTCDA for different types of vacancy sites at KCl step edges. [a]The respective sites are illustrated in Figure 3.18. [b]Formation energies of the respective defective step edge site (without molecules). [c]Net energy gains for molecular adsorption at the respective sites with respect to adsorption on flat terraces.

3.2.6.2 Formation of the adsorption sites

How does the PTCDA adsorption at the step defects, e.g., at a vacancy site, occur? One may envisage different kinetic pathways. Molecules may diffuse on the surface until they are trapped by a two atom wide vacancy at a step edge. However, given the comparatively

large formation energy of step-edge vacancies (see Table 3.7), this scenario appears unlikely. Another possibility is that the molecules adsorb at a step-edge kink site first, and then an additional row of K-Cl pairs(results from diffusing KCl molecules) is formed along the retracted part of the step edge. This possibility is suggested from the observation of the sites F and F_2 (see Figure 3.17), which are denoted as vacancy site+1. This type of site is obtained from the vacancy site in the same way; namely, by adding one additional row of ions on one side of the molecule. Hence, there is a strong indication that surface KCl diffusion is important for the formation of these sites. It should be noted that diffusion of KCl molecules instead of single ions is plausible because, as reported by Hove [175], the heat of sublimation of KCl is 2.2 eV and hence far smaller than the dissociation energy of KCl pairs (4.4 eV). A more probable pathway is the formation of the vacancy site directly upon molecular adsorption at the step edge. In order to probe this computationally, the formation energies of different vacancies configurations (without admolecules) have been calculated. Thereby, the energy differences are calculated between the straight steps and the defective steps assuming that the KCl at the steps is in equilibrium with bulk KCl, i.e., it has the same chemical potential. The defect formation energies obtained this way (second column in Table 3.7) need to be taken into account when comparing the molecular adsorption energies at defective steps, straight steps, and flat terraces. Obviously, even after the vacancy formation energy of 0.57 eV has been taken into account, there remains a net energy gain of -0.22 eV for molecular adsorption at the vacancy site versus the flat terrace site (third column in Table 3.7). The energy gain is reduced to -0.14 eV, but still significant when comparing the molecular adsorption at straight non-polar step edges with adsorption at vacancy sites. Thus, a molecular adsorption induced defect formation is at least thermodynamically conceivable. The experimental verification of the adsorption mechanism is difficult. However, two experimental observations support this scenario:
(i) Essentially only molecule-occupied step-edge vacancies are found with STM (Figure 3.17) suggesting that these vacancies are indeed formed subsequent to molecular adsorption.
(ii) At higher coverages the molecules are found to decorate and erode the entire step edge (see Appendix A.7), which is consistent with the scenario that KCl pairs are actively replaced by PTCDA at the step edges.
In fact, it appears that the intrinsic kink density on the [100] orientated steps is too small to serve as the only seed points for the formation of the observed density of molecule-occupied vacancy sites, thus supporting the suggested model of a molecular adsorption induced vacancy formation. However, the proposed mechanism is thermodynamically favourable only for vacancy sites. The formation energy of all other defects considered here exceeds the energy gain due to molecular adsorption at the defect rather than at the flat terrace, see third column in Table 3.7. The formation of these adsorption sites thus necessarily occurs kinetically, e.g., by adsorption of KCl molecules diffusing on the terraces at these sites, as described above. In these cases the attractive interaction of the PTCDA with the step edge does not overcompensate the additional line tension caused by the corresponding empty vacancy site.

3.3 Intermediate Conclusion

The so far shown results present an investigation of two π-extended molecules adsorbed on metallic and isolated surfaces. The two systems are similar in many aspects, e.g., the vdW-interactions play an important role in the adsorption and step edges initiate the structure formation. However, the structure formation in both systems are remarkably different. DIP are perylene-based molecules missing a functional group. Their adsorption on the comparatively reactive Cu(111) featuring three-fold symmetry gives rise to short-ranged orders where the molecules are dictated by the substrate symmetry. In an apparent contrast to the aforementioned case, the adsorption of the functional PTCDA molecules on an ionic surface with twofold symmetry is dominated by the electrostatic interactions. The molecules exclusively anchor to specific sites of the terraces and at step edges with their long-axes parallel to one of the <110> orientations of the surface. These aspects in combination with the considerable intermolecular interactions between heterogeneous sides of adjacent molecules enable the formation of long-range orders of molecules on the surface.

What we learn from the aforementioned results and which procedures can be thought of to assist in the formation of the LR ordered DIP structures on Cu(111)? One possibility is to increases the molecule–molecule interactions, so that they gain importance compared to the strong molecule–surface interactions. This could, e.g., be a complementary functional group or an adatom, like e.g. a mobile Cu atom. Such a partly catalytic and structure-controling effect of metal atoms has e.g. been described in Ref. [176]. Breaking the three-fold symmetry of the Cu(111) surface may also assist in LR ordering. This can be realized, e.g., by using a strained Cu(111) substrates. The first method has been applied by introducing copper-phthalocyanines (CuPc) or fluorinated copperphthalocyanines (F_{16}CuPc) [177] with DIP molecules. The influence of lattice strain on the adsorption of molecules on a surface has been already reported in section 3.2.4.3. A uniform strain was found to influence both the adsorption energies and the mobility of the molecules, such that the formation of phases which require a stronger reordering might be either promoted or hindered according to the strain parameter.

4 Free-Base Corroles on Ag(111): Multilayer Reference and On-surface Chemical Transformations

> Yesterday we obeyed kings and bent our necks before emperors. But today we kneel only to truth, follow only beauty, and obey only love.
>
> *(Khalil Gibran 1883-1931)*

This chapter reports density functional theory (DFT) calculations supported with scanning tunnelling microscopy (STM) and element-specific X-ray spectroscopy measurements to characterise the 2D molecular system of free-base corroles on Ag(111) and their on-surface chemical transformations. The role of the DFT calculations is important to draw the conclusions. In particular, they help to interpret and explain the experimental results. Furthermore, they enable in-depth analysis and monitoring of on-surface chemical reactions reaching the site-selective ones, thus, providing information not accessible to other techniques.

This work is a central part of the DACH I-958 project, titled "High valent metal tetrapyrroles for surface supported catalysis". The XPS, the NEXAFS and the Temperature Programmed Desorption (TPD) were measured in the group of J. V. Barth (Physics of surfaces and interfaces group, Physics Department E20, Technical University of Munich); the STM measurements were performed in the group of R. Koch (Institute of Semiconductor and Solid State Physics, Johannes Kepler University, Linz, Austria). Some of the achieved results, presented in this chapter, have been already published in Refs. [178, 179, 180, 181].

The upcoming sections are organised as follows: After a short introduction of the studied molecule, namely the 5,10,15-tris-(pentafluorophenyl)corrole (H_3TpFPC) (see section 4.1), the XPS and the NEXAFS spectroscopy characterisations of ultrapure multilayer samples are shown in section 4.2. In parallel, the respective X-ray fingerprints are simulated and accurately interpreted. In section 4.3, it is focused on the structural properties and X-ray spectroscopic signatures of the intact corrole species (see 4.3.2) and their subsequent changes corresponding to the singly dehydrogenated molecules (see 4.3.3) over (multiple) ring-closure reactions between the fluorophenyl rings and the macrocycle (above 430 K, see sections 4.3.4 and 4.3.5), up to the formation of inter-molecularly linked networks (above 550 K). This in-depth study highlights how the theory-aided approaches are capable of

giving insight into the complex chemistry of prototypical free-base corrole interfaces and discriminating highly similar structures such as tautomeric or isomeric configurations.

4.1 Corroles

The word corrole is a derivative from corrine, which is the active site of vitamin B_{12}. This name identifies the molecules whose macrocycle compose of four pyrrole moieties linked together by three carbon atoms in the meso-positions [182, 183]. Corroles are structurally close related to the well-known porphyrines in the sense that both species possess aromatic tetrapyrrole macrocycles. In contrast to porphyrins, corroles bear a direct pyrrole-pyrrole bond resulting into lower symmetry and smaller, congested cavity (see Figure 4.1) [184, 185, 186]. The latter property and the resulting changes in the electronic structure are responsible for the special properties of corroles compared to porphyrins. Corroles provide versatile coordination sites for catalytically active metal ions. Furthermore, they promote the stabilisation of metal ions in exceptionally high oxidation states such as +III, +IV and +V [187, 188, 189]. Therefore, they are distinctive candidates for various biomedicine, catalysis, sensor, as well as solar cell applications [190, 191].

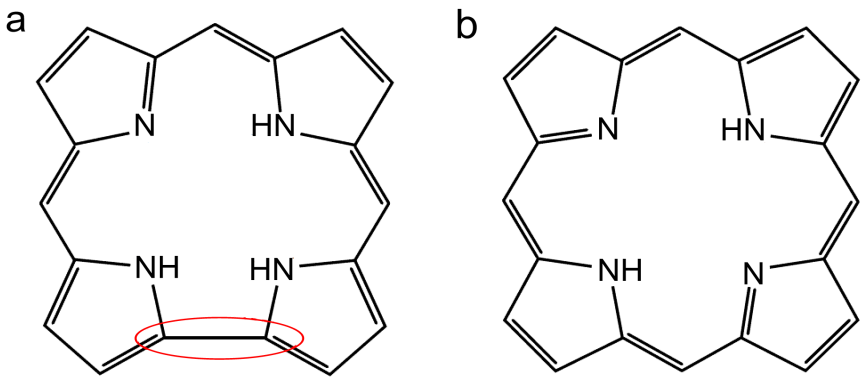

Figure 4.1: Chemical structure the central part of (a) a free-base corrole and (b) a free-base porphyrin. The red oval indicates the C-C bond which discriminates corroles from porphyrin (see text).

The history of corroles began in 1965 when Johnson and Kay chemically synthesised it for the first time [183]. Since then and for long time, the chemistry of corroles was prohibitively prevented as a result of the severe synthetic obstacles, namely the low reaction yield of the chemical process. However, Gross [192] and Paolesse [183] succeeded independently in the late 1990s to overcome these obstacles and synthesised corroles with aryl groups on the three meso-C atoms. After this finding and so far, many studies have been devoted to investigate the electronic properties and the functionality of different corrole products, opening up for new possibilities of fascinating applications in various fields such as, e.g., tumor elimination and atherosclerosis prevention [193].

The existence of aryl groups in the meso-positions of corroles stabilises their structures. In particular, the stability increases in cases where aryl groups have an electron-withdrawing nature such as, e.g., pentafluorophenyl (pFP) group. Like this, corrole derivatives which are obtained by substituting pFP groups in the meso-positions are reported to be considerably stable. For this reason, a prototypical molecule like, e.g., H_3TpFPC, which is studied here, is a suitable example for investigating the properties of corroles and their chemical derivates on surfaces.

4.2 Multilayers System

In this section a multitechnique X-ray study is employed to investigate condensed ultrathin films of prototypical H_3TpFPC corroles on Ag(111). The sample preparation and the measurement methodologies can be found in appendix B.

4.2.1 Free-base 5,10,15-tris(pentafluorophenyl)-corrole (H_3TpFPC)

The 5,10,15-tris (pentafluoro-phenyl)-corrole (H_3TpFPC) is one of the most stable corroles known to date [194]. Its liquid-phase derivatives are potential detectors for cancer cells, [195, 196, 197] while its metal complexes show efficient catalytic properties for atoms (oxygen) and functional groups (carbene, nitrene) [198, 199, 200, 201]. Some recent studies have concerned its unique structural properties [202, 203], its metal coordinated products [204, 205, 206], as well as the formation of (sub)monolayer structures on different surfaces [207, 180].

The structure of H_3TpFPC is composed of a tetrapyrrolic macrocycle where three pyrrole moieties are connected to each other via meso-carbon atoms (labelled as 5, 10 and 15 in Figure 4.2) and a characteristic direct C-C bond between moieties A and D. The three pentafluorophenyl rings (C_6F_5) are substituted at the meso-positions. The C:F:H:N element ratio is 37:15:11:4, whereby the macrocycle consists of 19 carbon and 4 nitrogen atoms (one iminic (=N) and three aminic (-NH) atoms). In principle, the positions of the H atoms within the molecular core define two tautomeric structures T1 and T2, where the non-protonated pyrrole to be the inner ring C (B) or the outer ring D (A), respectively (see also Figure 4.4). Furthermore, for each of these tautomers there might be a maximum of $2^3 \times 3^3 = 216$ conformers: $2^3 = 8$ variants obtained by the orientations of the three phenyl rings (clockwise or counterclockwise); each of them provides further 3^3 variants differing in the positions of the three H atoms (in front, behind, and in-plane). However, the present DFT total energy calculations, in the gas phase, conclude that only two of H atom configurations yield locally stable structures in the following: The H_D (H_C) in T1 (T2) is always found almost in-plain. In contrast, the other two H atoms (H_A and H_B) are shifted in front and behind the plane maximising their distance. As a result, 16 conformeric possible local minima for each tautomer are left. The present DFT calculations predict tautomer T1 to be more stable than T2 by 40 meV. This result is in line with

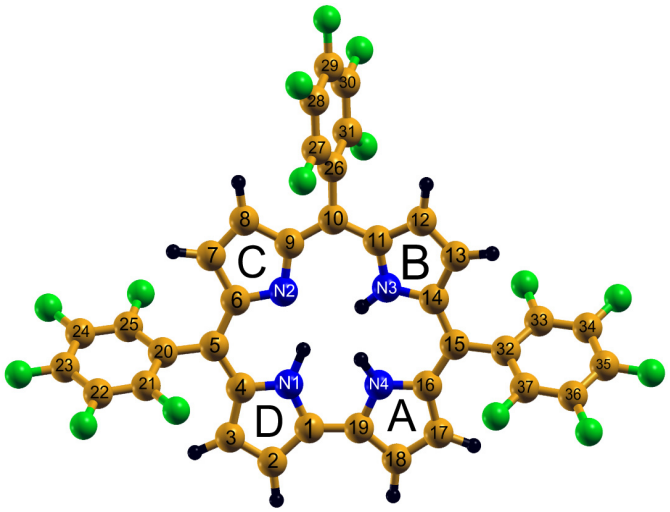

Figure 4.2: Schematic representation of 5,10,15-tris (pentafluoro-phenyl)-corrole (H_3TpFPC). C, N, F, and H atoms are represented in brown, blue, green, and black, respectively. The macrocycle consists of one iminic (=N) and three aminic (-NH) atoms (labeled as N2, and N1, N3, N4, respectively). The C atoms within the macrocycle are labeled from 1 to 19. Those within the phenyl rings are labeled from 20 to 37. The pyrrole rings are connected to each other via meso carbon atoms 5, 10 and 15 and a direct C1-C19 bond. The three fluorophenyl rings (C_6F_5) are substituted at the three meso-positions 5, 10, and 15. The letters A-D denote the chemically inequivalent pyrrole rings.

other previous calculations [202] as well as previously reported X-ray crystal structure [208], where tautomer T1 (depicted in Figure 4.2) is reported to be most dominant.

4.2.2 XP spectra

Figures 4.3 (b, c) present the measured XP spectra of the H_3TpFPC multilayer. The C 1s XP spectra exhibits an isolated peak at the binding energy E_B = 287.8 eV and a double peak structure with local maxima at 284.4 and 285.5 eV. The percentage area of these peaks is almost 48:24:28, respectively. The measured N 1s XP spectrum of the H_3TpFPC multilayer consists of two clearly separated peaks at 400.1 and 397.9 eV with relative peak area of almost 3:1 (Figure 4.3 c). In order to rationalise the experimental spectra, the contributions of the individual atoms to the total spectrum are analysed. H_3TpFPC exhibits no structural symmetry and, strictly speaking, all atoms are chemically inequivalent. However, to ease the discussion, the carbon atoms with *similar* chemical nature (presence of more or less electronegative elements in the vicinity of the respective carbon atom) can be grouped into one "type". Apparently, this classification yields four carbon types (see Figure 4.3 a): From higher to lower binding energy the peaks correspond to C directly connected to fluorine (C1, green), the carbon atoms of the C_6F_5 rings linked to the macrocycle (C2, purple), the carbons with N neighbours (C3, yellow), and macrocycle

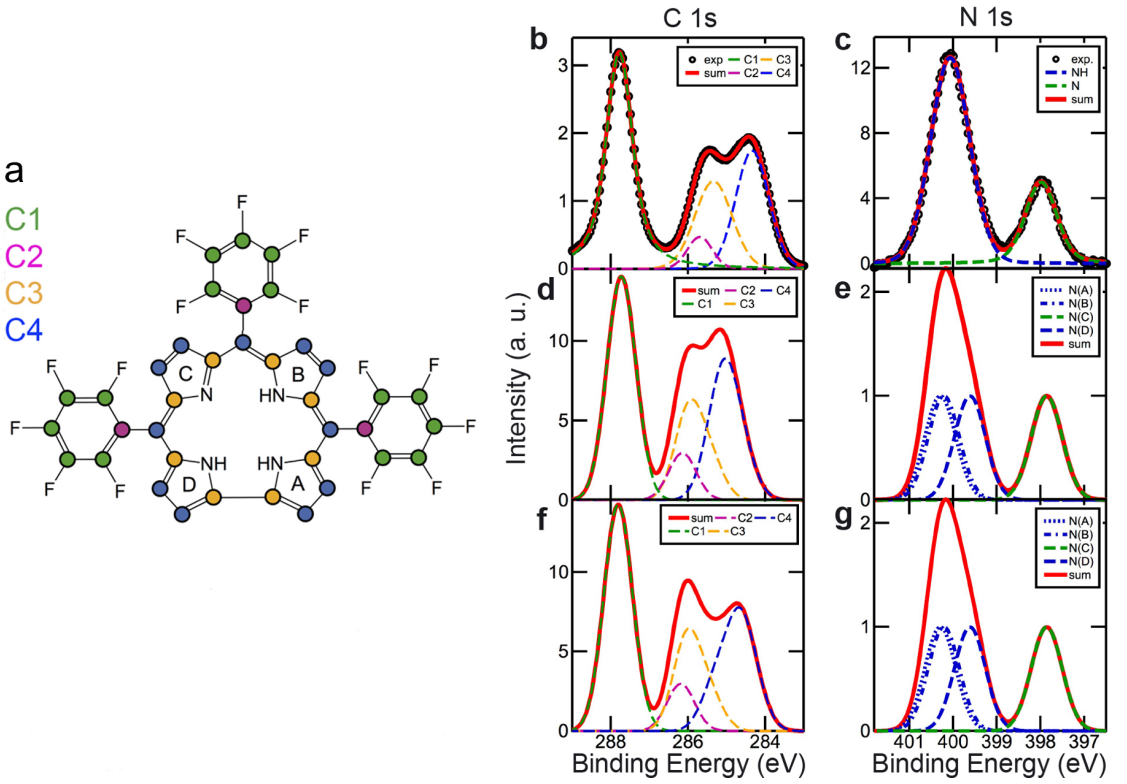

Figure 4.3: (a) Schematic model of free-base corrole (H_3TpFPC). Colors mark carbon atoms categorised as chemically equivalent. Experimental XP spectra of the (b) C 1s region and (c) N 1s region of a H_3TpFPC multilayer grown on Ag(111) compared with the corresponding simulated spectra (DFT-calculated CLS energies assuming a 0.7 eV Gaussian line width): (d and e) from gas phase modelling, (f and g) for the crystalline structure; also given: contributions of the different atom types as defined in (a).

C atoms without nitrogen neighbours (C4, blue), respectively. The experimental spectrum can be, then, nicely interpreted by fitting its features with four components corresponding to the four carbon types with relative energetic positions of C1: 287.8 eV, C2: 285.7 eV, C3: 285.3 eV, and C4: 284.3 eV with the percentage ratios of 48:6:21:25, respectively. The latter percentage is in reasonable agreement with the expected ratios (15:3:8:11), taking into account the uncertainty of the experimental fitting procedure. The features of the N 1s spectrum with the relative peak areas of 3:1 can be straightly assigned to aminic (blue) and iminic (green) components similar to those appearing for porphyrin species (Figure 4.3 c).

The interpretation of the recorded XPS spectra are rationalised and confirmed by the DFT calculations. As an approach to model the multilayer structure, *(i)* the periodic molecular crystal structure, which is recently determined experimentally by XRD [204], is employed. *(ii)* Beside the solid state, the case of fully relaxed molecules in the gas phase, i.e., isolated molecules in periodically repeated boxes, is used as a model to account for the

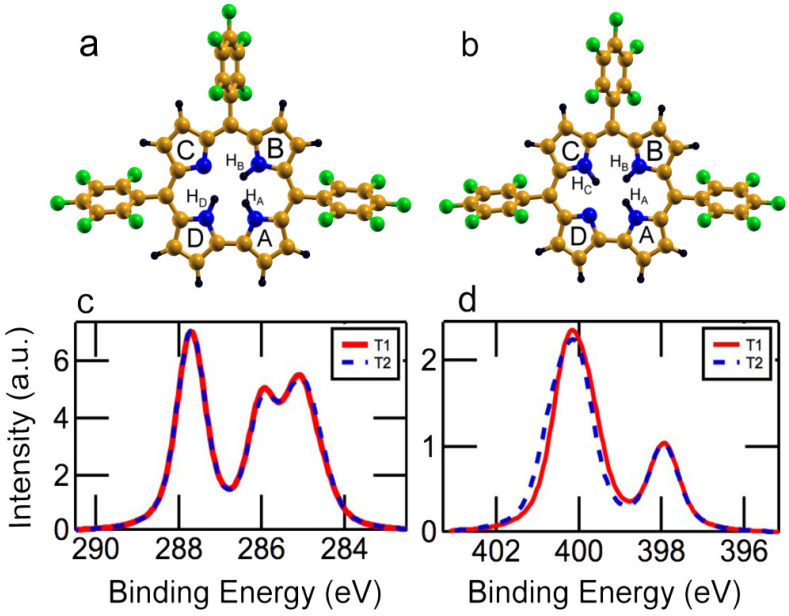

Figure 4.4: Ball-and-stick models of the (a) tautomer T1 and (b) tautomer T2 structures differing in the position of the iminic =N contrasting the three aminic -NH. As a consequence of the steric interactions, the inner hydrogen atom H_A has been moved away (upward) from the plane, while H_B has been moved downward (T1). For tautomer T2, the up and down arrangement of the inner hydrogen atoms is inverted. (c) Calculated C 1s and (d) N 1s XP spectra for the T1 (red) and T2 (blue) tautomers.

molecular structure. Figure 4.3 d presents the calculated C 1s XP spectra of the molecule in gas phase. Thereby, the total spectrum (red curve) represents the sum over all 37 C atoms. Furthermore, the contributions of the four carbon types are depicted following the aforementioned assignment (C1, C2, C3 and C4). The calculated spectrum shows in its overall shape a very good correlation to the experimental data supporting the assignment of the four components to carbon types differing from each other by the electronegativity of the neighbouring atoms. However, the C3 group exhibits a considerable deviation from a Gaussian line shape. Moreover, the spreading of the spectrum is underestimated by about 20%. A possible explanation for the compressed spectrum might be attributed to the semilocal exchange-correlation functionals and the approximated description of excitonic effects [209]. However, it is more likely that the description of the experimentally investigated multilayer system by isolated molecules is incomplete since it completely neglects the intermolecular interactions. The latter argument is supported by comparing the calculated XP spectrum of the crystalline structure (Appendix A.8) [204] with that of the isolated molecule (Figure 4.3 d and f). Here, intermolecular interactions, which were completely absent for gas-phase molecules, are now responsible for the outward shift (0.3 eV) of the C4 peak with respect to the rest of the spectrum ($C4^{bulk}$: 284.7 eV instead of $C4^{gas}$: 285.0 eV), yielding a broader spectrum by 11%. However, even larger broadening is

expected for the experimentally investigated multilayer system, providing inhomogeneities and additional interaction with the substrate still neglected in the crystalline system.

The DFT-calculated XP spectra of the four nitrogen atoms (4.3 e, g) interpret the experimental data perfectly and further substantiate the assignment of the aminic and iminic components. Notably, the calculated carbon and nitrogen XP spectra of tautomer T2 (Figure 4.4) can barely be distinguished from those of T1 presented in 4.3 d (C 1s) and 1e (N 1s). Accordingly, at least with the current state-of-the-art resolution, XPS cannot serve as a means to address tautomerism in corrole interfaces.

4.2.3 NEXAFS spectra

The recorded NEXAFS spectra of the relevant absorption edges (C and N) are obtained for a multilayer sample with the same thickness as in the XPS. In parallel, the respective K-edges are calculated for the isolated molecules and the crystalline structure.

Carbon K-edge. Figure 4.5, top panel, displays the measured NEXAFS spectra for the multilayer sample deposited onto Ag(111) substrate and hold at 300 K. The spectra are recorded for 25°, 53° and 90° incidence. The pronounced absence of dichroism indicates the absence of well-ordered films; it indicates an at least partially disorder arrangement of the molecules within the thin film or a formation of small crystallites with different orientations. Within the π^* region of the spectra (between 283 and 290 eV), four maxima are distinguishable (labelled as A, B, C and D at binding energies of 284.5, 285.8, 287.9 and 289.1 eV, respectively), whereas in the σ^* region (above 290 eV) broad complex resonances are superimposed onto the ionisation edge.

The calculated C K-edge NEXAFS spectrum for an isolated fully relaxed H_3TpFPC molecule is depicted on Figure 4.5, middle panel. As already mentioned for the XP spectra, the total spectrum presents the sum over all non-equivalent 37 C atoms. Furthermore, the individual contributions of the four C types are presented in the lower part of the spectrum. The overall spectrum correlates with the experiment very well, and the classification of the C atoms into four types allows a reasonable interpretation of the spectrum. The first peak A` results from excitations of C4 atoms (blue line) into the lowest macrocyclic $\pi^*$ orbital. The second peak B` includes contributions from both macrocyclic (C3, yellow), (C4, blue) and fluorophenylic (C2, purple) atoms. The strong C` feature carries some contributions from the macrocycle (blue and yellow) but is mainly dominated by transitions from outer C1 atoms (green) into the fluorophenyl π^* orbitals. However, despite the overall agreement, there are some discrepancies. *(i)* The experimentally measured peak (C) is predicted as a double peak structure (C_a` and $C_b$`) and *(ii)* the experimentally quite distinct peak D is not fully reproduced by the minor shoulder D` in the calculated spectrum. The latter carries contributions from all C types, especially C3 and C4 into higher macrocyclic $\pi^*$ orbitals. These deviations might be explained by assuming that the energy of the $C_b$` resonance is underestimated in the calculations yielding, in turn, contribution to the experimental peak D. However, it is more probable that

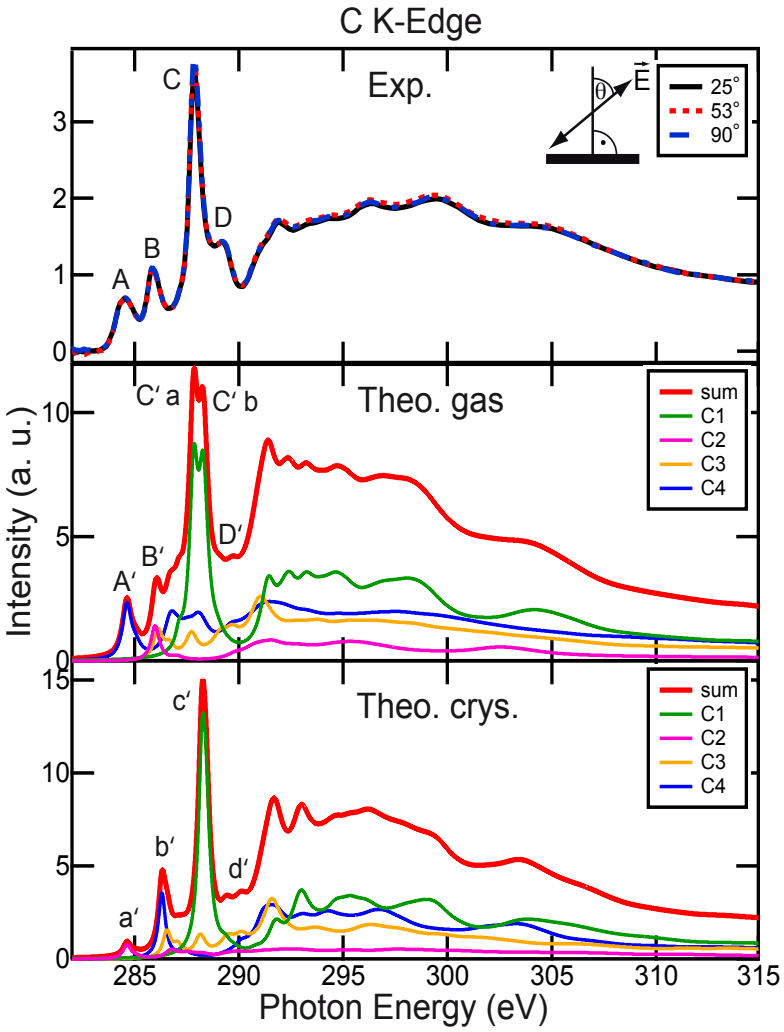

Figure 4.5: Experimental NEXAFS carbon K-edge spectra of a 3H- TpFPC multilayer on Ag(111) (top panel), which were measured at three photon incidence angles, θ (25° in black, 53° in red, and 90° in blue), and comparison with the DFT calculated, angle-integrated signatures of the gas phase (middle) and crystal phase (bottom) for tautomer T1.

the intermolecular interactions, not taken into account in the calculations for gas-phase molecules, are responsible for these deviations. To verify this assumption, the calculated gas-phase NEXAFS spectrum (Figure 4.5, middle) is compared to that (Figure 4.5, bottom) obtained for the crystalline structure (see Appendix A.8). Notably, despite that the structure of the individual molecules do not change considerably within the crystalline structure, pronounced changes in the calculated spectra of the latter can be observed. The contributions of the fluorophenyl rings components (C1 and C2) exhibit considerable changes in the range between 287 and 296 eV. Thereby, the spurious splitting of the C̀ peak is actually lifted. Furthermore, the separation of the c̀ and b̀ peaks around 287 eV becomes

more evident, since here the underlying contribution of the C4-type atoms (macrocycle C atoms without nitrogen neighbours) is strongly reduced. Also the spectral shape in the high-energy regime, in particular the peak at 296 eV is now better reproduced.

Nevertheless, the spectrum for a crystalline phase does not reproduce the experimental one 1:1. The intensity of the peak d̀ is still apparently underestimated. The remained discrepancy can be, tentatively, attributed to the variation of the individual molecular orientation within the thin multilayer film, which is neglected within the theoretical modelling.

Recently, NEXAFS measurements have been conducted by Nardi *et al.* on a tetrakis (pentafluorophenyl)-porphyrin (2H-TPP(F)), which is a system featuring a molecular structure closely related to H_3TpFPC but with a porphine macrocycle [210]. Their measured C K-edge signals are pretty similar to the presented here despite the structural differences between the two studied systems. This corroborates the conclusion drawn by Nardi *et al.* that for these compounds the building-block principle is valid and that fluorophenyl and macrocycle moieties constitute hardly interacting spectral signatures. This also indicates that the contraction of the corrolic macrocycle as a result of the direct C-C bond should not significantly contribute to the measured spectra. In line with this conclusion, the calculations predict almost coincident C K-edge spectra of the two tautomers (T1 and T2) similar to the carbon and nitrogen XP spectra.

Nitrogen K-edge. This situation changes significantly in case of the N K-edge. Figure 4.6 compares the measured spectrum (top panel) with the calculated NEXAFS spectra for the gas and crystal phases (middle and bottom panels, respectively). Again, the measured spectra barely show dichroism with varying incidence angle (θ), confirming the conclusion of the absence of orientational order in the thin film already drawn from the C K-edge. Within the π^* region four peaks are discernible (E-H at 397.9, 400.3, 402.1, and 403.1 eV, respectively). The peak (I at 406.6 eV) is situated in the σ^* region, while the residual part of this region (energies larger than 410 eV) presents continuous broad features.

The calculated N K-edge XAS spectrum of tautomer T1 in the gas phase approach already reproduces the overall shape of the measured spectrum and its major features (Figure 4.6, middle panel, red solid line). Furthermore, it shows many peaks within σ^* region with a clearer definition compared to the smeared out character in the experimental spectra. The absence of these discernible features in the experimental spectra can be attributed to statistical broadening introduced by multilayer anisotropies. The deconvolution of the total spectrum into contributions of the individual nitrogen atoms allows for better interpretation of the spectral aspects: The first peak (È) results only from the N 1s transitions of the iminic N_C atom into the unoccupied π^* molecular orbitals (blue line), The second peak F̀ contains contributions from the iminic N_C nitrogen atom and from all other three aminic nitrogens (green, grey, brown lines) to higher π^* molecular orbitals of the macrocycle. Thus, the energy splitting of the first two peaks in the experimental spectrum (397.9 vs 400.3 eV) reflects the difference between the binding energy of the aminic and iminic N 1s core levels (2.2 eV). The third feature is a single peak at 402.4 eV and results from transitions of all nitrogen atoms into the higher-lying π^* orbitals.

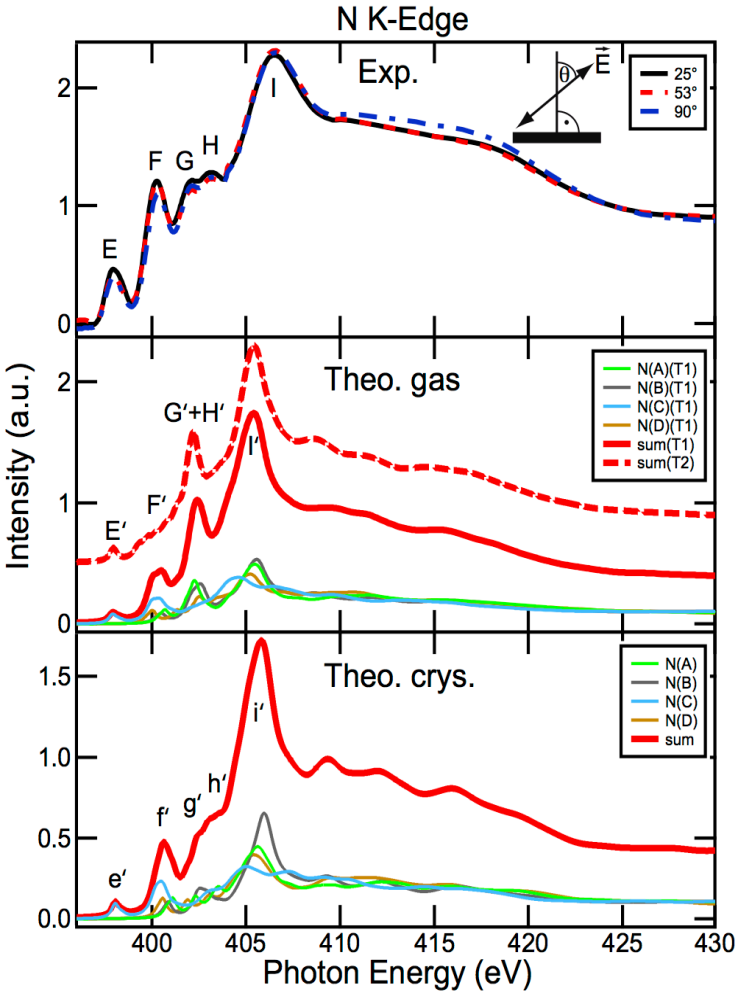

Figure 4.6: Comparison of experimental NEXAFS N K-edge spectra (top) of a multilayer of H_3TpFPC on Ag (111) measured for three incidence angles, θ (25° in black, 53° in red, and 90° in blue) with the theoretical gas-phase signatures calculated for tautomers T1, T2 (middle) and crystal phase (T1, bottom). For the DFT calculated, angular averaged spectra, the contributions from the four nitrogen atoms (A-D, see Figure 4.3) are also presented.

This peak is denoted as G`+H` since it relates to two experimental peaks G and H. The resonance I consists of contributions from σ^* resonances related to the N-C bonds of the three aminic N atoms (green, grey, and brown lines) with a leading shoulder resulting from N_C σ^* resonances. Interestingly, the characteristic peak F` is nearly completely suppressed for tautomer T2 (middle panel, red dashed line), indicating that tautomer T1 is the highly dominant species in the multilayer sample.

The global picture is further corroborated by analysing the influence of intermolecular interactions within the crystal phase onto the shape of the nitrogen absorption edge.

Figure 4.6, bottom panel, compares the crystal phase spectra with those from tautomer T1 in the gas phase. The calculation of the N K-edge XAS for the crystal phase results into overall restructuring and significant improvements which yield better agreement with the experimental data. The sharpened appearance of the feature f̀ is now slightly better interpreted. More significant is the splitting of the feature G̀+H̀ into a series of shoulders (one for g̀ and two for h̀). These changes originate from a downshift of N_B transitions and a splitting of N_A transitions improving the similarity to the experiment.

All in all, the calculated N K-edge unfolds an intriguing sensitivity to the noncovalent, and thus weak, intermolecular interactions present in the thin film samples. Furthermore, it reveals that in UHV grown multilayer films the tautomer T1 is largely dominant in full accordance with earlier reports on crystals obtained by evaporation from ethyl acetate which also consisted of well-defined tautomers [208].

4.2.4 Intermediate conclusion

The so far presented discussions enabled an unprecedented insight into the complex molecular structure of prototypical free-base corroles. Note that the employed plane-wave based approach within density functional theory (DFT) for extended, (quasi-)periodic molecular structures represents an extension from the solid state physics towards hybrid systems (i.e., adsorbed molecules on surfaces). The employed approach provided *(i)* an excellent agreement between experimental and theoretical spectra, *(ii)* enabled an accurate description of the free-base corrole electronic structure and *(iii)* proven a high ability to capture even small changes in the electronic structure. Thus, it represents a particular tool to straightforwardly treat low symmetry adsorbate structures on surfaces.

4.3 On-surface Chemical Transformations

In the previous section, it was mentioned that the employed approach is proven to be highly sensitive to small variations of the electronic structures (gas phase or crystalline phase) and able to discriminate between similar structures (tautomers). Thus, it represents an ideal starting point to tackle the problem of this section, namely the description of the complex chemistry of corroles in the adsorbed state and the subsequent on-surface chemical transformations.

4.3.1 Experimental results

Upon depositing H_3TpFPC molecules on Ag(111) and annealing the surface up to higher temperatures, it is expected that the molecules might undergo chemical reactions upon thermal annealing. In this context, this section introduces some experimental results which evidence for such chemical transformations.

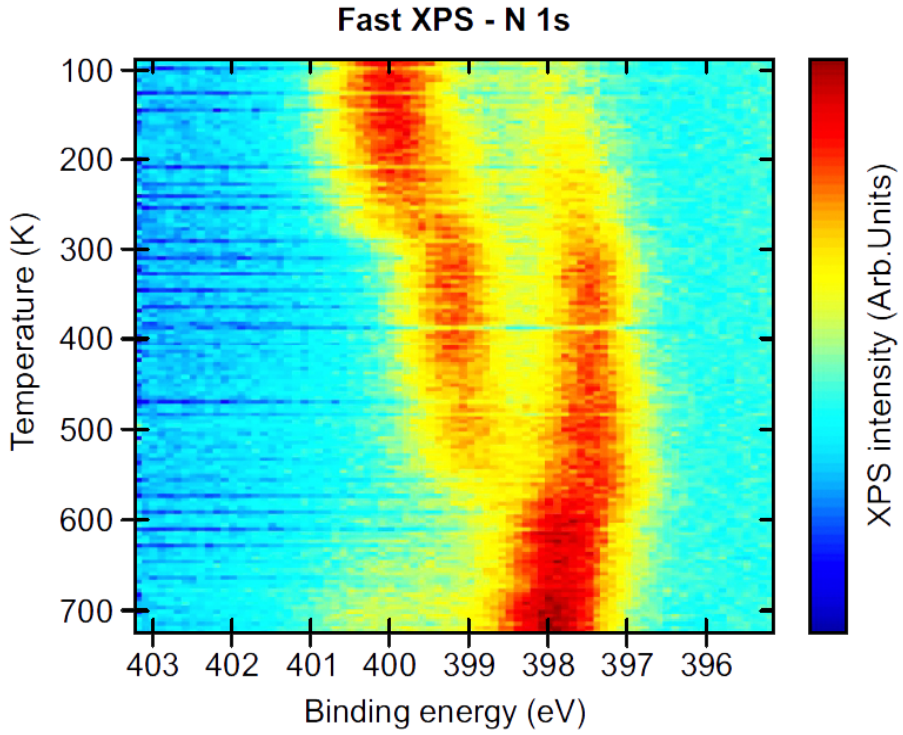

Figure 4.7: Fast-XPS N 1s measurement acquired for H_3TpFPC deposited onto a cold substrate (90 K). Then, the temperature was linearly raised up to 710 K at a rate of 0.1 K. The acquisition time for each XPS spectrum is 50 s.

Fast-XPS Measurements. The first experimental evidence for the on-surface thermally induced chemical activity is provided by analysing the N 1s fast-XPS for H_3TpFPC film deposited onto cold Ag(111) and subsequently annealed to higher temperatures. Figure 4.7 is a 2D plot showing the measured intensity of the photoelectrons signals in the N 1s region of a sample deposited at 90 K and subsequently heated up from 90 K up to 710 K. Thereby, the spectra are recorded in series for increased temperatures at a rate of 0.1 K/s. Since the heating rate is small, the measured temperature during recording the spectrum (50 s) can be assumed as constant.
Between 90 K and 300 K, the spectrum consists of two distinct energy regions with clearly different intensities. At the beginning, the relative intensities of these regions is almost 3:1 at binding energies of 400 (peak 1) and 397.8 eV (peak 2). However, the intensity of peak 2 gradually increases on the expense of that of peak 1, with an apparent shift of both peaks to lower binding energies. Between 300 and 400 K, a dramatic change of the relative peak intensities is observed. The two peaks become almost equivalent in intensity and shifted to binding energies of 399.4 and 397.6 eV. The situation changes again for temperatures above 550 K and the relative intensities of peak 1 and 2 are inverted to 1:3, respectively.

Temperature-programmed desorption (TPD) measurement.

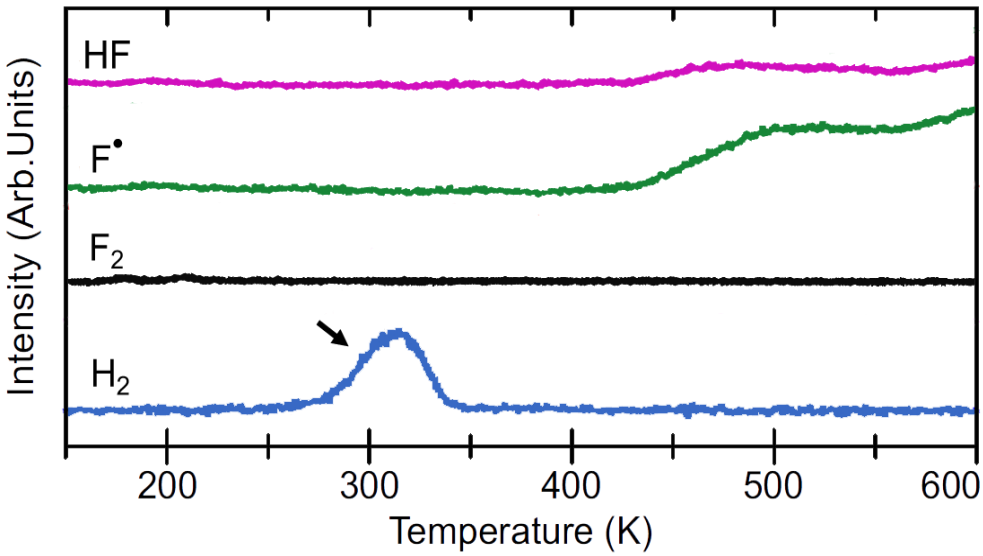

Figure 4.8: Temperature-programmed desorption (TPD) measurement of H_3TpFPC deposited onto Ag(111) at 150 K and linearly heated up to 600 K (heating rate of 0.25 K/s). From top to bottom the curves represent the by mass spectrometry detected desorption of HF, $F^{\bullet}$, F_2 and H_2 from the surface when elevating the temperature. The arrow near the H_2 spectrum is a guide to the eye, where it indicates the peak of the released hydrogen at around RT.

A further corroboration of the chemical activity is supplied by temperature-programmed desorption (TPD). For this purpose, H_3TpFPC molecules were deposited on Ag(111) which is kept at 150 K and then heated in a controlled (programmed) mode up to 600 K at a rate of 0.25 K/s, while the masses of H_2, F, HF, and F_2 were monitored (see Figure 4.8). The intensities of the recorded curves are in line with the fast-XPS measurements (see Figure 4.8). In the H_2 channel (blue) a feature starting below 300 K reveals desorption of molecular H_2 at around room temperature. Since direct formation of molecular hydrogen is unlikely [211], the peak indicates releasing of H atoms from the corrole molecules. Starting at 430 K, HF (pink) desorbs from the surface as a result of a further chemical transformation. The fact that no H_2 desorption is registered at the same time indicates that hydrogen abstraction takes place in close vicinity of fluorine abstraction positions. The F signal (green) starts to rise at the same temperature confirming the close relation of the fluorine and hydrogen producing reaction. At higher temperatures (> 500 K) the shape of the F peak differs from the HF signal. Since the atomic H signal can not be distinguished from the residual gas in the chamber, it remains unclear if additional F abstraction pathways or the recombination/desorption kinetic changes take place.

Beside the fast-XPS and TPD measurements, scanning tunnelling microscopy (STM) measurements were undertaken on molecular monolayers deposited on Ag(111) at 200 K and

subsequently annealed to higher temperatures (330 K, 430 K, 450 K, 470 K, 490 K, 510 K and 700 K). This apparently induces the new chemical states and a variety of corresponding structural orderings. These structures and their simulations will be discussed in details in the remainder of this section[1].

4.3.2 Adsorption of H_3TpFPC on Ag(111)

4.3.2.1 Single-molecule adsorption

As a starting point of the investigations, the most stable structure of single H_3TpFPC on Ag(111) needs to be decided. For this purpose, a set of XY-coordinates is introduced to identify the molecular spatial orientation. The coordinates are determined in a way allowing the meso-carbon atoms 5 and 15 to lie on the X-axis, while the meso-carbon 10 to lie on the Y-axis (Figure 4.9). The origin of the coordinate system "c" is considered as the reference for the molecular registry, while the angle θ, which indicates the azimuthal orientation of the Y-axis with respect to the <110> orientation of the surface, is taken as a reference for the molecular orientation. Then, the adsorption energies are calculated for a variety of molecular registries and orientations. In particular, the reference "c" has been laterally moved on 15 non-equivalent grids of points within the surface unit cell. On such sites, the cases where θ = 0, 10, 20, and 30° are considered. The positions of the references were assured by restricting the movement of the carbon atom C10 laterally, while all other atoms are allowed to move and relax freely. The results are depicted in Figure 4.9 b, where the adsorption energies (in eV) are compiled with respect to the most stable structure. The calculations predict very low diffusion barriers of maximum 25 meV. In other words, the molecule is highly free to diffuse laterally and rotationally already at low temperatures which, thus, enables an efficient molecular aggregation.

In its most stable structure (Figure 4.10 a and position 3 on Figure 4.9 b), the H_3TpFPC molecule adsorbs with its macrocycle tilted by 20° with respect to the surface. Thereby, the C1-C19 bond is closer to the surface, while the central pentafluorophenyl ring (in meso-position 10) is pushed upward and rotated by about 66° with respect to the surface. The other two fluorophenyl rings in meso-positions 5 and 15 (Figure 4.10) are rotated in a similar fashion. Both exhibit a rotation angle β of about 37°. The aforementioned Y-axis is parallel to one of the three <112> directions of the surface, i.e. θ = 30°, while the reference "c" is located in between top and hollow positions of the surface. Thereby, the N2 and the N3 atoms of the molecule (see Figure 4.9 a) are located on atop of two Ag atoms. The adsorption energy of this structure amounts to -2.46 eV. It is important to note, that H_3TpFPC molecules interact rather weakly with the Ag(111) substrate. An analysis of calculated charge densities yields only minor charge transfer (below 0.2 electrons) and

[1] It should be noted that H_3TpFPC molecules are stable in the solid state phase up to 460 K (the temperature for which the molecules were sublimated from a source), while some of the reported evidences of the on-surface chemical activity are observed at about 300 K and 430 K confirming the fundamental catalytic role of the surface in the reactions.

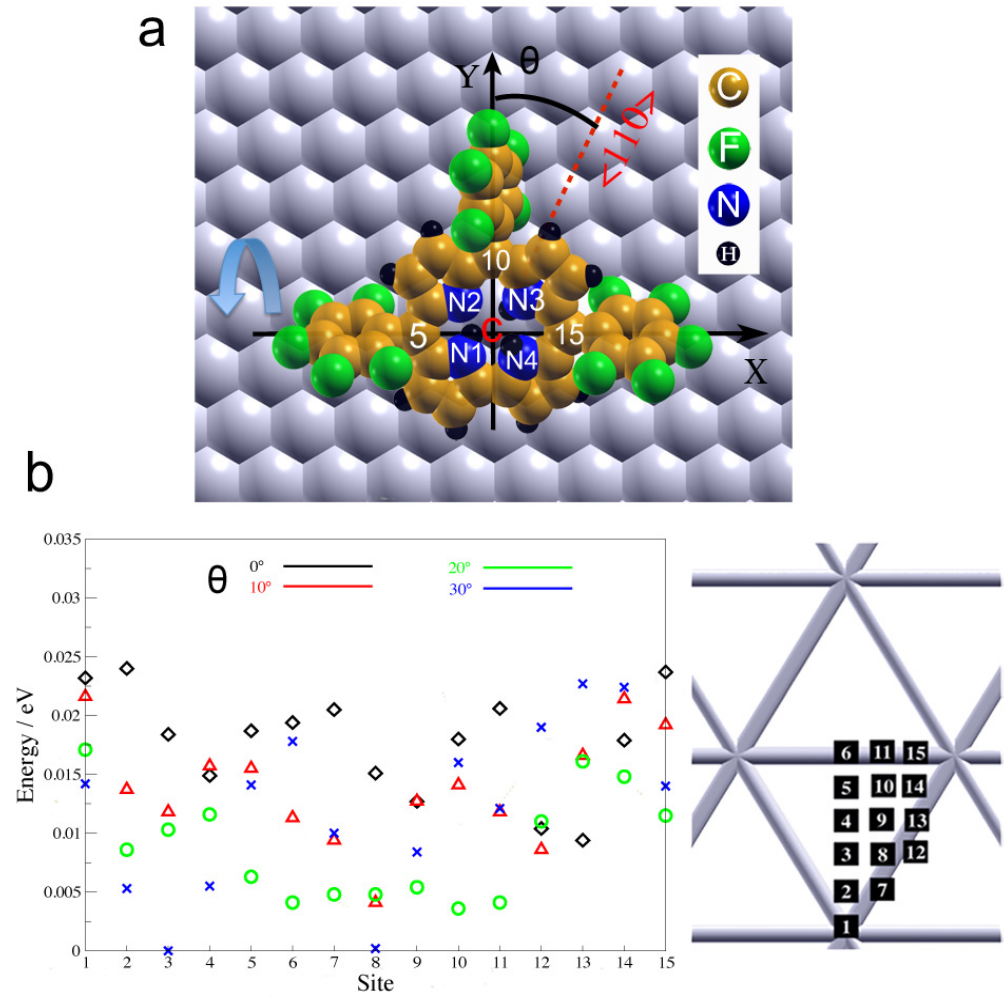

Figure 4.9: (a) A set of xy-coordinates introduced within the macrocycle of H_3TpFPC on Ag(111) to define its geometrical properties. The origin of the coordinates "c" is considered as a reference for the registry of the molecule with respect to the surface, while the angle θ accounts for the molecular orientation (see text). The arrow on the left side is a guide to the eye marking the rotation of the phenyl rings in these meso-positions. (b) Calculated adsorption energies of H_3TpFPC on Ag(111) where the reference point "c" is laterally moved on the 15 non-equivalent grid points (shown on the right panel) and for each site the orientations θ = 0, 10, 20, and 30° are considered. The energy of most stable structure (site 3) is considered as a 0 energy in eV.

excludes covalent bonding between the molecule and substrate. The molecules adsorb at relatively large distances (r_1 = 4.6 Å, r_2 = 3.6 Å, Figure 4.10 b) as dictated by the dominating weak van der Waals interactions.

Note also that beside the aforementioned stable structure there is an equivalent stable structure resulting from the rotation of the phenyl ring in the meso-position 10 in the

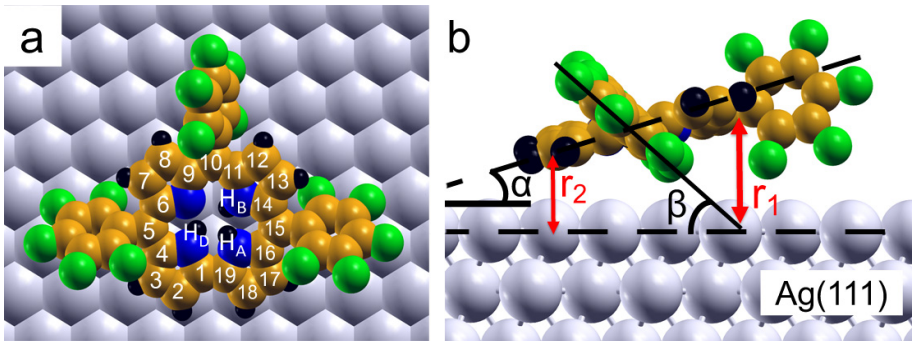

Figure 4.10: (a) Top-view and (b) side view of a single H_3TpFPC molecule adsorbed on Ag(111) in the most stable structure. With respect to macrocyclic plane, the inner hydrogen atom H_A is shifted upwards, H_B downwards (or oppositely), while H_D is almost in plane. The macrocyclic C atoms are numerated from 1 to 19. The quantity r_1 (r_2) is the vertical distance between the meso C10 (C1/ C19) and the underlying surface. The tilt angles of the macrocycle α and of the phenyl rings β with respect to the surface are also indicated.

opposite fashion but with the same angle (see Appendix A.10). Conversely, a rotation of one of both phenyl rings in the meso-positions 5 and 15 yields less stable structures with geometries exclusively deviating from the most stable structure, despite the stable and less stable structures have the same registries and azimuthal orientations with respect to the underlying substrate.

4.3.2.2 STM contrast

For a in-depth characterisation of the conformational properties of H_3TpFPC on Ag(111), molecular monolayers were deposited onto the surface kept at 200 K and studied by means of STM measurements. Based on the fast-XPS data, it is assumed that no chemical reactions take place at this temperature (all molecules are still in the H_3TpFPC state).

Figure 4.11 c shows the STM image of submonolayer H_3TpFPC/Ag(111), recorded after deposition of approximately 0.5 monolayers of molecules onto Ag(111) held at 200 K, while figure 4.11 a exhibits a single H_3TpFPC molecule laterally displaced from the rim of the molecular island by controlled STM manipulation. The topographic configuration of the displaced molecule exhibits an almost equilateral triangular-like shape consisting of three discernible protrusions at its corners. One of these lobes (the middle one) looks slightly brighter than the others. The simulated STM micrograph of the most stable structure (see Figure 4.10 b) confirms the observed topographic shape of single molecule. The characteristic protrusions are attributed to the three pentafluorophenyl groups possessing higher geometries than the molecular macrocycle. In particular, the pentafluorophenyl ring in the meso-position 10, which exhibits higher geometries than those in the other meso-positions, is responsible for the brighter lobe shown in the experimental and simulated topographies.

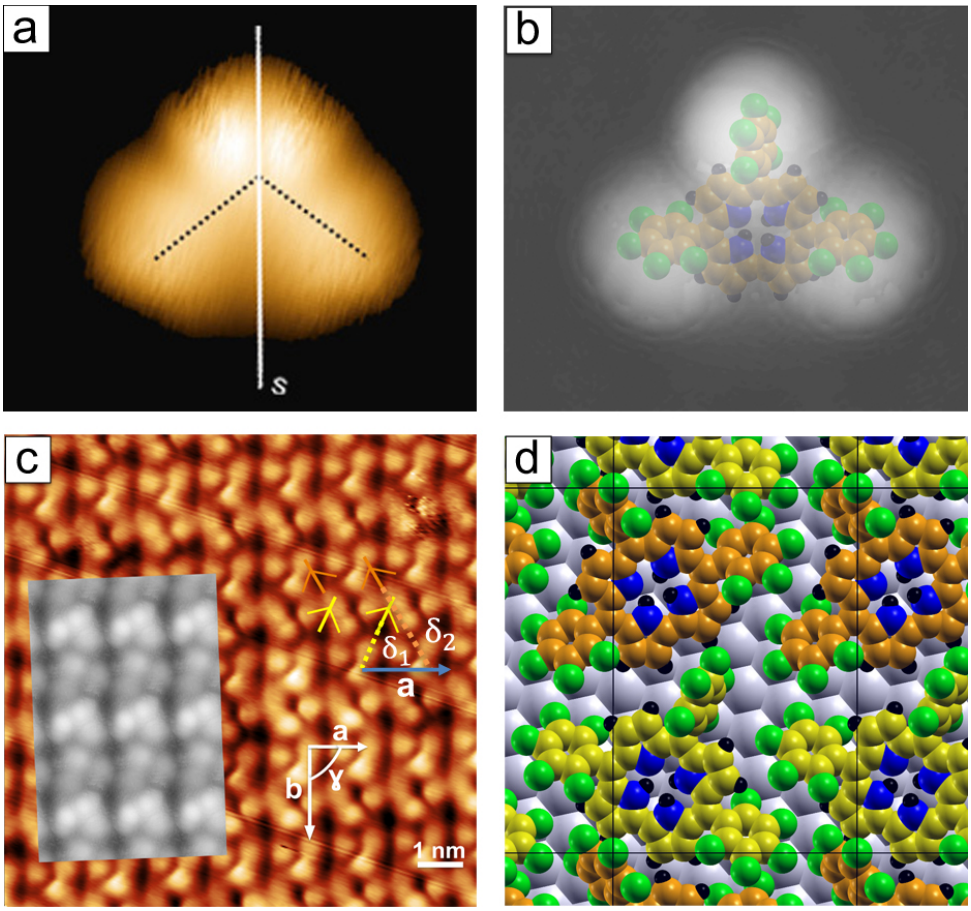

Figure 4.11: (a) A measured STM image (3×3 nm^2, +1 V, 50 pA) of a single H_3TpFPC/Ag(111) deposited at 200 K. The line "s" indicates the molecular short axis. The dotted lines highlight the triangle-like shape of the molecule. (b) Simulated STM image of single H_3TpFPC molecule on Ag(111) in its most stable configuration. The geometries of the molecules are overlaid on the simulation. (c) STM images of submonolayer H_3TpFPC/Ag(111), after deposition of approximately 0.5 monolayers onto the Ag(111) substrate held at 200 K showing the detail image of regular H_3TpFPC island, 11.5×11.5 nm^2, z-scale 100 pm, +1.5 V, 100 pA. (d) Top view of the theoretically calculated structure for H_3TpFPC on Ag(111). Yellow and brown colours (on c and d) highlight different orientations of individual molecules in the structure. Shown in grey is the simulated STM image of the calculated structure (d) obtained using the Tersoff-Hamann approach [127].

The molecules deposited at 200 K form well-ordered structures within islands of up to 100 nm diameter. The regular structure is described by periodic two-dimensional surface unit cell defined by the vectors $\vec{a} = 1.51 \pm 0.1$ nm, $\vec{b} = 2.34 \pm 0.1$ nm, as well as the enclosed angle $\gamma = 93 \pm 5^{o}$ (see Figure 4.11 c). The vector $\vec{a}$ is azimuthally rotated by $\phi = 36 \pm 5^{o}$ with respect to Ag<110> direction. Within a unit cell, two triangular-like topographic shapes are discernible and can be attributed to two molecules differently oriented within

the unit cell. The first shape is denoted as type 1 (marked yellow), while the second shape as type 2 (marked brown). The relative orientation of the two molecules within the unit cell can be described by the azimuthal orientations of their short-axes with respect to $\vec{a}$: $\delta_1 = 72 \pm 5^o$ and $\delta_2 = 119 \pm 5^o$ are obtained for type 1 and type 2, respectively (see Figure 4.11 c).

To verify the experimental packing structure of the regular structure, total energy calculations have been performed. Thereby, a variety of plausible possibilities to arrange two H_3TpFPC molecules within two-dimensional unit cell of dimensions close to the experiment have been tested. Within each tested two-dimensional cell, a variety of different registries and orientations as well as partial overlap between the neighbouring molecules have been considered. The most stable structure is shown on Figure 4.11 d, while the corresponding simulated STM image, using the Tersoff-Hamann model [127], is overlaid on the left inset of Figure 4.11 c. The parameters of the calculated cell are: $\vec{a} = 1.56$ nm, $\vec{b} = 2.34$ nm, $\gamma = 90^o$, $\phi = 40.45^o$, $\delta_1 = 67^o$ and $\delta_1 = 121^o$. The epitaxy matrix of the calculated structure is $\begin{pmatrix} \vec{a} \\ \vec{b} \end{pmatrix} = \begin{pmatrix} 6 & 4 \\ 2 & 7 \end{pmatrix} \begin{pmatrix} \vec{x}_1 \\ \vec{x}_2 \end{pmatrix}$, where $\vec{x}_1$ and $\vec{x}_2$ are the lattice vectors of Ag(111) forming an angle of 120^o. Within a unit cell, the two molecules exhibit almost the same tilting geometries. The molecular macrocycles are tilted by about 20^o (α) with the respect to the surface. The pyrrole-pyrrole bonds are closer to the surface while the phenyl rings in the meso-position 10 are pushed upwards. Indeed, the calculations predict a shingle-like packing of neighbouring molecules enabled by partial overlap between tilted corroles.

4.3.2.3 NEXAFS spectra of H_3TpFPC on Ag(111)

Beside the STM measurements, angle-dependent C and N K-edge NEXAFS measurements are carried out to characterise the conformational properties of H_3TpFPC on Ag(111). Thereby, a sub-monolayer coverage (nominally 0.9 ML) of H_3TpFPC is deposited onto Ag(111) and held at 200 K (see appendix B for further information on the measurements). As previously mentioned, it is supposed that at 200 K H_3TpFPC has not undergone any chemical transformations yet.

NEXAFS C K-edge. Figure 4.13 a shows the measured C K-edge NEXAFS spectra recorded at different incident angles ($\theta = 25$, 53 and 90^o). The apparent dichroism in the spectra indicates the existence of a predominant conformation of the corroles adsorbed in a well-ordered fashion. The overall appearance of the spectra and energetic positioning of the characteristic features spectra are strongly similar to the multilayer data (see section 4.2) except a slight broadening presumably induced by the minor influence of the noble metal support on the unoccupied orbitals. The π^* region (283-290 eV) includes four maxima: A, B, C and D at binding energies of 284.5, 285.8, 287.9 and 289.1 eV, respectively, while broad resonances are superimposed onto the ionisation edge in the σ^* region (above 290 eV).

It is possible to provide an approximate estimation of the molecular geometries by a direct curve-fitting analysis of the measured angle-dependent NEXAFS spectra close to the edge (see Ref. [128] and Appendix B). Figure 4.13 c shows exemplary a zoom into the π^* region of the 25° spectrum. The spectrum can be decomposed into two types of contributions: The component which exhibits a pronounced angular dependence (blue) can be attributed to the macrocycle carbon atoms, while the other is attributed to the pentafluorophenyl rings (yellow) showing less angular dependence. By comparing the trends of the normalised intensities as functions of the incident angle θ to theoretical curves [128] predicted for a π system on a threefold symmetric surface (red curves, Figure 4.13 d), the following adsorption geometry can be estimated: The macrocycle is tilted by approximately $\alpha = 30 \pm 5°$ and the fluorophenyl rings are rotated by $\beta = 50 \pm 5°$ with respect to the surface. Notably, the values of β is in good agreement with that obtained from the DFT-calculated structure (48°). The latter value is acquired by weighting the three derived values (37°, 37°, and 66°) with the respective angle (θ) integrated analytical cross section expected from a Stöhr-analysis [128] (see Appendix B).

In order to interpret the detailed features of the measured spectrum, angle-dependent C and N K-edge NEXAFS spectra are calculated for the molecule in the isolated and monolayer approaches (see section 4.3.2.2). Notably, if the molecular adsorption geometries are correctly calculated and interpreted, the calculated XAS spectra for both K-edges (N as well as C) are not considerably modified by the presence of the substrate (see also Appendix A.9); the minimal difference is related to CLS shifts induced by the underlying surface [212] and are calculated to be below 0.1 eV (see Figure 4.12). Therefore, if not stated otherwise, the calculated spectra are obtained for structures relaxed on the surface but without considering the surface explicitly in the XAS calculations. This reduces the numerical costs for the XAS spectra by about two orders of magnitude and allows for a systematic comparison of a large number of different structures.

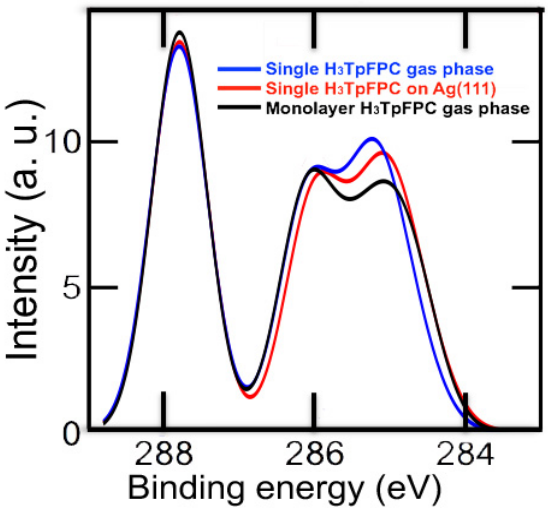

Figure 4.12: calculated C 1s XPS spectrum of single H_3TpFPC in gas phase (blue), on the surface (red) and in monolayer approach without considering the surface beneath it.

Figure 4.13 b exhibits the calculated angle-dependent C K-edge NEXAFS spectra of the isolated adsorbed molecule for the incident angles of 25°, 53°, and 90°. Notably, the calculated spectra of the monolayer structure (see Figure 4.11) are almost coincident with those for the single molecule approach. The agreements between the measured and calculated spectra are very good in term of overall shape of the spectra, the positions of

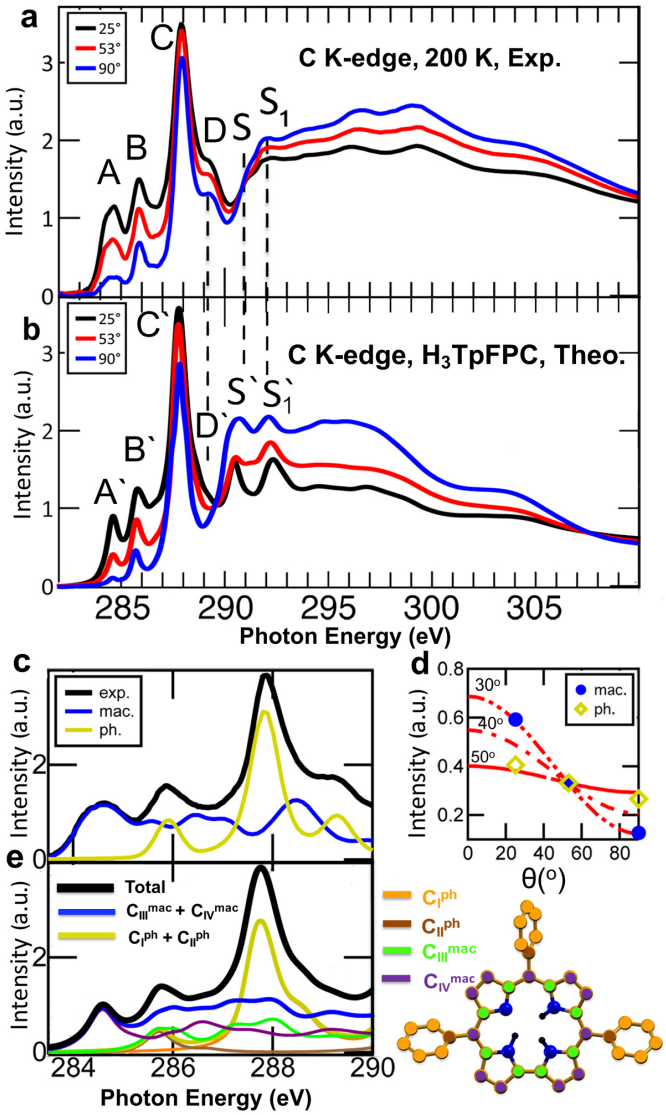

Figure 4.13: (a) Measured angle-dependent C K-edge NEXAFS spectra of H_3TpFPC deposited onto the Ag(111) substrate at 200 K for 25°, 53° and 90° incidence. (b) Calculated NEXAFS C K-edge spectra for DFT-optimised H_3TpFPC geometries (incident angles as reported in the experiment), whereby experimental CLS have been used to align the contributions of individual atoms. (c) Zoom into the π^* region of the 25° experimental spectrum deconvoluted into macrocyclic (blue) and fluorophenylic (yellow) contributions. (d) Tilt angles of the macrocycle (∼30°) and the fluorophenyl groups (50°) derived from (c) and related angle-dependent data. (e) Zoom into the π^* region of the theoretical 25° spectrum; besides the different C types (see right inset), also the macrocyclic (blue) and the fluorophenylic (yellow) contributions are shown.

the characteristic maxima (within the π^* region, the first three peaks A`, B` and C` are at binding energies of 284.5, 285.8 and 287.8 eV, respectively). Also, the relative intensity

of the first two peaks (B/A) and the relative trends of the peak intensities within the π^* and σ^* regions (the calculated intensities of the individual peaks qualitatively agree with the measurements where they decrease for larger incident angles within the π^* region and behave oppositely within the σ^* regions).

Figure 4.13 e shows a zoom into the π^* region of the theoretical 25° spectrum. Similar to the multilayer system, it is possible to comprehensively decompose the total spectrum into the corresponding contributions of four carbon types (see section 4.2 for further information). The first peak $\grave{\text{A}}$ results only from excitations of C_{IV}^{mac} carbon atoms into the lowest macrocyclic π^* orbitals. The second peak $\grave{\text{B}}$ includes contributions from both macrocyclic (C_{III}^{mac}, C_{IV}^{mac}) and fluorophenylic (C_{II}^{ph}) atoms. Peak $\grave{\text{C}}$ includes contributions from the macrocyclic C_{III}^{mac} and C_{IV}^{mac} atoms, but it is dominated by excitations of the fluorophenylic C_{I}^{ph} atoms into the lowest macrocyclic π^* orbitals. Obviously, the macrocyclic contributions ($\grave{\text{A}}$ and partially $\grave{\text{B}}$) have been largely suppressed for $\theta = 90°$ as a result of the nearly planar geometry of the corrole macrocycle.

Despite the good agreement, similar to the multilayer system, there are some discrepancies for energies above the main peak C (see Figure 4.13 a, b). (*i*) The peak D is less discernible in the calculated spectra and (*ii*) the S peak is predicted to be shifted to lower binding energies in contrast to a shift to higher energies for multilayer structures. Importantly, the calculated anisotropy in the S/S_1 range is predicted to be much stronger than in the measurement where it almost vanishes. Again, the discrepancy can be attributed to approximate description of the experimental situation by the employed theoretical modelling. For the as-deposited (200 K) sample the experimental situation clearly deviates from an ideal periodic model. The NEXAFS measurements perform a macroscopic average and, thus, they might include signals from molecules with differently oriented fluorophenyl side groups due to (*i*) molecules in different islands, (*ii*) molecules being adsorbed at step edges and surface defects and (*iii*) molecules in disordered and partially overlapping configurations. Nevertheless, the experimental results exhibit in many respects the same tendency as the calculated model structure of isolated molecular adsorbates.

NEXAFS N K-edge. The angle-dependent XAS N K-edges spectra have been also measured for H_3TpFPC deposited with a submonolayer coverage (0.9 ML) onto the surface kept at temperature of 200 K during the whole deposition and measurement procedure. The spectra (Figure 4.14 a) show a pronounced dichroism confirming the preferentially ordered molecular arrangement concluded from the C K-edges. Within the π^* region four peaks can be identified for each spectrum (E, F, G and H at 398.4, 400.4, 402.0 and 403.2 eV), while a further peak I (407.0 eV) is found within the σ^* region.

The calculated N K-edge spectra of the isolated adsorbed molecule show a very good agreement with the experimental data, regarding the overall shapes of the spectra, the energetic positions of the peaks ($\grave{\text{E}}$, $\grave{\text{F}}$, $\grave{\text{G}}$ and $\grave{\text{H}}$ at 398.4, 400.6, 401.8 eV and 402.9 eV) as well as the angle-dependence of the peak intensities within the π^* and σ^* regions (Figure 4.14 b). The apparent vanishing dichroism interpreted at 403.8 eV (the resulting crossing points in Figure 4.14 a and b separate the π^* and σ^* spectral regions) agrees very well with

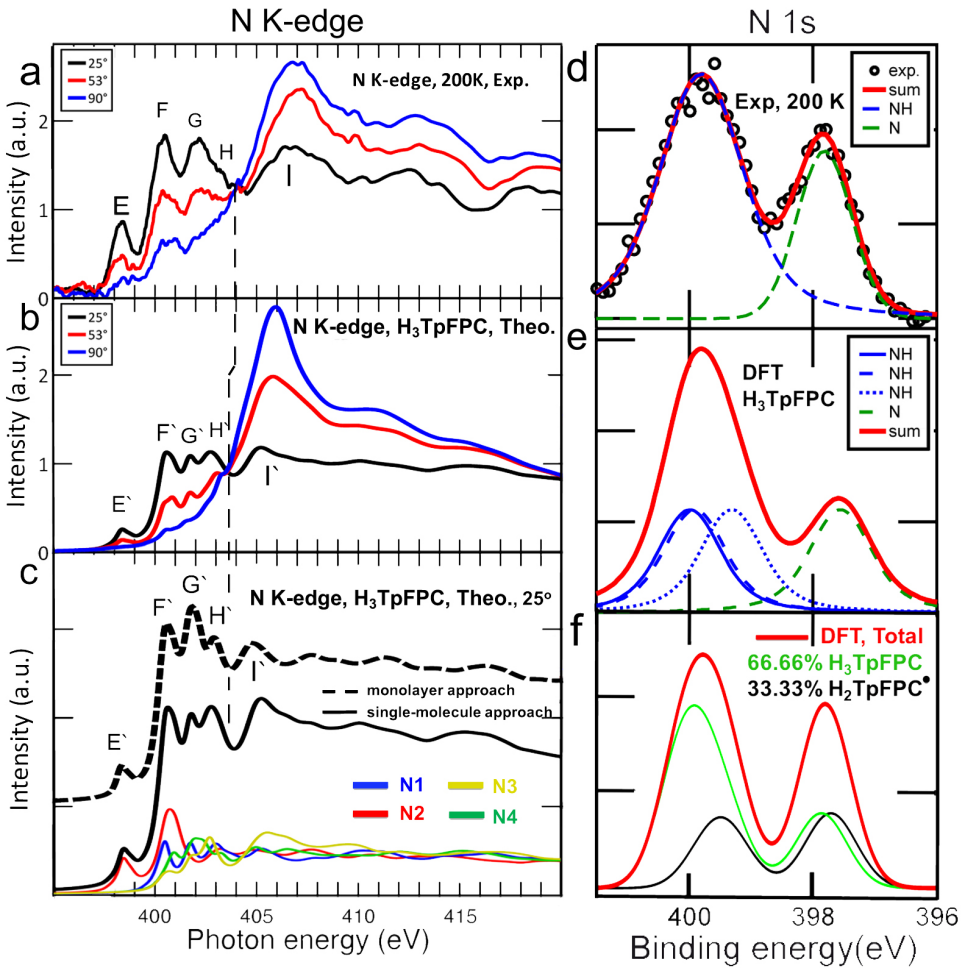

Figure 4.14: (a) Experimental NEXAFS spectra of the N K-edge as deposited onto the substrate and measured at 200 K for 25°, 53°, and 90° incidences. (b) Calculated angle-dependent N K-edge NEXAFS spectra of the structure shown in Figure 4.10 for the respective incident angles. (c) Zoom into the π^* region of the 25° DFT-calculated spectra for single molecule as well as monolayer adsorption. Thereby, the contributions of the different N atoms (Figure 4.9) are shown. The vertical hairline highlights the crossing point separating the π^* and σ^* regions. (d) XPS N1s signature of TpFPC thin films on Ag(111) deposited at 200 K. The N-H/N= ratio of 32:68 indicates that the dehydrogenation reaction has already occurred for each third of molecules. (e) Calculated XPS N1s signature for pure H_3TpFPC film (see Figure 4.11). (f) Calculated N 1s XPS signal combines those from dehydrogenated/ intact molecules in the ratio of 1:2.

that in the experiment (404.0 eV). However, the relative intensities of the peaks slightly differ from the experiment, most apparent for peak E which is more prominent in the experiment.

In order to explain this result, the total spectrum has been deconvoluted into the contributions of the four nitrogen types (Figure 4.14 c). Similar to the multilayer system,

the first resonance (E`) results from the N 1s transitions of the iminic N2 atom into the unoccupied $\pi^*$ molecular orbitals (red line), while the other peaks contain contributions from all N atoms into the higher laying orbitals. Thus, the intensity of the peak E` is a characteristic parameter where it is sensitive to the amount of iminic nitrogen species in the sample and should increase when H_3TpFPC is converted to H_2TpFPC$^\bullet$ (as it will be shown in the next section). Indeed, the N1s XPS signature of the spectrum deposited at 200 K (Figure 4.11 d) apparently deviates form that of the multilayer system or from the calculated signature of the monolayer of H_3TpFPC. The N-H to N= intensity ratio is 75:25 in the latter, while it is 68:32 in the sample deposited at 200 K. Indeed, the calculations reproduce the N1s signature of the 200 K sample by assuming that each third molecule of the experimental film has undergone the dehydrogenation reaction (see Figure 4.11 e, f). This suggests that depositing H_3TpFPC onto the Ag(111) surface held at 100 K and annealing to 200 K (as carried out for temperature-programmed desorption and fast-XPS experiments reported in section 4.3.1 leave more molecules intact (in the H_3TpFPC state) than directly depositing onto the substrate at 200 K (Most likely dehydrogenation take place with or immediately after adsorption). This demonstrates that the predictive power of the calculations is high enough to enable the identification of imperfections in realistic samples. Noteworthy, quantitatively determining the ratio of chemical species from the measured XPS intensities alone is prone to artefacts from diffraction effects [95], thus the employed NEXAFS-based analysis helps to improve the validity of the chemical analysis.

When inspecting the higher energy resonance, mainly G` and H`, the relative intensity of G is more dominating in the experiment. A similar dominating resonance G` is present in the theoretical spectrum of a periodic monolayer. This again demonstrates how sensitive features of NEXAFS signatures are to the local environment.

4.3.3 On-surface dehydrogenation and radical formation

In section 4.3.1, the presented TPD and fast-XPS measurements showed clear evidences for on-surface thermally triggered chemical transformations of free-base corroles on Ag(111). This section concerns the first transformation takes place at around room temperature. For a sample annealed to around this temperature, it has been shown that the N 1s XPS peak intensity ratio dramatically changes to almost 1:1 and H_2 molecules are detected to desorb form the surface (see section 4.3.1 for more details).

For further corroboration, additional C and N 1s XPS measurements are carried out for a monolayer of H_3TpFPC grown at 200 K and subsequently annealed to 330 K. In comparison to the multilayer reference (see section 4.2), both the C 1s and the N 1s regions (Figure 4.15 b, c) show apparent changes in their spectral shapes, while the F 1s region remains unchanged. The formerly low energy double peak structure of C 1s region of intact H_3TpFPC appears now as a dominating asymmetric peak at 284.5 eV with a small shoulder at 286 eV. In the N 1s data, two signals with an area ratio of almost 1:1 replace the original 3:1 ratio.

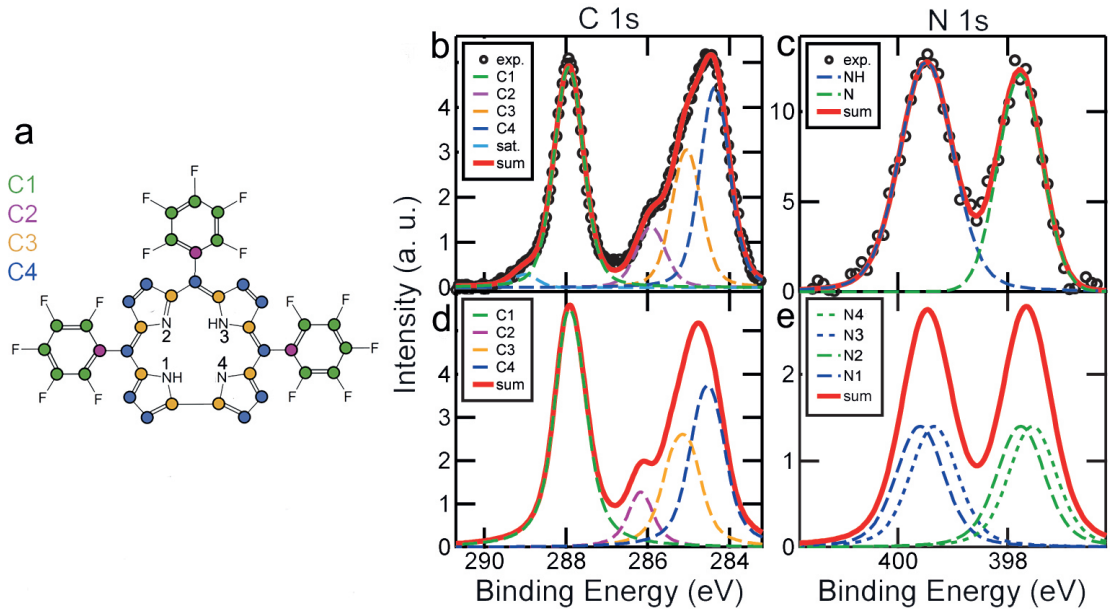

Figure 4.15: (a) Schematic model of H_2TpFPC$^\bullet$. Colours indicate the four carbon types as defined in Figure 4.3. Experimental XP (b) C 1s and (c) N 1s spectra of a monolayer of H_3TpFPC deposited onto Ag(111) at 200 K and annealed to 330 K. Calculated (d) C 1s and (e) N 1s CLS energies of H_2TpFPC$^\bullet$ assuming a 0.7 eV Gaussian line width. Contributions from the chemically inequivalent carbon and nitrogen species are plotted.

To explain the aforementioned experimental results at RT (release of H_2, the increase of the iminic component and the shapes of C and N 1s XPS signals), one could think of different scenarios. A cleavage of a molecular H-C bond from those close to the surface and a formation of a C-Ag covalent bond is a suggested pathway. Thereby, it is assumed that a charge transfer between the molecule and the surface *might* induce a new charge redistribution within the molecular structure enabling a modification of the iminic/aminic ratio. However, such charge distribution should presumably affect the whole macrocycle in a statistical manner causing shifts in binding energies of all atoms and a subsequent broadening of the spectrum. Furthermore, this effect looks to be very weak to induce a shift of 2 eV of a N 1s component towards lower binding energies. Indeed, all possibilities for such as well as similar scenarios have been calculated and shown that the 3:1 aminic/iminic ratio is barely changed enabling us to discard this possibility.
It is more reasonable to explain the experimental results by assuming that all molecules have, simply, undergone a single deprotonation/ dehydrogenation reaction by activating one of stable N-H bond from the core of the molecule (as shown exemplary in Figure 4.16) yielding two aminic and two iminic nitrogen atoms within each molecule. Then, the activated H atoms resulting from different molecules recombine together on the surface and desorb in the aforementioned H_2 form observed in the TPD measurements (a well-known process on noble metal surfaces) [211].

In order to be more accurate, the experimental line shape in Figure 4.15 c can be best described by assuming that 90 % of the molecules have undergone the deprotonation/ dehydrogenation reaction, while the other 10% are still in the H_3TpFPC state (Note that the intensity of the =N peak is slightly higher than that corresponding to -NH). More complicated state mixture with a statistical deprotonation/ dehydrogenation reactions, e.g., resulting into a variety of differently dehydrogenated species with 3, 2, 1, or no H atoms attached to the N atoms, can be ruled out. Such mixture would induce a significant broadening of both C and N 1s XPS signatures (like that shown in Figure 4.14). However, such broadening is apparently absent in case of a H_3TpFPC/Ag annealed to RT (see Figure 4.15) rendering this scenario as improbable.

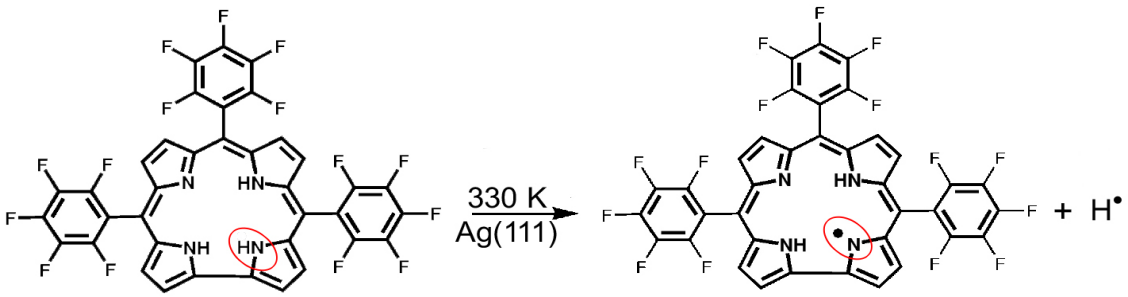

Figure 4.16: Formal scheme of the dehydrogenation reaction inferred from combined XPS, TPD and theoretical analysis. The product on left is H_3TpFPC; H_2TpFPC$^\bullet$ specie is on right. The red ovals indicate the site of the reaction.

In order to corroborate this possibility, C 1s and N 1s CLSs (see Figure 4.15 d, e) have been calculated for the singly dehydrogenated structures (Figure 4.15 a). The high degree of agreement between the calculated and experimental spectra further confirms this scenario. The two iminic/aminic nitrogen atoms (N1 and N4)/ (N1 and N3) are now situated at binding energies of about 376.6 eV/ 399.4 eV, respectively. The C K-edge can be again decomposed into the previously mentioned four carbon types contributions (see Figure 4.15 a). Compared to the calculated spectrum of H_3TpFPC, the macrocyclic components (C3 and C4) are shifted now to lower binding energies yielding enhanced agreement with the experiment.

The upcoming discussions will show that the activation of a N-H bond forms a corrole radical, thus this structure will be denoted as H_2TpFPC$^\bullet$.

4.3.3.1 Adsorption of H_2TpFPC$^\bullet$ on Ag(111)

Upon the dehydrogenation reaction, the calculated geometries of individual H_2TpFPC$^\bullet$ molecules are left almost unchanged (the registry and the orientation of H_2TpFPC$^\bullet$ are supposed to be identical to those of H_3TpFPC). The actual changes are restricted to a planarisation of the remaining N-H bonds within the macrocycle. Thereby, the driving force

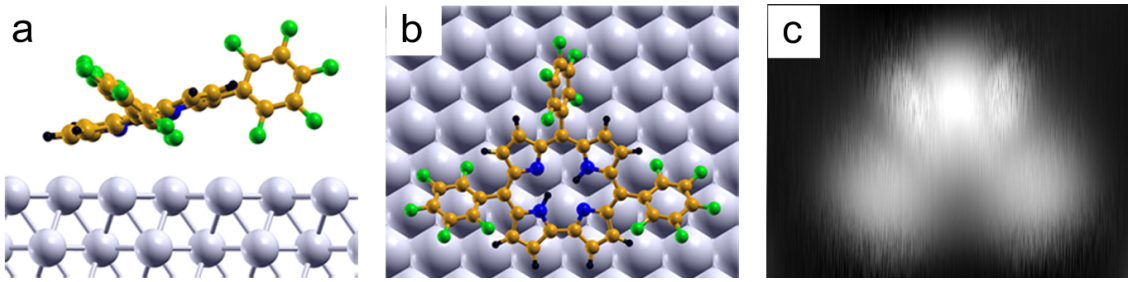

Figure 4.17: (a) Side and (b) top views of the DFT-calculated single H_2TpFPC$^\bullet$ molecule on Ag(111). (c) Measured STM image (3×2.5 nm^2, +0.3 V, 200 pA) of a single H_2TpFPC$^\bullet$ adsorbed on Ag(111) manipulated from the rim of the monolayer, deposited at 200 K and annealed to 330 K. Note that the dimensions of (b) and (c) are not on the same scale.

for an out-of-plane relaxation of the inner H-atoms is reduced resulting in a more flat molecular structure, stronger bound to the substrate: the adsorption energy per a H_2TpFPC$^\bullet$ molecule is -3.22 eV, while it is -2.46 eV for H_3TpFPC. Similar to H_3TpFPC, the macrocycle of single H_2TpFPC$^\bullet$ exhibits a tilting angle of almost 20°; the pentaflurophenyl rings are, respectively, inclined in the meso-positions 5/15 and 10 by 37° and 65°. The recorded STM image of a single H_2TpFPC$^\bullet$ (4.17 c) exhibits high similarity to that of H_3TpFPC (see Figure 4.11 a) confirming the almost identical geometries for both states. Apparently, the central lobe exhibits two wings on its right and left sides. At the current stage, there is no clear explanation for this observation. However, some speculations are presented in Appendix A.12.

A deeper insight into the ordering of H_2TpFPC$^\bullet$ on Ag(111) can be obtained by performing STM measurements on a monolayer of H_3TpFPC deposited on Ag(111) at 200 K and subsequently annealed to 330 K. Identical results are also obtained by a direct deposition of molecules at around 360 K (compare Refs. [180] and [181] for further details). The STM image reveals a well-ordered two-dimensional regular arrangement within a network. The periodicity of this structure can be described by repeated oblique unit cells of dimensions $\vec{a} = 1.5 \pm 0.2$ nm, $\vec{b} = 1.9 \pm 0.2$ nm and the angle $\gamma = 78 \pm 5°$ (see Figure 4.18 a). The vector $\vec{a}$ is azimuthally almost parallel to a $\vec{Ag} < 11\bar{2} >$ direction of the surface. A primitive unit cell of H_2TpFPC$^\bullet$ looks somehow similar to that at 200 K. However, it is smaller by by about 20% and, more interestingly, it exhibits a non-trivial pattern. In other words, the characteristic triangular shape of a single corrole is apparently not discernible within the monolayer and the protrusions in the STM images lack an obvious relation with the functional groups of individual molecules. The particularity of this case is being rare throughout the literature [213, 207]. It is reported to be promoted by interdigitation, partial overlap, or stacking of neighbouring molecules.

The resolving of the non-trivial molecular network (description of the relative molecular positions and their azimuthal orientations) is carried out by our collaborators. Thereby, they developed and applied a straightforward method combining the STM imagining and the manipulation techniques. The developed method consists of two steps: First, a sin-

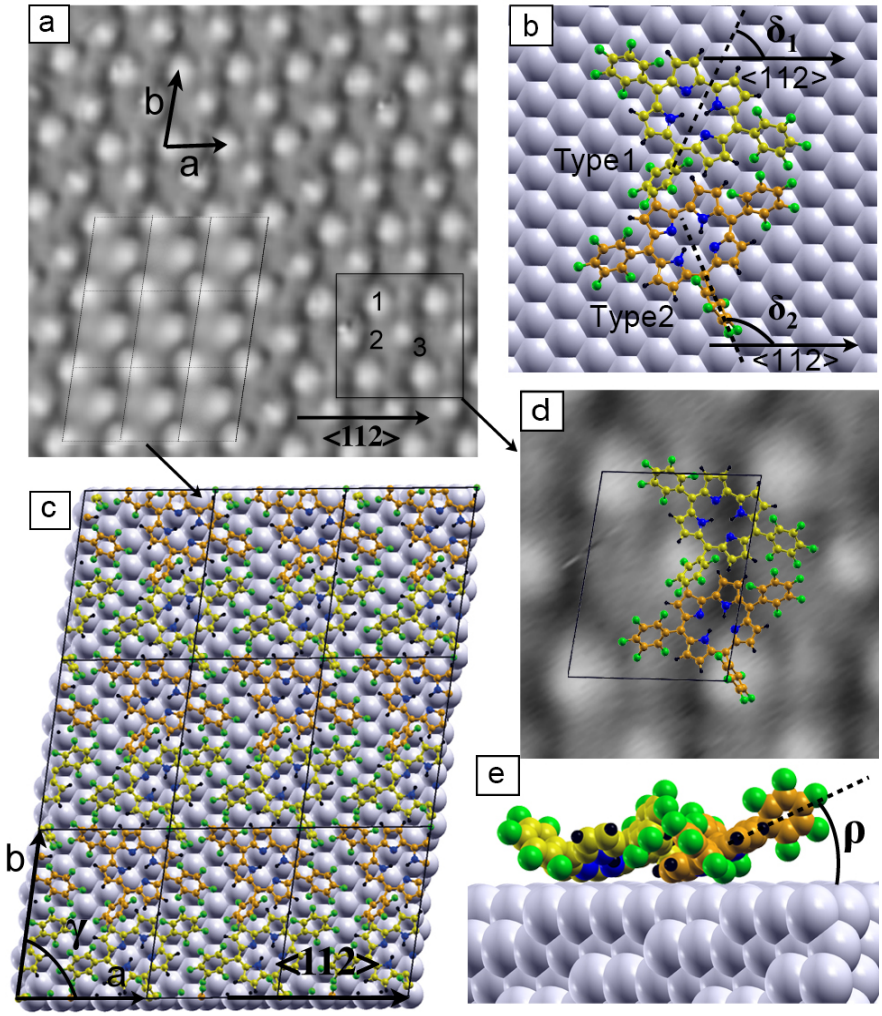

Figure 4.18: (a) A representative STM image of a monolayer network of H_2TpFPC$^\bullet$/Ag(111) (11.3×11.3 nm^2, +0.3 V, 100 pA, z-scale is 0.2 nm). The lattice parameters $\vec{a}$, $\vec{b}$ and γ are indicated. (b) Structural model of H_2TpFPC$^\bullet$/Ag(111) molecular network. Each unit cell contains two differently oriented molecules labeled as Type1 and Type 2. The orientations of the molecules within a unit cell are identified by the orientations of their short axes (dotted black lines) with respect to the $\vec{A}g$<112> orientation of the surface (i.e. δ_1 and δ_2). (c) Top view of the calculated structure model of H_2TpFPC$^\bullet$/Ag(111) within periodic unit cells. The cell parameters ($\vec{a}$, $\vec{b}$ and γ) and two types of molecules (differently coloured) are shown. The simulated STM image of this structure is overlaid on (a). (d) Calculated structure is overlaid on 3×3 nm^2 of the molecular network showing the relation between the different grey regions and the molecular geometries. (e) side view of shingle-like structure enabled by the tilted adsorption geometries of the neighbouring molecules.

gle corrole molecule was laterally manipulated from the rim of the deposited monolayer. Then, a pixel-to-pixel subtraction of the STM images before and after the manipulation

have been applied. This enabled an identification of the azimuthal orientations of the individual corroles within the molecular structure before the displacement and helps to completely characterise of the molecular network (see Ref. [180] for details). In brief, the experimental characterisations show that a structural primitive unit cell consists of two differently oriented molecules similar to that reported for a monolayer at 200 K (see section 4.3.2.2), but with slightly different azimuthal orientations with respect to $\vec{a}$: $\delta_1 = 66 \pm 5^o$, $\delta_2 = 108 \pm 5^o$ (Figure 4.18 b). Furthermore, they indicate that the pFP groups in meso-position 10 are responsible for the brightest protrusions within the unit cell.

The calculations verify and further illustrate the measured packing structure of the molecular network. The basic idea of the calculations is to find a stable structure consists of two differently oriented H_2TpFPC$^\bullet$ molecules arranged within two-dimensional unit cell of dimensions close to the experiment. To achieve such configuration, a large variety of different possible crystal basis parameters and molecular geometries have been concerned. Thereby, the cell parameters ($\vec{a}$, $\vec{b}$ and γ), the relative azimuthal molecular orientations (δ_1 and δ_2), different possible adsorption registries as well as the partial overlap between molecules have been tested. For each configuration, the adsorption energy has been calculated.
The most stable structure obtained from the calculations is shown in Figure 4.18 c. This structure is described by $\vec{a}$, $\vec{b}$ and the enclosed angle γ and exhibits an epitaxy matrix of $\begin{pmatrix} \vec{a} \\ \vec{b} \end{pmatrix} = \begin{pmatrix} 6 & 3 \\ 1 & 7 \end{pmatrix} \begin{pmatrix} \vec{x}_1 \\ \vec{x}_2 \end{pmatrix}$[2], where $\vec{x}_1$ and $\vec{x}_2$ are the lattice vectors of Ag(111) forming an angle of 120°. By this, the calculated structure has dimensions of $\vec{a} = 1.485$ nm, $\vec{b} = 1.926$ nm, the angle $\gamma = 81.72^o$ and the vector $\vec{a}$ is parallel to $\vec{A}g$<112>. Within each unit cell, the molecules of type 1 (type 2) are azimuthally oriented with δ_1 (δ_2) = 64° (112°) with respect to Ag<112> confirming the experimental results formerly deduced form the manipulation experiment. The non-trivial aspects of this structure are obviously enabled between tilted molecules partially overlapped (π-stacking) within relatively small cells. The partial overlap appears between the pentafluorophenyl in meso-position 10 of type 1(2) corroles and pyrrole group D(A) of neighbouring corroles (the respective separation of 0.45 nm). A similar interaction is also observed between the pentafluorophenyls in meso-positions 5 and 15 of neighbouring corrole molecules (respective separation of 0.5 nm). These separations are, indeed, close to the common π-stacked molecular networks [214] leading to a shingle-like packing of molecules along the $\vec{b}$ direction. Note, that the non-trivial structures were not observed in cases where the molecules form monolayers with lower dense packing than the present case, e.g., H_3TpFPC/Ag and H_3TpFPC/Au [207]. In the latter case, it is proposed that a monolayer of H_3TpFPC exhibits a different side-tilted configuration on Au (111) with relatively less dense packing of almost 22%.

The simulated STM image of the calculated structure (Figure 4.18 c) is overlaid on the left part of the measured one (Figure 4.18 a). Apparently, the simulated image exhibits a

[2] Note that for 200 K the epitaxy matrix was $\begin{pmatrix} \vec{a} \\ \vec{b} \end{pmatrix} = \begin{pmatrix} 6 & 4 \\ 2 & 7 \end{pmatrix} \begin{pmatrix} \vec{x}_1 \\ \vec{x}_2 \end{pmatrix}$.

high degree of agreement with the experiment, whereby it is difficult to differentiate one from the other. Even small details, like e.g., the experimentally observed difference in intensity of the lobes attributed to the pentafluorophenyl in meso-position 10 of the two types of molecules (type 1 appears less bright than type 2 in experimental images), have been well reproduced by the simulations. Thus, it is confirmed that the molecular packing of H_2TpFPC$^\bullet$/Ag(111) exhibits the characteristic properties of a non-trivial network. The grey micrographs within each primitive cell can categorised into 3 regions (see Figure 4.18 a, d): The brightest one (region 1) is mainly attributed to the phenyl rings in the meso-positions 10, exhibiting higher geometries than those in the other meso-positions (region 2). The twisted dark regions are attributed to the molecular macrocycles tilted by $\rho = 22^o$ with respect to the surface plane (see Figure 4.18 e).

4.3.3.2 Formation of corrole radical on Ag(111)

Throughout previous discussions, the experimental and theoretical investigations have enabled a deep insight into the chemical transformation taking place at around room temperature and a complete characterisation of the geometrical properties of H_2TpFPC$^\bullet$ on Ag(111). Indeed, the suggested scenario assuming an activation of a N-H bond is a reasonable explanation for the experimental observations. However, it remains elusive if such interaction should yield an anion (deprotonation reaction) or a corrole radical bearing unpaired electron density within its structure (dehydrogenation reaction).

The clarification of this aspect has been achieved by STM measurements, whereby the STM tip was used a as local probe to feature the zero-bias Kondo resonance [216, 217, 218] at a submonolayer level. In principle, the detection of a Kondo resonance (see Appendix A.13), which is absent for bare Ag(111), provides a clear evidence for the radical nature and enables us to exclude the possibility of anion formation. For this purpose, they induced an arranged monolayer of H_2TpFPC$^\bullet$ on Ag(111) by depositing a monolayer of H_3TpFPC on Ag(111) at 200 K and annealing the surface to 330 K. Then, they performed conductance measurements in a narrow region around the Fermi energy, where the signals have been recorded by averaging 10 independent measurements while locating the tip over different positions of the monolayer (see Appendix B for further details). Figure 4.19 a presents the characteristic minimum of the tunnel conductance (dI/dV) laying slightly below the Fermi level by about 3.4 mV. This detected signal is a clear evidence of the existence of unpaired electron (spin) density within the monolayer structure. Furthermore, they successfully imaged the spatial distribution of the radical electron spin density within the individual H_2TpFPC$^\bullet$ molecules with subnanometer resolution by STM. Figure 4.19 b, c present representative STM images of the corrole monolayer, showing the topographic contrast (b) and the radical signal (c), i.e., the height of the Kondo signal, measured over the same image frame with submolecular resolution.

The calculations support the experimental measurements in three main aspects. First, the shift of the characteristic Kondo resonance slightly below the Fermi energy indicates

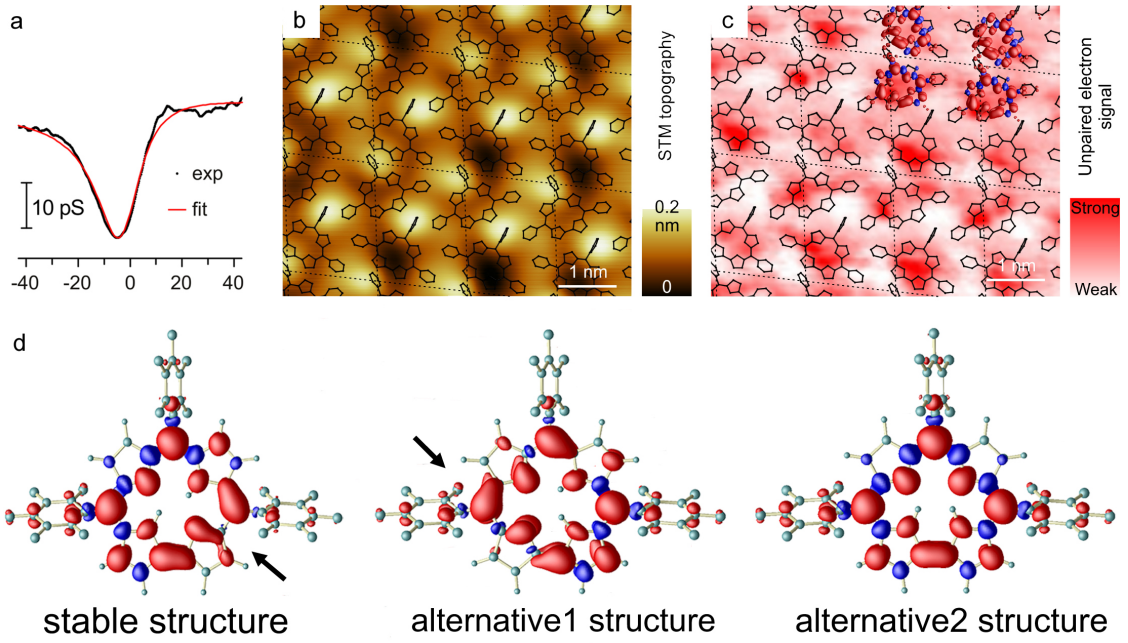

Figure 4.19: (a) Scanning tunnelling conductance (dI/dV) spectrum of the H_2TpFPC$^\bullet$ corrole radical on Ag(111) obtained by STM; the experimental curve (black) represents the average of 10 independent measurements performed over different individual corrole molecules within the monolayer and is numerically fitted (red) by a Fano line shape [215] with parameters q = 0.18; E_K = 2.8; Γ = 10.2. (b) Representative STM image of H_2TpFPC$^\bullet$/Ag(111); +0.3 V, 100 pA, 6 × 5 nm^2). (c) Same image frame as in (b) showing the spatial distribution of the electron spin density (Kondo signal obtained from the magnitude of the local tunnel conductance at -3 mV sample bias as recorded experimentally by scanning conductance spectroscopy; average of 10 consecutive frames, equivalent to 15 h of total measuring time). (d) DFT-calculated distribution of the unpaired electron spin density $m = n_\uparrow(\vec{r}) - n_\downarrow(\vec{r})$, where m > 0 (m < 0) is plotted in red (blue), given for the preferential structure and the other two alternatives. The arrows are guides to the eye indicating the position of the unpaired spin density.

particle-hole asymmetry due to a partial negative charge transfer from the Ag substrate to the H_2TpFPC$^\bullet$ molecule. This experimental finding is corroborated by the calculations yielding a partial charge transfer from the metallic surface to the molecule of approximately -0.2 e (where e is the elementary charge). Second, the calculated structural monolayer model (see Figure 4.18) is overlaid on the measured map of radical signal enabling, thus, the precise identification of its distribution within individual corrole molecules in the monolayer with high precision (see Figure 4.19 c). Apparently, the unpaired electron is always observed at the macrocycle. This means that the dehydrogenation does not affect exclusively one of the pyrrole groups, but the SOMO is delocalised all over the conjugated macrocycle. Third, the distribution of the unpaired electron spin density (about 0.8 electron per molecule) is calculated and visualised for the three H_2TpFPC$^\bullet$ possible structures (see Figure 4.19 d). For the preferential structure (as shown later), the strong unpaired electron spin density is calculated to be centred at the lower right

half of the macrocycle (defined by an imaginary line through the two remaining aminic -NH atoms). Nevertheless, having in mind a possible thermal movement of the central H atom, the alternative 1 structure cannot be conclusively excluded. It shows a slightly different distribution of the spin density, thereby providing a reasonable explanation for the fluctuations visible in the experimental Kondo image. However, the symmetric alternative 2 structure exhibits no particular unpaired spin density centred in a certain part of the molecule.

The importance of the presented finding is their novelty. The existence of a stable corrole radical species has been revealed only very recently in liquid phase by the Bröring group [219], while this is the first time to report an on-surface stable corrole radicals. Note that H_2TpFPC$^\bullet$ is stable in temperature range up to about 400 K, where both TPD (Figure 4.8) and temperature-programmed N 1s XPS (Figure 4.7) data exhibit no evidence of additional chemical reactions up to this temperature.

4.3.3.3 Site of the dehydrogenation reaction

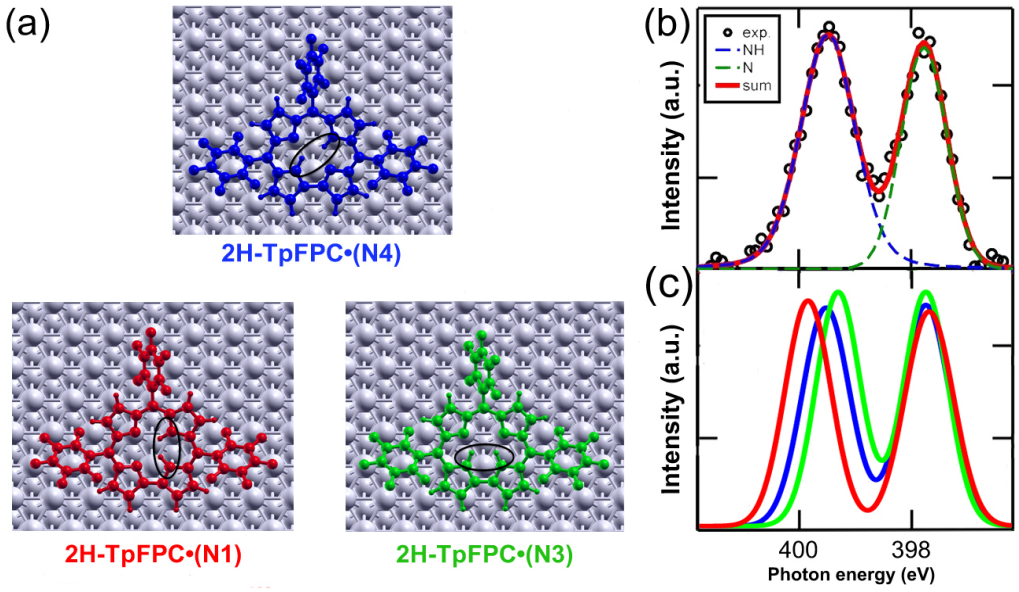

Figure 4.20: (a) Different suggested H_2TpFPC$^\bullet$ structures, which result from the dehydrogenation reaction, denoted according to the position of the released H atom. The black ovals mark the remaining hydrogen atoms within each structure. (b) The measured XPS N K-edge of a submonolayer of H_3TpFPC deposited on Ag(111) at 200 K and annealed to 330 K. The 1:1 peak intensity of aminic (-NH) and iminic (N=) nitrogen atoms provides direct information on the dehydrogenation reaction. (c) The calculated CLS of the three possibilities of the dehydrogenation reactions, coloured as shown in (a). The signals related to the iminic (N=) atoms are aligned to that of the measured XPS spectrum.

The dehydrogenation step results into a pronounced change in the related NH/N= XPS peak intensity ratio from 3:1 to 2:2 and minimal changes in the molecular geometries. However, the site of the dehydrogenated reaction remains elusive. In other words, it is unclear if a certain N-H bond is solely activated from the core of the molecule, or even if the three possibilities are equally probable. The calculations show that the structures of the three $H_2TpFPC^{\bullet}$ tautomers are highly similar (see Figure 4.20 a; the tautomers are denoted according to the position of the released H atom). However, the so-called $H_2TpFPC^{\bullet}$(N1) (red) and $H_2TpFPC^{\bullet}$(N3) (green) exhibit more pronounced buckling of the macrocycle due to shorter H to H distances than the already discussed structure $H_2TpFPC^{\bullet}$(N4). Furthermore, they are slightly less stable than $H_2TpFPC^{\bullet}$(N4) by 0.055 eV and 0.045 eV, respectively.

In principle, one could gain further information on the site of the interaction by calculating and comparing the activation barriers of different N-H bonds at RT. In order to perform such step, one has to compare a huge variety of 3D potential energy surfaces which concern all plausible diffusion paths of the released hydrogen atom. Given the large size of the investigated system and the unlimited number of possible diffusion paths, this mission is not only computationally impractical, it is also impossible, at least for the state-of-art computers.
One could argue that $H_2TpFPC^{\bullet}$(N4) is energetically more stable than the other tautomers and it should be directly considered the dominant species, even without performing any further calculations. However, the small energy differences between $H_2TpFPC^{\bullet}$ tautomers do not exhibit the final proof to conclude the site of the interaction. In particular, an activation of the N1-H or N3-H bonds might require less *activation energy* than that of N4-H bond enabling the stability of the corresponding structure and hindering further tautomerisations towards $H_2TpFPC^{\bullet}$(N4). Moreover, other (even contrasted) results might be obtained if different numerical parameters (functional, vdW approximation, etc) would be employed to investigate the present system.

To solve this puzzle without performing such complex calculations explicitly, it might be more helpful to compare the calculated XAS fingerprints of different structural candidates with the measured XPS and NEXAFS data. In fact, the calculated N 1s CLS spectra cannot clearly distinguish between these tautomeric structures. Figure 4.20 b, c compare the calculated N 1s spectra of different $H_2TpFPC^{\bullet}$ tautomers with the measured one. Actually, the three spectra are almost coincident up to $\pm$ 0.1 eV, rendering this method as non-conclusive to identify the site of the dehydrogenation interaction.

In the following, it is demonstrated that NEXAFS is sensitive to the dehydrogenation place and is able to settle this dispute.

NEXAFS C K-edges. In order to measure the NEXAFS C K-edges absorption spectra of $H_2TpFPC^{\bullet}$, a submonolayer sample with a coverage of 0.4 ML has been deposited onto the Ag(111) surface held at room temperature (RT). Again, the XPS N 1s signature of this film suggests that dehydrogenation occurred for 90% of the molecules (see Figure A.11 c in Appendix A.14).

Figure 4.21 a compares exemplarily the measured $\theta = 25^{o}$ curve of this sample with that of the sample held at 200 K (see Figure 4.13 a). Apparently, the spectra of the two phases are similar in their overall shapes except the characteristic feature Cp of the H_2TpFPC$^{\bullet}$ spectrum presented at 287 eV. The C K-edge have been again curve-fitted by assuming a π system on a threefold symmetric surface (see section 4.3.2.3 for comparison). The fitted curves indicate a tilting angle $\beta = 50 \pm 5^{o}$ for the fluorophenyl rings and a considerably flattened orientation of the macrocycle $\alpha = 20 \pm 5^{o}$. These values are in full agreement with the calculated adsorption geometries: $\alpha_{calc} = 20^{o}$ and $\beta_{calc} = 48^{o}$ (weighted average of 65°, 37° and 37°, see section 4.3.3.1).

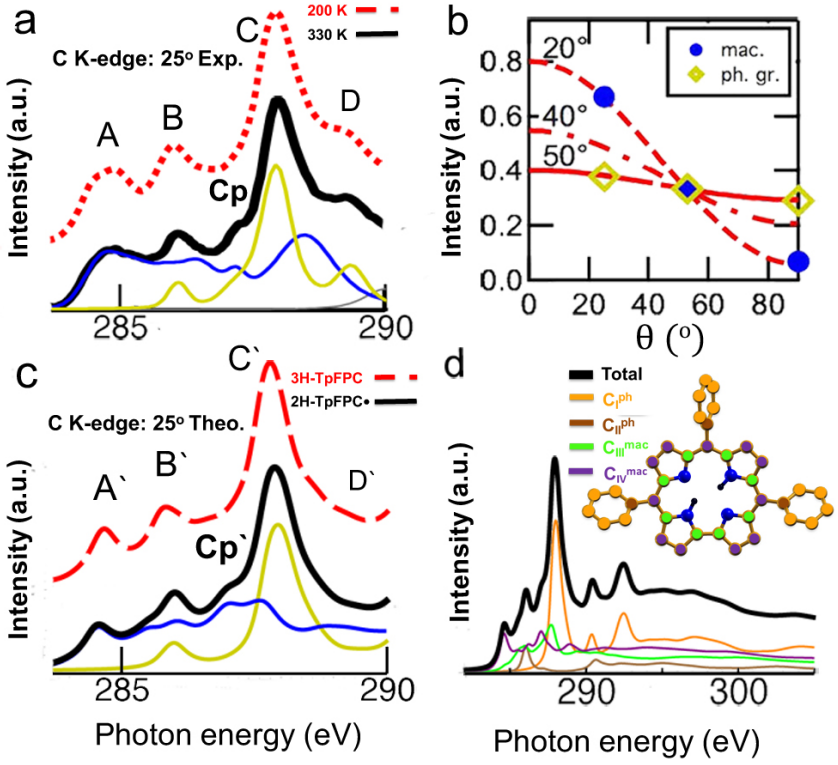

Figure 4.21: (a) Measured and (c) calculated NEXAFS C K-edge of H_2TpFPC$^{\bullet}$ compared to that of H_3TpFPC for $\theta = 25^{o}$, with a decomposition into macrocyclic (blue) and fluorophenylic (yellow) components. (b) Tilt angles of the macrocycle (∼20°) and the fluorophenyl groups (50°) derived from the angle-dependence of the different contributions depicted in (a, bottom). (d) Decomposition of the total C K-edge spectra of H_2TpFPC$^{\bullet}$ into contributions of different C types (shown for $\theta = 25^{o}$).

The calculated spectra of the structures shown in Figure 4.17 and Figure 4.18 are almost identical and represent the experimental data very well. Even the small shoulder C`p is also predicted within the theoretical C K-edge spectra (shown for the $\theta = 25^{o}$ while tha data for 53° and 90° are shown in Appendix A.11). Again, the total spectrum can be decomposed into the aforementioned four types of carbon atoms previously discussed

for H_3TpFPC (see Figure 4.21 d). The extra peak C̀p originates from the macrocyclic C^{mac}_{III} and C^{mac}_{IV} carbon atoms (all except those in the meso-positions 5, 10 and 15; Figure 4.21 d). Note that the peak C̀p is a characteristic feature. Therefore, it can serve as an indicator for the existence of dehydrogenated H_2TpFPC$^{\bullet}$ species, whereby its intensity can be related to the number of radicals within the sample.

NEXAFS N K-edges. In order to investigate the influence of the dehydrogenation on the N K-edge, a sample with a coverage of 0.8 ML has been prepared by evaporating the molecules on the silver surface held at 200 K and subsequent annealing to 330 K for 10 min. Utilising the same sample as for the C K-edges was prohibited by the insufficient signal-to-noise ratio due to its lower coverage.

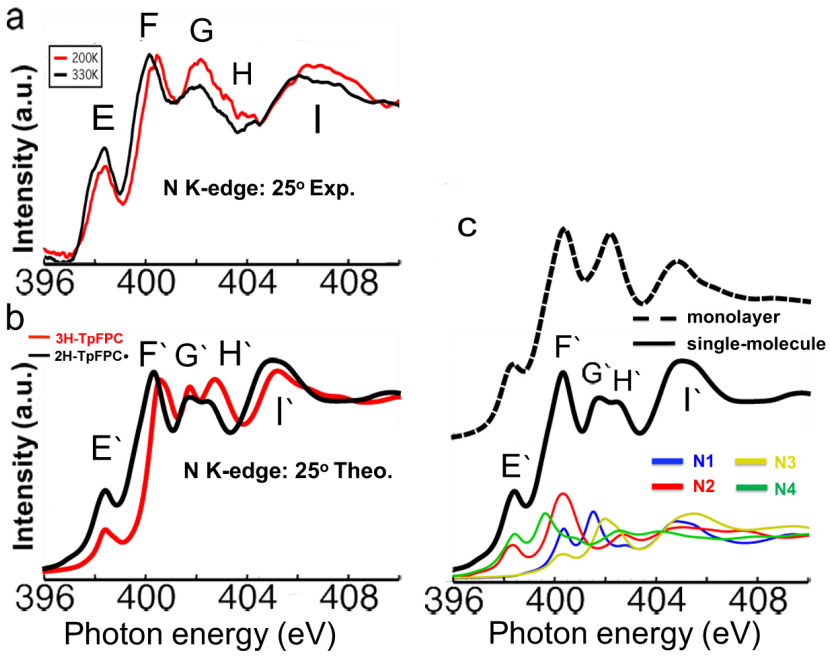

Figure 4.22: (a) Measured and (b) calculated NEXAFS N K-edge of the phase annealed at 330 K (H_2TpFPC$^{\bullet}$) compared to that of as deposited 200 K (H_3TpFPC); (c) Decomposition of the total N K-edge spectra of H_2TpFPC$^{\bullet}$ into contributions of different N types. The total spectrum corresponding to single molecule adsorption (full line) is in good agreement with that of monolayer coverage (dashed line). All spectra belong to θ=25° incidence.

Figure 4.22 a exhibits the annealed phase (330 K; black curve) compared to those of the low temperature phase (200 K; red curve). Thereby, the spectrum of $\theta = 25°$ curves are displayed as they exhibit the clearest features, while the 53° and 90° spectra are shown in Appendix A.11). Obviously, the intensities of peaks E and G (together with the shoulder H) are increased. The energetic positioning of peaks F to I are rigidly shifted by about 0.3 eV towards lower photon energies.

Figure 4.22 b compares the calculated N K-edges XAS spectra of H_3TpFPC (red) and

H_2TpFPC$^\bullet$ (black) for the case of single molecules. The calculations reproduce the experimentally observed red shift (Figure 4.22 a) with almost 0.4(1) eV for the peaks F̀-Ì. However, the intensity of theoretical peak È appears to be considerably increased compared to the experiment. To explain these aspects, the spectrum of the H_2TpFPC$^\bullet$ has been decomposed into contributions from two aminic -NH (N3, N1) and two iminic =N (N2 and N4) nitrogen atoms (Figure 4.22 c). Apparently, the peak È originates now predominantly from N 1s transitions of both iminic atoms, N4 and N2, into the unoccupied π^* molecular orbitals. Thus, the dehydrogenation of the N4 atoms results in an initial state shift of the related resonance. In principle, the intensity of peak E of H_2TpFPC$^\bullet$ should be twice like that of H_3TpFPC if all molecules have undergone the dehydrogenation transformation. Indeed, a detailed inspection of the XPS N 1s signature of this film (see Figure A.11 d) indicates that almost three out of four molecules are actually dehydrogenated. Thus, the smaller increase of the intensity of peak E in experiment represents the smaller percentage of molecules changing their chemical state as compared to the ideal theoretical cases. Note that the other peaks contain contributions from all N atoms into the higher lying π^* orbitals, each shifted correspondingly to the lower binding energies, because they all carry contributions related to N4. Despite the energy shift, the spectral shape of each N atom remains almost the same. Obviously, hydrogen release from the N4 atom also affects all other N. This is in line with the observation of a Kondo signature related to unpaired electrons statistically distributed over the entire macrocycle (see section 4.3.3.2).

To further demonstrate the chemical sensitivity of theoretical approach, the N K-edge of the periodic structure (Figure 4.18) has been calculated and depicted on Figure 4.18 c (top). The corresponding spectrum exhibits a very good agreement with that of the single molecule counterpart. However, there is a moderate change in the features G̀ and H̀, where they appear as a single peak and resemble the experimental spectrum more closely. This demonstrates that even minor intermolecular interactions have impact on the NEXAFS spectra and that the employed approach is able to capture their essential influence.

The employed approach is not only able to catch the small changes of the microstructure, it can also recognise the position of dehydrogenation reaction. Figure 4.23 exhibits the calculated spectra of the three possible H_2TpFPC$^\bullet$ tautomers depicted in Figure 4.20 a (they are also differently coloured). In both H_2TpFPC$^\bullet$(N1/N3) configurations (denoted as alternative1/ alternative2, respectively), significant differences between the DFT-calculated N K-edge spectra and the measurement are observed: The peak F at 400.2 eV splits up into a double peak, while the pairs G and H (at 402.0 and 403.0 eV) appear as a small peak at 402.6 eV. According to these calculations, the tautomeric structures 2HTpFPC$^\bullet$(N1/N3) can be excluded from contributing dominantly to the observed spectra, thus our approach has the capability of resolving products resulting from site-selective reactions.

Coming back to the calculated adsorption energies of different possible states (alternative1/2 are energetically less stable than H_2TpFPC$^\bullet$(N4) by 0.055 eV and 0.045 eV), it is possible to roughly calculate the ratio of each tautomer within the sample by employing

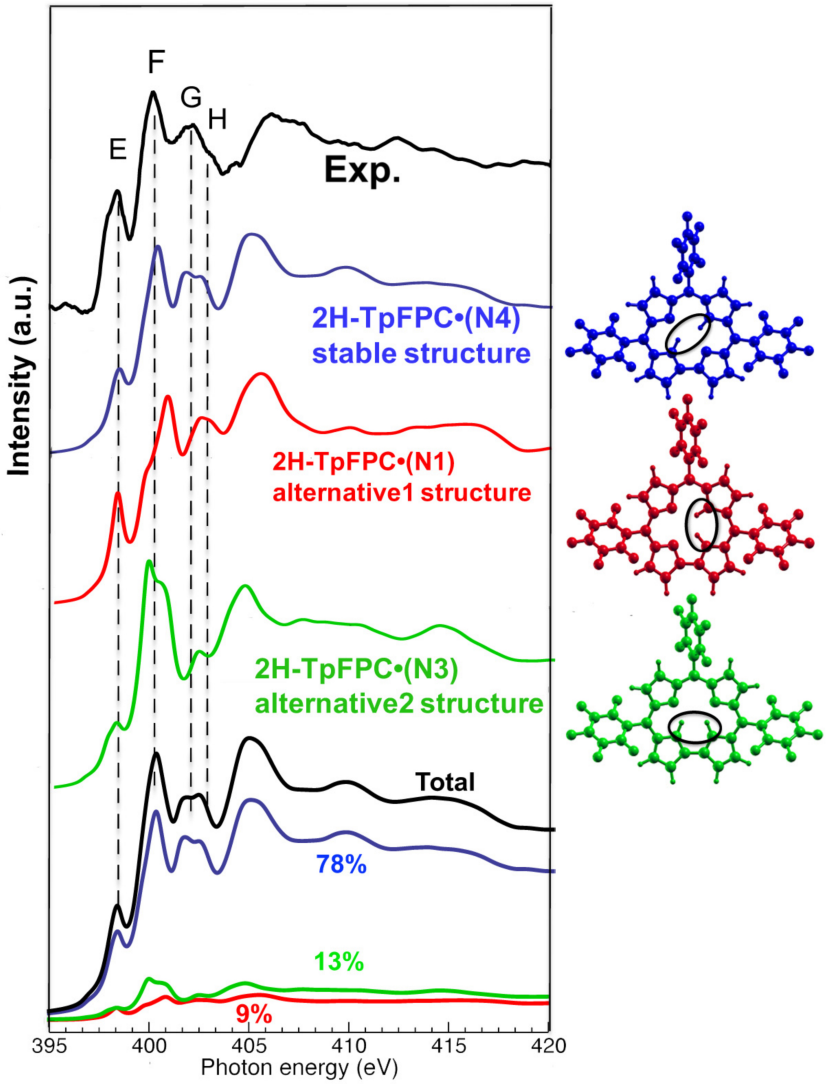

Figure 4.23: Comparison of the measured and calculated NEXAFS N K-edge of the most stable structure H_2TpFPC$^\bullet$(N4) and the two tautomeric alternatives H_2TpFPC$^\bullet$(N1/N3). All spectra are shown for θ=25°. The most stable structure (blue) results from cleavage of the N4-H bond, while the alternatives 1/2 (red/green) are a consequence of hydrogen release from N1-H and N3-H bond, respectively. The corresponding structures are depicted in the right panel. Vertical lines denote the energetic positions (photon energies) of the peaks in the experimental spectrum. The spectrum in the lower panel exhibits the summation of the three spectra in percentages calculated by employing the Boltzmann's formula (4.1).

the Boltzmann distribution formula:

$$\frac{F_i}{F_j} = exp\left\{\frac{E_j - E_i}{KT}\right\} \tag{4.1}$$

This formula gives the probability that a system will be in a certain state F_i as a function of that state's energy E_i. At 300 K, the probabilities of the stable state, alternative 1 and alternative 2 are estimated to about 78%, 9% and 13%, respectively. In order to address how this distribution is reflected in the calculated N K-edge NEXAFS spectra, the three spectra are summed with the respective ratios (see Figure 4.23). Apparently, the total spectrum is barely different from that of the stable structure. Only the valley between the two peaks E and F and the shape of the peak F are slightly improved enhancing the agreement with the experiment.

4.3.4 Intramolecular ring closure

Up to temperature of 400 K, the TPD results confirm the stability of $H_2TpFPC^{\bullet}$ species and the occurrence of no further chemical transformations. However, the detection of HF and $F^{\bullet}$ at around 430 K indicates a further chemical reaction taking place at around this temperature (see section 4.8 for details). The following part of this work provides a possible explanation of such transformation pathway. Thereby, the type of the interaction, the induced geometrical changes of the molecule, the corresponding CLS, the simulated STM topographies and the calculations of the angle-dependent NEXAFS fingerprints (to identify the site of the interaction) are discussed in detail.

4.3.4.1 XP spectra

In order to get further information about the interaction takes place at 430 K, H_3TpFPC molecules have been deposited on Ag(111) and annealed to this temperature. After such thermal treatment, the XPS C 1s signature is significantly changed, where the spectrum exhibits a complex shape with six distinguishable components. Most obvious, the formerly isolated (C_I^{ph}) peak related to the fluorophenyl carbons now exhibits a low energy shoulder at 286.7 eV (C_{VI}, see Figure 4.24). Furthermore, a novel double peak structure is discernible between 284 and 285 eV. However, the XPS N 1s exhibits almost no changes in the 1:1 aminic/iminic ratio indicating the absence of further dehydrogenation reactions.

In order to report on the chemical transformation at this temperature, one can rely on the experimental hints. Beside the TPD results, the fact that the most prominent changes are related to (C_I^{ph}) and (C_{IV}^{mac}) carbon types suggests a chemical transformation at a position where these types are mutually close. One proposed pathway is to assume a ring-closure reaction between a fluorophenyl and a pyrrole moiety within a molecule (intramolecular interaction) as depicted in Figure 4.24 c creating a new species denoted as $H_2TpFPC^{\bullet}$(rc). Apparently, such cyclisation interaction goes along with an activation of both H and F atoms at short enough time scales (ps) enabling efficient recombination and desorption of HF molecule and allowing a formation of a C-C bond between one of the C_6F_5 groups and a pyrrole moiety of the molecule itself (red oval on Figure 4.24 c). Similar ring closure

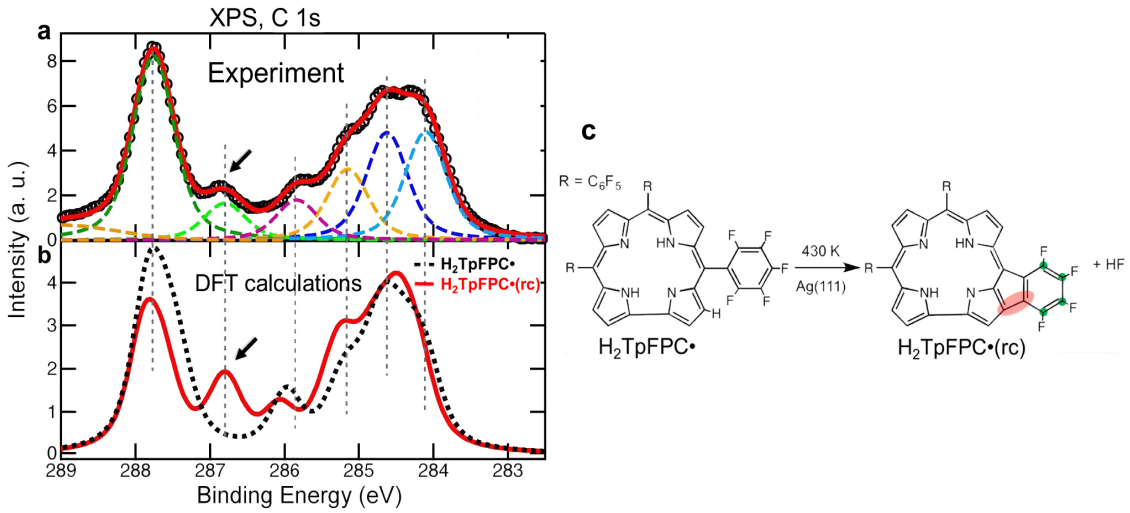

Figure 4.24: (a) Measured XPS C 1s spectrum of H_3TpFPC deposited onto Ag(111) at 200 K and subsequently annealed to 430 K. (b) Calculated XPS signatures of H_2TpFPC$^\bullet$ (dotted) and that after a single ring-closure reaction (red). The arrows indicate the characteristic peak related to the chemical transformation takes place at around 430 K. (c) Formal reaction scheme of the ring closure reaction between a pyrrole and a fluorophenyl moiety. The red oval marks the C-C bond as a result of the ring closure reaction. The four green circles indicate the carbon atoms responsible for the characteristic peak at binding energy of 286.7 eV in the XPS C 1s spectrum.

reactions have been reported previously for tetraphenyl-porphyrin compounds on the same surface [220, 221, 106, 222].

To corroborate the suggested transformation, the structure of single H_2TpFPC$^\bullet$(rc) has been relaxed on the Ag(111) surface and, then, the corresponding CLS signals have been calculated. The theoretical C 1s spectrum of the assumed H_2TpFPC$^\bullet$(rc) species (Figure 4.24, bottom panel, red line) indeed exhibits a significantly altered shape as compared to the previous H_2TpFPC$^\bullet$ spectrum (330 K, dotted line). Importantly, the feature at 286.7 eV is quite discernible and originates from the four C atoms of the fluorophenyl moiety involved in the ring closure and still connected to F (indicated green circles on Figure 4.24 c). The energetic separation of the fluorinated carbon peaks (C_I^{ph} and C_{VI}) allows utilising the ratio of the two peaks for the determination of the reaction progress. In the experimental spectrum the area of the C_{VI} peak is less than the 10:4 ratio expected for a situation where all molecules have already undergone a single ring-closure reaction (the calculated one). Consistently, the shape of the experimental spectrum can best be described by a combination of the features of H_2TpFPC$^\bullet$ and H_2TpFPC$^\bullet$(rc) and the HF peak in the TPD data has not yet reached its maximum at 430 K.

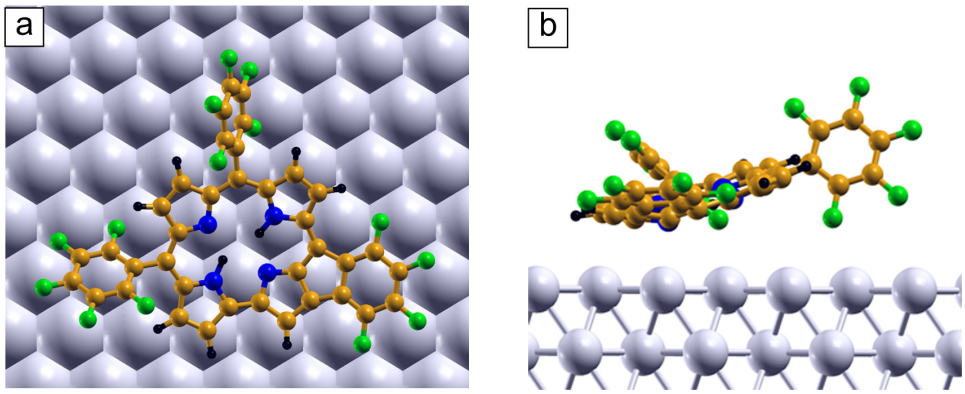

Figure 4.25: (a) Top and (b) side views of singly ring-closed corrole gained from first principles calculations.

4.3.4.2 Structure formation of H_2TpFPC$^\bullet$(rc) on Ag(111)

The molecular transformation toward H_2TpFPC$^\bullet$(rc) is accompanied with characteristic changes of the molecular geometries. Figure 4.25 shows the calculated geometries of a single H_2TpFPC$^\bullet$(rc) on Ag(111) assuming its registry and orientation to be similar to both H_3TpFPC and H_2TpFPC$^\bullet$ species. The ring closure reaction is connected with a flattening of the molecular structure yielding stronger binding to the substrate. As an example, for the structure depicted in Figure 4.25, the calculated adsorption energy is -3.49 eV (more stable than H_2TpFPC$^\bullet$ by 0.3 eV). The flattened phenyl ring is parallel to the substrate while the phenyl rings in the meso-positions 5 and 10 are still inclined by about 37° and 67° with respect to the surface. Furthermore, the macrocycle plane, now including the transformed fluorophenyl ring, is slightly bent and in average inclines a reduced angle of 14° with respect to the substrate.

Considering the geometries of the adsorbed molecule, it is rather notable that a ring-closed molecule exhibits a reduced symmetry compared to the previously studied species (H_3TpFPC and H_2TpFPC$^\bullet$), most prominent in the part related to the flattened phenyl ring. This aspect has been reflected in the recorded and simulated STM images (Figure 4.26). Figures 4.26 a shows an experimental STM image of a single corrole, manipulated from densely packed molecular islands, resulted from deposition of H_3TpFPC on Ag(111) at 200 K and subsequent annealing to 430 K. Figures 4.26 b is a simulation of the ring-closed structure depicted in (c). Indeed, the agreement between the recorded and the simulated images is very good evidencing the ring closure interaction as a reasonable explanation for the chemical transformation at this temperature. Obviously, both topographies show the characteristic triangular shape of the molecule with asymmetric appearance of the side lobes. Within the calculated micrographs, the side lobes have different brightness, while it is difficult to define the previously mentioned short axis to divide the measured image into two symmetric parts (as previously done for H_3TpFPC and H_2TpFPC$^\bullet$). This indeed confirms the occurrence of the ring closure in one of the both

side lobes. In this context, it is important to note that the site of the reduced symmetry aspect was always observed in the same place for all measured STM images indicating a type of a high regioselectivity of the ring-closure reaction.

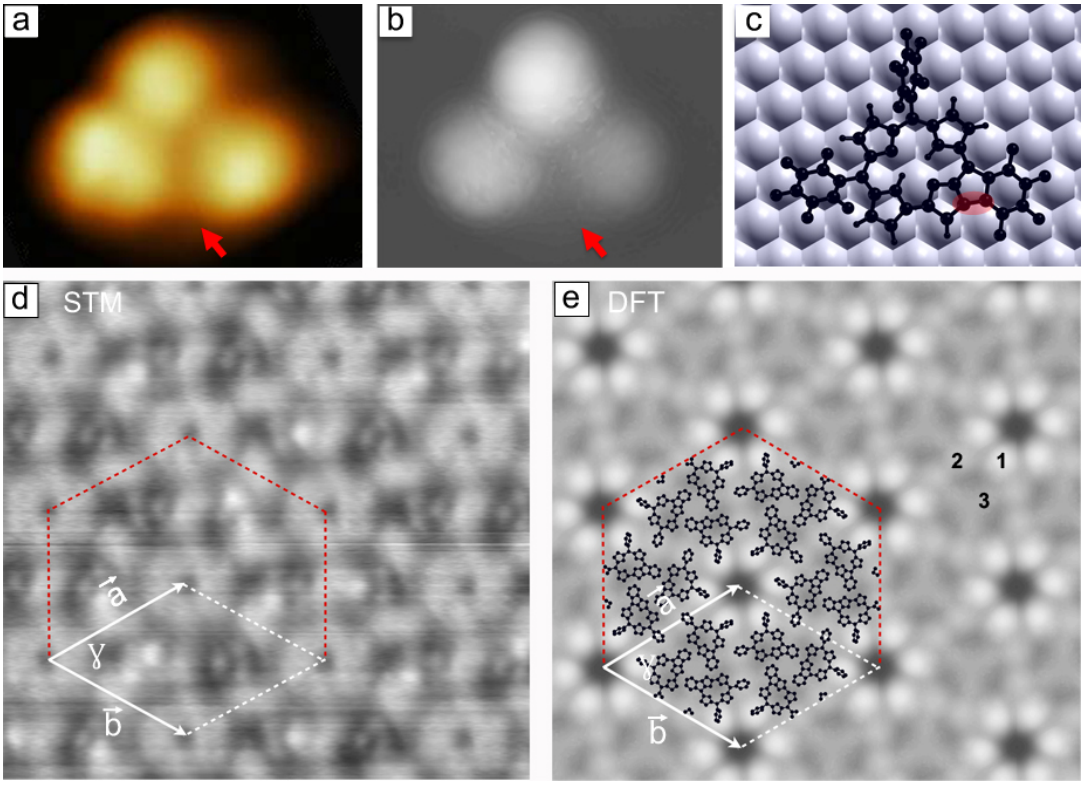

Figure 4.26: (a) Experimental STM image (+1 V, 100 pA, 3×3 nm^2, 5K) of single H_2TpFPC$^\bullet$(rc) (ring-closed species), manipulated from the monolayer which is prepared by depositing H_3TpFPC on Ag(111) at 200 K and subsequent annealing to 430 K. (b) DFT-calculated STM image of (c) the molecular structure of the ring-closed radical species. The arrows (in a and b) and the oval (in c) mark the position of ring closure reaction (as guide to the eye). (d) Experimental STM image (+0.2 V, 1 nA, 10 × 10 nm^2, 5K) and (e) DFT-calculated STM image of an idealised monolayer of ring-closed corrole after annealing to 430 K; in (d) the regular unit cell is indicated by vectors $|\vec{a}| = |\vec{b}| \approx 3.4$ nm, angle $\gamma = 60^o$; in (e) the regular molecular arrangement of the monolayer is overlaid, as obtained from DFT optimisation.

Intriguingly, the molecular transformation into H_2TpFPC$^\bullet$(rc) is accompanied by a change of the molecular monolayer into a regular and highly symmetric structure (see Figure 4.26 d). The hexagonal lattice can be described by repeated rhombic unit cells of dimensions $|\vec{a}| = |\vec{b}| \approx 3.4 \pm 0.1$ nm and the angle $\gamma = 60^o$. Obviously, this unit cell, which has an area of 10 nm^2, is three times bigger than that of H_3TpFPC. Therefore, it is plausible to suppose that it involves six singly ring-closed corroles within it. Moreover, the molecules should be arranged in a way enabling the six-fold symmetry observed in the experiment. Apparently, this molecular structure can no longer be resolved by means of the method

reported in section 4.3.3.1. Thus, the upcoming discussions completely rely on the theoretical data.
In order to resolve such complex structure, one has to figure out some reasonable configurations which enable an arrangement of six singly ring-closed molecules within a unit cell of dimensions close to the experiment. Moreover, the arrangement should be energetically favourable and able to reproduce the protrusions as well as the local symmetry of the experimental image. In particular, there are two complications concerning resolving this structure. First, there is no experimental hints about the molecular arrangement within the unit cell. Second, the structure is pretty large and requires long time to be calculated. Despite these complications, the structure was successfully resolved as it follows: First, a set of six equivalent singly ring-closed corroles were juxtaposed around the vertex of a hexagon (a reference point) in a six-fold symmetrical shape, whereby the phenyl rings in the meso-positions 10 were allowed to lie near the top of the hexagon. Then, the whole set (six molecules) was gradually rotated around the reference until some possible arrangements, which allow a dense packing of the molecules within a unit cell of dimensions close to the experiment, were achieved. These two steps were repeated for a variety of structures different in the local rotations of the molecules around their centres and for the cases where the meso-positions 5 and 15 being near the top of the hexagon. Finally, all constructed structures were calculated and the corresponding STM images were simulated.

The best obtained structure and the corresponding STM simulation are shown on Figure 4.26 e. The transformation matrix with respect to Ag(111) is described by $\begin{pmatrix} \vec{a} \\ \vec{b} \end{pmatrix} = \begin{pmatrix} 13 & 4 \\ 9 & 13 \end{pmatrix} \begin{pmatrix} \vec{x}_1 \\ \vec{x}_2 \end{pmatrix}$, where $\vec{x}_1$ and $\vec{x}_2$ are the lattice vectors of Ag(111) forming an angle of 120°. As it is previously discussed, the phenyl rings are responsible for the protrusions observed in the STM data (Figure 4.26 e). The central C_6F_5 groups at the meso-positions C10, which look as being forced to be grouped together in a hexagonal arrangement, provide the hexagonal bright part of the STM image (region 1, Figure 4.26 e). The phenyl rings in the meso-positions 5 provide a less bright lobes (regions 2), while the flattened ones provide region 3.

4.3.4.3 Site-selective cyclisation reaction

The recorded STM topographies have provided strong indications for a high selectivity of the ring-closure transformation. They claim that all manipulated ring-closed molecules show the characteristic reduced symmetry at the same site of the molecule. In line with this observation, a monolayer of singly ring-closed corroles exhibits an increased pseudosymmetry of approximately P6 compared to the previously discussed corrole species whose two-dimensional space group has an apparent P1 symmetry, which rather points out that all ring-closed molecules have the same state e.g., similar to the idealised theoretical model shown in Figure 4.26 e. Indeed, the structure depicted in Figures 4.26 e and 4.24 c is only one of six ring closure reactions, which could possibly occur at different

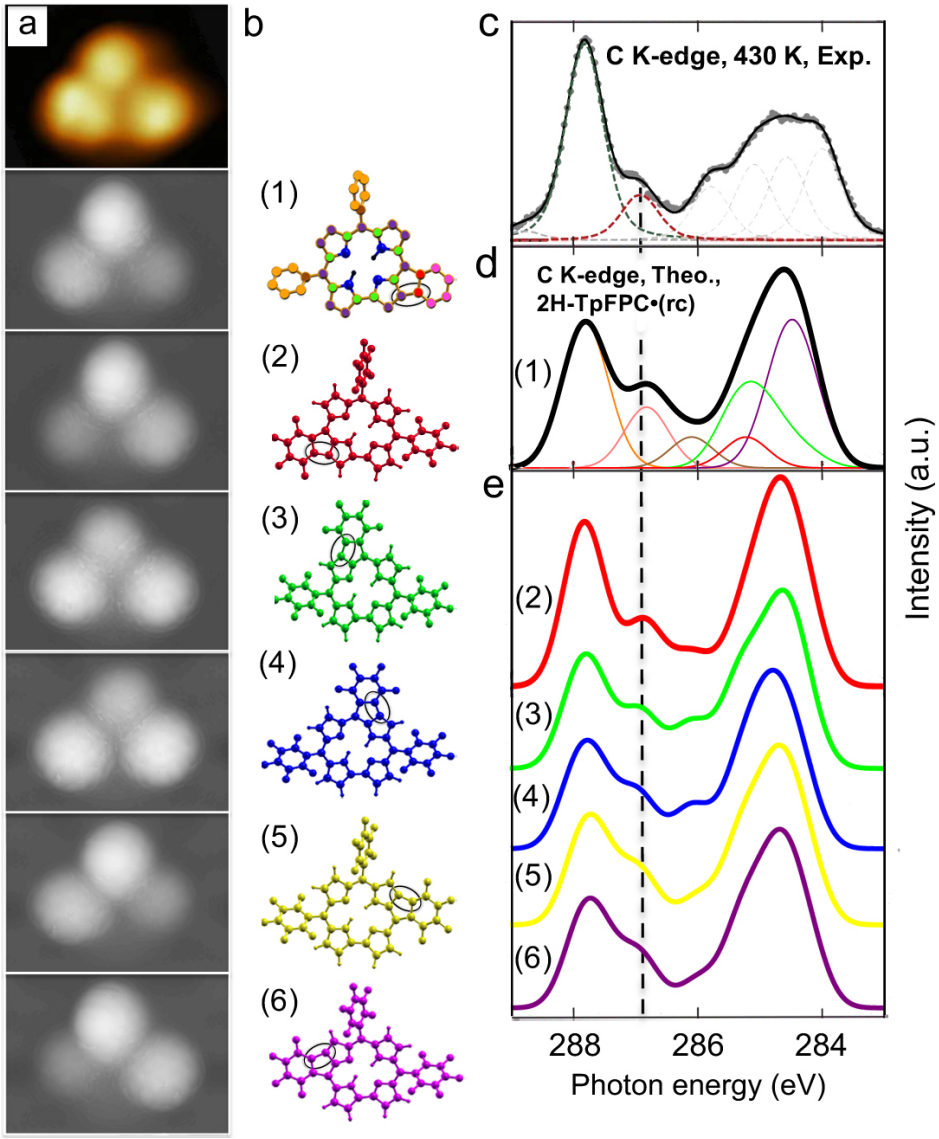

Figure 4.27: (a) The measured STM image shown in Figure 4.26 a is compared to the calculated STM images corresponding to (b) the six possible singly ring-closed structures differing in the position of the ring closure. The ovals mark the C-C bond between the phenyl rings and the pyrrole moieties as a result of the ring closure. (c) Experimental XPS C K-edge of a H_3TpFPC adsorbed on Ag(111) at 200 K and annealed to 430 K. The peak at 286.8 eV (where the dashed line is plotted) is a clear evidence of the ring-closure reaction towards H_2TpFPC$^{\bullet}$(rc). (d) Calculated CLS of one (out of six) possibilities for a ring-closure reaction. The characteristic peak exists in all spectra giving information about the type of the reaction, but not where it happens. The decomposition of the total spectrum into contributions from different C types (left side) is shown. (e) Calculated CLS of the other five possibilities of the ring-closure reaction. The spectra which are labelled from 1 to 6 correspond to the structures shown on the left side.

positions (two possibilities at each pyrrole ring). Up to this point, it is unclear if any of these six ring closure reactions occurs first and which one if this does happen.

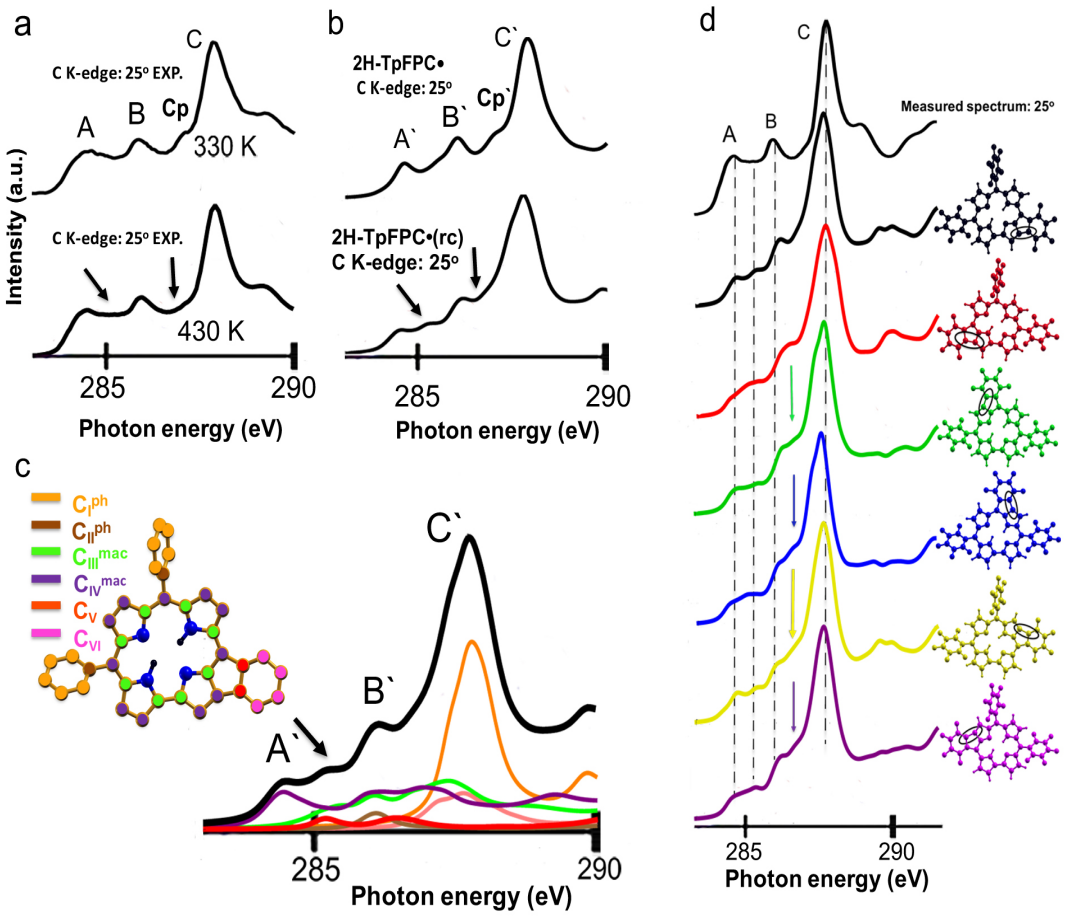

Figure 4.28: (a) Measured and (b) calculated C K-edge NEXAFS of H_2TpFPC$^\bullet$ (top) and H_2TpFPC$^\bullet$(rc) (bottom), shown for an incident angle of 25°. (c) Decomposition of (b, bottom) into the contribution of six C types. Canted arrows emphasise the new ring-closure-induced features. Vertical arrows mark the valley between peak B and C as an evidence of the selectivity of this reaction. (d) Experimental and calculated NEXAFS C K-edge spectra for the six possible singly ring-closed structures differing in the position of the ring closure. The black ovals highlight the carbon-carbon bond resulting form the ring-closure reaction. The colored arrows on the calculated spectra mark the most prominent deviation from the experiment.

In order to have deeper insight into the site of the ring closure transformation, the six possible tautomers were, first, relaxed on the surface assuming their registries and orientations to be similar to H_2TpFPC$^\bullet$. Indeed, the other tested registries and orientations confirm that these factors minimally effect the geometries of the adsorbed molecules. Then, the STM images corresponding to the aforementioned structures are calculated and compared to the measured one (see Figure 4.27 a). If one does not consider the calculated STM

topographies, the six structures appear at the first glance to be highly similar. However, each tautomer provides a different topography upon adsorption on the surface, which is apparently reflected in the simulated STM images. Obviously, the structures denoted as (3) and (4) strongly deviate from the measured STM image, since the reduced symmetry aspect does not appear in one of the side lobes. This is rather plausible having in mind its essential role for stabilising the adsorption geometry, it is rather unlikely that the central strongly tilted C_6F_5 group bound to C10 is involved in an initial ring closure. Indeed, the remaining four STM images are almost identical rendering the tiny differences as not conclusive to decide the site of the ring closure.

Beside the STM topographies, the C 1s CLS signals of the six $H_2TpFPC^{\bullet}$(rc) possibilities have been calculated (see Figure 4.27 c). The decomposition of the DFT-calculated spectra comprises six components corresponding to the different types of carbon atoms: Besides the previously identified four C types (C_I^{ph}, C_{II}^{ph}, C_{III}^{mac} and C_{IV}^{mac}, see Figure 4.13 e and Figure 4.21 d), two additional components are now present, one corresponding to the two carbon atoms directly involved in the ring closure reaction and thus connecting the macrocycle with one of the phenyl rings involved in the ring-closure reaction (C_V, marked in red), and the other including the remaining C atoms in the ring-closed phenyl ring (C_{VI}, marked in pink). Apparently, the shoulder feature at 286.7 eV exist in all spectra rendering that, despite being a clear indicator for a cyclisation reaction, it is not specific enough to distinguish where does the cyclisation occur.

To investigate the influence of the ring closure reaction on the experimental C K-edge spectra, the 0.8 ML sample discussed in Figure 4.22 is annealed at 430 K for 10 min and its spectra were measured. In Figure 4.28 a, the $\theta = 25^{o}$ curve is compared to that of the previous $H_2TpFPC^{\bullet}$ dominated phase (i.e. annealed to 330 K). Despite clearly different C 1s XPS signals, the C K-edges NEXAFS spectra of the two species are almost identical. However, the characteristic peak Cp has disappeared in the latter. Besides, this spectrum exhibits a new feature (highlighted by the canted arrow) at 285.2 eV, in which the valley between peaks A and B is occupied by an additional peak.
In order to identify the origin of this new peak, the C K-edges corresponding to structure (1) presented in Figure 4.27 have been calculated and compared to that of $H_2TpFPC^{\bullet}$ (Figure 4.28 b). Despite the rather small differences between the two spectra, the new feature at 285.2 eV is also discernible in the calculated spectra (canted arrow). As already mentioned, the DFT-calculated spectra in Figure 4.28 c comprises six components. The components C_{VI} (marked in pink) contribute to the main peak at 288 eV and cannot be resolved experimentally. The DFT calculations interpret the new feature (at 285.2 eV) as a result of excitations of C_V atoms into the higher lying π^* states. A second peak at 287 eV originates from the same atom types; the energetic position of these two extra peaks remains almost the same regardless of the specific position of the ring closure.

To test the ability of the employed approach to address the reaction site-selectivity, the NEXAFS C K-edge spectra for the six configurations associated to the possible ring closure reactions have been calculated (Figure 4.28). Clearly, the valley between peak B and main peak C (marked by a vertical arrow as a guide to the eye) is site-specific: For all but

the described above configurations (denoted as structure (1) and (2), see Figures 4.27), this valley has been lifted and peak B evolves into a shoulder of the main peak C. This observation renders these ring-closure structures the most likely to occur.

4.3.5 Temperature-induced Structures of corrole

Upon annealing to temperatures higher than 430 K, the previously presented experimental findings (see section 4.3.1), e.g., the desorption of both $F^{\bullet}$ and HF molecules indicated by TPD and the change of -NH/=N- intensities at T > 550 K observed by Fast N 1s XPS measurements, indicate the occurrence of further chemical reactions. The following discussions try to *roughly* report and speculate on such transformations without identifying their sites within the molecular structure. The determination of the latter is still an open question and requires further experimental and theoretical investigations. However, this shortly presented study represents a starting point in this direction.

4.3.5.1 Multiple intramolecular ring-closure reactions

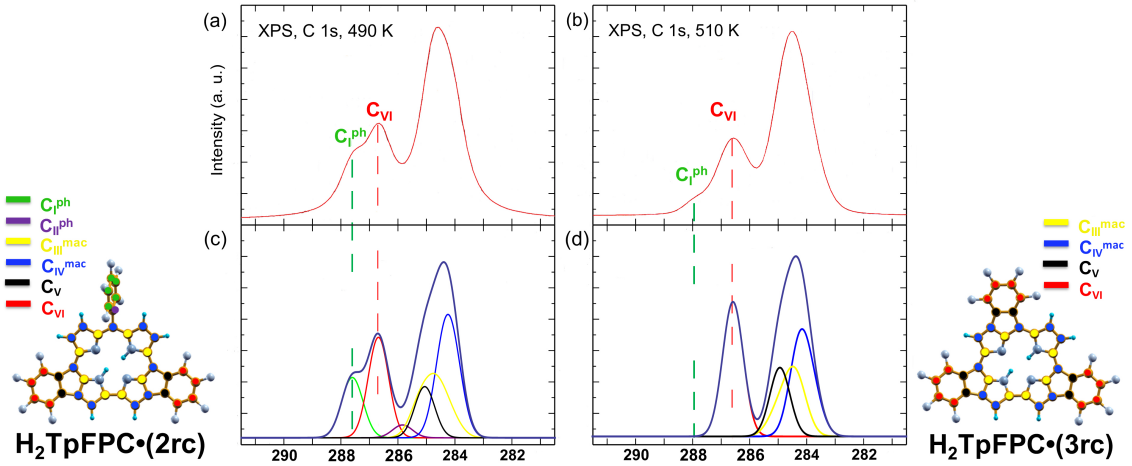

Figure 4.29: (a, b) Experimental XPS C K-edge of a H_3TpFPC adsorbed on Ag(111) at 200 K and annealed to (a) 490 K and (b) 510 K, respectively. (c) DFT-calculated CLS of a free-base corrole undergone twofold ring-closure reactions (H_2TpFPC$^{\bullet}$(2rc)). The total spectrum can be fitted with six components coloured as shown in the Figure on the left side. (d) DFT-calculated CLS for a molecule has undergone threefold ring-closure reactions. In such species, the overall spectrum can be fitted with four components as shown in the model on the right-side panel. The peak at about 288 eV (green dashed line) indicates the carbon atoms within the phenyl rings which have not undergone the ring closure interaction. The peaks at 286.8 eV (red dashed line) indicates those which have already done the ring closure interactions.

Figure A.12 of Appendix A.15 presents C and N 1s XPS measurements carried out for a monolayer of H_3TpFPC grown at 200 K and subsequently annealed to 430, 450, 470,

490, 510 and 530 K, respectively. Compared to the spectrum at 430 K, the measured C 1s spectra show upon increasing the annealing temperature a progressive increase of the C_{VI} intensity with a simultaneous decrease of the C_I^{ph} intensity. These changes are accompanied with a slight increase in the intensity of the macrocyclic region (peaks at binding energies < 286 eV) and a negligible or even no shift in the binding energies of all peaks. At about 510 K, the C_I^{ph} peak is almost vanished except a small peak at 288 eV. For all aforementioned temperatures, an almost 1:1 ratio of the -NH/=N- peak intensities indicates no further dehydrogenation reaction up to 530 K.

A plausible explanation for the chemical transformation up to 530 K is to suppose that further intramolecular ring-closure reactions occur between the pyrrole carbons and the C_6F_5 groups (twofold or in maximum threefold within each molecule). Thereby, the intensity of peak C_{VI}, which results from the carbon atoms within the phenyl ring incorporated in the ring-closed interaction, is increased on the expense of that related to C_I^{ph}. The almost disappearance of the C_I^{ph} at $T > 510$ K indicates that most molecules have undergone the fully (threefold) ring closure reactions. Nevertheless, the small contribution at 288 eV suggests residual molecules with still tilted C_6F_5-group (less than 15%).

To corporate the suggested chemical pathways up to 530 K, all possible structures comprising twofold or threefold ring-closure reactions have been modelled. For each structure, the corresponding STM images, CLS and NEXAFS fingerprints have been calculated. Figures 4.29 (a, c) compare *exemplary* the calculated C 1s CLS of a structure undergone twofold ring closure reactions ($H_2TpFPC^{\bullet}$(2rc)) with the measured C 1s XPS of the structure annealed to 490 K. Apparently, the calculated spectrum reproduces all experimental peaks in term of their positions and intensities very well. Similar to $H_2TpFPC^{\bullet}$(rc), the spectrum can be fitted with six components, but with relative peak intensities of C_{VI}:C_I^{ph} of 8:5 instead of 4:10 for $H_2TpFPC^{\bullet}$(rc). If one assumes that all singly ring-closure products are somehow possible, a $H_2TpFPC^{\bullet}$(2rc) has 12 tautomers with almost coincident CLS signals (see Figures A.13 and A.14). Therefore, it should be borne in mind that it is unknown at the current stage if the phase at 490 K consists of $H_2TpFPC^{\bullet}$(2rc) in one tautomer, or a mixture of different tautomers, or rather a mixture of different species with single, twofold and threefold ring-closure reactions. Furthermore, it still unclear why the first ring-closure interaction should be selective while the second as non-selective. In Appendix A.16, some indications about the role of the spin density to initiate site-selective chemical reactions have been presented.

Upon increasing the annealing temperature from 490 to 510 K, the intensity of C_{VI} peak is dramatically increased while that of C_I^{ph} is almost suppressed indicating this temperature as crucial to enable the molecules to undergo the threefold closure reactions. Figures 4.29 (b and d) present a comparison between the measured C 1s XPS of the structure annealed to 510 K and the calculated C 1s CLS of a molecule undergone threefold ring closure reactions ($H_2TpFPC^{\bullet}$(3rc)). The agreements between the measurement and the calculations are very good in terms of the peak positions and somehow the relative intensities. The idealised theoretical model assumes that no tilted phenyl rings still exist but all have done

the reaction. Thus, it includes no contributions from the C_I^{ph} carbons (at about 288 eV), but it exhibits two peaks at binding energies of about 286.8 and 284.5 eV with relative intensities of 75:100. The peak at 286.8 eV results from the C_{VI} atoms, while that at 284.5 eV from the C_{III}^{mac}, C_{IV}^{mac} and C_V atoms. The measured spectrum is different from the calculated one in three aspects. First, it includes a small peak at 288 eV which is absent in the calculated spectrum. Second, the relative intensity of the already mentioned peaks is 40:100 while it is 75:100 in the calculations. Third, all peaks exhibit a larger broadening compared to that in the calculations. These deviations can be explained by supposing that the measured spectrum at 510 K (Figure 4.29 c) is not a pure $H_2TpFPC^{\bullet}$(3rc) phase, but rather a mixture of molecules with still tilted C_6F_5-group responsible for the small peak at 288 eV (15%), molecules with threefold ring closures (55%) and maybe interconnected molecules (30%) responsible for the high intensity of macrocyclic region (see the next section). Again, it should be noted that it can not be concluded from the CLS measurements if any of the eight possible $H_2TpFPC^{\bullet}$(3rc) tautomers is dominant (see the third column in Figures A.15 and A.16). The calculated CLS of all possibilities are almost coincident rendering again that CLS is a quite trustable method to identify the type of the interaction but not to identify its site.

The situation changes considerably when comparing the STM images of different possible $H_2TpFPC^{\bullet}$(2rc) as well as $H_2TpFPC^{\bullet}$(3rc) tautomeric structures. The first column in Figures A.13 and A.14 compares the 12 possible tautomeric structures of $H_2TpFPC^{\bullet}$(2rc) (labeled from 1 to 12). In all these structures, the occurrence of a twofold ring closure reaction yields a further flattened geometries of the molecule, where the macrocycle and two out of three phenyls are parallel to the surface. Like this, the estimated tilting angle of the macrocycle with respect to the underlaying surface (α) is about 7°. In general, the calculated STM images of all structures exhibit the typical shape of corroles with one lobe is brighter than the other two. The brighter lobe results from the still tilted phenyl ring exhibiting higher geometries than the ring-closed ones. However, supposing that the interactions take place at particular sites of the molecule yields a significantly different geometrical structure and, thus, different STM image (see the second column of Figures A.13 and A.14). As an example, structure like $H_2TpFPC^{\bullet}$(2rc)(1, 2, 10) generate symmetric micrographs, while structure like $H_2TpFPC^{\bullet}$(2rc)(7, 8, 9, 11) generate asymmetric ones. In contrast to the previously discussed $H_2TpFPC^{\bullet}$(rc) product, the existence of some structures like $H_2TpFPC^{\bullet}$(2rc)(6, 12) generate topographies with a tendency towards four lobes. These discussions can be also extended to the case of $H_2TpFPC^{\bullet}$(3rc) tautomers (see Figures A.15 and A.16). Upon a threefold ring closure reaction, the three flattened phenyl rings are parallel to the macrocyclic plane. This yields a completely flat molecule parallel to Ag(111), i.e., $\alpha \approx 0°$. The STM images of these species are symmetric in cases of, e.g., $H_2TpFPC^{\bullet}$(3rc)(1, 3), asymmetric in cases of $H_2TpFPC^{\bullet}$(3rc)(4, 5) and exhibit four protrusions in cases of $H_2TpFPC^{\bullet}$(3rc)(6, 8). Obviously, the latter feature results from the pyrrole moieties existing now in-plane with the other three ring-closed phenyl rings.

In order to provide a further support to the theoretically expected ring-closures trans-

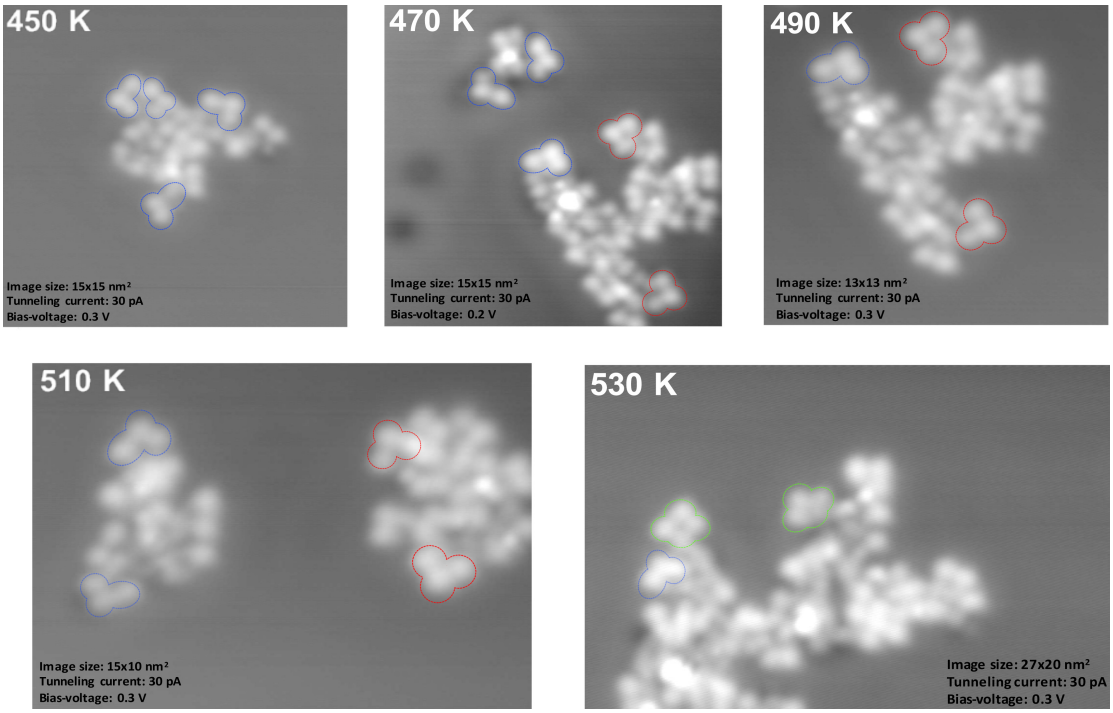

Figure 4.30: Selected STM images for a monolayer of H_3TpFPC deposited on Ag(111) at 200 K and successively annealed to 450, 470, 490, 510 and 530 K. The dimensions of each image are presented on it (for further details, please look in the master thesis of Jeffrey Schuster from the Johannes Kepler University Linz). The blue (red) shapes indicate the ring-closed molecule which generate asymmetric (symmetric) STM topographies. The green shapes indicate those which result in fourfold STM topographies (see text for details).

formations, Mr. Jeffrey Schuster (from the group of R. Koch at the Johannes Kepler University Linz) has performed STM measurements on samples prepared by depositing H_3TpFPC on Ag(111) at 200 K and annealing them to the temperature of interest (450, 470, 490, 510 and 530 K). Thereby, he repeated the measurements for four different coverages (see his thesis for further details). His results show that irrespective of the annealing temperature or coverage, corrole molecules exhibit a completely arbitrary arrangement within disordered islands, that even local orders have been not observed. This result is in line with the measurement of Stefano Tebi, who found that upon increasing the annealing temperature from 430 K to 460 K the well-order hexagonal structure was completely lost (see our together publication [181]). The results of J. Schuster provide a type of support to the expected chemical transformations. According to his measurements, a structure annealed to 450 K exhibits a single brighter lobe per each corrolic molecule. Upon increasing the temperature, the number of which progressively decreases in line with the expected transformations from H_2TpFPC$^{\bullet}$(2rc) towards H_2TpFPC$^{\bullet}$(3rc) species. Furthermore, he noticed that the molecules within a sample annealed to 530 K are strongly interconnected as previously deduced from the CLS results.

The formation of disordered arrangements upon annealing to the different temperatures might indicate that the second and the third ring closure reactions are non-selective anymore. In other words, if there is a possibility that two or more tautomers of each species together coexist, where each tautomer has a different registry and orientation with respect to the underlying surface, one should expect high configurational entropy contributions at T > 430 K. Like this, the energy barrier that needs to be overcome starting from a disordered phase might be high enough to circumvent a collective rearrangement toward ordered phases. Figure 4.30 might provide a first clue in this direction. Since it is difficult to distinguish individual molecules within the centres of islands comprising either overlapped or interconnected molecules, overviews from their frayed edges have been shown for all annealing temperatures. Within such regions, the characteristic triangular shapes typical for corroles (irrespective of their chemical state) are visible. Notably, within each sample many symmetric (red), asymmetric (blue) topographic appearance can be recognised. Within a sample annealed to 530 K, topographies with 4-lobes could be also identified (compare with Figures A.13, A.14, A.15 and A.16). Despite it is impossible to distinguish by means of the current STM measurements between the geometrically almost coincident H_2TpFPC$^\bullet$(2rc) and H_2TpFPC$^\bullet$(3rc) structures, it is possible to provide an evidence that different products can be together exist upon annealing to a given temperature, which enhances the assumptions behind the disordered phases. However, such STM study lacks the accuracy since it speculates the correspondence of three neighboured lobes to a single individual molecule, while they might belong to several neighbouring molecules. For better comparison with the theoretically predicted structures, a more systematic STM investigation is required. Thereby, a large number of molecules should be individually manipulated out of the disordered islands and their height profiles should be systematically investigated.

Another possible way to conclude on the selectivity/ non-selectivity of the multiple ring closure reactions is to have NEXAFS spectra measured for a sample annealed to the aforementioned temperatures. The fourth columns of Figures A.13, A.14, A.15 and A.16 just show the calculated angle-dependant NEXAFS spectra for the 12 possible H_2TpFPC$^\bullet$(2rc) and 8 possible H_2TpFPC$^\bullet$(3rc) tautomers for incident angles of θ = 25, 53 and 90^o. Unfortunately, no experimentally reference data are available to compare with. However, from our DFT-calculations, we could speculate that this method might enable us to report on the site-selectivity of the chemical reaction, since each of the 12 H_2TpFPC$^\bullet$(2rc) and 8 H_2TpFPC$^\bullet$(3rc) tautomers has different geometrical aspects yielding, thus, different NEXAFS spectra.

4.3.5.2 Inter-molecular linking: covalent corrole network

Upon annealing to temperature close to 550 K, the N 1s XPS measurements show a strong decrease of the pyrrolic N-H signal intensity suggesting further dehydrogenation reactions. At this temperature, the progressive desorption of F atoms within TPD indicates

additional defluorination processes rendering further chemical transformations. According to the above results, such transformations can no longer be explained by ring closures within individual molecular species. Instead, it is more probable that the already flattened molecules tend to reduce their intermolecular distances reaching a type of network-like structure.

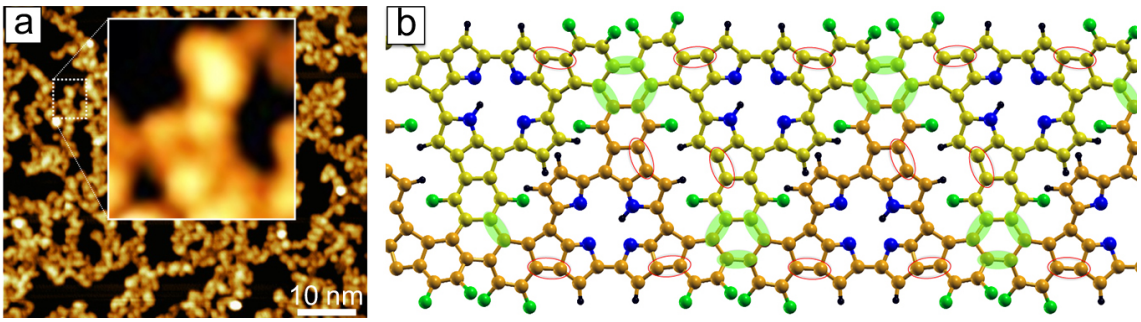

Figure 4.31: (a) Experimental STM image of corrole radical layer on Ag(111) annealed to 700 K; inset: magnified detail. b) Simplified model of a regular patch of covalently-linked corrole molecules. Green (red) ovals indicate intermolecular (intramolecular) reactions.

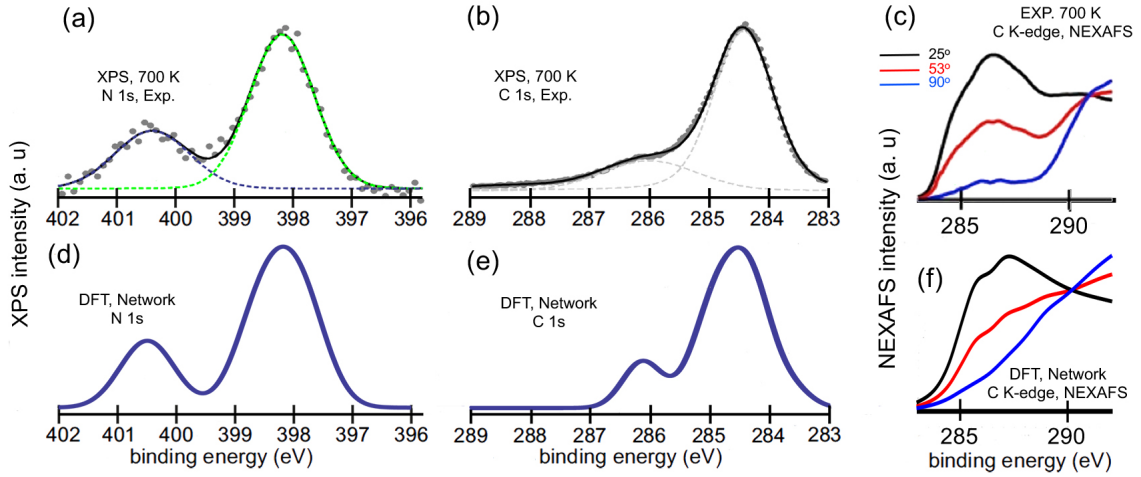

Figure 4.32: (a) N 1s, (b) C 1s XPS and (c) C 1s NEXAFS spectra recorded for a H_3TpFPC monolayer deposited on Ag(111) at 200 K and annealed to 700 K. DFT-calculated (d) N 1s, (e) C 1s CLS and (f) C 1s NEXAFS spectra of the modelled network shown in Figure 4.31 b.

This scenario has been confirmed by the accompanied STM, XPS and NEXAFS measurements. Figure 4.31 a is an STM image of a monolayer of H_3TpFPC deposited on Ag(111) at 200 K and then annealed to 700 K. The image shows the bare Ag(111) as black regions and extended stripes of corrolic molecules in a complex network form. The conformation of the latter is apparently different from the previously shown islands at temperatures up to 510 K, where the characteristic triangular shapes of individual molecules are completely absent here (see Figure 4.31 a). Instead, the molecules appear to form a reticulum

with disordered compact layer of height of 1.4 Å excluding, thus, the possibility of vertical stacking. However, it is impossible to conclude from the current STM image on the survival of the molecular macrocycles. Therefore, XPS N and C 1s spectra have been measured for a sample annealed to 700 K. The XPS N 1s (Figure 4.32 a) exhibits a two peak feature of intensity 1:3 of NH/N= indicating *(i)* no third dehydrogenation up to 700 K and *(ii)* no particular changes in the chemical environment of the nitrogen atoms, i.e., the survival of the macrocycles. The XPS C 1s edge (Figure 4.32 b) shows a dominant peak at 284.5 eV typical for π-conjugated networks and a broadened feature with low intensity probably resulting from the carbon atom in the vicinity of still existing Florine atoms. Interestingly, after 700 K annealing, the angle-dependent carbon K-edge spectra (Figure 4.32 c) have lost the sharp feature at 288 eV and exhibit strong and nearly uniform dichroism throughout the whole π^* range (below 290 eV). Such spectra indicate an overall flattened orientation of the surface supported corroles, where the originally tilted phenyl rings have been incorporated into a more planarized structure. Similarly, a broad absorption feature is typical for conjugated π-electronic systems such as graphene [223] or nitrogen-doped graphitic carbon networks [224]. However, the corrolic structure exhibits an increased broadening resulting from the apparent irregular porosity of the structure.

In order to model the network-like structure, one should figure out some models starting from the following experimental indications:

- Each molecule has undergone the threefold ring closure reaction.
- Each molecule has undergone two dehydrogenation reactions.
- The macrocycle survives indicting an intermolecular linking between the ring-closed phenyl rings.
- There still F atoms within the molecular structure (see Ref. [181]).

Figure 4.31 b is a schematic representation of a tentatively suggested model which fulfil all aforementioned requirements. The structure consists of two molecules (differently coloured) forming C-C bonds between the ring-closed phenyl rings of neighboured molecules. The agreement of the experimental XPS and NEXAFS signatures with those of the model-based calculations is striking (see Figure 4.32 c, f), whereby intermolecular binding is shown to start around 500 K and the formation of a network-like structure seems to be almost completed at 700 K. Although further structural modifications can be expected after thermal annealing, these findings, thus, evidence that the corrole character survives such thermal treatment and qualify the network-like structure as a promising starting point for the future fabrication of catalytically active interfaces.

5 Summary and Outlook

A journey of a thousand miles
begins with a single step.

(Lao Tze)

The present thesis introduces DFT calculations in collaboration with experimental measurements on three prototypical organic molecules adsorbed on different surfaces. It aimed at providing a solid knowledge about the mechanism of the structure formation in systems like, e.g., a perylene-based molecule on a reactive surface and a functional molecules on ionic surfaces. Moreover, it aimed at addressing the identification of unknown molecular species and their on-surface covalent conversions with help of theoretical spectroscopy. For all investigated systems, the calculations provide information on the geometry and the electronic structure as well as spectroscopic properties of molecules in gas phase or adsorbed on a surface. The role of the different interactions such as purely electrostatic, covalent or van der Waals between the molecules as well as between the molecule and the substrate have been clarified. Furthermore, chemical reactions of the constituents have been calculated giving, thus, information on the reaction thermodynamics. The calculations helped not only in understanding the experimental data by suggesting models, which confirm or refute the measurements. They even motivated the preparation of new experiments basing on the theoretically achieved results. Like this, they decisively assisted by setting up the experiments cost- and time-efficiency.

It was demonstrated that first principles calculations have been performed to investigate the self-organisation patterns of the perylene-based diindenoperylene (DIP) molecules on Cu(111) surfaces. The calculations show a strong influence of the substrate on the geometric and the electronic properties of single molecules. Furthermore, they show an increase of the adsorption energy by going from isolated molecules to short-range and long-range ordered structures. The calculated adsorption geometries are in very good agreement with the experimental data available. The relatively low diffusion barriers calculated, in conjugation with the energetic most favourable adsorption at step edges, suggest that the ordering of the molecular films may be initiated by straight steps and extends from there over the terraces. In addition to the most favourable, theoretically calculated long-range structure, experimentally less stable short-range ordered structures are found. The experimental observation of the energetically less favoured order has been ascribed to thermal effects as well as to the preparation conditions (i.e., kinetically stabilised structure). This point of view is supported by STM measurements showing a co-existence of both phases.

A second class of molecules, the perylene-3,4,9,10-tetracarboxyl acid dianhydride (PTCDA) molecules adsorbed on both KCl(100) and NaCl(100) surfaces, is studied herein. Thereby, the adsorption of single molecules as well as monolayers on both terraces and at step edges have been studied in detail. The calculations show that a PTCDA molecule exhibits site-specific adsorption on plane terraces, where it exhibits an arch-type distortion, its long axes is parallel to a <110> orientation of the surface and its centre resides above a surface anion with its carboxyl oxygen atoms above the surface cations. The calculated potential energy surfaces with corrugation below 1 eV and diffusion barriers of about 0.6 eV explains the kinetic stability on terraces at low temperatures and the mobility of the molecules to thermodynamically more favourable step sites at elevated temperatures. The calculations address also on the monolayer structures on KCl and NaCl(100). In both cases, the molecule is less distorted compared to the single molecule. Naturally, in these structures, the molecule–surface interaction is reduced in favour of stronger molecule–molecule interactions. In agreement with the experiment, the calculations confirm the role of the step edges to initiate the structure formations (the adsorption on step sites to be energetically favourable compared to the adsorption on terraces). A PTCDA molecule anchors to specific sites of step edges where it protrudes into them forming a vacancy site while its registry and orientation are similar to the geometries of the molecule at terraces sites. Remarkably, the calculations indicate that the formation of vacancy sites by expelling a KCl molecule is a thermodynamically favoured process. As a consequence the formation of and the adsorption at these vacancy sites is always possible and does not require the presence of defects at the step edge ahead. In general, the adsorption aspects of single molecules on KCl(100) and NaCl(100) (i.e., the two similar surfaces with different lattice constants) are highly similar. However, higher adsorption energies and stronger distortion for NaCl have been obtained. Apparently, the same holds for the diffusion barriers and for the adsorption of the molecule at step edges. The smaller lattice constant of NaCl results in lower lateral diffusion barriers for PTCDA molecules compared to KCl(100).

This work also provides new detailed insight into the complex on-surface chemistry of corroles. Corroles are tetrapyrrole macrocycles with a broad range of applications in various fields of science from physics and chemistry to bioscience and medicine. Information for the related corrole interfaces, however, was scarce. Here, DFT-based total energy and spectroscopy calculations in collaboration with XPS, NEXAFS spectroscopy, STM, and TPD measurements were presented to investigate the chemical states and the conformation of the free-base corrole in the adsorbed state and unraveled the annealing induced chemical reactions in a site-selective fashion. As a prototype example, the free-base 5,10,15-tris(pentafluorophenyl)corroles (H_3TpFPC) adsorbed on Ag(111) has been investigated.

As a pre-step, a plane-wave based approach within density functional theory (DFT) for extended, (quasi)periodic molecular structures have been employed to provide the spectroscopic fingerprints of all relevant core-level regions and absorption edges of the ultra-pure corrole multilayer samples. Important in this context to confirm that this approach represents an extension from the solid state physics towards hybrid systems (i.e., adsorbed

molecules on surfaces). By employing this approach, the calculated XPS and NEXAFS spectra showed in their overall shapes a high degree of agreement with the experiment. This allowed for a thorough analysis of each spectrum into contributions of individual atoms to the total spectra and enabled an accurate description of the free-base corrole electronic structure. Noteworthy, the overall calculated shape of the simulated crystal phase XAS spectra reproduced the experimental data to a level surpassing previous investigations [225, 95]. The employed computational approach achieves in the raising edge a description of similar quality as usually obtained with more expensive time-dependent DFT methods [226, 227], which are typically restricted to gas-phase calculations. It exhibites a high sensitivity toward intermolecular interactions and addressed their necessity to include in the modelling. Furthermore, it showed a high sensitivity to capture the characteristic features resulting from small variations in the electronic structure, e.g., tautomers. The calculations identified that the molecular species remain intact and appear in a single tautomer (with the iminic N at an inner pyrrolic ring) in the partially disordered thin film investigated. Such comprehensive understanding of the electronic structure of corroles represented the basis to extend the computational approach to investigate the more complex architectures of molecular corroles adsorbates on solid surfaces.

Surface-adsorbed corroles feature multiple potential reactions upon thermal annealing. By employing the above mentioned technique in combinations with a novel advancement of applying DFT on calculating the angle-dependent NEXAFS features, the on-surface thermally induced chemical conversions have been unraveled and explained at the microscopic level. First, the as-deposited low temperature (200 K) phase was analysed (the molecules are still in the H_3TpFPC state). A single H_3TpFPC molecule adsorbs on Ag(111) with a near-to-planar macrocycle tilted approximately 20^o with respect to the surface plane, contrasting the typical saddle-shape of related porphyrinic species. The tilted adsorption geometries enabled the neighboured molecules to adsorb in a shingle-like conformations within arranged monolayers. The calculated C and N angle-dependent K-edges are in excellent agreement with the experiment allowing, thus, for a comprehensive decomposition of the overall spectra into contributions of chemically different atoms. The as-deposited phase is taken as a reference XAS spectrum for subsequent changes. Upon annealing to 330 K, an activation of a N-H bond from a pyrrole ring of H_3TpFPC is reported. Such dehydrogenation process yields a change of the related aminic/iminic XPS peak intensity ratio from 3:1 to 2:2, and generates a stable radical species exhibiting electron spin (magnetisation density) at specific intramolecular positions. Actually, the dehydrogenation step leads the overall adsorption geometry of single molecules almost unchanged. Nevertheless, the thermal annealing leads to considerable changes in the STM pattern now exhibiting a non-trivial monolayers. The dehydrogenation process provides a distinctive feature in the C K-edge NEXAFS spectrum and can serve as an indicator for the formation of the chemical-converted species. The calculated N K-edge NEXAFS went beyond the resolving power of other techniques and provided detailed information on the specific N-H termination (at which hydrogen release takes place).

A further thermal treatment at 430 K triggers a ring closure between one of the C_6F_5

side groups and the macrocycle. Such chemical transformation is accompanied with characteristic changes in the C 1s XPS signature, a flattening of the corrolic structure and a characteristic change of the molecular layer into a hexagonal arrangement. Whereas XPS is unable to unravel which of the six possible and energetically equivalent ring-closure reactions first occurs, NEXAFS spectroscopy strikingly enables the discrimination between the different ring-closure reactions. Upon further increase of annealing temperatures (above 430 K), further ring-closure reactions accompanied with more flattening of species were reported. However, since no experimental data are available to compare with, the question about the selectivity or non-selectively of further intramolecular reaction is still open. Remarkably, upon increasing the annealing temperature to 700 K, intermolecular reactions are enabled. This yielded a network-like structure of corroles, where their main character of the individual molecular species survive upon thermal treatment.

All-in-all, the present work provides a cornerstone for comprehensive characterisation of two-dimensional molecular architectures. It represents a detailed reference for further investigations in related or similar systems. The observed reactions provide a basis for novel synthesis protocols for corrole compounds hardly accessible with solution chemistry. Furthermore, the results of this thesis represent an important step forward in the context of on-surface synthesis. By exemplarily obtaining profound insight into the on-surface chemistry of free-base corrolic species adsorbed on a noble metal this work highlights how angle-dependent XAS combined with accurate theoretical modelling can serve for the investigation of on-surface reactions, whereby even highly similar molecular structures, such as tautomers and isomers, can be distinguished. This allows for an extension of the traditional use of NEXAFS measurements for obtaining moiety-specific adsorption geometries to the timely topic of on-surface synthesis. The capability to resolve closely related low-symmetry structures such as tautomers and isomers is specifically attractive for the investigation of larger molecular systems featuring the same moiety at multiple sites such as tetrapyrrolic systems or conjugated hydrocarbons and related derivatives.

For the future work, we are looking forward to explain the metastable states of PTCDA on KCl(100) (see Appendix A.3), to have better understanding about the so-called metal/insulator/organic interfaces (see Appendix A.6) and to further investigate if a single $H_2TpFPC^{\bullet}$ could behave as a nanomechanical resonator (see Appendix A.12). Remarkably, we have some indications about the role of the spin density to initiate *site-selective* chemical interactions (see Appendix A.16). Such observation could be supported by investigating other systems which undergo site-selective chemical transformations and identify the role of spin density in such process. It is also planned to extend the employed computational approach to other corrole interfaces and the related on-surface chemistry, whereby specifically metalated derivatives are highly attractive for functional architectures. The further investigations of artificial two-dimensional molecular architectures (see section 4.3.5.2) are of great interest. The resulting π-conjugated systems might have a great impact on various fields of timely research, e.g., alternative energy sources, energy storage devices as well as systems for water splitting and CO_2 reduction.

A Supplementary Information

A.1 Saw-tooth model to model the step edges

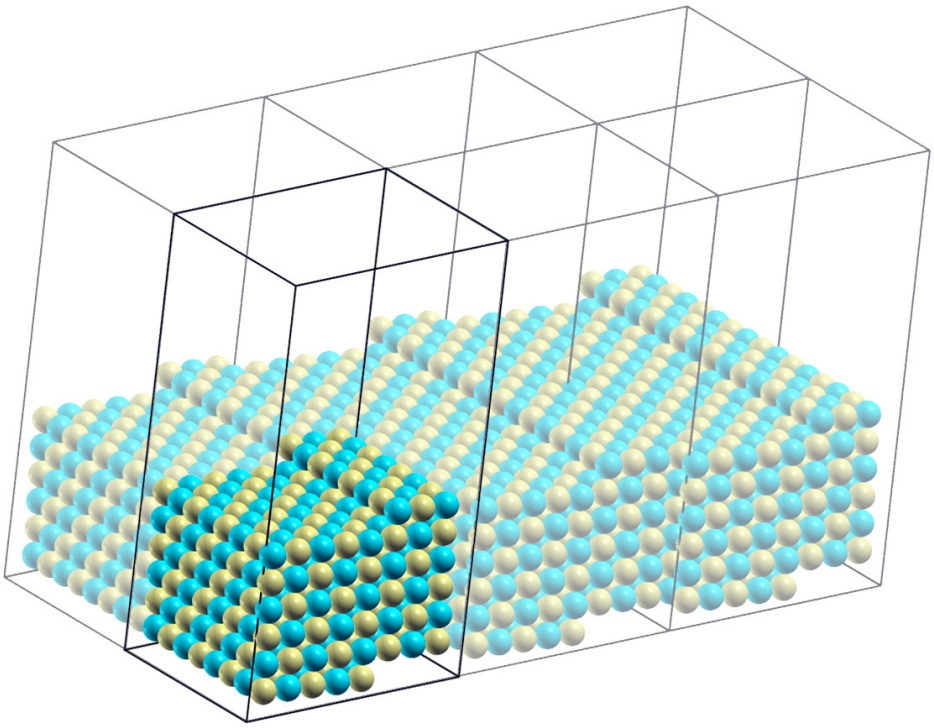

Figure A.1: A 3 × 2 representation of the so-called saw-tooth model, which is used to model the step edges of KCl and NaCl(100) in periodic supercells. As an example, the defect-free non-polar step edge has been shown. The supercell is shown slightly darker than its periodic images.

A.2 KCl and NaCl properties

A necessary step before investigating the adsorbed system is to optimise the KCl and NaCl bulk parameters and to generate the KCl and NaCl(100) surfaces. Using the previously mentioned DFT-D approximation [61, 62], the calculations predict the bulk lattice constants of KCl and NaCl within an error bar less than 1%. The calculated lattice constants

Reference	Δ_1	Δ_2	Δ_3	d_1	d_2	d_3
Experiment						
Ref. [228]	0.03(5)	-0.01(2)	-0.01(4)	3.14(3)	3.15(3)	3.14(4)
Theory						
Ref. [17]	0.03	-0.01	0.00	3.07	3.13	3.11
Ref. [18]	-0.06	0.03	-0.01	3.10	3.13	3.12
This work	0.03	-0.01	0.00	3.13	3.12	3.13
Experiment						
Ref. [228]	0.07(3)	-0.01(4)	-0.00(3)	2.76(2)	2.80(3)	2.81(5)
Theory						
Ref. [17]	0.09	-0.05	0.02	2.72	2.84	2.78
Ref. [18]	0.04	-0.02	0.01	2.78	2.80	2.80
This work	0.06	-0.01	0.00	2.81	2.79	2.79

Table A.1: Relaxation of the ions in the topmost three layers of the (100) surfaces of KCl (top part of the table) and NaCl (bottom part) compared with experimental findings and previous calculations. The quantity Δ_i expresses the shift of the ions in the *ith* layer, and d_i expresses the distance between layers numbered i and i+1. Values in [Å].

are 6.25 Å for KCl (Experiment: 6.29 Å [229], 6.24 Å [230]) and 5.6 Å (Experiment: 5.60 Å [229], 5.595 Å [230], 5.63 Å [231]) for NaCl.

The (100) surfaces of both KCl and NaCl consist of alternating cation-anion pairs in almost coplanar arrangement. In particular, the topmost two layers of this surface are slightly displaced from the coplanar layer [228, 172, 17, 18]. The calculations confirm this effect: The surface anions in the first layer are displaced upwards by 0.03 Å (KCl) and 0.06 Å (NaCl), and the surface cations are displaced by the same amount downwards. The second layer exhibits a smaller relaxation than the first one, but in the opposite direction for the surface cations and anions. Using the description of the surface rumpling, employed by Vogt et *al.* in Ref. [228], where a positive rumpling means an outward movement of the anion, a negative value a inward movement, the calculated results are summed up in the top (bottom) part of Table A.1 for the (100) surfaces of KCl (NaCl).

A.3 Metastable states of PTCDA on KCl(100)

In his work, Alexander Paulheim observed that the fluorescence (FL) spectra of PTCDA on KCl(100) depends on the substrate temperature (T) (see his thesis, University of Bonn, 2018). For T > 20 K, he had previously found that the spectrum exhibits a single 0-0 peak at 19995 cm^{-1}. This state has been assigned to the known stable structure presented in section 3.2.4 (this state will be denoted here as TS3, see Figure A.2). However, for T < 20 K, he observed two additional peaks in the fluorescence (FL) spectra which are Blue-shifted with respect to TS3 by +17 cm^{-1} and +30 cm^{-1}. Upon increasing the temperature, the

intensities of the additional peaks gradually decrease on the expense of that corresponds to TS3. At T > 20 K, both peaks completely disappear. From the already published results [171, 158], it can be discarded that the molecules can be diffused to the step edges at these temperatures. They are rather states where the molecule still adsorb at terraces sites. Thus, we label them as TS1 and TS2 (TS: from terrace site).

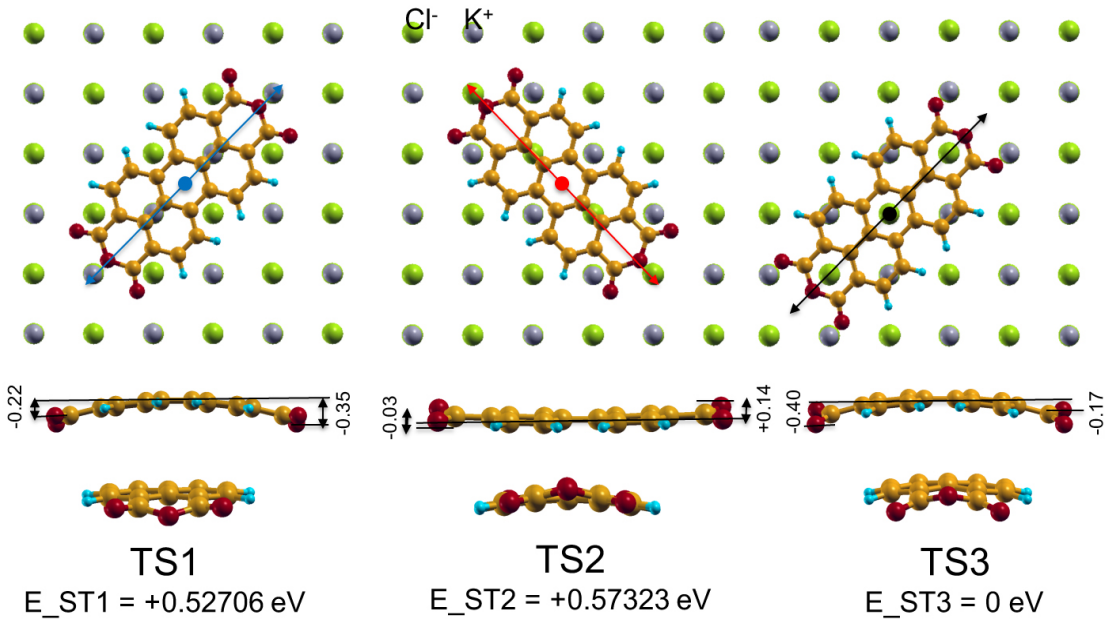

Figure A.2: (left) and (middle) Assumed structures corresponding to the so-called precursor states (TS1 and TS2). (right) The stable structure (TS3) shown for comparison. The upper parts of all Figures show top-views of the adsorbed molecule. The lower parts show two side-views of each structure. The azimuthal orientations are similar for all states. However, the registries are different yielding different geometries. The (+)/(-) signs indicate the upwards/downwards movements of the oxygen atoms with respect to the backbone of the molecule. The adsorption energy of TS3 is considered as a reference (in eV).

In our so far crude understanding, the observed two peaks can be corresponded to two terraces states which are stable at very low temperatures but unstable upon slightly increasing the temperature. Therefore, these two state can be tentatively denoted as meta stable states. In principle, it would be conceivable to suppose that molecules which are evaporated at low temperatures, where the thermal energy is very low, might adapt two different azimuthal orientations different from TS3. However, Paulheim et *al.* showed that the polarisation dependance of all peaks (TS1, TS2 and TS3) is the same. Thus, it can be anticipated that PTCDA in these two states is azimuthally oriented with its long-axis parallel to one of the $<1\bar{1}0>$ orientations of the surface.

Question. What is the nature of such two states and can we find a potential energy hypersurface that exhibits beside TS3 two meta-stable states correspond to TS1 and TS2? The barrier for crossing into TS3 needs to be compatible with T ≈ 20 K, i.e., in the order

of 25.$\frac{20K}{300K}$ ∼1-2 meV.

Primary results. Paulheim *al.* denoted this meta stable states as precursor states, whereby it is assumed that the adsorption of the molecule from the planar to the final state TS3 takes place in two steps: (planar geometries → precursor state) then (precursor state → final state). For the geometries of the suggested precursor state, it is assumed that during the adsorption process, oxygen atoms might first "down" on one side of the molecular axis, while atoms on the other side still be in the undistorted, planar configuration. The latter intermediate state might be stable at very low temperatures (< 20 K), but can be crossed under thermal effects at temperatures (T > 20 K). Indeed, A. Paulheim et *al.* supposed that symmetric or asymmetric partial torsions take place for the precursor state and, thus, one can correspond one to TS1 and the other to TS2.

Unfortunately, the DFT-calculations discard these possibilities. All structures which start from such or similar geometries have been converged to TS3 with no indications to other stable states. Moreover, for all tested cases, which start from geometries where the centre of the molecule residing on an anion and its long-axis along an <1$\bar{1}$0> orientation, the structures continue converging towards TS3 with no indications for any other local minima (except TS3). Based on these calculations, one could think of other scenarios to explain the presence of TS1 and TS2. In the following, two possibilities are shortly presented.

(i) The peaks in the FL spectrum might results from structures where the molecular axes are parallel to a <1$\bar{1}$0> direction of the surface but with their centres not directly above an anions (e.g., the left and middle structures in Figure A.2). Indeed, the calculations show that these structures are stable even when all atoms are left to freely relax in all directions. The geometries of these structures are completely different from TS3 (see Figure A.2 for comparison) and they are less stable by +0.52 and +0.57 eV, respectively. To rationalise such possibility, one assumes that upon the molecular adsorption at very low temperature, the molecules have a chance to statically distribute on all sites of the surface. They have, then, a chance to stick at some local energy minima as long as some barriers exist (they should be few meV in this case) to prevent the molecule cross to TS3 at a given temperature. Upon increasing the temperature, the molecules receive an activation energy enabling them to cross the barriers to reach the global minimum. At the moment, the calculations still yield no barriers (0 eV) upon crossing from both assumed states to TS3 (see Figure 3.13). However, this point is still under debate and should be better explained.

(ii) Another possibility is to suppose that an extra adatoms (a cation) exists on the surface at low temperature. Such adatoms might exist underneath the molecule at given positions effecting, thus, its geometries and resulting into the states TS1 and TS2. Upon increasing the temperature, one could imagine that these adatoms diffuse to the step edges leaving the molecule in its geometries corresponding to TS3.

To confirm these assumption, to determine the exact molecular bending and geometry and to be able to assign the adsorption complexes to the respective optical signals, further calculations are necessary. This work is in process.

A.4 PTCDA/KCl(100) on Ag(100)

Figure A.3 shows a structural model of PTCDA adsorbed on bilayer KCl film on Ag(100) in most stable structure. The calculations show that the inclusion of Ag(100) beneath the bilayer KCl film results into a considerable change of the lateral diffusion barriers. The epitaxy of KCl(100) on Ag(100) has been modelled starting from a previously published work (see Ref. [168]).

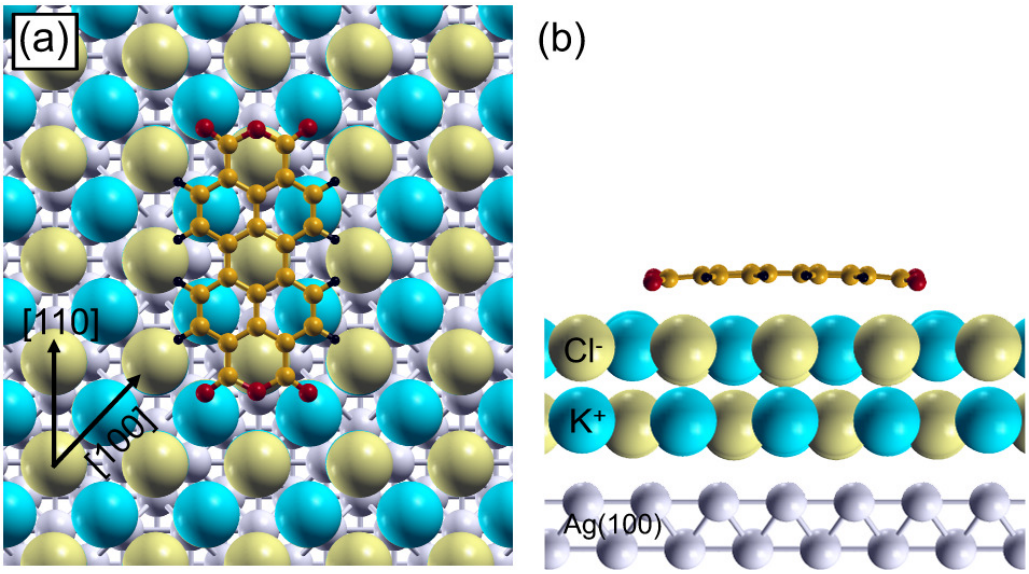

Figure A.3: (a) Top view and (b) side view of PTCDA on two layers of KCl on top of an Ag(100) substrate in the SQ structure (see 3.2.4.1). The structural configuration of this structure has been modelled as described in ref [168].

A.5 Change of diffusion barriers: PTCDA on KCl(100)

Figure A.4 shows how the diffusion barriers of PTCDA on KCl(100) could be changed if any compression/expansion of the KCl lattice constant could happen. A possible reason for such effect might be the mismatch between the lattice constants of the ionic surface and that of the underlying metal surface (here Ag(100)). If this effect could exist, the diffusion barriers should be reduced/increased by compression/expansion of the KCl lattice constant.

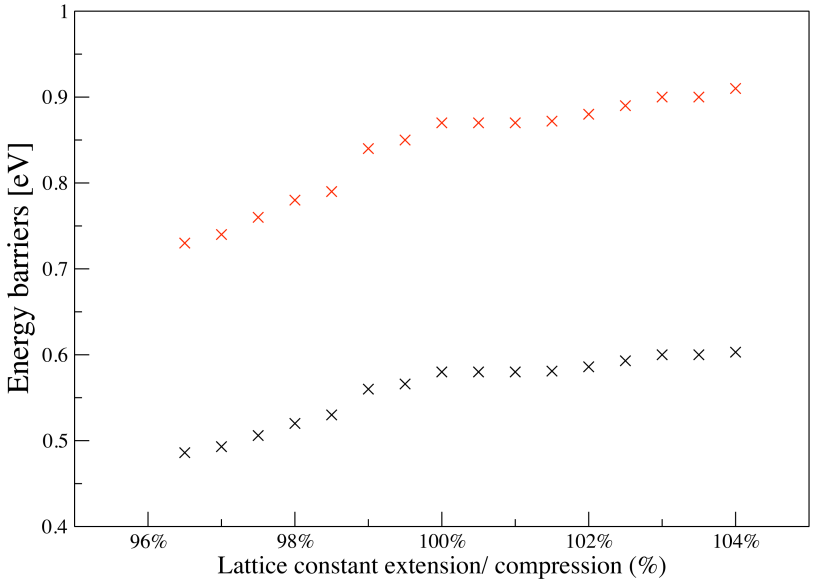

Figure A.4: Changes of the surface maximum corrugation (red points) and the diffusion barriers (black points) of PTCDA on KCl(100) upon the expansion/compression of the lattice constant of KCl(100) film.

A.6 Metal/Insulator/Organic interfaces

In section 3.2.4.3, it has been mentioned that the existence of metallic layers beneath thin, insulating layers of KCl modifies the diffusion barriers of PTCDA molecules. Nevertheless, the calculations there were just introduced in order to *qualitatively* confirm the change of the diffusion barriers. Thereby PTCDA is simply tested in few structures on two layers of KCl(100) constructed on Ag(100) without any further physical considerations of such particular system. However, it was explicitly mentioned that the detailed investigations of the metal/insulator/organic interface is out of the scope of the present work.

Upon a direct adsorption of an organic molecule on a metallic surface, it is well tabulated within the literature that the transferred charge density is distributed over *all* molecules causing each of them to be partially charged [232, 233]. Similar conclusions supporting the delocalised charge distribution fashion have been widely confirmed by DFT-based calculations employing different exchange-correlation (xc) functionals (either semi-local or hybrid functionals) [234, 235, 236, 237, 238, 239, 240]. However, this is not the case when a thin layer of isolator, e.g. two layers of NaCl or KCl, is introduced between the organic and the metal interfaces. The mechanism of the charge transfer in the organic/isolator/metal interface is still unclear and under debate. Two paradoxical scenarios are suggested within the literature. The first one supports the aforementioned fractional charge transfer causing each molecule to be partially charged (see the work of Michael G. Ramsey, University of

Graz). However, a second scenario suggests that some molecules are integer charged, while others remain neutral (see Ref. [241, 242, 243]). According to Hofmann et *al.* [244], DFT-based calculations which employ semi-local functionals, e.g. PBE, tend to underestimate the total energy at fractional electron numbers. Thus, they fail to interpret the latter effect because they tend to artificially overdelocalise electrons, causing unphysical distribution of the charges (such behaviour in the GGA functional class is known as many-electron self-interaction error [245]). However, employing a hybrid exchange-correlation functional with sufficiently fraction of Hartree-Fock (HF) exchange is able to capture this effect because the HF is free of the self-interaction error.

The detailed understanding of this interface in PTCDA/thin KCL(100)/Ag(100) is still an open question and could be studied starting from the already existing structures. Thereby, one should take care of the things missing in the calculations presented in 3.2.4.3, namely the employed functionals and the induced dipoles. Besides, we need XPS measurements which compare the C and O 1s edges of the following two systems: (1) A reference system of PTCDA on enough thick (more than 10 layers) KCl(100) on Ag(100), where the enough thickness of the isolator prevents the metallic states from overlapping with those of the adsorbed molecules, and (2) a system of PTCDA on thin film (no more than 2 layers) of KCl(100) on Ag(100). If the charge transfer in system (2) induces a mixture of charged and neutral species, it should be reflected in the XPS spectra resulting into an appearance of further peaks shifted possibly in a range of 1 eV compared to system (1).

A.7 Eroded KCl step edges upon molecular adsorption

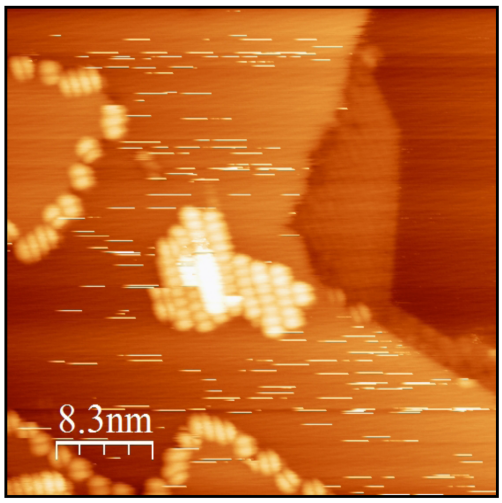

Figure A.5: A 41.7 nm × 41.7 nm STM image exhibiting the eroded <100> step edge of KCl upon adsorption of further PTCDA at step sites (U_{bias} = -3 V, I = 58 pA).

A.8 Structure of H_3TpFPC corrole in crystalline phase

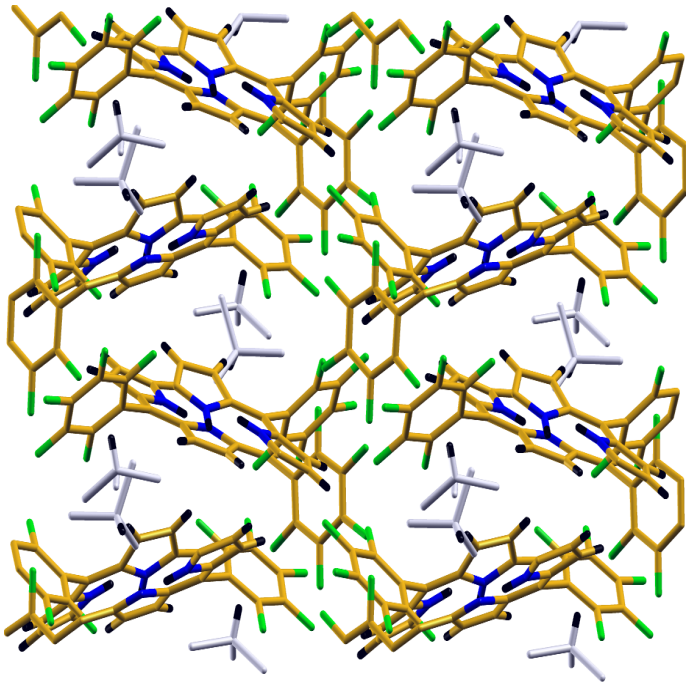

Figure A.6: This monoclin structure (a =14.816 Å, b =10.282 Å, c =14.887 Å; β=118.435°) with two corroles and 4 $CHCl_3$ molecules in the unit cell). Coordinates according to Ref. [204], where also further details of the structure are available.

A.9 Influence of including the Ag(111) surface within the XAS calculations

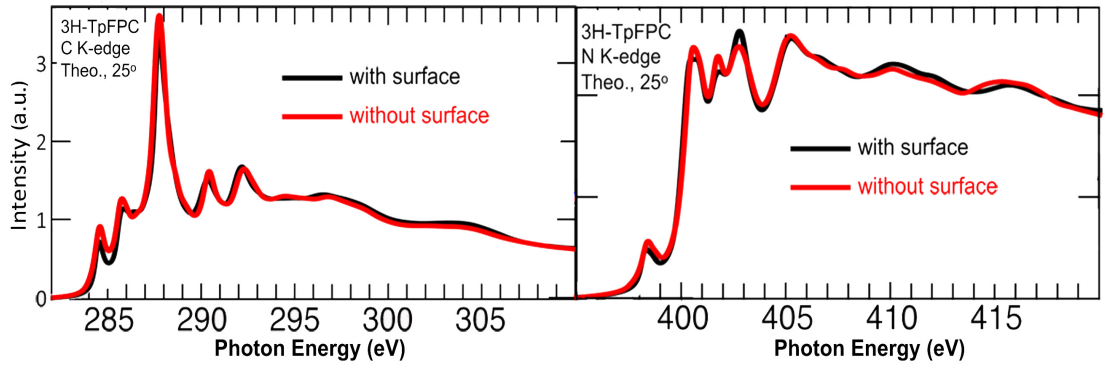

Figure A.7: (left) Calculated NEXAFS C and (right) N K-edge of H_3TpFPC (shown for $\theta = 25°$) with and without including the surface in the XAS calculations.

A.10 Influence of rotating the phenyl ring fashion

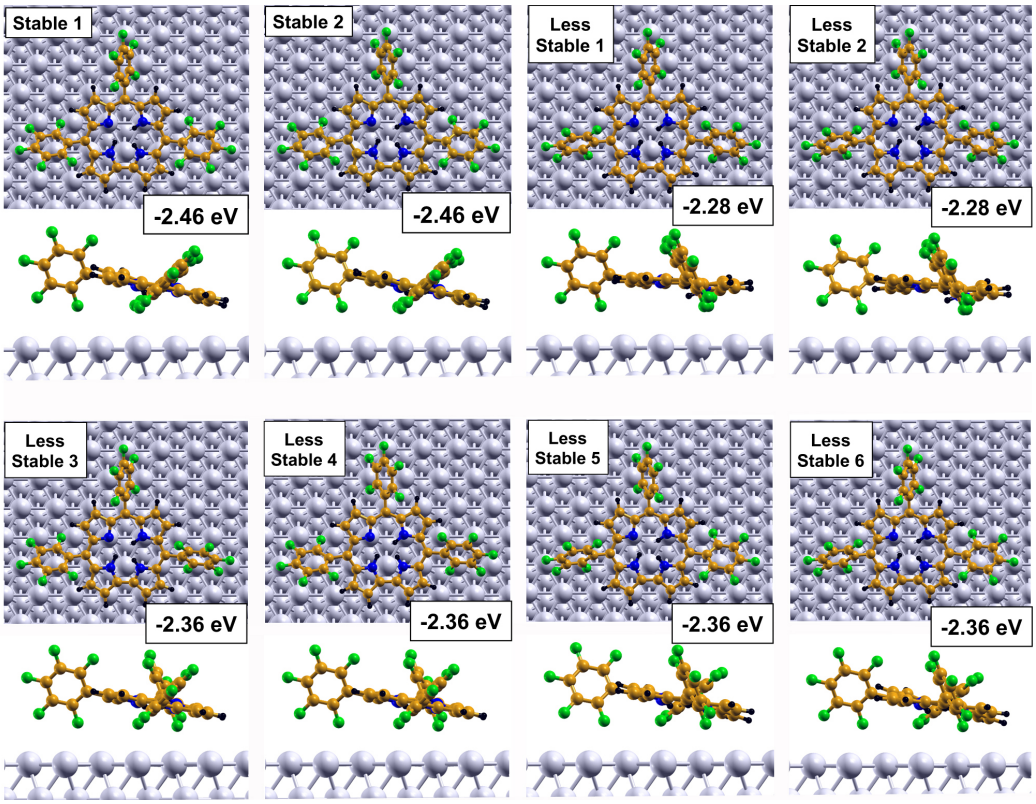

Figure A.8: Top-views and side-views of the possible 8 structures of single H_3TpFPC on Ag(111) which are similar in their orientation and registries with respect to the underlaying surface, but different from each other in the orientation of the phenyl rings clock-/counterclockwise. The respective adsorption energies are also depicted.

A.11 NEXAFS H_2TpFPC$^\bullet$

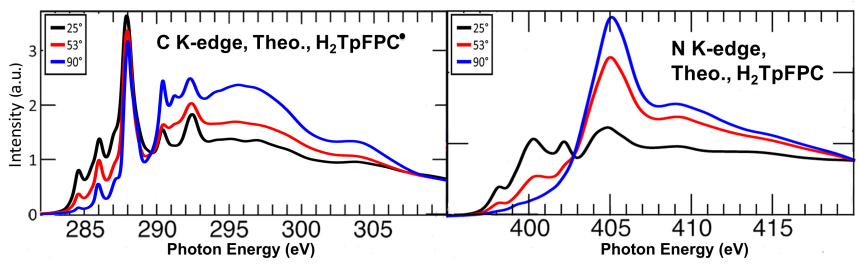

Figure A.9: (left) Calculated NEXAFS C and (right) N K-edge spectra of DFT-optimised monolayer of H_2TpFPC$^\bullet$ geometries, performed for the incident angles for 25°, 53° and 90°.

A.12 Corroles as a Nanomechanical Resonator

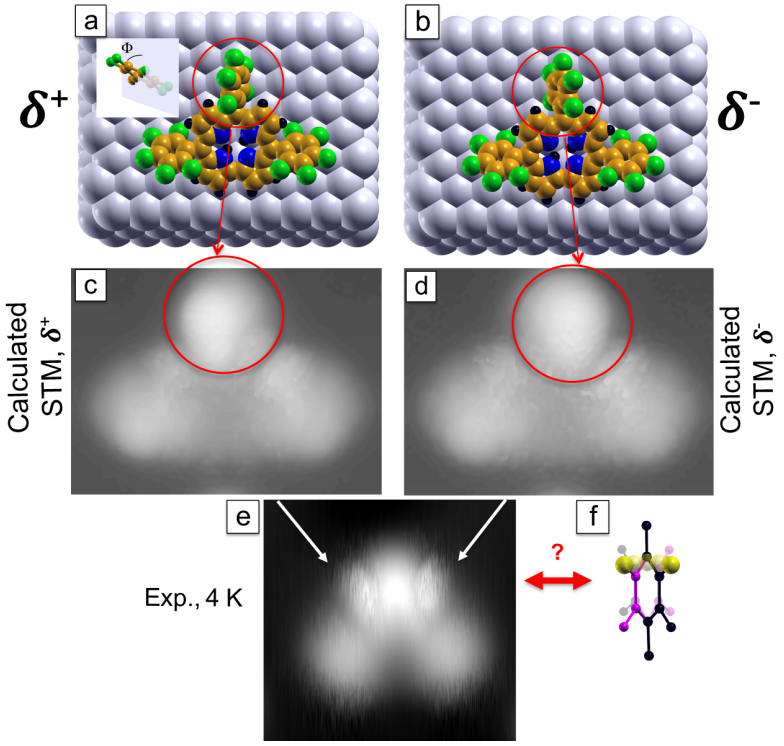

Figure A.10: The most two stable structures of H_2TpFPC$^\bullet$ on Ag(111) are denoted as (a) δ^+ and (b) δ^-. The structures are different only in the orientation of the phenyl ring in the meso position 10. This is reflected in the corresponding STM images (c) and (d), respectively. (e) Measured STM image for a single corrole manipulated from the monolayer. The latter is realised by depositing H_3TpFPC on Ag(111) at RT and further annealing to 360 K. Thus the structure corresponds to the so-called H_2TpFPC$^\bullet$. The measurement of the STM is done at T = 4K. (f) Imagined representation of the vibration of the central phenyl ring of H_2TpFPC$^\bullet$ between the two stable phases δ^+ and δ^- (coloured in purple and black). The top-most Fluorine atom, which is the centre of the bright lobe is coloured in yellow.

Motivation. In section 4.3.2 it was mentioned that H_3TpFPC adsorbs on Ag(111) in its most stable structure in two structures which are similar in their registries and orientations with respect to Ag(111) but different in the rotation fashion of the phenyl ring in the meso-position 10 (Phy). Apparently, the same holds also for H_2TpFPC$^\bullet$ (see Figure A.10 a, b). We denote these structures as δ^-/ δ^+ according to the rotation of Phy clockwise/ anticlockwise around the carbon in meso position, respectively. For both H_3TpFPC and H_2TpFPC$^\bullet$, it has been shown that Phy is tilted with about 65° with respect to the underlaying surface (i.e., by 25° with respect to a plane perpendicular to the surface (Φ), see the upper part of Figure A.10 a). Like that, it can be considered that Φ = +25° in case of structure δ^+ and -25° in case of structure δ^-. The calculated STM images of these two structures are similar in terms that they exhibit the characteristic three lobes known

for these corrole species. However, the centre of the brightest lobe is shifted to the left or to the right of an imaginary line bisects the molecule in δ^+ and δ^-, respectively (see Figure A.10 c, d). In comparison, the measured STM image of H_2TpFPC$^\bullet$ (Figure A.10 e), which is measured at T = 4 K, exhibits two wings on the right and left sides of the central lobe, marked be two white arrows (see Figure A.10 e).

Question. Is it possible that Phy undergoes a (periodic) oscillatory motion between δ^+ and δ^- with a particular frequency ω at T = 4 K (Figure A.10 f)? This vibration should be thermally activated and might be realised as a result of the titled molecular geometries and the weak vdW-interaction with the surface. However, the existing barriers to be crossed should not exceed few meV.

The importance of such system that it might represent a nanomechanical resonator similar to that shown in Ref. [246], but with dimensions smaller by two orders: The nanomechanical resonator system presented in ref. [246] based on one-dimensional chains with a length of 3 to 12 monomers, while the diameter of Phy is less than 3 Å.

The primary total energy calculations done by rotating Phy between δ^+ and δ^- for each 5° show that an energy barrier of 10 meV (25 meV) is required to allow H_2TpFPC$^\bullet$ (H_3TpFPC) to cross between its two stable states. The saddle points of these barriers exist for $\Phi = 0°$. Despite the calculated barries are in orders of meVs, they are still high compared to the surface temperature (4 K).

To continue such work, combined theoretical and experimental investigations are required. In particular, radiofrequency scanning tunnelling microscopy (rf-STM) are needed to confirm the vibration of the system at such and elevated temperatures (see Ref. [246] for further details). In parallel, the calculations should further include the influence of an electric field to take into account the effect of the STM-tip (see Ref. [247]), which might increases the vertical adsorption distance and, thus, a decrease of the barriers.

A.13 The concept of surface Kondo effect

The Kondo effect describes the unusual behaviour of the electric resistivity of conducting materials with magnetic impurities upon decreasing the temperature below a given value [248, 249]. The effect was first explained as a structural defects of the material. However, its observation only in materials with magnetic impurities [250], allowed for suggesting the magnetic origin of such phenomenon [251]. In early 1960s, Jun Kondo explained the effect theoretically, where he showed that the conduction electrons are scattered by localised magnetic electrons and the scattering rate should diverge as the temperature approaches 0 K causing the change of the resistivity. Later, it was explained that the interaction between the electronic states of the magnetic impurity and the conduction bands creates virtual bond states close to the Fermi level and known as Kondo resonance. Nowadays, the experimental detection of the surface Kondo resonances provides a direct evidence of the magnetic property of the investigated system. For the case of radical molecules adsorbed

on a metallic surface (like the studied here, namely H_2TpFPC$^\bullet$ or H_2TpFPC$^\bullet$(rc) on Ag(111)), the unpaired spin electrons behave as a magnetic impurity and the Kondo effect arises from the dispersion of the conducting electrons of the surface by such impurities.

In principle, the virtual states originating the surface Kondo resonance should have a Lorentzian distribution. However, by measurement with STS the Kondo resonance has a particular lineshape called the Fano lineshape [252, 253]. The shape of the Kondo resonance is influenced by many effects. Typically, the interaction with other impurities [254] and the existence of an electric field [255] cause shift or splitting of the feature, the increased temperature causes a broadening [256], while the charge transfer causes a shift (few meV) of the Kondo resonance peak due to particle-hole asymmetry [257].

Experimentally, the identification of the Kondo resonance by STS requires four criteria which should fulfilled: *(i)* The resonance peak is centred at 0 eV (few meV shift are explained with the particle-hole asymmetry argument). *(ii)* The fit with the Fano curve is consistent. *(iii)* The temperature-induced broadening of the Kondo peak is reproduced. *(iv)* An external B-field causes a split of the peak.

A.14 Dehydrogenation ratios in films of different thicknesses

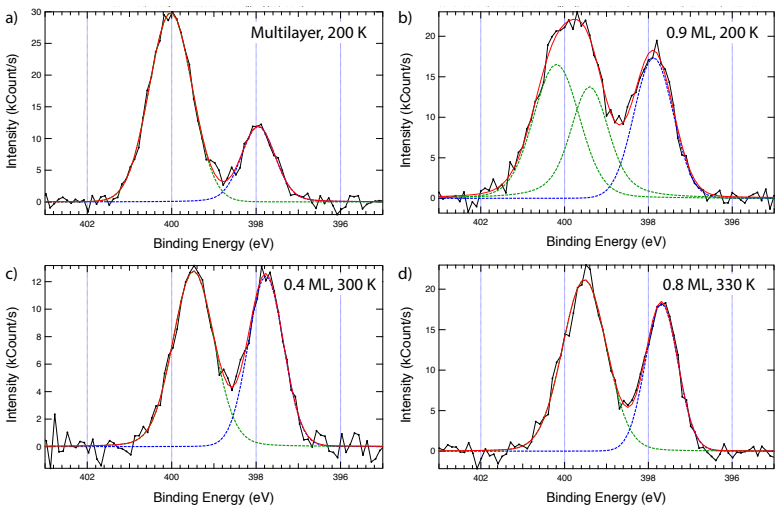

Figure A.11: XPS N 1s signature of TpFPC thin films on Ag(111). a) Spectrum of a multilayer film grown and recorded at 200 K. The N-H (green) to N= (blue) intensity ratio is 75:25 indicating that intact H_3TpFPC molecules are deposited onto the metal surface generating a chemically pure film in those layers not in contact with the substrate. b) The spectrum of the as-deposited low-temperature phase (200 K). c) The spectrum of the sample utilised for the C K-edge investigation of the H_2TpFPC$^\bullet$ phase (see Figure 4.21).The N-H/N= ratio of 44:56 indicates that the dehydrogenation reaction has occurred for 89% of the molecules. d) The spectrum of the sample utilised for the N K-edge investigation of the H_2TpFPC$^\bullet$ phase (see Figures 4.22). The N-H/N= ratio of 38:62 indicates that the dehydrogenation reaction has occurred for 76% of the molecules.

A.15 Multiple ring-closure reactions: Experimental XP spectra

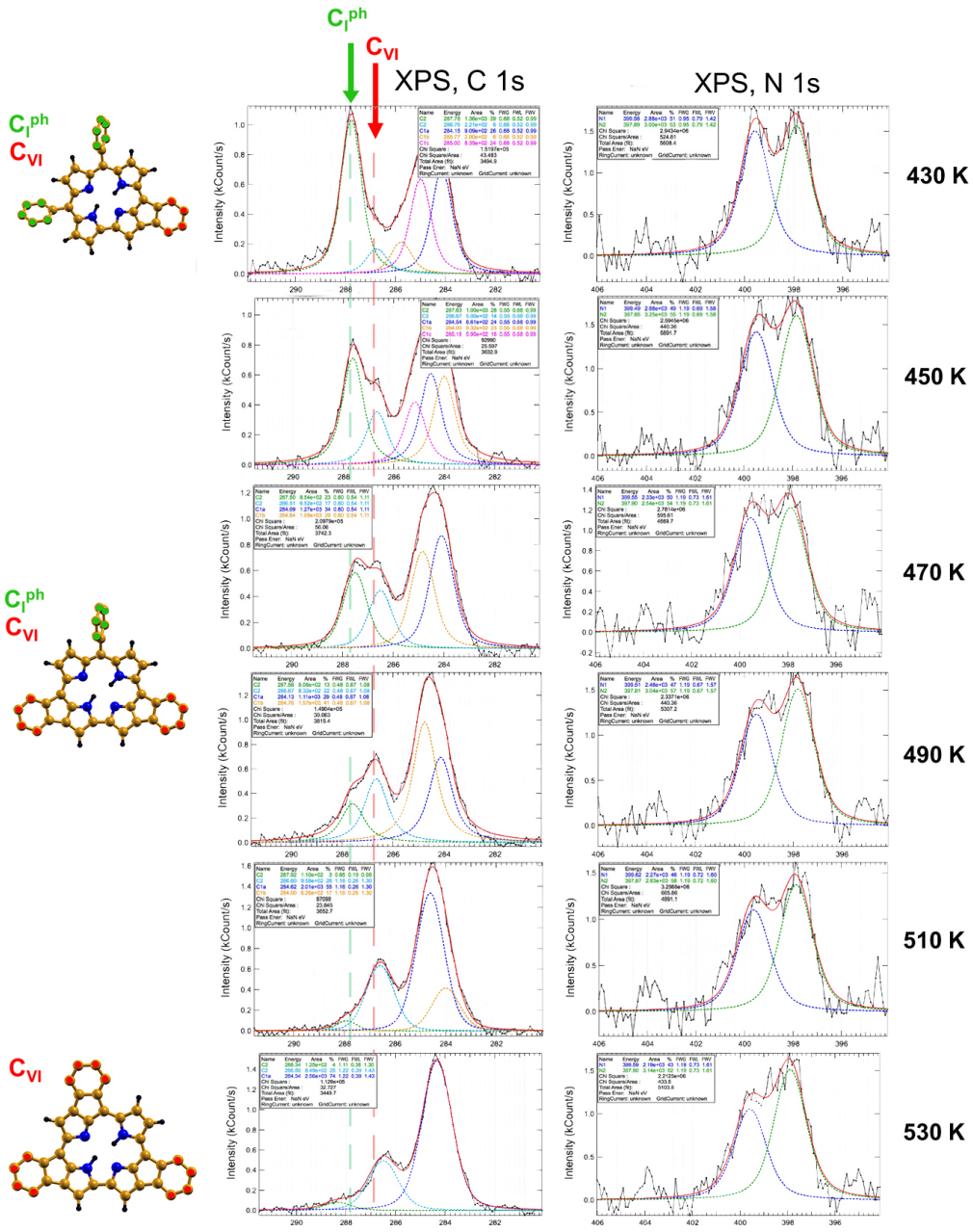

Figure A.12: Experimental XPS C and N K-edges of a H_3TpFPC adsorbed on Ag(111) at 200 K and annealed to 430, 450, 470, 490, 510 and 530 K, respectively. On the left side, the suggested models for single and multiple ring closure reactions are depicted. The green dashed line / the red dashed line is corresponded to the carbon atoms which have not undergone / have undergone the ring closure reaction.

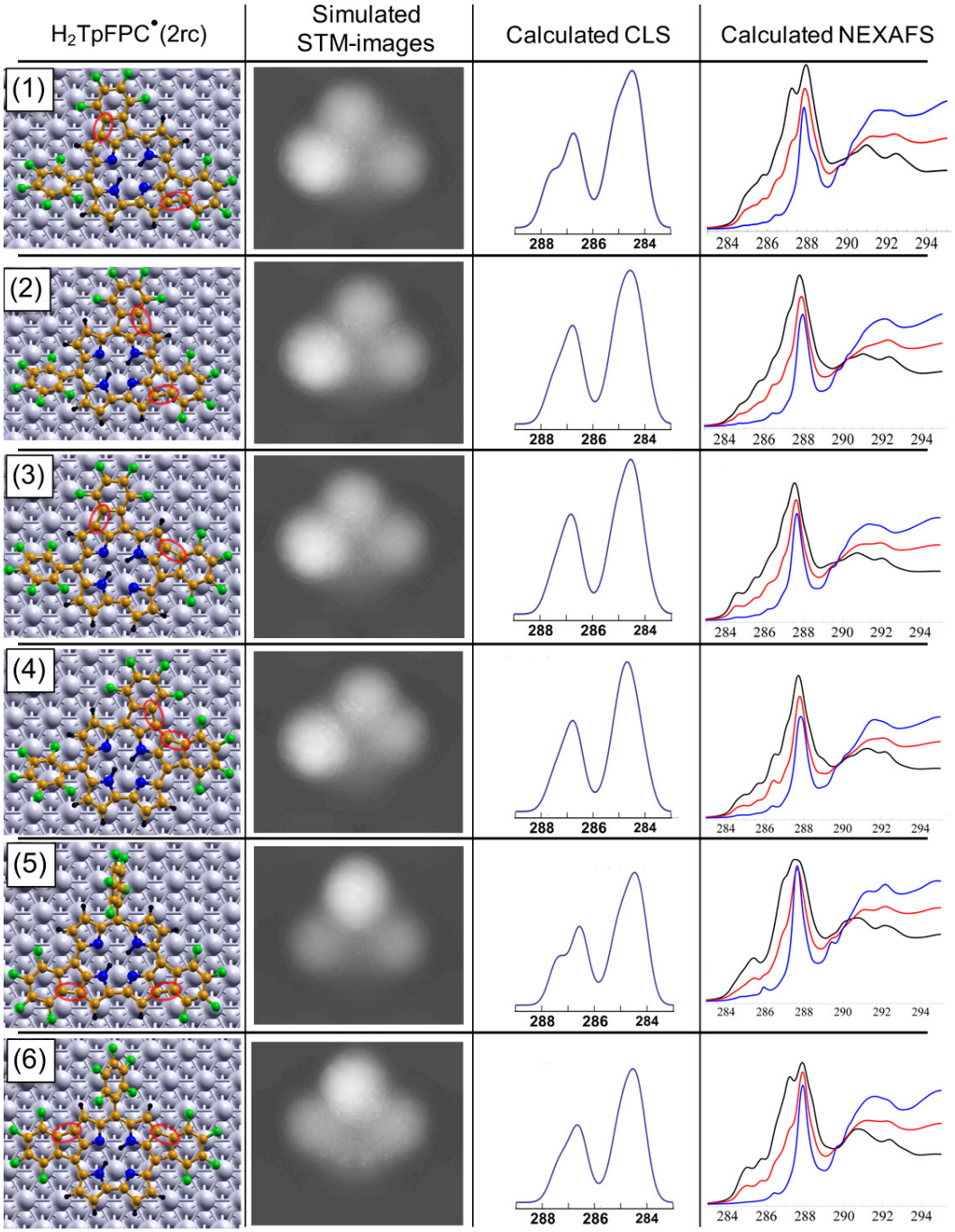

Figure A.13: Calculated six (out of 12) possible structures of H_2TpFPC$^\bullet$(2rc) tautomers labelled from 1 to 6 (see also Figure A.14). The red ovals indicate the sites of the ring closure interaction within the structure. The corresponding calculated STM-images (second column), CLS (third column) and NEXAFS signals (fourth column) for incident angles of $\theta = 25$, 53 and 90° have been shown.

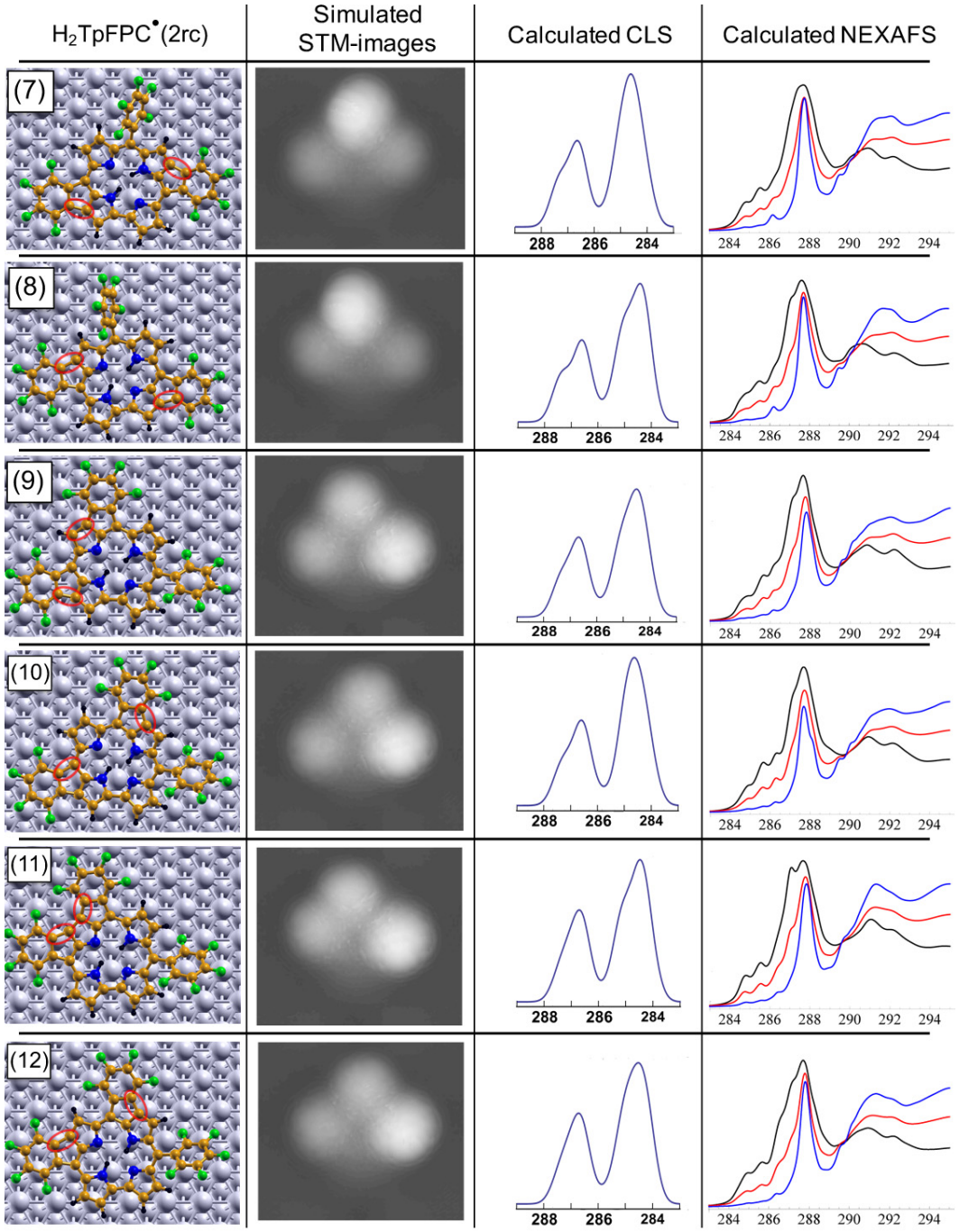

Figure A.14: Calculated six possible structures of H_2TpFPC$^{\bullet}$(2rc) tautomers labelled from 7 to 12 (see also Figure A.13).

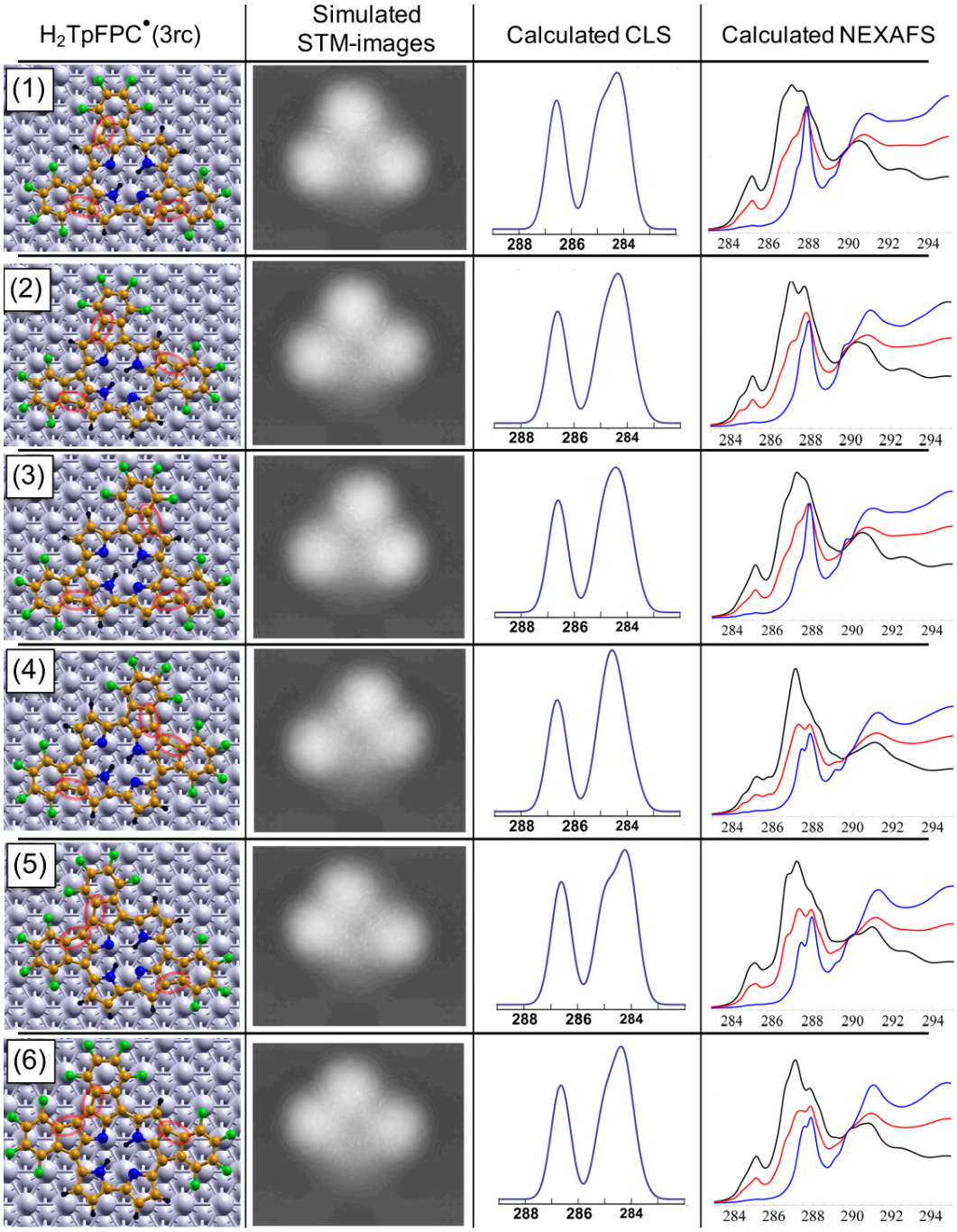

Figure A.15: Calculated six (out of 8) possible structures of H_2TpFPC$^\bullet$(3rc) tautomers labelled from 1 to 6 (see also Figure A.16). The red ovals indicate the sites of the ring closure interaction within the structure. The corresponding calculated STM-images (second column), CLS (third column) and NEXAFS signals (fourth column) for incident angles of $\theta = 25$, 53 and 90° have been shown.

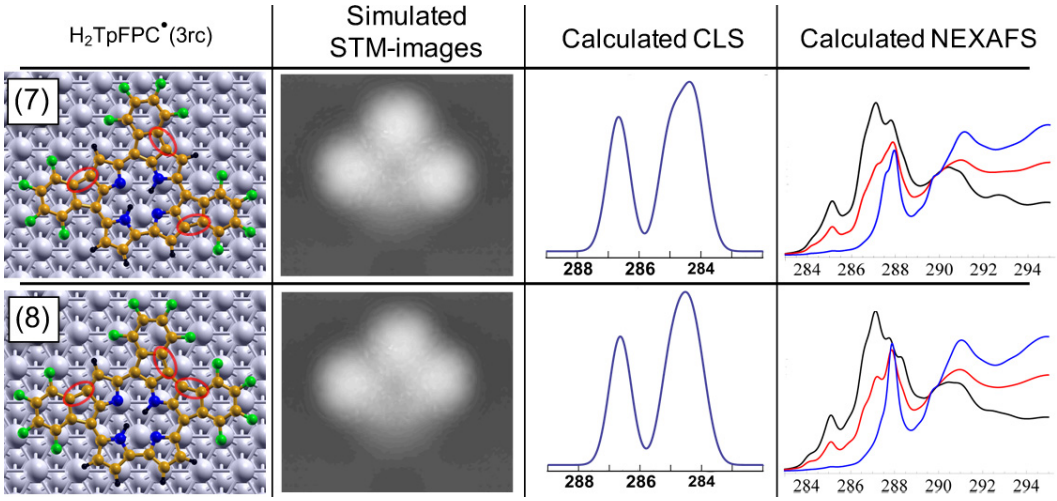

Figure A.16: Calculated 2 (out of 8) possible structures of H_2TpFPC$^\bullet$(3rc) tautomers labelled as 7 and 8 (see also Figure A.15).

A.16 Role of Spin density to initiate Cyclisation Reactions

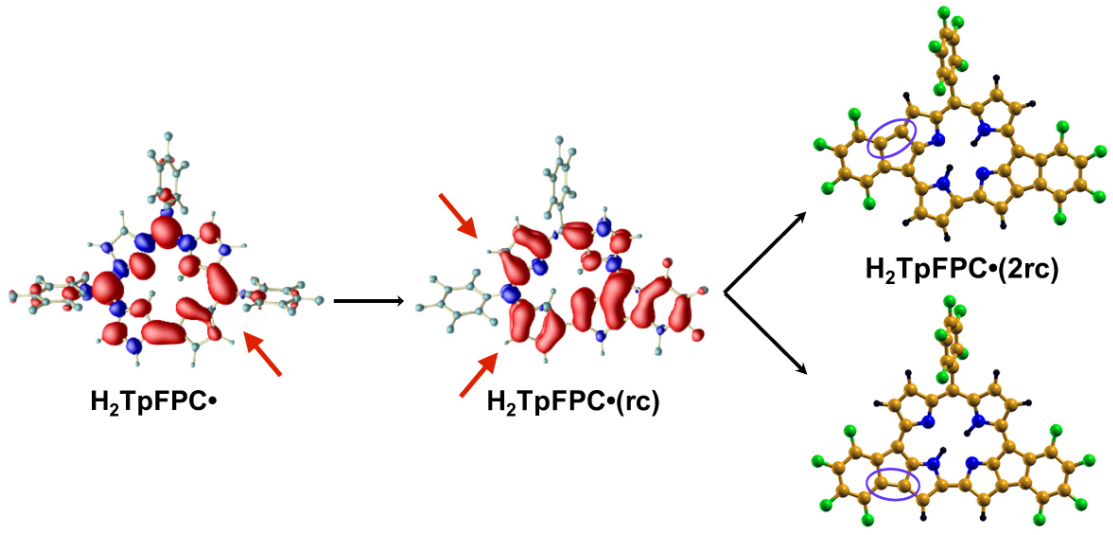

Figure A.17: Representation of the H_2TpFPC$^\bullet$, H_2TpFPC$^\bullet$(rc) and two tautomers of H_2TpFPC$^\bullet$(2rc). DFT-calculated distribution of the unpaired electron spin density $m = n_\uparrow(\vec{r}) - n_\downarrow(\vec{r})$, where m > 0 (m < 0) is plotted in red (blue), given for the first two species. The red arrows are guides to the eye indicating the position of the unpaired spin density. The latter is spatially distributed in the lower-right part of H_2TpFPC$^\bullet$ but in the lower and upper left-side parts of H_2TpFPC$^\bullet$(rc). The purple ovals indicate the C-C bond as a result of the second ring closure reaction.

It has been mentioned in sections 4.3.4 and 4.3.5 that the first on-surface ring closure reaction of free base corroles on Ag(111) upon thermal annealing is probably selective, resulting into highly ordered hexagonal structures, while the second is probably not selective resulting into disordered phases. Here, one should ask what is the reason behind such contradictive behaviours. We assume a role of the distribution of the spin density to initiate the aforementioned reactions. Figure A.17 (left) shows the spin density distribution in $H_2TpFPC^{\bullet}$. Apparently, the unpaired spin density is localised in the lower-right part of the molecule where the selective ring-closure reaction takes place in the subsequent species, namely $H_2TpFPC^{\bullet}$(rc). However, after the first ring closure reaction, the spin density is changed and the unpaired spin density is, now, equally localised in the lower and upper left-side parts of $H_2TpFPC^{\bullet}$(rc) exactly in the sites where the second ring-closure reactions should take place. Both observations indicate the aforementioned role of the spin density to initiate the interaction. However, such assumptions need further experimental and theoretical investigations as already mentioned in 4.3.5.

B Experimental methods

DIP on Cu(111)

The experiments presented here are related to section 3.1 and were done in the group of C. Ocal from the Instituto de Ciencia de Materiales de Barcelona (ICMAB-CSIC). The measurements were carried out at room temperature using a commercial STM/nc-AFM (Specs GmbH) in ultra high vacuum (UHV), base pressure of about 5×10^{-10} mbar. A KolibriSensor was used to perform simultaneous STM and non-contact atomic force microscopy (AFM) in the frequency modulation mode. The metallic tip, with resonant frequency $f_0 \approx 1$ MHz, was operated at an oscillation amplitude A = 200 pm after being in situ cleaned by Ar^+ sputtering. The Cu(111) single crystal (MatekGmbH, Germany), was prepared by repeated cycles of Ar^+ sputtering plus annealing at 240 °C. Diindenoperylene was evaporated from a Knudsen cell at 225 °C at a rate of 0.05 ML min^{-1}.

PTCDA on KCl and NaCl

These measurements, which are related to section 3.2, were performed in the group of M. Sokolowski from the university of Bonn. The experiments have been performed under ultrahigh vacuum in a two chamber apparatus. The base pressure was 2×10^{-10} mbar. One chamber was equipped with a variable temperature STM manufactured by RHK technology, the other was used for KCl film preparation and PTCDA deposition. The STM can be operated with the sample being cooled by a liquid He cryostat. The cryostat is at about 12 K and the sample temperature, which cannot be measured precisely at low temperature, is reckoned to be below 40 K. The STM tip was made from Pt-Ir. Given bias voltages (U_{bias}) refer to the voltage at sample with respect to the tip. All STM images shown in section 3.2 were recorded in constant current mode.
In the preparation chamber, the sample was cooled by liquid nitrogen and the lowest temperature during PTCDA deposition was about 100 K. The Ag(100) surface was prepared by the cycles of sputtering with 700 eV Ar^+ ions and annealing at 820 K. Thin epitaxial KCl films were then grown on the Ag(100) substrate at a rate of 0.2 atomic layers per min, while the sample was at temperatures between 300 and 450 K. KCl was thermally sublimated from a boron-nitride crucible. Details of the preparation of the KCl films are reported in Ref. [168]. It is found that KCl grows on Ag(100) in the form of a wetting layer consisting of two atomic layers (bilayer), on top of which layers of monatomic height

nucleate. This is in contrast to what it is erroneously concluded from our earlier STM experiments [168]. This type of growth scenario seems to be typical for many alkali halides [258]. PTCDA was deposited from a Knudsen cell onto the KCl films at a sample temperature of 100 or 300 K. After the deposition at 100 K, the sample was transferred into the STM chamber as fast as possible and cooled down there below 40 K.

Corroles on Ag(111)

In this section, the experimental methodologies to investigate free-base H_3TpFPC on Ag(111) are presented. The synthesis of the molecule was performed by Wolfgang Schöfberger (Institute of Organic Chemistry, Johannes Kepler University Linz). The measurements of the STM and the radical delocalisation within the monolayer were carried out in the group of R. Koch (Institute of Semiconductor and Solid State Physics Johannes Kepler University Linz). The measurements of the XPS, the NEXAFS and the TPD were performed in the group of J. V. Barth (Technical University of Munich, Germany).

Molecule Synthesis. H_3TpFPC was synthesised according to previously reported procedures [204]. H_3TpFPC were purified by preparative HPLC, and subsequently analysed by ^{1}H, ^{13}C, and ^{19}F NMR spectroscopy.

Sample Preparation. The Ag(111) substrate was cleaned by several cycles of Ar^+ ion sputtering (600 eV) and thermal annealing (700 K). Samples were prepared by thermal evaporation of the H_3TpFPC molecules from a quartz crucible, kept at 460 K, onto the Ag(111). Depending on the experiment, the surface was kept at 200 K or at room temperature (see chapter 4 for further details).

Scanning Tunnelling Microscopy (STM). The prepared samples were in situ transferred into the STM chamber. STM experiments were performed at 5 K, base pressure of $< 10^{-10}$ mbar, employing electrochemically etched tungsten tips thermally deoxidised by flash-annealing above 1070 K. STM images were analysed using the program WSxM [259]. The lateral manipulation of single molecules was performed in constant current mode (10 mV, 5 nA) with the tip moved at a speed of about 0.02 nm s^{-1} during manipulation. For manipulation, the tip was moved over a selected molecule, switch to manipulation parameters (5 nA) and displace the STM tip along a defined path; after manipulation the parameters are restored for imaging (100 pA).

Radical delocalisation within the molecule. In order to illustrate if the radical is localised in a well-defined area or is delocalised over a large region, the spatial distribution of the unpaired radical electron within the individual corrole molecules with sub-nanometre resolution by STM is imaged. The experiment consists of the measurement of the dc tunnel conductance ($\partial I_{dc}/\partial V$) in the proximity of the Fermi energy. The measurement is performed pixel-by pixel, in order to build a ($\partial I_{dc}/\partial V$) map showing the conductance value in each point of the image. The Kondo signal is detected during the measurement by the oscillating reference signal necessary for measuring using a lock-in amplifier. In the

specific case, the measurement with a bias voltage of -3 mV and a lock-in reference signal with amplitude 5 mV rms was performed. The width of the oscillation is large enough to collect the Kondo signal, revealing its intensity in the different position over the $H_2TpFPC^{\bullet}$ monolayer. Because of the negative Kondo signal detected over the $H_2TpFPC^{\bullet}$ monolayer, stronger Kondo signal in specific regions of the molecule, results in a lower conductance value. In other words, the measurement represents a Kondo map of the $H_2TpFPC^{\bullet}$ monolayer. The result of the experiment is shown in Figure 4.19. The topographic STM image (b) and the spatial distribution of the unpaired radical electron (c) over the same image frame are juxtaposed. The Kondo map of Figure 4.19 c is obtained by averaging of 15 h consecutive measurements. To improve the quality of the data, each pixel in each measurement is acquired in ≈11 ms. This time is long enough to obtain a reliable conductance measurement. For acquiring a full frame (128 ×128 pixels) a total time of 3657 s (> 1 h) is required. The 15 consecutive images are acquired sequentially, without any interruption between the different frames. This results in a total acquisition time of ≈15 h. In order to correct the lateral drift (normal, for such a long measurement) each image is cut, selecting always the same spatial region. The resulted frames are finally averaged, resulting in the Kondo map of Figure 4.19 c. Topographic images are acquired immediately before and after the conductance measurement and compared, in order to exclude massive changes of the tip during the acquisition of the conductance images. The topography shown in Figure 4.19 b was acquired immediately after the Kondo map. Notice that the topographic image in Figure 4.19 b is acquired at the same bias voltage and tunnel current (+0.3 V, 100 pA) of the images used for the characterisation of the corroles regular network.

X-ray Photoelectron Spectroscopy (XPS). All measurements were performed at room temperature (except those related to cold phase, which were measured at 200 K) in normal emission geometry at the BESSY II synchrotron in Berlin, using the HE-SGM beamline (1500 l/mm monochromator grating; 200 μm slit width; Scienta R3000 hemispherical analyser; base pressure 1×10^{-9} mbar and the UE56-2 PGM-2 undulator beamline (movable end station with a base pressure of 8×10^{-11} mbar; SPECS Phoibos 100 CCD analyser; 10 μm exit slits after monochromator; entrance slits after undulator aperture were appropriately closed to reduce photon flux and minimise beam damage). Sample position was frequently changed between different spectra to avoid artifacts due to radiation damage. The fast XPS data were recorded in single bunch mode to ensure negligible beam damage throughout the extended acquisition time. The C 1s spectra were acquired with a pass energy of 10 eV and N 1s and F 1s with 20 eV. The photon energy $h\nu$ was adjusted such that the kinetic energy of the electrons was approximately 150 eV (C 1s, 435 eV; N 1s, 550 eV, F 1s, 850 eV). The binding energy scale was calibrated against the Ag $3d_{5/2}$ peak (368.3 eV) or the Fermi edge (0 eV) of the substrate. The spectra were fitted with peaks exhibiting a Voigt line shape after a Shirley (C 1s), linear (F 1s), or polynomial background of fifth-order (N 1s) background subtraction.

Near-Edge X-ray-Absorption Fine-Structure (NEXAFS). The measurements were performed at the HE-SGM dipole magnet beamline of the BESSY II synchrotron in Berlin. NEXAFS spectra were recorded at 200 K for the low temperature phase, and

at room temperature (RT) for the subsequent derivatives, in normal emission geometry. A monochromator grating of 1500 Lmm^{-1} and slit widths of 200 μm were used in partial electron yield mode at a retarding voltage of -150 and -250 V for the C and N K-edge, respectively. The spectra were measured at different incident angles θ (25, 53, and 90° = normal incidence) inclined by the electric-field vector $\vec{E}$ of the incident light (linear polarisation P = 90%) and the surface normal (see also Figure 2.7). After subtraction of the signal of the bare crystal from the averaged data, the resulting spectra were normalised to an edge jump of one. For obtaining an experimental NEXAFS tilt angle β, the theoretical angle-dependences of the intensity I of a resonance corresponding to the case of threefold or higher substrate symmetry as described in Ref. [112] was employed: $I(\beta,\theta) = PI^{\parallel} + (1-P)I^{\perp}$ in which $I^{\parallel} = \frac{A}{3}[1+\frac{1}{2}(3\cdot cos^2\theta - 1)(3\cdot cos^2\beta - 1)]$, $I^{\perp} = \frac{1}{2}A\cdot sin^2\beta$, and A accounts for the angle-integrated cross-section normalised to one.
When the same molecular moiety is present on the surface with several inclinations β_ν, the determined experimental estimate is compared with the theoretical average of the DFT-calculated tilt angles of the individual moieties, weighted by the inverse angle-integrated cross-sections A_i with $A_i = \int_0^{90} I(\beta_i,\theta)d\theta$.

Temperature-Programmed Desorption (TPD). The measurements were performed with a custom-built UHV chamber previously mounted at the UE-56-2 PGM-2 beamline. The base pressure was improved to 3×10^{-11} mbar during the measurements, to reduce the background pressure of H_2 close to the detection limit of the mass spectrometer. A liquid nitrogen cooled quadrupole mass spectrometer equipped with a Feulner cup was employed, which can be brought near to the sample to within a few mm. The heating rate was controlled by a proportional-integral-derivative controller. The cleanliness of the Ag(111) substrate and the coverage and chemical state of the corrole layers were assessed by XPS using a standard dual anode X-ray tube with Mg and Al K_α lines. However, XPS was not performed prior to TPD measurements to avoid possible effects of radiation damage.

C Abbreviations

AFM	atomic force microscopy
BE	binding energy
BZ	Brillouin zone
CLS	core level shift
DIP	Diindenoperylene
DFT	density functional theory
GGA	generalised gradient approximation
H_3TpFPC	5,10,15-tris-(pentafluorophenyl)corrole
HK	Hohenberg-Kohn
KS	Kohn-Sham
LA	long axis
LDA	local density approximation
LR	long range
MM	molecule-molecule interactions
MS	molecule-surface interactions
MP	Monkhorst-Pack
NEXAFS	Near-Edge X-ray-Absorption Fine Structure
PAW	projected augmented wave method
pFP	pentafluorophenyl
PES	potential energy surface
PTCDA	perylene-3,4,9,10-tetracarboxylic diahydride
QE	quantum expresso
RT	room temperature
SR	short range

STM	scanning tunneling microscopy
T	temperature
TPD	Temperature Programmed Desorption
VASP	Vienna ab-initio simulation package
vdW	van-der-Waals
XAS	X-ray absorption spectra
xc	exchange-correlation
XPS	X-ray Photoelectron Spectroscopy

D Publications

1. H. Aldahhak, W. G. Schmidt, E. Rauls, Surf. Sci., 2013, 617, 242-248.
2. Q. Guo, A. Paulheim, M. Sokolowski, H. Aldahhak, E. Rauls, W.G. Schmidt, The Journal of Physical Chemistry C, 2014, 118, 29911-29918.
3. H. Aldahhak, W.G. Schmidt, E. Rauls, Surf. Sci., 2015, 641, 278-281.
4. A. Paulheim, C. Marquardt, H. Aldahhak, E. Rauls, W.G. Schmidt, M. Sokolowski, The Journal of Physical Chemistry C, 2016, 120, 11926-11937.
5. A. Paulheim, C. Marquardt, M. Sokolowski, M. Hochheim, T. Bredow, H. Aldahhak, E. Rauls, W.G. Schmidt, Physical Chemistry Chemical Physics, 2016, 18, 32891-32902.
6. H. Aldahhak, S. Matencio, E. Barrena, C. Ocal, W.G. Schmidt, E. Rauls, Phys. Chem. Chem. Phys., 2015, 17 (14), 8776-8783.
7. H. Aldahhak, E. Rauls, W.G. Schmidt, Surf. Sci., 2015, 641, 260-265.
8. H. Aldahhak, M. Paszkiewicz, F. Allegretti, D. A. Duncan, S. Tebi, P. S. Deimel, P. Casado Aguilar, Y.-Q. Zhang, A. C. Papageorgiou, R. Koch, J. V. Barth, W. G. Schmidt, S. Müllegger, W. Schöfberger, F. Klappenberger, E. Rauls, and U. Gerstmann, J. Phys. Chem. C 2017, 121, 2192-2200.
9. S. Tebi, M. Paszkiewicz, H. Aldahhak, F. Allegretti, S. Gonglach, M. Haas, M. Waser, P. S. Deimel, P. C. Aguilar, Y-Q. Zhang, A. C. Papageorgiou, D. A. Duncan, J. V. Barth, W. G. Schmidt, R. Koch, U. Gerstmann, E. Rauls, F. Klappenberger, W. Schöfberger, S. Müllegger, ACS Nano 2017, 11, 3383-3391.
10. S. Tebi, H. Aldahhak, G. Serrano, W. Schöfberger, E. Rauls, W. G. Schmidt, R. Koch, S. Müllegger, Nanotechnology, 2016, 27, 025704-025708.
11. H. Aldahhak, M. Paszkiewicz, E. Rauls, F. Allegretti, S. Tebi, A. Papageorgiou, Y. Zhang, L. Zhang, T. Lin, T. Paintner, R. Koch, W. G. Schmidt, J. V. Barth, W. Schöfberger, S. Müllegger, F. Klappenberger, U. Gerstmann, Chem. Eur. J. 2018, 24, 6787-6797.
12. W. Schöfberger, F. Faschinger, S. Chattopadhyay, S. Bhakta, B. Mondal, J. A. A. W. Elemans, S. Müllegger, S. Tebi, R. Koch, F. Klappenberger, M. Paszkiewicz, J. V. Barth, E. Rauls, H. Aldahhak, W. G. Schmidt, A. Dey, Angewandte Chemie International Edition, 2016, 55 (7), 2350-2355.

13. Unraveling the Oxidation and Spin State of Mn-Corrole through X-ray Spectroscopy and Quantum Chemical Analysis, M. Paszkiewicz, T. Biktagirov, H. Aldahhak, F. Allegretti, E. Rauls, W. Schöfberger, W. G. Schmidt, J. V. Barth, U. Gerstmann, F. Klappenberger, Journal of Physical Chemistry Letters, accepted.
14. Catalytic active membrane formation - temperature study of manganese 5,10,15-tris(pentafluorophenyl) corrole on Ag(111). R. Kakavandi, M. Paszkiewicz, H. Aldahhak, S. Tebi, E. Rauls, U. Gerstmann, Y.-Q. Zhang, W. Schöfberger, S. Müllegger, R. Koch, W. G. Schmidt, J. V. Barth and F. Klappenberger, (in preparation).
15. Precursor States in Adsorption of PTCDA on KCl(100) (in preparation).
16. Thermal induced multiple intra-cyclisations of H_3TpFPC on Ag(111) (in preparation).
17. Insight into oxidation states of copper complexes. A combined experimental and theoretical X-ray spectroscopic study (in preparation).

E Acknowledgements

At the end of this work, I would like to express my sincere thanks to all people who academically and spiritually supported me during the intensive work to complete this thesis.

First and foremost, my profound gratitude goes to Prof. Dr. rer. nat. habil. Wolf Gero Schmidt for giving me the chance to do the thesis in his group and for helping me to grow in the field of research. His unconditional support, guidance, insightful comments and readiness to discuss scientific and even personal problems have enormously inspired me to go through the rough road and to continue to the end.

I am pretty indebted to Prof. Eva Rauls for her continuous support and fruitful discussions. Her wise counsel and sympathetic ear have provided unending inspiration to my work and life. I liked the work with her too much and I feel always being lucky to have such person in my life.

Very special thanks go to Dr. Uwe Gerstmann for his tremendous academic and personal support. During our work on calculations of X-ray spectroscopy, he answered the endless questions I had. I am very thankful to his immense knowledge, amicable character and positive disposition, which encouraged me to complete this thesis.

Many thanks to our experimental colleagues: Dr. Stefan Müllegger and Stefano Tebi from the University of Linz as well as Dr. Florian Klappenberger and Mateusz Paszkiewicz from the University of Munich for the extremely fruitful cooperation and supplying the required experimental data.

Words cannot express my feelings when I speak about my current and former colleagues: Martin Babilon, Martin Rohrmüller, Timur Biktagirov, Andreas Lücke, Arthur Riefer, Christian Braun, Sergej Neufeld, Marc Landmann, Achraf Jaadouni, Daijiro Nozaki, Dr. Simone Sanna, Yanlu Li, Kris Holtgrewe, Nora Jenny Vollmers and Matthias Witte. Thank you all for pleasant atmosphere, for nice memories and for offering help in different ways. For the help in organisation issues, I deeply praise the enormous amount of help from Simone Lange.

For generous grants of computing time, The Paderborn Centre for Parallel Computing (PC^2) is deeply acknowledged.

I owe a lot to my family and friends. Whatever happened, my family is my lifeboat. My father, mother and all sisters and brothers sacrificed too much for me. I love you all and I am deeply thankful to your invaluable support. Special acknowledgments go to the

invaluable treasures: my wife Yara Memar and my daughter Faia. You gave the sweet taste to my life and this thesis is dedicated to you.

Bibliography

[1] Dimas G. de Oteyza, E. Barrena, H. Dosch, and Y. Wakayama. Nanoconfinement effects in the self-assembly of diindenoperylene (DIP) on Cu(111) surfaces. *Phys. Chem. Chem. Phys.*, 11:8741–8744, 2009.

[2] N. L. Dmitruk, O. Yu. Borkovskaya, O. I. Mayeva, G.Ya. Kolbasov, and I. B. Mamontova. Self-organized technology of anisotropic etching of semiconductors for optoelectronics application. *Materials Science and Engineering: B*, 88(2):277–281, 2002.

[3] J. Shen, D. Wang, E. Langlois, W. A. Barrow, P. J. Green, C. W. Tang, and J. Shi. Degradation mechanisms in organic light emitting diodes. *Synthetic Metals*, 111-112:233 – 236, 2000.

[4] S. T. Lee, Z. Q. Gao, and L. S. Hung. Metal diffusion from electrodes in organic light-emitting diodes. *Applied Physics Letters*, 75(10):1404–1406, 1999.

[5] H. Aziz and Z. D. Popovic. Degradation Phenomena in Small-Molecule Organic Light-Emitting Devices. *Chemistry of Materials*, 16(23):4522–4532, 2004.

[6] J. McElvain, H. Antoniadis, M. R. Hueschen, J. N. Miller, D. M. Roitman, J. R. Sheats, and R. L. Moon. Formation and growth of black spots in organic light-emitting diodes. *Journal of Applied Physics*, 80(10):6002–6007, 1996.

[7] M. I. Arroyo-Villan, G. A. Diaz-Quijada, M. S. A. Abdou, and S. Holdcroft. Poly(n-(3-thienyl)alkanesulfonates): Synthesis, Regioregularity, Morphology, and Photochemistry. *Macromolecules*, 28(4):975–984, 1995.

[8] F. Tran, R. Laskowski, P. Blaha, and K. Schwarz. Performance on molecules, surfaces, and solids of the Wu-Cohen GGA exchange-correlation energy functional. *Phys. Rev. B*, 75:115131, Mar 2007.

[9] N. Karl. Charge carrier transport in organic semiconductors. *Synthetic Metals*, 133-134:649–657, 2003.

[10] M. B. Casu, I. Biswas, B. E. Schuster, M. Nagel, P. Nagel, S. Schuppler, and T. Chassé. Molecular orientation in diindenoperylene thin films deposited on polycrystalline gold. *Applied Physics Letters*, 93(2):024103, 2008.

[11] J. Wagner, M. Gruber, A. Hinderhofer, A. Wilke, B. Bröker, J. Frisch, P. Amsalem, A. Vollmer, A. Opitz, N. Koch, F. Schreiber, and W. Brütting. High Fill Factor and Open Circuit Voltage in Organic Photovoltaic Cells with Diindenoperylene as Donor Material. *Advanced Functional Materials*, 20(24):4295–4303, 2010.

[12] M. Müller, A. Paulheim, A. Eisfeld, and M. Sokolowski. Finite size line broadening and superradiance of optical transitions in two dimensional long-range ordered molecular aggregates. *The Journal of Chemical Physics*, 139(4):044302, 2013.

[13] O. Bauer, G. Mercurio, M. Willenbockel, W. Reckien, C. Heinrich Schmitz, S. Fiedler, B.and Soubatch, T. Bredow, F. S. Tautz, and M. Sokolowski. Role of functional groups in surface bonding of planar π-conjugated molecules. *Phys. Rev. B*, 86:235431, Dec 2012.

[14] J. Repp, G. Meyer, S. M. Stojković, A. Gourdon, and C. Joachim. Molecules on insulating films: Scanning-tunneling microscopy imaging of individual molecular orbitals. *Phys. Rev. Lett.*, 94:026803, Jan 2005.

[15] M. Müller, A.Paulheim, C. Marquardt, and M. Sokolowski. Spectroscopy of isolated PTCDA molecules on the KCl(100) surface: Vibrational spectra and azimuthal orientation. *The Journal of Chemical Physics*, 138(6):064703, 2013.

[16] P. K. de Boer and R. A. de Groot. The origin of the conduction band in table salt. *American Journal of Physics*, 67(5):44–445, 1999.

[17] G. C. Benson and T. A. Claxton. Application of a shell model to the calculation of the surface distortion in alkali halide crystals. *The Journal of Chemical Physics*, 48(3):1356–1360, 1968.

[18] F. W. de Wette, W. Kress, and U. Schröder. Relaxation of the rocksalt (001) surface: Alkali halides, MgO, and PbS. *Phys. Rev. B*, 32:4143–4157, Sep 1985.

[19] R. G. Parr and W. Yang. *Density-Functional theory of atoms and Molecules*. Oxford University Press, New York, 1989.

[20] M. R. Dreizler and E. K. U. Gross. *Density Functional theory: An approach to the quantum many-body Problem*. Springer, Berlin, 1990.

[21] W. Kohn. Nobel lecture: Electronic structure of matter-wave functions and density functionals. *Rev. Mod. Phys.*, 71:1253–1266, Oct 1999.

[22] J. Kohanoff. *Electronic Structure Calculations for Solids and molecules: Theory and Computational Methods*. CAMBRIDGE UNIVERSITY PRESS, 2006.

[23] M. Born and R. Oppenheimer. Zur quantentheorie der molekeln. *Annalen der Physik*, 389(20):457–484, 1927.

[24] P. Hohenberg and W. Kohn. Inhomogeneous electron gas. *Phys. Rev.*, 136:B864–B871, Nov 1964.

[25] W. Kohn and L. J. Sham. Self-consistent equations including exchange and correlation effects. *Phys. Rev.*, 140:A1133–A1138, Nov 1965.

[26] R. Taton. Inventaire chronologique de l'œuvre de lagrange. *Revue d'histoire des sciences*, 27(1):3–36, 1974.

[27] N. Agraït, A. L. Yeyati, and J. M. van Ruitenbeek. Quantum properties of atomic-sized conductors. *Physics Reports*, 377(2):81–279, 2003.

[28] W. Koch and M. Holthausen. *A Chemist's Guide to Density Functional Theory.* Wiley, 2nd ed., 2008.

[29] M. Gell-Mann. Specific Heat of a Degenerate Electron Gas at High Density. *Phys. Rev.*, 106:369–372, Apr 1957.

[30] D. M. Ceperley and B. J. Alder. Ground State of the Electron Gas by a Stochastic Method. *Phys. Rev. Lett.*, 45:566–569, Aug 1980.

[31] J. P. Perdew and A. Zunger. Self-interaction correction to density-functional approximations for many-electron systems. *Phys. Rev. B*, 23:5048–5079, May 1981.

[32] J. P. Perdew and Z. Wang. Accurate and simple analytic representation of the electron-gas correlation energy. *Phys. Rev. B*, 45:13244–13249, Jun 1992.

[33] D. R. Hamann. H_2O hydrogen bonding in density-functional theory. *Phys. Rev. B*, 55:R10157–R10160, Apr 1997.

[34] J. P. Perdew, J. A. Chevary, S. H. Vosko, K. A. Jackson, M. R. Pederson, D. J. Singh, and C. Fiolhais. Atoms, molecules, solids, and surfaces: Applications of the generalized gradient approximation for exchange and correlation. *Phys. Rev. B*, 46:6671–6687, Sep 1992.

[35] J. P. Perdew, K. Burke, and M. Ernzerhof. Generalized Gradient Approximation Made Simple. *Phys. Rev. Lett.*, 77:3865–3868, Oct 1996.

[36] B. Hammer, L. B. Hansen, and J. K. Nørskov. Improved adsorption energetics within density-functional theory using revised Perdew-Burke-Ernzerhof functionals. *Phys. Rev. B*, 59:7413–7421, Mar 1999.

[37] Z. Wu and R. E. Cohen. More accurate generalized gradient approximation for solids. *Phys. Rev. B*, 73:235116, Jun 2006.

[38] C. Carmer. *Essentials of Computational Chemistry: Theories and Models.* Willy, 2002.

[39] Felix Bloch. Über die quantenmechanik der elektronen in kristallgittern. *Zeitschrift für Physik*, 52(7):555–600, Jul 1929.

[40] D. J. Chadi and M. L. Cohen. Special Points in the Brillouin Zone. *Phys. Rev. B*, 8:5747–5753, Dec 1973.

[41] H. J. Monkhorst and J. D. Pack. Special points for Brillouin-zone integrations. *Phys. Rev. B*, 13:5188–5192, Jun 1976.

[42] M. Methfessel and A. T. Paxton. High-precision sampling for Brillouin-zone integration in metals. *Phys. Rev. B*, 40:3616–3621, Aug 1989.

[43] N. Marzari, D. Vanderbilt, A. De Vita, and M. C. Payne. Thermal Contraction and Disordering of the Al(110) Surface. *Phys. Rev. Lett.*, 82:3296–3299, Apr 1999.

[44] L. Bengtsson. Dipole correction for surface supercell calculations. *Phys. Rev. B*, 59:12301–12304, May 1999.

[45] J. Neugebauer and M. Scheffler. Adsorbate-substrate and adsorbate-adsorbate interactions of Na and K adlayers on Al(111). *Phys. Rev. B*, 46:16067–16080, Dec 1992.

[46] J. C. Phillips and L. Kleinman. New Method for Calculating Wave Functions in Crystals and Molecules. *Phys. Rev.*, 116:287–294, Oct 1959.

[47] D. R. Hamann, M. Schlüter, and C. Chiang. Norm-conserving pseudopotentials. *Phys. Rev. Lett.*, 43:1494–1497, Nov 1979.

[48] D. Vanderbilt. Soft self-consistent pseudopotentials in a generalized eigenvalue formalism. *Phys. Rev. B*, 41:7892–7895, Apr 1990.

[49] P. E. Blöchl. Projector augmented-wave method. *Phys. Rev. B*, 50:17953–17979, Dec 1994.

[50] P. E. Blöchl, O. Jepsen, and O. K. Andersen. Improved tetrahedron method for Brillouin-zone integrations. *Phys. Rev. B*, 49:16223–16233, Jun 1994.

[51] U. von Barth and C. D. Gelatt. Validity of the frozen-core approximation and pseudopotential theory for cohesive energy calculations. *Phys. Rev. B*, 21:2222–2228, Mar 1980.

[52] R. P. Feynman. Forces in molecules. *Phys. Rev.*, 56:340–343, Aug 1939.

[53] A. C. Hurley. The electrostatic calculation of molecular energies-i. methods of calculating molecular energies. *Proceedings of the Royal Society of London A: Mathematical, Physical and Engineering Sciences*, 226(1165):170–178, 1954.

[54] M. Di Ventra and S. T. Pantelides. Hellmann-feynman theorem and the definition of forces in quantum time-dependent and transport problems. *Phys. Rev. B*, 61:16207–16212, 2000.

[55] J. P. Perdew, J. A. Chevary, S. H. Vosko, K. A. Jackson, M. R. Pederson, D. J. Singh, and C. Fiolhais. Atoms, molecules, solids, and surfaces: Applications of the generalized gradient approximation for exchange and correlation. *Phys. Rev. B*, 46:6671–6687, Sep 1992.

[56] C. D. Sherrill, T. Takatani, and E. G. Hohenstein. An Assessment of Theoretical Methods for Nonbonded Interactions: Comparison to Complete Basis Set Limit Coupled-Cluster Potential Energy Curves for the Benzene Dimer, the Methane Dimer, Benzene-Methane, and Benzene-H_2S. *The Journal of Physical Chemistry A*, 113(38):10146–10159, 2009.

[57] W. Kohn, Y. Meir, and D. E. Makarov. Van der Waals Energies in Density Functional Theory. *Phys. Rev. Lett.*, 80:4153–4156, May 1998.

[58] M. Lein, J. F. Dobson, and E. K. U. Gross. Toward the Description of van der Waals Interactions within DensityFunctional Theory. *Journal of Computational Chemistry*, 20:12–22, 1999.

[59] J. F. Dobson and B. P. Dinte. Constraint Satisfaction in Local and Gradient Susceptibility Approximations: Application to a van der Waals Density Functional. *Phys. Rev. Lett.*, 76:1780–1783, Mar 1996.

[60] Y. Andersson, D. C. Langreth, and B. I. Lundqvist. van der Waals Interactions in Density-Functional Theory. *Phys. Rev. Lett.*, 76:102–105, Jan 1996.

[61] F. Ortmann, F. Bechstedt, and W. G. Schmidt. Semiempirical van der Waals correction to the density functional description of solids and molecular structures. *Phys. Rev. B*, 73:205101, May 2006.

[62] F. Ortmann, W. G. Schmidt, and F. Bechstedt. Attracted by long-range electron correlation: Adenine on graphite. *Phys. Rev. Lett.*, 95:186101, Oct 2005.

[63] E. R. McNellis, J. Meyer, and K. Reuter. Azobenzene at coinage metal surfaces: Role of dispersive van der Waals interactions. *Phys. Rev. B*, 80:205414, Nov 2009.

[64] E. Rauls, W. G. Schmidt, T. Pertram, and K. Wandelt. Interplay between metal-free phthalocyanine molecules and Au(110) substrates. *Surface Science*, 606(13):1120–1125, 2012.

[65] C. Thierfelder, M. Witte, S. Blankenburg, E. Rauls, and W. G. Schmidt. Methane adsorption on graphene from first principles including dispersion interaction. *Surface Science*, 605(7):746–749, 2011.

[66] F. London. Über einige Eigenschaften und Anwendungen der Molekularkräfte. *Z. Phys. Chem. Abt. B*, 12:222, 1930.

[67] F. London. Zur Theorie und Systematik der Molekularkräfte. *Z. Phys.*, 63:245, 1930.

[68] A. Saranin A. Zotov M. Katayama K. Oura, V. Lifshits. *Surface Science- An Introduction.* Springer, Berlin, 2003.

[69] C. N. Berglund and W. E. Spicer. Photoemission studies of copper and silver: Theory. *Phys. Rev.*, 136:A1030–A1044, Nov 1964.

[70] C. Nordling, E. Sokolowski, and K. Siegbahn. Precision Method for Obtaining Absolute Values of Atomic Binding Energies. *Phys. Rev.*, 105:1676–1677, Mar 1957.

[71] U. Gelius. Binding Energies and Chemical Shifts in ESCA. *Physica Scripta*, 9(3):133, 1974.

[72] J. M. Hollander and W. L. Jolly. X-ray photoelectron spectroscopy. *Accounts of Chemical Research*, 3(6):193–200, 1970.

[73] P. E. Sobol K. D. Bomben J. F. Moulder, W. F. Stickle. *Handbook of X-Ray Photoelectron Spectroscopy: A Reference Book of Standard Spectra for Identification and Interpretation of XPS Data.* Physical Electronics, 1995.

[74] I. Gilmore J. C. Vickerman. *Surface Analysis: The Principal Techniques.* Wiley, 2nd edition, 2009.

[75] M. Weinert and R. E. Watson. Core-level shifts in bulk alloys and surface adlayers. *Phys. Rev. B*, 51:17168–17180, Jun 1995.

[76] P. H. Citrin and D. R. Hamann. Measurement and calculation of polarization and potential-energy effects on core-electron binding energies in solids: X-ray photoemission of rare gases implanted in noble metals. *Phys. Rev. B*, 10:4948–4963, Dec 1974.

[77] N. D. Lang and A. R. Williams. Core holes in chemisorbed atoms. *Phys. Rev. B*, 16:2408–2419, Sep 1977.

[78] A. R. Williams and N. D. Lang. Core-Level Binding-Energy Shifts in Metals. *Phys. Rev. Lett.*, 40:954–957, Apr 1978.

[79] S. García-Gil, A. García, and P. Ordejón. Calculation of core level shifts within DFT using pseudopotentials and localized basis sets. *The European Physical Journal B*, 85(7):239, Jul 2012.

[80] Y. Miyamoto and A. Oshiyama. Effect of anisotropic Coulomb field on Si 2p core levels in oxidized silicon. *Phys. Rev. B*, 44:5931–5934, Sep 1991.

[81] X. Blase, A. J. R. da Silva, X. Zhu, and S. G. Louie. Si 2p core-level chemical shifts at the H/Si(111)-(1×1) surface. *Phys. Rev. B*, 50:8102–8105, Sep 1994.

[82] E. Pehlke and M. Scheffler. Evidence for site-sensitive screening of core holes at the Si and Ge (001) surface. *Phys. Rev. Lett.*, 71:2338–2341, Oct 1993.

[83] W. Kossel. Zum Bau der Röntgenspektren. *Zeitschrift für Physik*, 1(1):119–134, Feb 1920.

[84] R. de L. Kronig. Zur theorie der feinstruktur in den röntgenabsorptionsspektren. *Zeitschrift für Physik*, 70(5):317–323, May 1931.

[85] J. Stöhr, K. Baberschke, R. Jaeger, R. Treichler, and S. Brennan. Orientation of Chemisorbed Molecules from Surface-Absorption Fine-Structure Measurements: CO and NO on Ni(100). *Phys. Rev. Lett.*, 47:381–384, Aug 1981.

[86] F. Rodrigues, D. Galante, G. M. do Nascimento, and P. S. Santos. Interionic Interactions in Imidazolic Ionic Liquids Probed by Soft X-ray Absorption Spectroscopy. *The Journal of Physical Chemistry B*, 116(5):1491–1498, 2012.

[87] Z. Andrea, M. Valentina, A. Giuliana, and D. Paola. On the possibility of using XANES to investigate bromide-based ionic liquids. *Chemical Physics Letters*, 591:32–36, 2014.

[88] C. Ehlert, M. Holzweber, A. Lippitz, W. E. S. Unger, and P. Saalfrank. A detailed assignment of NEXAFS resonances of imidazolium based ionic liquids. *Phys. Chem. Chem. Phys.*, 18:8654–8661, 2016.

[89] W. Wurth, J. Stöhr, P. Feulner, X. Pan, K. R. Bauchspiess, Y. Baba, E. Hudel, G. Rocker, and D. Menzel. Bonding, structure, and magnetism of physisorbed and chemisorbed O_2 on Pt(111). *Phys. Rev. Lett.*, 65:2426–2429, Nov 1990.

[90] F. Sette, J. Stöhr, E. B. Kollin, D. J. Dwyer, J. L. Gland, J. L. Robbins, and A. L. Johnson. Na-induced bonding and bond-length changes for CO on Pt(111): A near-edge x-ray-absorption fine-structure study. *Phys. Rev. Lett.*, 54:935–938, Mar 1985.

[91] C. M. Kim, H. S. Jeong, and E. H. Kim. NEXAFS and XPS characterization of molecular oxygen adsorbed on Ni(100) at 80 K. *Surface Science*, 459(1):L457–L461, 2000.

[92] D. A. Outka, J. Stöhr, W. Jark, P. Stevens, J. Solomon, and R. J. Madix. Orientation and bond length of molecular oxygen on Ag(110) and Pt(111): A near-edge X-ray-absorption fine-structure study. *Phys. Rev. B*, 35:4119–4122, Mar 1987.

[93] S. A. Krasnikov, C. M. Doyle, N. N. Sergeeva, A. B. Preobrajenski, N. A. Vinogradov, Y. N. Sergeeva, A. A. Zakharov, M. O. Senge, and A. A. Cafolla. Formation of extended covalently bonded Ni porphyrin networks on the Au(111) surface. *Nano Research*, 4(4):376–384, Apr 2011.

[94] W. Auwärter, F. Klappenberger, A. Weber-Bargioni, A. Schiffrin, T. Strunskus, C. Wöll, Y. Pennec, A. Riemann, and J. V. Barth. Conformational Adaptation and Selective Adatom Capturing of Tetrapyridyl-porphyrin Molecules on a Copper (111) Surface. *Journal of the American Chemical Society*, 129(36):11279–11285, 2007.

[95] K. Diller, F. Klappenberger, M. Marschall, K. Hermann, A. Nefedov, C. Wöll, and J. V. Barth. Self-metalation of 2H-tetraphenylporphyrin on Cu(111): An x-ray spectroscopy study. *The Journal of Chemical Physics*, 136(1):014705–014717, 2012.

[96] S. A. Krasnikov, N. N. Sergeeva, M. M. Brzhezinskaya, A. B. Preobrajenski, Y. N. Sergeeva, N. A. Vinogradov, A. A. Cafolla, M. O. Senge, and A. S. Vinogradov. An x-ray absorption and photoemission study of the electronic structure of Ni porphyrins and Ni N-confused porphyrin. *Journal of Physics: Condensed Matter*, 20(23):235207, 2008.

[97] A. Bianconi. Surface X-ray absorption spectroscopy: Surface EXAFS and surface XANES. *Applications of Surface Science*, 6(3):392–418, 1980.

[98] R. Püttner, C. Kolczewski, M. Martins, A. S. Schlachter, G. Snell, M. Sant'Anna, J. Viefhaus, K. Hermann, and G. Kaindl. The C 1s NEXAFS spectrum of benzene below threshold: Rydberg or valence character of the unoccupied σ-type orbitals. *Chemical Physics Letters*, 393(4):361–366, 2004.

[99] J. G. Chen. NEXAFS investigations of transition metal oxides, nitrides, carbides, sulfides and other interstitial compounds. *Surface Science Reports*, 30(1):1–152, 1997.

[100] G. Hähner. Near edge X-ray absorption fine structure spectroscopy as a tool to probe electronic and structural properties of thin organic films and liquids. *Chem. Soc. Rev.*, 35:1244–1255, 2006.

[101] G. Witte T. Breuer, M. Klues. Characterization of orientational order in π-conjugated molecular thin films by NEXAFS. *Journal of Electron Spectroscopy and Related Phenomena*, 204:102–115, 2015.

[102] J. Stöhr. *NEXAFS Spectroscopy, The Angular Dependence of Resonance Intensities.* Springer Berlin Heidelberg, 1992.

[103] A. Nefedov and C. Wöll. *Advanced Applications of NEXAFS Spectroscopy for Functionalized Surfaces.* Springer, Berlin Heidelberg, 2013.

[104] A. P. Hitchcock and D. C. Mancini. Bibliography and database of inner shell excitation spectra of gas phase atoms and molecules. *Journal of Electron Spectroscopy and Related Phenomena*, 67(1):1–132, 1994.

[105] O. Dhez, H. Ade, and S. G. Urquhart. Calibrated nexafs spectra of some common polymers. *Journal of Electron Spectroscopy and Related Phenomena*, 128(1):85–96, 2003.

[106] G. Di Santo, S. Blankenburg, C. Castellarin-Cudia, M. Fanetti, P. Borghetti, L. Sangaletti, L. Floreano, A. Verdini, E. Magnano, F. Bondino, C. A. Pignedoli, M.-T. Nguyen, R. Gaspari, D. Passerone, and A. Goldoni. Supramolecular Engineering through Temperature-Induced Chemical Modification of 2H-Tetraphenylporphyrin on Ag(111): Flat Phenyl Conformation and Possible Dehydrogenation Reactions. *Chemistry-A European Journal*, 17(51):14354–14359, 2011.

[107] K. Weiss, G. Beernink, F. Dötz, A. Birkner, K. Müllen, and C. Wöll. Template?Mediated Synthesis of Polycyclic Aromatic Hydrocarbons: Cyclodehydrogenation and Planarization of a Hexaphenylbenzene Derivative at a Copper Surface. *Angewandte Chemie International Edition*, 38(24):3748–3752, 1999.

[108] S. Weigelt, C. Busse, C. Bombis, M. M. Knudsen, K. V. Gothelf, T. Strunskus, C. Wöll, M. Dahlbom, B. Hammer, E. Lægsgaard, F. Besenbacher, and T. R. Linderoth. Covalent Interlinking of an Aldehyde and an Amine on a Au(111) Surface in Ultrahigh Vacuum. *Angewandte Chemie*, 119(48):9387–9390, 2011.

[109] V. K. Kanuru, G. Kyriakou, S. K. Beaumont, A. C. Papageorgiou, D. J. Watson, and R. M. Lambert. Sonogashira Coupling on an Extended Gold Surface in Vacuo: Reaction of Phenylacetylene with Iodobenzene on Au(111). *Journal of the American Chemical Society*, 132(23):8081–8086, 2010.

[110] M. Di Giovannantonio, M. El Garah, J. Lipton-Duffin, V. Meunier, L. Cardenas, Y. Fagot Revurat, A. Cossaro, A. Verdini, D. F. Perepichka, F. Rosei, and G. Contini. Insight into Organometallic Intermediate and Its Evolution to Covalent Bonding in Surface-Confined Ullmann Polymerization. *ACS Nano*, 7(9):8190–8198, 2013.

[111] G. Hähner, M. Kinzler, Ch. Wöll, M. Grunze, M. K. Scheller, and L. S. Cederbaum. Near edge x-ray-absorption fine-structure determination of alkyl-chain orientation: Breakdown of the "building-block" scheme. *Phys. Rev. Lett.*, 67:851–854, Aug 1991.

[112] J. Stöhr and D. A. Outka. Determination of molecular orientations on surfaces from the angular dependence of near-edge X-ray-absorption fine-structure spectra. *Phys. Rev. B*, 36:7891–7905, Nov 1987.

[113] M. P. Lopez Sancho, J. M. Lopez Sancho, J. M. L. Sancho, and J. Rubio. Highly convergent schemes for the calculation of bulk and surface Green functions. *Journal of Physics F: Metal Physics*, 15(4):851, 1985.

[114] G. M. Su, S. N. Patel, C. D. Pemmaraju, D. Prendergast, and M. L. Chabinyc. First-Principles Predictions of Near-Edge X-ray Absorption Fine Structure Spectra of Semiconducting Polymers. *The Journal of Physical Chemistry C*, 121(17):9142–9152, 2017.

[115] K. Diller, F. Klappenberger, F. Allegretti, A. C. Papageorgiou, S. Fischer, A. Wiengarten, S. Joshi, K. Seufert, D. Écija, W. Auwärter, and J. V. Barth. Investigating the molecule-substrate interaction of prototypic tetrapyrrole compounds: Adsorption and self-metalation of porphine on Cu(111). *The Journal of Chemical Physics*, 138(15):154710, 2013.

[116] K. Diller, Y. Ma, Y. Luo, F. Allegretti, J. Liu, B. Z. Tang, N. Lin, J. V. Barth, and F. Klappenberger. Polyphenylsilole multilayers - an insight from x-ray electron spectroscopy and density functional theory. *Phys. Chem. Chem. Phys.*, 17:31117–31124, 2015.

[117] M. Taillefumier, D. Cabaret, A.-M. Flank, and F. Mauri. X-ray absorption near-edge structure calculations with the pseudopotentials: Application to the K edge in diamond and α-quartz. *Phys. Rev. B*, 66:195107, Nov 2002.

[118] C. Gougoussis, M. Calandra, A. P. Seitsonen, and F. Mauri. First-principles calculations of x-ray absorption in a scheme based on ultrasoft pseudopotentials: From α-quartz to high-T_c compounds. *Phys. Rev. B*, 80:075102, Aug 2009.

[119] P. Giannozzi, S. Baroni, N. Bonini, M. Calandra, R. Car, C. Cavazzoni, D. Ceresoli, G. L. Chiarotti, M. Cococcioni, I. Dabo, A. D. Corso, S. de.Gironcoli, S. Fabris, G. Fratesi, R. Gebauer, U. Gerstmann, C. Gougoussis, A. Kokalj, M. Lazzeri, L. Martin-Samos, N. Marzari, F. Mauri, R. Mazzarello, S. Paolini, A. Pasquarello, L. Paulatto, C. Sbraccia, S. Scandolo, G. Sclauzero, A. P. Seitsonen, A. Smogunov, P. Umari, and R. M. Wentzcovitch. QUANTUM ESPRESSO: a modular and open-source software project for quantum simulations of materials. *Journal of Physics: Condensed Matter*, 21(39):395502, 2009.

[120] C. Brouder. Angular dependence of X-ray absorption spectra. *Journal of Physics: Condensed Matter*, 2(3):701, 1990.

[121] C. Lanczos. Solution of systems of linear equations by minimized iterations. *J. Res. Natl. Bur. Stand*, 49:33–53, 1952.

[122] R. Haydock, V. Heine, and M. J. Kelly. Electronic structure based on the local atomic environment for tight-binding bands. II. *Journal of Physics C: Solid State Physics*, 8(16):2591, 1975.

[123] G. Kresse and J. Furthmüller. Efficiency of ab-initio total energy calculations for metals and semiconductors using a plane-wave basis set. *Computational Materials Science*, 6(1):15–50, 1996.

[124] G. Kresse and J. Hafner. Ab initio molecular dynamics for liquid metals. *Phys. Rev. B*, 47:558–561, Jan 1993.

[125] D. D. Johnson. Modified broyden's method for accelerating convergence in self-consistent calculations. *Phys. Rev. B*, 38:12807–12813, Dec 1988.

[126] G. Kresse and D. Joubert. From ultrasoft pseudopotentials to the projector augmented-wave method. *Phys. Rev. B*, 59:1758–1775, Jan 1999.

[127] J. Tersoff and D. R. Hamann. Theory of the scanning tunneling microscope. *Phys. Rev. B*, 31:805–813, Jan 1985.

[128] J. Stöhr and D. A. Outka. Determination of molecular orientations on surfaces from the angular dependence of near-edge x-ray-absorption fine-structure spectra. *Phys. Rev. B*, 36:7891–7905, 1987.

[129] R. Buczko, G. Duscher, S. J. Pennycook, and S. T. Pantelides. Excitonic Effects in Core-Excitation Spectra of Semiconductors. *Phys. Rev. Lett.*, 85:2168–2171, Sep 2000.

[130] B. Walker and R. Gebauer. Ultrasoft pseudopotentials in time-dependent density-functional theory. *The Journal of Chemical Physics*, 127(16):164106, 2007.

[131] E. Gaudry, D. Cabaret, C. Brouder, I. Letard, A. Rogalev, F. Wilhlem, N. Jaouen, and P. Sainctavit. Relaxations around the substitutional chromium site in emerald: X-ray absorption experiments and density functional calculations. *Phys. Rev. B*, 76:094110, Sep 2007.

[132] A. Juhin, C. Brouder, M.-A. Arrio, D. Cabaret, P. Sainctavit, E. Balan, A. Bordage, A.P. Seitsonen, G. Calas, S. G. Eeckhout, and P. Glatzel. X-ray linear dichroism in cubic compounds: The case of Cr^{3+} in $MgAl_2O_4$. *Phys. Rev. B*, 78:195103, Nov 2008.

[133] D. Cabaret, F. Mauri, and G. S. Henderson. Oxygen K-edge XANES of germanates investigated using first-principles calculations. *Phys. Rev. B*, 75:184205, May 2007.

[134] C. Ehlert, W. E. S. Unger, and P. Saalfrank. C K-edge NEXAFS spectra of graphene with physical and chemical defects: a study based on density functional theory. *Phys. Chem. Chem. Phys.*, 16:14083–14095, 2014.

[135] G. M. Rignanese and A. Pasquarello. Nitrogen 1s core-level shifts at the NH_3 saturated Si(100)-2×1 surface: a first-principles study. *Surface Science*, 490(1):614–618, 2001.

[136] G. M. Rignanese and A. Pasquarello. Nitrogen bonding configurations at nitrided Si(001) surfaces and Si(001)-SiO_2 interfaces: A first-principles study of core-level shifts. *Phys. Rev. B*, 63:075307, Jan 2001.

[137] O. Bunău and Y. Joly. Self-consistent aspects of X-ray absorption calculations. *Journal of Physics: Condensed Matter*, 21(34):345501, 2009.

[138] H. Aldahhak, S. Matencio, E. Barrena, C. Ocal, W. G. Schmidt, and E. Rauls. Structure formation in diindenoperylene thin films on copper(111). *Phys. Chem. Chem. Phys.*, 17:8776–8783, 2015.

[139] H. Aldahhak, E. Rauls, and W. G. Schmidt. Diindenoperylene adsorption on Cu(111) studied with density-functional theory. *Surface Science*, 641:260–265, 2015.

[140] A. K. Tripathi and J. Pflaum. Correlation between ambipolar transport and structural phase transition in diindenoperylene single crystals. *Applied Physics Letters*, 89(8):082103, 2006.

[141] A. C. Dürr, F. Schreiber, M. Münch, N. Karl, B. Krause, V. Kruppa, and H. Dosch. High structural order in thin films of the organic semiconductor diindenoperylene. *Applied Physics Letters*, 81(12):2276–2278, 2002.

[142] X. N. Zhang, E. Barrena, D. G. de Oteyza, E. De Souza, and H. Dosch. Growth of diindenoperylene single crystals on amino-functionalized SiO_2 surfaces. *Journal of Applied Physics*, 104(10):104308, 2008.

[143] S. Kowarik, A. Gerlach, S. Sellner, F. Schreiber, L. Cavalcanti, and O. Konovalov. Real-time observation of structural and orientational transitions during growth of organic thin films. *Phys. Rev. Lett.*, 96:125504, Mar 2006.

[144] S. Sellner, A. Gerlach, F. Schreiber, M. Kelsch, N. Kasper, H. Dosch, S. Meyer, J. Pflaum, M. Fischer, and B. Gompf. Strongly Enhanced Thermal Stability of Crystalline Organic Thin Films Induced by Aluminum Oxide Capping Layers. *Advanced Materials*, 16(19):1750–1753, 2004.

[145] C. Bürker, N. Ferri, A. Tkatchenko, A. Gerlach, J. Niederhausen, T. Hosokai, S. Duhm, J. Zegenhagen, N. Koch, and F. Schreiber. Exploring the bonding of large hydrocarbons on noble metals: Diindoperylene on Cu(111), Ag(111), and Au(111). *Phys. Rev. B*, 87:165443, Apr 2013.

[146] B. Schuler, W. Liu, A. Tkatchenko, N. Moll, G. Meyer, A. Mistry, D. Fox, and L. Gross. Adsorption Geometry Determination of Single Molecules by Atomic Force Microscopy. *Phys. Rev. Lett.*, 111:106103, Sep 2013.

[147] X. N. Zhang, D. G. de Oteyza, Y. Wakayama, and H. Dosch. STM study of diindenoperylene molecules on Cu(100) surfaces: Mobility, stability and epitaxy. *Surface Science*, 603(21):3179–3183, 2009.

[148] D. G. de Oteyza, E. Barrena, M. Ruiz-Osés, I. Silanes, B. P. Doyle, J. E. Ortega, A. Arnau, H. Dosch, and Y. Wakayama. Crystallographic and Electronic Structure of Self-Assembled DIP Monolayers on Au(111) Substrates. *The Journal of Physical Chemistry C*, 112(18):7168–7172, 2008.

[149] S. Wippermann and W. G. Schmidt. Entropy explains metal-insulator transition of the Si(111)-In nanowire array. *Phys. Rev. Lett.*, 105:126102, Sep 2010.

[150] H. Huang, J.-T. Sun, Y. P. Feng, W. Chen, and A. T. S. Wee. Epitaxial growth of diindenoperylene ultrathin films on Ag(111) investigated by LT-STM and LEED. *Phys. Chem. Chem. Phys.*, 13:20933–20938, 2011.

[151] T. Trevethan and A. L. Shluger. Building blocks for molecular devices:π-organic molecules on the MgO (001) surface. *The Journal of Physical Chemistry C*, 111(42):15375–15381, 2007.

[152] B. Hoff, M. Gingras, R. Peresutti, C. R. Henry, A. S. Foster, and C. Barth. Mechanisms of the adsorption and self-assembly of molecules with polarized functional groups on insulating surfaces. *The Journal of Physical Chemistry C*, 118(26):14569–14578, 2014.

[153] P. Rahe, M. Kittelmann, J. L. Neff, M. Nimmrich, M. Reichling, P. Maass, and A. Kühnle. Tuning molecular self-assembly on bulk insulator surfaces by anchoring of the organic building blocks. *Advanced Materials*, 25(29):3948–3956, 2013.

[154] B. Such, T. Trevethan, T. Glatzel, S. Kawai, L. Zimmerli, E. Meyer, A. L. Shluger, C. H. M. Amijs, P. de Mendoza, and A. M. Echavarren. Functionalized truxenes: Adsorption and diffusion of single molecules on the KBr(001) surface. *ACS Nano*, 4(6):3429–3439, 2010.

[155] L. Nony, F. Bocquet, F. Para, F. Chérioux, E. Duverger, F. Palmino, V. Luzet, and C. Loppacher. Dipole-driven self-organization of zwitterionic molecules on alkali halide surfaces. *Beilstein Journal of Nanotechnology*, 3:285–293, 2012.

[156] H. Aldahhak, W. G. Schmidt, and E. Rauls. Adsorption of PTCDA on NaCl(100) and KCl(100). *Surface Science*, 617:242–248, 2013.

[157] H. Aldahhak, W. G. Schmidt, and E. Rauls. Single PTCDA molecules on planar and stepped KCl and NaCl(100) surfaces. *Surface Science*, 641:278–281, 2015.

[158] Q. Guo, A. Paulheim, M. Sokolowski, H. Aldahhak, E. Rauls, and W. G. Schmidt. Adsorption of PTCDA on terraces and at steps sites of the KCl(100) surface. *The Journal of Physical Chemistry C*, 118(51):29911–29918, 2014.

[159] A. Paulheim, C. Marquardt, H. Aldahhak, E. Rauls, W. G. Schmidt, and M. Sokolowski. Inhomogeneous and homogeneous line broadening of optical spectra of PTCDA molecules adsorbed at step edges of alkali halide surfaces. *The Journal of Physical Chemistry C*, 120(22):11926–11937, 2016.

[160] A. Paulheim, C. Marquardt, M. Sokolowski, M. Hochheim, T. Bredow, H. Aldahhak, E. Rauls, and W. G. Schmidt. Surface induced vibrational modes in the fluorescence spectra of PTCDA adsorbed on the KCl(100) and NaCl(100) surfaces. *Phys. Chem. Chem. Phys.*, 18:32891–32902, 2016.

[161] M. Mura, X. Sun, F. Silly, H. T. Jonkman, G. A. D. Briggs, M. R. Castell, and L. N. Kantorovich. Experimental and theoretical analysis of H-bonded supramolecular assemblies of PTCDA molecules. *Phys. Rev. B*, 81:195412, May 2010.

[162] H. Karacuban, S. Koch, M. Fendrich, T. Wagner, and R. Möller. PTCDA on Cu(111) partially covered with NaCl. *Nanotechnology*, 22(29):295305–9, 2011.

[163] M. Möbus, N. Karl, and T. Kobayashi. Structure of perylene-tetracarboxylic-dianhydride thin films on alkali halide crystal substrates. *Journal of Crystal Growth*, 116(3):495–504, 1992.

[164] D. Schlettwein, A. Back, B. Schilling, T. Fritz, and N. R. Armstrong. Ultrathin films of perylenedianhydride and perylenebis(dicarboximide) dyes on (001) alkali halide surfaces. *Chemistry of Materials*, 10(2):601–612, 1998.

[165] S. A. Burke, J. M. Topple, and P. Grütter. Molecular dewetting on insulators. *Journal of Physics: Condensed Matter*, 21(42):423101, 2009.

[166] T. Dienel, C. Loppacher, S. C. B. Mannsfeld, R. Forker, and T. Fritz. Growth-mode-induced narrowing of optical spectra of an organic adlayer. *Advanced Materials*, 20(5):959–963, 2008.

[167] S. A. Burke, W. Ji, J. M. Mativetsky, J. M. Topple, S. Fostner, H. J. Gao, H. Guo, and P. Grütter. Strain induced dewetting of a molecular system: Bimodal growth of PTCDA on NaCl. *Phys. Rev. Lett.*, 100:186104, May 2008.

[168] M. Müller, J. Ikonomov, and M. Sokolowski. Structure of epitaxial layers of KCl on Ag(100). *Surface Science*, 605(11):1090–1094, 2011.

[169] S. A. Burke, J. M LeDue, J. M. Topple, S. Fostner, and P. Grütter. Relating the functional properties of an organic semiconductor to molecular structure by nc-AFM. *Advanced Materials*, 21(20):2029–2033, 2009.

[170] E. Le Moal, M. Müller, O. Bauer, and M. Sokolowski. Stable and metastable phases of PTCDA on epitaxial NaCl films on Ag(100). *Phys. Rev. B*, 82:045301, Jul 2010.

[171] A. Paulheim, M. Müller, C. Marquardt, and M. Sokolowski. Fluorescence spectroscopy of PTCDA molecules on the KCl(100) surface in the limit of low coverages: site selection and diffusion. *Phys. Chem. Chem. Phys.*, 15:4906–4913, 2013.

[172] B. Li, A. Michaelides, and M. Scheffler. Density functional theory study of flat and stepped NaCl(001). *Phys. Rev. B*, 76:075401, Aug 2007.

[173] F. Mohn, J. Repp, L. Gross, G. Meyer, M.S. Dyer, and M. Persson. Reversible bond formation in a gold-atom-organic-molecule complex as a molecular switch. *Phys. Rev. Lett.*, 105:266102, Dec 2010.

[174] J. Repp. *Rastertunnelmikroskopie und -Spektroskopie an Adsorbaten auf Metall- und Isolatoroberflächen.* Dissertation, Freie Universität, Berlin, 2002.

[175] J. E. Hove. Surface adsorption and migration energies for KCl. *Phys. Rev.*, 99:430–434, Jul 1955.

[176] S. Blankenburg, E. Rauls, and W. G. Schmidt. Catalytic Action of a Cu(111) Surface on Tetraazaperopyrene Polymerization. *The Journal of Physical Chemistry Letters*, 1(22):3266–3270, 2010.

[177] D. G. de Oteyza, H. Barrena, E.and Dosch, J. E. Ortega, and Y. Wakayama. Tunable symmetry and periodicity in binary supramolecular nanostructures. *Phys. Chem. Chem. Phys.*, 13:4220–4223, 2011.

[178] H. Aldahhak, M. Paszkiewicz, F. Allegretti, D. A. Duncan, S. Tebi, P. S. Deimel, P. Casado A., Y.-Q. Zhang, A. C. Papageorgiou, R. Koch, J. V. Barth, W. G. Schmidt, S. Müllegger, W. Schöfberger, F. Klappenberger, E. Rauls, and U. Gerstmann. X-ray Spectroscopy of Thin Film Free-Base Corroles: A Combined Theoretical and Experimental Characterization. *The Journal of Physical Chemistry C*, 121(4):2192–2200, 2017.

[179] H. Aldahhak, M. Paszkiewicz, E. Rauls, F. Allegretti, Tebi S., A. C. Papageorgiou, Y.-Q. Zhang, L. Zhang, T. Lin, T. Paintner, R. Koch, W. G. Schmidt, J. V. Barth, W. Schöfberger, S. Müllegger, F. Klappenberger, and U. Gerstmann. Identifying On-Surface Site-Selective Chemical Conversions by Theory-aided NEXAFS Spectroscopy: The Case of Free-Base Corroles on Ag(111). *Chemistry-A European Journal*, 24(26):6787–6797, 2018.

[180] S. Tebi, H. Aldahhak, G. Serrano, W. Schöfberger, E. Rauls, W. G. Schmidt, R. Koch, and S. Müllegger. Manipulation resolves non-trivial structure of corrole monolayer on Ag(111). *Nanotechnology*, 27(2):025704, 2016.

[181] S. Tebi, M. Paszkiewicz, H. Aldahhak, F. Allegretti, S. Gonglach, M. Haas, M. Waser, P. S. Deimel, P. C. Aguilar, Y.-Q. Zhang, A. C. Papageorgiou, D. A. Duncan, J. V. Barth, W. G. Schmidt, R. Koch, U. Gerstmann, E. Rauls, F. Klappenberger, W. Schöfberger, and S. Müllegger. On-Surface Site-Selective Cyclization of Corrole Radicals. *ACS Nano*, 11(3):3383–3391, 2017.

[182] Z. Gross and N. Galili. N-Substituted Corroles: A Novel Class of Chiral Ligands. *Angewandte Chemie International Edition*, 38(16):2366–2369, 1999.

[183] R. Paolesse, S. Mini, F. Sagone, T. Boschi, L. Jaquinod, D. J. Nurco, and K. M. Smith. 5,10,15-triphenylcorrole: a product from a modified rothemund reaction. *Chem. Commun.*, 14:1307–1308, 1999.

[184] A. E. Meier-Callahan, H. B. Gray, and Z. Gross. Stabilization of High-Valent Metals by Corroles: Oxo[tris(pentafluorophenyl)corrolato]chromium(V). *Inorganic Chemistry*, 39(16):3605–3607, 2000.

[185] D. T. Gryko and B. Koszarna. Refined methods for the synthesis of meso-substituted A_3- and trans-A_2B-corroles. *Org. Biomol. Chem.*, 1:350–357, 2003.

[186] Y. S. Balazs, I. Saltsman, A. Mahammed, E. Tkachenko, G. Golubkov, and Z. Levine, J.and Gross. High-resolution NMR spectroscopic trends and assignment rules of metal-free, metallated and substituted corroles. *Magnetic Resonance in Chemistry*, 42(7):624–635, 2004.

[187] I. Aviv and Z. Gross. Corrole-based applications. *Chem. Commun.*, 20:1987–1999, 2007.

[188] I. Aviv-Harel and Z. Gross. Aura of Corroles. *Chemistry-A European Journal*, 15(34):8382–8394, 2009.

[189] A. Mahammed and Z. Gross. Highly efficient catalase activity of metallocorroles. *Chem. Commun.*, 46:7040–7042, 2010.

[190] J. Radecki, I. Stenka, E. Dolusic, and W. Dehaen. Corroles as receptors in liquid membrane electrodes and their potentiometric response towards salicylic acid. *Electrochimica Acta*, 51(11):2282–2288, 2006.

[191] D. Walker, S. Chappel, B. S. Mahammed, A.and Brunschwig, J. R. Winkler, H. B. Gray, A. Zaban, and Z. Gross. Corrole-sensitized TiO_2 solar cells. *Journal of Porphyrins and Phthalocyanines*, 10(11):1259–1262, 2006.

[192] Z. Gross, N. Galili, and Saltsman I. The First Direct Synthesis of Corroles from Pyrrole. *Angewandte Chemie International Edition*, 38(10):1427–1429, 1999.

[193] I. Aviv-Harel and Z. Gross. Coordination chemistry of corroles with focus on main group elements. *Coordination Chemistry Reviews*, 255(7):717–736, 2011.

[194] G. R. Geier, J. F. B. Chick, J. B. Callinan, C. G. Reid, and W. P. Auguscinski. A Survey of Acid Catalysis and Oxidation Conditions in the Two-Step, One-Flask Synthesis of Meso-Substituted Corroles via Dipyrromethanedicarbinols and Pyrrole. *The Journal of Organic Chemistry*, 69(12):4159–4169, 2004.

[195] D. Aviezer, S. Cotton, M. David, A. Segev, N. Khaselev, N. Galili, Z. Gross, and A. Yayon. Porphyrin Analogues as Novel Antagonists of Fibroblast Growth Factor and Vascular Endothelial Growth Factor Receptor Binding That Inhibit Endothelial Cell Proliferation, Tumor Progression, and Metastasis. *Cancer Res.*, 60(11):2973–2980, 2000.

[196] J. Bendix, I. J. Dmochowski, H. B. Gray, A. Mahammed, L. Simkhovich, and Z. Gross. Structural, Electrochemical, and Photophysical Properties of Gallium(III) 5,10,15-Tris(pentafluorophenyl)corrole. *Angewandte Chemie International Edition*, 39(22):4048–4051, 2000.

[197] A. Mahammed and Z. Gross. Aluminum corrolin, a novel chlorophyll analogue. *Journal of Inorganic Biochemistry*, 88(3):305–309, 2002. 30th Anniversary.

[198] G. Golubkov, J. Bendix, H. B. Gray, A. Mahammed, I. Goldberg, A. J. DiBilio, and Z. Gross. High-Valent Manganese Corroles and the First Perhalogenated Metallocorrole Catalyst. *Angewandte Chemie*, 113(11):2190–2192, 2001.

[199] Z. Gross, L. Simkhovich, and N. Galili. First catalysis by corrole metal complexes: epoxidation, hydroxylation, and cyclopropanation. *Chem. Commun.*, pages 599–600, 1999.

[200] Z. Gross, G. Golubkov, and L. Simkhovich. Epoxidation Catalysis by a Manganese Corrole and Isolation of an Oxomanganese(V) Corrole. *Angewandte Chemie International Edition*, 39(22):4045–4047, 2000.

[201] L. Simkhovich, A. Mahammed, I. Goldberg, and Z. Gross. Synthesis and Characterization of Germanium, Tin, Phosphorus, Iron, and Rhodium Complexes of Tris(pentafluorophenyl)corrole, and the Utilization of the Iron and Rhodium Corroles as Cyclopropanation Catalysts. *Chemistry-A European Journal*, 7(5):1041–1055, 2001.

[202] J. Capar, J. Conradie, C. M. Beavers, and A. Ghosh. Molecular Structures of Free-Base Corroles: Nonplanarity, Chirality, and Enantiomerization. *The Journal of Physical Chemistry A*, 119(14):3452–3457, 2015.

[203] Z. Gross, N. Galili, L. Simkhovich, I. Saltsman, M. Botoshansky, D. Bläser, R. Boese, and I. Goldberg. Solvent-Free Condensation of Pyrrole and Pentafluorobenzaldehyde: A Novel Synthetic Pathway to Corrole and Oligopyrromethenes. *Organic Letters*, 1(4):599–602, 1999.

[204] L. M. Reith, M. Stiftinger, U. Monkowius, G. Knör, and W. Schöfberger. Synthesis and Characterization of a Stable Bismuth(III) A_3-Corrole. *Inorganic Chemistry*, 50(14):6788–6797, 2011.

[205] W. Schöfberger, F. Faschinger, S. Chattopadhyay, S. Bhakta, B. Mondal, J. A. A. W. Elemans, S. Müllegger, S. Tebi, R. Koch, F. Klappenberger, M. Paszkiewicz, J. V. Barth, E. Rauls, H. Aldahhak, W. G. Schmidt, and A. Dey. A Bifunctional Electrocatalyst for Oxygen Evolution and Oxygen Reduction Reactions in Water. *Angewandte Chemie International Edition*, 55(7):2350–2355, 2016.

[206] S. Kuck, G. Hoffmann, M. Bröring, M. Fechtel, M. Funk, and R. Wiesendanger. "Naked" Iron-5,10,15-triphenylcorrole on Cu(111): Observation of Chirality on a Surface and Manipulation of Multiple Conformational States by STM. *Journal of the American Chemical Society*, 130(43):14072–14073, 2008.

[207] M. Rashidi, S. Müllegger, M. Roithner, W. Schöfberger, and R. Koch. Spectroscopic Scanning Tunneling Microscopy Studies of Single Surface-Supported Free-Base Corroles. *Journal of the American Chemical Society*, 134(1):91–94, 2012.

[208] T. Ding, J. D. Harvey, and C. J. Ziegler. N-H tautomerization in triaryl corroles. *Journal of Porphyrins and Phthalocyanines*, 09(01):22–27, 2005.

[209] R. Buczko, G. Duscher, S. J. Pennycook, and S. T. Pantelides. Excitonic Effects in Core-Excitation Spectra of Semiconductors. *Phys. Rev. Lett.*, 85:2168–2171, 2000.

[210] M. Vittorio Nardi, R. Verucchi, L. Pasquali, A. Giglia, G. Fronzoni, M. Sambi, G. Mangione, and M. Casarin. XAS of tetrakis(phenyl)- and tetrakis(pentafluorophenyl)-porphyrin: an experimental and theoretical study. *Phys. Chem. Chem. Phys.*, 17:2001–2011, 2015.

[211] M. Röckert, M. Franke, Q. Tariq, D. Lungerich, N. Jux, M. Stark, A. Kaftan, S. Ditze, H. Marbach, M. Laurin, J. Libuda, H.-P. Steinrück, and O. Lytken. Insights in Reaction Mechanistics: Isotopic Exchange during the Metalation of Deuterated

Tetraphenyl-21,23D-porphyrin on Cu(111). *The Journal of Physical Chemistry C*, 118(46):26729–26736, 2014.

[212] K. Diller, R. J. Maurer, M. Müller, and K. Reuter. Interpretation of x-ray absorption spectroscopy in the presence of surface hybridization. *The Journal of Chemical Physics*, 146(21):214701, 2017.

[213] S. Kuck, M. Prostak, M. Funk, M. Bröring, G. Hoffmann, and R. Wiesendanger. Disposition of the axial ligand in the physical vapor deposition of organometallic complexes. *Journal of Vacuum Science and Technology A*, 28(4):795–798, 2010.

[214] C. Janiak. A critical account on π-π stacking in metal complexes with aromatic nitrogen-containing ligands. *J. Chem. Soc., Dalton Trans.*, pages 3885–3896, 2000.

[215] U. Fano. Effects of configuration interaction on intensities and phase shifts. *Phys. Rev.*, 124:1866–1878, Dec 1961.

[216] V. Madhavan, W. Chen, T. Jamneala, M. F. Crommie, and N. S. Wingreen. Tunneling into a Single Magnetic Atom: Spectroscopic Evidence of the Kondo Resonance. *Science*, 280(5363):567–569, 1998.

[217] J. Li, W.-D. Schneider, R. Berndt, and B. Delley. Kondo Scattering Observed at a Single Magnetic Impurity. *Phys. Rev. Lett.*, 80:2893–2896, Mar 1998.

[218] S. Müllegger, M. Rashidi, M. Fattinger, and R. Koch. Surface-Supported Hydrocarbon π Radicals Show Kondo Behavior. *The Journal of Physical Chemistry C*, 117(11):5718–5721, 2013.

[219] P. Schweyen, K. Brandhorst, R. Wicht, B. Wolfram, and M. Bröring. The Corrole Radical. *Angewandte Chemie International Edition*, 54(28):8213–8216, 2015.

[220] A. C. Papageorgiou, S. Fischer, S. C. Oh, Ö. Sağlam, J. Reichert, A. Wiengarten, K. Seufert, S. Vijayaraghavan, D. Écija, W. Auwärter, F. Allegretti, R. G. Acres, K. C. Prince, K. Diller, F. Klappenberger, and J. V. Barth. Self-Terminating Protocol for an Interfacial Complexation Reaction in Vacuo by Metal-Organic Chemical Vapor Deposition. *ACS Nano*, 7(5):4520–4526, 2013.

[221] G. Di Santo, C. Castellarin-Cudia, M. Fanetti, B. Taleatu, P. Borghetti, L. Sangaletti, L. Floreano, E. Magnano, F. Bondino, and A. Goldoni. Conformational Adaptation and Electronic Structure of 2H-Tetraphenylporphyrin on Ag(111) during Fe Metalation. *The Journal of Physical Chemistry C*, 115(10):4155–4162, 2011.

[222] A. Wiengarten, Julian A. Lioyd, K. Seufert, J. Reichert, W. Auwärter, R. Han, D. A. Duncan, F. Allegretti, S. C. Fischer, S.and Oh, Ö. Sağlam, L. Jiang, S. Vijayaraghavan, D. Écija, A. C. Papageorgiou, and J. V. Barth. Surface-Assisted Cyclodehydrogenation; Break the Symmetry, Enhance the Selectivity. *Chemistry - A European Journal*, 21(35):12285–12290, 2015.

[223] D. Pacilé, M. Papagno, A. Fraile Rodríguez, M. Grioni, L. Papagno, Ç. Ö. Girit, J. C. Meyer, G. E. Begtrup, and A. Zettl. Near-Edge X-Ray Absorption Fine-Structure Investigation of Graphene. *Phys. Rev. Lett.*, 101:066806, Aug 2008.

[224] Y. Gao, G. Hu, J. Zhong, Z. Shi, Y. Zhu, D. S. Su, J. Wang, X. Bao, and D. Ma. Nitrogen-Doped sp^2-Hybridized Carbon as a Superior Catalyst for Selective Oxidation. *Angewandte Chemie International Edition*, 52(7):2109–2113, 2013.

[225] N. Schmidt, R. Fink, and W. Hieringer. Assignment of near-edge x-ray absorption fine structure spectra of metalloporphyrins by means of time-dependent density-functional calculations. *The Journal of Chemical Physics*, 133(5):054703, 2010.

[226] N. A. Besley and F. A. Asmuruf. Time-dependent density functional theory calculations of the spectroscopy of core electrons. *Phys. Chem. Chem. Phys.*, 12:12024–12039, 2010.

[227] O. Bunău and Y. Joly. Time-dependent density functional theory applied to x-ray absorption spectroscopy. *Phys. Rev. B*, 85:155121, Apr 2012.

[228] J. Vogt and H. Weiss. The structure of NaCl(100) and KCl(100) single crystal surfaces: a tensor low energy electron diffraction analysis. *Surface Science*, 491:155–168, 2001.

[229] S. Froyen and M. L. Cohen. Structural properties of NaCl and KCl under pressure. *Journal of Physics C: Solid State Physics*, 19(15):2623, 1986.

[230] H. A. Hellwege and K. H. Landolt-Börnsteinr. *Structure Data of Organic Crystals.* Springer Verlag, Berlin, 1971.

[231] D. R. Lide and H. Frederikser. *handbook of chemistry and physics.* CRC Press, 1995.

[232] Z. G. Soos and B. J. Topham. Surface dipole of F4TCNQ films: Collective charge transfer and dipole-dipole repulsion in submonolayers. *Organic Electronics*, 12(1):3944, 2011.

[233] O. L. A. Monti. Understanding Interfacial Electronic Structure and Charge Transfer: An Electrostatic Perspective. *The Journal of Physical Chemistry Letters*, 3(17):2342–2351, 2012.

[234] X. Crispin, V. Geskin, A. Crispin, J. Cornil, R. Lazzaroni, W. R. Salaneck, and J.-L. Brédas. Characterization of the Interface Dipole at Organic/ Metal Interfaces. *Journal of the American Chemical Society*, 124(27):8131–8141, 2002.

[235] H. Vázquez, F. Flores, and A. Kahn. Induced density of states model for weakly-interacting organic semiconductor interfaces. *Organic Electronics*, 8(2):241–248, 2007. Coupled States of Excitons, Photons, and Plasmons in Organic Structures.

[236] F. Flores, J. Ortega, and H. Vázquez. Modelling energy level alignment at organic interfaces and density functional theory. *Phys. Chem. Chem. Phys.*, 11:8658–8675, 2009.

[237] L. Romaner, D. Nabok, P. Puschnig, E. Zojer, and C. Ambrosch-Draxl. Theoretical study of PTCDA adsorbed on the coinage metal surfaces, Ag(111), Au(111) and Cu(111). *New Journal of Physics*, 11(5):053010, 2009.

[238] B. Bröker, R.-P. Blum, J. Frisch, A. Vollmer, O. T. Hofmann, R. Rieger, K. Müllen, J. P. Rabe, E. Zojer, and N. Koch. Gold work function reduction by 2.2 eV with an air-stable molecular donor layer. *Applied Physics Letters*, 93(24):243303, 2008.

[239] M. DellAngela, G. Kladnik, A. Cossaro, A. Verdini, M. Kamenetska, I. Tamblyn, S. Y. Quek, J. B. Neaton, D. Cvetko, A. Morgante, and L. Venkataraman. Relating Energy Level Alignment and Amine-Linked Single Molecule Junction Conductance. *Nano Letters*, 10(7):2470–2474, 2010.

[240] A. Hauschild, K. Karki, B. C. C. Cowie, M. Rohlfing, F. S. Tautz, and M. Sokolowski. Molecular Distortions and Chemical Bonding of a Large π-Conjugated Molecule on a Metal Surface. *Phys. Rev. Lett.*, 94:036106, Jan 2005.

[241] W. Osikowicz, X. Crispin, C. Tengstedt, L. Lindell, T. Kugler, and W. R. Salaneck. Transparent low-work-function indium tin oxide electrode obtainedby molecular scale interface engineering. *Applied Physics Letters*, 85(9):1616–1618, 2004.

[242] C. Tengstedt, M. Unge, M. P. de Jong, S. Stafström, W. R. Salaneck, and M. Fahlman. Coulomb interactions in rubidium-doped tetracyanoethylene: A model system for organometallic magnets. *Phys. Rev. B*, 69:165208, Apr 2004.

[243] N. Johansson, T. Osada, S. Stafström, W. R. Salaneck, V. Parente, D. A. dos Santos, X. Crispin, and J. L. Brédas. Electronic structure of tris(8-hydroxyquinoline) aluminum thin films in the pristine and reduced states. *The Journal of Chemical Physics*, 111(5):2157–2163, 1999.

[244] O. T. Hofmann, P. Rinke, M. Scheffler, and G. Heimel. Integer versus Fractional Charge Transfer at Metal(/Insulator)/Organic Interfaces: Cu(/NaCl)/TCNE. *ACS Nano*, 9(5):5391–5404, 2015.

[245] P. Mori-Sánchez, A. J. Cohen, and W. Yang. Many-electron self-interaction error in approximate density functionals. *The Journal of Chemical Physics*, 125(20):201102, 2006.

[246] S. Müllegger, M. Rashidi, K. Mayr, M. Fattinger, A. Ney, and R. Koch. Radio-Wave Oscillations of Molecular-Chain Resonators. *Phys. Rev. Lett.*, 112:117201, Mar 2014.

[247] S. Müllegger, E. Rauls, U. Gerstmann, S. Tebi, G. Serrano, S. Wiespointner-Baumgarthuber, W. G. Schmidt, and R. Koch. Mechanism for nuclear and electron spin excitation by radio frequency current. *Phys. Rev. B*, 92:220418, Dec 2015.

[248] M. Ternes, A. J Heinrich, and W. D. Schneider. Spectroscopic manifestations of the Kondo effect on single adatoms. *Journal of Physics: Condensed Matter*, 21(5):053001, 2009.

[249] A. C. Hewson and J. Kondo. Kondo effect. *Scholarpedia*, 4(3):7529, 2009.

[250] S. T. Sekula. Resistance Minimum and Resistivity of Copper at Low Temperatures. *Phys. Rev. Lett.*, 3:416–418, Nov 1959.

[251] S. H. Liu. Effect of Short-Range Spin Correlation on the Electrical Resistivity of Dilute Magnetic Alloys. *Phys. Rev.*, 132:589–595, Oct 1963.

[252] U. Fano. Effects of Configuration Interaction on Intensities and Phase Shifts. *Phys. Rev.*, 124:1866–1878, Dec 1961.

[253] T. Komeda, H. Isshiki, J. Liu, Y.-F. Zhang, N. Lorente, K. Katoh, B. K. Breedlove, and M. Yamashita. Observation and electric current control of a local spin in a single-molecule magnet. *Nature Communications*, 2:217, 2011.

[254] W. Chen, T. Jamneala, V. Madhavan, and M. F. Crommie. Disappearance of the kondo resonance for atomically fabricated cobalt dimers. *Phys. Rev. B*, 60:R8529–R8532, Sep 1999.

[255] S. M. Cronenwett, T. H. Oosterkamp, and L. P. Kouwenhoven. A Tunable Kondo Effect in Quantum Dots. *Science*, 281(5376):540–544, 1998.

[256] K. Nagaoka, T. Jamneala, M. Grobis, and M. F. Crommie. Temperature Dependence of a Single Kondo Impurity. *Phys. Rev. Lett.*, 88:077205, Feb 2002.

[257] A. C. Hewson. *The Kondo Problem to Heavy Fermions*. Cambridge Studies in Magnetism. Cambridge University Press, 1993.

[258] F. Matthaei, S. Heidorn, K. Boom, C. Bertram, A. Safiei, J. Henzl, and K. Morgenstern. Coulomb attraction during the carpet growth mode of NaCl. *Journal of Physics: Condensed Matter*, 24(35):354006, 2012.

[259] I. Horcas, R. Fernández, J. M. Gómez-Rodríguez, J. Colchero, J. Gómez-Herrero, and A. M. Baro. WSXM: A software for scanning probe microscopy and a tool for nanotechnology. *Review of Scientific Instruments*, 78(1):013705, 2007.